Synthesis and self-assembly of molecular motors at interfaces

Wenzhi Wang

To cite this version:

Wenzhi Wang. Synthesis and self-assembly of molecular motors at interfaces. Other. Université de Strasbourg, 2021. English. NNT : 2021STRAF060 . tel-04743346

HAL Id: tel-04743346
https://theses.hal.science/tel-04743346v1

Submitted on 18 Oct 2024

UNIVERSITÉ DE STRASBOURG

ÉCOLE DOCTORALE DE SCIENCES CHIMIQUES (ED 222)

INSTITUR CHARLES SADRON, (UPR22-CNRS)

THÈSE présentée par :

Wenzhi WANG

soutenue le : 23 septembre **2021**

pour obtenir le grade de : **Docteur de l'université de Strasbourg**

Discipline/ Spécialité : Chimie supramoléculaire

Synthèse et auto-assemblage de moteurs moléculaires aux interfaces

THÈSE dirigée par :

Mme MOULIN Émilie	Directrice de Recherche, CNRS
M. GIUSEPPONE Nicolas	Professeur, Université de Strasbourg

RAPPORTEURS

Mme PASC Andreea	Professeure , Université de Lorraine
M. FUKS Gad	Maître de conferences HDR, Université de Perpignan

Table of content

I would like to dedicate this thesis in memory of my grandpa Wanyi WANG 王萬義

Acknowledgment

My deepest gratitude goes first and foremost to two of my supervisors, Prof. Nicolas Giuseppone and Dr. Emilie Moulin. for their constant encouragement and guidance. They give me a chance to become a member of the SAMS group. During the past three years, they gave me an interesting research area and offered me tremendous help. When I met difficulties in the experiments, they always offered instructive advice and useful suggestions. Their gifted knowledge in chemistry impressed me deeply. I am deeply grateful for their help in the completion of this thesis!

I would like to thank Prof. Mihail Barboiu, who led me into the world of ion channels. I am so lucky that can work in the IEM, Montpellier for nearly two months. His enthusiastic spirit and energetic research motivation let me how a perfect chemist could be. My experience in Montpellier is one of the best moments in my Ph.D. life!

Thank Dr. Andreas Vargas Jentzsch assist me solved the questions and assistance in the CD, patch-clamp, UV-vis, and all other experiments. Thank Odile Gavat for purifying my precious compounds by using the HPLC. Thank Marie-Céline Samy-Arlaye for always assist me to practice my poorly french and for her great help in the lab stuff.

Thank Gad Fuks from Université de Perpignan and Andrea Pasc (Université de Lorraine), for their examination of my thesis.

Thank Jean-Marc for his help in the HRMS test and Patrick Allgayer makes the perfect gel mold and clamp. Thank Leandro Jacomine for his help in the angle contact test. Thank Odile Lemble and Estelle Brunette for their help in the administration stuff.

I would also like to thanks all our lab 206 members, both currently and previously. Dr. Jean-Rémy Colard-Itté, Dr. Damien Dattler, Dania Daou, Dr. Erol Licsandru, Dr. Melodie Galerne, Dr. Pierre Lutz, Dr. Xuyang Yao for their daily help in the lab. And I would also thank other members in the SAMS group, Alessandro Cavasso, Alexis Perrot, Chuan Gao, Christian C. Carmona Vargas, Dr. Christian Rete, Dr. Shoichi Tokunaga, Dr. Flavio Picini, Dr. Lara Faour, Joakim Heiser, Dr. Frédéric Ribeiro, Maria Jesus Aguilera Roldan, Dr. Xianhe Liu, Dr. Xiaoqin Zhou, Philippe Schiel, Thiebault Chavez, Raphaël Pauchet, Sergio Fernandes, Nicolas Capit. For their help in all areas.

Thank Shaoping Zheng, Libo Huang, Dandan Su from the Institut Européen des Membranes, Montpellier, for they share their ‘know-how’ in the ion channel with me selflessly.

Special thanks should go to our ‘Coffee group’ in ICS, Yazhao Liu, Da Shi, Wenbing Wu, without the happy time together with them, the lab life will be less fantastic. Thanks to our ‘Travel group’: Yongxiang Zheng, Jun Sun, Yaowei Hu, we have nearly reached every corner of Alsace and Bartenwutenbourg in the past three years, it’s a great enjoyable time on the weekends! I would like to thank all the friends during my Ph.D. life, for their accompany and friendship, Lihan Sun, Chenhao Yao, Fangyu Fu, Huan Xu, Hongwei Li, Peizhao Liu, Xiao Wang, Xuwei Liu, Yao Zheng, Yue He, Yun Wang, and many others, we shared numerous exciting moments during these years, it’s a precious memory in my life.

Thanks to the University of Strasbourg and Institut Charles Sadron provides so convenient facilities for my Ph.D. research. Thanks to the Chinese Scholarship Council (CSC) provide me financial support during my Ph.D. career.

I would like to thank my grandparents, my aunt, my sisters, my brothers, and all my family members, their help and assistance let me know how precious the love is.

Last, my thanks would go to my beloved parents for their loving considerations and great confidence in me all through these years. They give me life and raised me, they always help me and encourage me. Without their great love, I cannot become what I am now.

Abbreviations and symbols

°C	celsius degree
Å	Ångstrom
B18C6	benzo[18]crown-6
Boc	tert-butyloxycarbonyl
Bn	benzyl
DCC	dicyclohexylcarbodiimide
CD	circular dichroism
COSY	correlation spectroscopy
δ	chemical shift
DCM	dichloromethane
DB24C8	dibenzo-[24]crown-8
DDQ	2,3-dichloro-5,6-dicyano-1,4-benzoquinone
DIEA	N,N-diisopropylethylamine
DIBAL-H	diisobutylaluminium hydride
DLS	dynamic ligation screening
DMF	N,N-dimethylformamide
DMSO	dimethylsulfoxide
DTT	dithiothreitol
EA	ethacrynic acid
EDC	1-ethyl-3-(3-dimethylaminopropyl)carbodiimide
EDTA	ethylenediaminetetraacetic acid
eq	equivalents
ESI	electrospray ionization
FDA	US Food and Drug Administration
g	gram
GC	gas chromatography
h	hour
HOBt	hydroxybenzotriazole
HPLC	high performance liquid chromatography
HPTS	8-hydroxypyrene-1,3,6-trisulphonic acid
Hz	Hertz
J	coupling constant
K	Kelvin
Ka	association constant
Kd	dissociation constant
K	equilibrium constant
kDa	kilodalton
μL	microliter
mol	micromole
mmol	millimole
MALDI-TOF	matrix assisted laser desorption/ionization time of flight
L	liter

LC/MS	liquid chromatography coupled to mass spectrometry
Me	methyl
mg	milligram
MHz	megahertz
min	minutes
mL	milliliter
mM	millimolar
mmol	millimole
mol	mole
MS	mass spectrometry
MW	micro wave
m/z	mass-to-charge ratio
NBS	N-bromosuccinimide
nM	nanomolar
NIR	near infrared
PBS	phosphate buffered saline
PDMS	polydimethylsiloxane
PEG	polyethylene glycol
PMDTA	*N,N,N′,N″,N″*-pentamethyldiethylenetriamine
PU	Polyurethane
SEM	scanning electronic microscopy
SPPS	solid-phase peptide synthesis
Sti	stilbene
t	time
*t*Bu	tert-butyl
TEA	triethylamine
TFA	trifluoroacetic acid
THF	tetrahydrofurane
TLC	thin layer chromatography
Trt	trityl
UPLC	ultra performance liquid chromatography
Upy	2-ureido-4[1H]-pyrimidinone
UV	ultra violet
v/v	volume per volume
Vis	visible
w/v	weight per volume
W	watt

Abstract

In nature, biological molecular motors play a key role in maintaining cells out of thermodynamic equilibrium and provide living systems with a number of advanced properties such as motions, transport, and catalysis of highly energetic molecules (e.g. ATP). To gain insights into these natural molecular motors and mimic their functional behaviors, scientists have designed in the past decades various kinds of molecular machines that can perform tasks. Among them, the amplification of individual molecular motions to the macroscopic scale has become one of the most interesting challenges to address. In addition, the utilization of artificial molecular motors in confined space is also a promising direction to mimic their biological counterpart which often function in denses matrices to achieve transport or catalysis. This work describes how unidirectional rotary molecular motors can work inside lipid bilayer membranes for the transport of alkali ion, and how they can produce collective motions to bend self-standing macroscopic gels to lift weights.

The first chapter is a selected bibliography of representative artificial molecular machines described to date, such as rotaxanes, catenanes, and light rotary molecular motors. A focus is made on the functioning principles of Feringa's light-rotary molecular motors because they are at the basement of a major part of the work pursued in this thesis. The prominent applications of these rotary motors are also introduced.

The second chapter describes how synthetic molecular motors can selectively boost ion transportation. A molecular motor-based compound bearing two 18-crown-6-ether macrocycles has been synthesized and investigated. The compound reveals good transportation activity for alkali ions because of the self-assembly property of the molecule and the cavity of the crown ether macrocycles. Under UV irradiation, the transportation activity is highly enhanced, owing to the rotation of the molecular motor. A series of experiments such as the HPTS fluorescence test and patch-clamp has been performed and prove this unprecedented observation. In particular, a number of control experiments supports how the out-of-equilibrium rotation of the molecular motor plays an important role in ion transportation.

The third chapter is focused on the collective motion of individual rotary molecular motors crosslinked in chemical gels. Contractile gels reported previously have been optimized and used for macroscopic and anisotropic actuations in order to perform weight lift-up tasks. The results show that such gels can undergo perfect directional actuation with high force.

The last part of this manuscript is dedicated to experimental protocols and descriptions of new chemical products.

Chapter 1: Light-driven molecular motors

1.1 Introduction

In the biological world, cells and organisms are maintained alive by a series of proteins that perform a variety of functional tasks out of thermodynamic equilibrium, going from transport to motion and catalysis.[1] In the past decades, scientific researchers have understood that these proteins often involve controlled internal motions of their subcomponents, and this is why they named them as biological machines or motors. The most famous motor proteins are certainly ATP synthase[2], myosin[3], and kinesin[4]. Their discovery and the understanding of their functioning principles have triggered the research interest towards the construction of artificial molecular machines.

In his 1959 famous speech 'There's plenty of room at the bottom', Richard Feynman proposed an unprecedented idea of building nanomachines.[5] In his idea, he suggested using small building blocks composed of atoms to construct molecular machines.

Inspired by natural biological motors, scientists have designed different types of artificial molecular motors that can be manipulated by various stimuli and perform several types of mechanical work.[6] Further, they envisionned that molecular motors can be used in many types of applications such a drug delivery, information storage and novel materials construction.[7] In 2016, the Nobel prize for Chemistry has been awarded to Professors Sauvage[8], Stoddart[9] and Feringa[10], for their prominent work in the development of molecular machines (**Figure 1**).

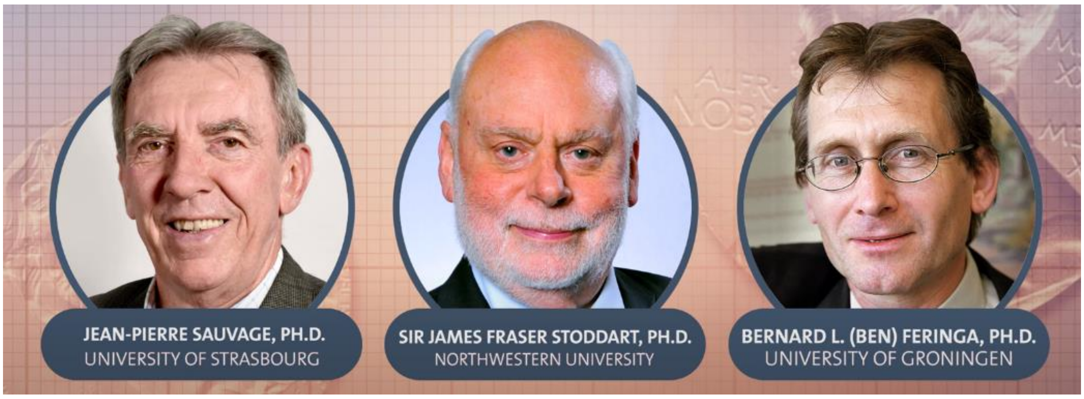

Figure 1. 2016 Nobel chemistry prize laureates. For their research of molecular machines: Catenane (Sauvage), Rotaxane (Stoddart), Molecular motor (Feringa).

Molecular motors can be defined as molecules that can respond to certain stimuli and actuate in a well-defined and controllable manner to generate mechanical work.[11] However, it is nontrivial to produce mechanical work and controllable movement at molecular scale. At the nanoscale level, molecular motors are in equilibrium with the omnipresent thermal noise caused by the Brownian motion of surrounding molecules, and have to work against this very strong disordering effect[12]. Hence the directionaliy of the motion is rapidly lost. In addition, at nanoscale, viscosity is stronger than inertial force by many orders of magnitudes, and therefore, the physical laws and functioning principles used by macroscopic motors do not apply at the molecular level[13]. Instead, molecular motors must absorb input of energy to bias Brownian motion in order to achieve mechanical cycles away from thermal equilibrium.

According to different structural properties, artificial molecular motors can be defined in several types: small size organic motors and large synthetic macromolecule motors. In any type of molecular motor, the input of energy is a vitally important thing to be considered. Molecular motors can be operated by diverse stimuli such as pH change[14], light irradiation[15] or chemical fuels[16]. But to undergo controllable motions, molecular machines should also present important structural features which allow precise displacements of several of their subcomponents. In particular, mechanical bonds that support the construction of interlocked molecules, and isomerization of configurational bonds, have been used to construct molecular machines. We will describe in the following parts some key examples of these categories.

1.2 Catenanes

A catenane is one of the most fundamental and simplest mechanically interlocked molecules, comprising of two or more rings closed with one another[17]. The catenane cannot be disassembled unless one of the units to be covalently broken. Nomenclature of catenanes are generally described as below:

$$[n]\text{catenane}$$

Where “n” represents the number of interlocked rings; for example a [2]catenane contains two interlocked rings.

Wasserman and coworkers firstly reported the synthesis of [2]catenane by statistical threading method, but in an extremely low yield.[18] Since then, chemists make efforts to improve the synthetic efficiency by directed design. Inspired by the weak noncovalent interaction-driven molecular recognition and self-assembly methods from supramolecular chemistry, Sauvage and coworkers developed a noncovalent template-based synthesis method of [2]catenane in 1983.[19] Numerous noncovalent interactions have been applied to the templated-directed synthesis of catenanes, such as metal-ligand coordination, dipole-dipole, hydrogen bonding and van der Waals, to induce an interwoven assembly of two or more molecules to be mechanically interlocked. The covalently captured complementary motifs used to construct the catenanes usually adopt the thermodynamically favored geometry. Owing to the reversibility of reactions under thermodynamic control, “proofreading” and “error checking” processes take place during the synthetic process, which provides huge advantages for the construction of interlocked molecules. Representative thermodynamically controlled reactions use to efficiently access interlocked molecules are metal-ligand coordination, imine bond formation/exchange, olefin metathesis, disulfide formation. A series of complementary recognition motifs and templates have been applied to the construction of [2]catenanes. The most commonly used templates are metal cations, donor/acceptor, hydrogen bonds, halogen bonds, hydrophobic effect and radical pairing.

As metionned above, the first template-directed synthesis of [2]catenane was reported by Sauvage and coworkers in 1983 (**Figure 2**)[20]. In this catenane, two phenanthroline moieties are bound in an orthogonal manner with the presence of copper(I), whose coordination prefers a tetrahedral geometry. The 2,9-diphenyl-1,10-phenanthroline ligand threads into the cavity of the macrocycle. Subsequently, Williamson etherifications of the phenolic moieties lead to macrocyclization and formation of the [2]catenane. The copper-free [2]catenane was obtained after demetallation with potassium cyanide.

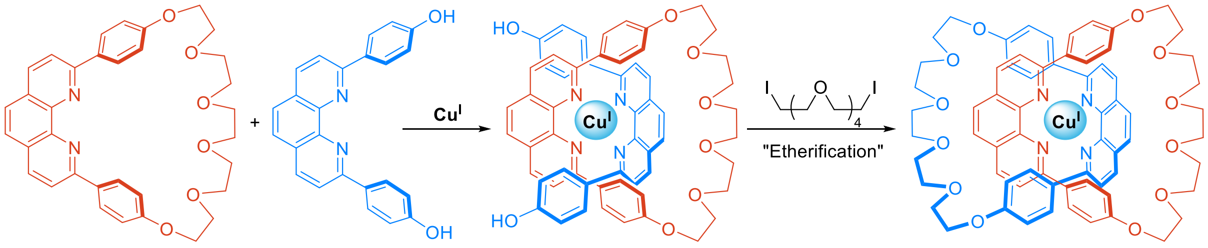

Figure 2. Cu(I)-phen coordination-directed synthesis of [2]catenane reported by Sauvage.

The development of various kinds of catenanes enriched greatly the topologies found in this large familly. Further, scientists tried to develop catenane-based molecular machines and motors, by controlling the intramolecular motion inside the catenanes. The design of such kind of catenane is based on the introduction of different stations on a large macrocycle, which is interlocked with a smaller ring, and with that smaller ring being capable of binding at these stations. In such kind of catenane rotor, the larger ring behaves as the stator while the smaller ring is the rotator.

In 2003, the Leigh group reported the first example of unidirectional movement in [3]catenane rotor (**Figure 3**).[21] The system consists of two macrocycles interlocked with each other through the benzylic amide. The larger macrocycle has four distinct stations: a fumaramide with secondary amides (A), a fumaramide with tertiary amides (B), a succinic amide ester (C), and an isolated amide (D). The affinity sequence of the different stations of the macrocycles is A> B> C> D.

At first, the two macrocycles are at stations A and B. Irradiating the system at λ = 350 nm (condition 1), fumaramide A photoisomerizes to a lower binding affinity conformation for the blue ring, which can move freely. Therefore, the blue ring moves counterclockwise to station C, because the clockwise direction is blocked by the red macrocycle. Irradiating the system at λ = 254 nm (condition 2), fumaramid B undergoes photoisomerization and causes the red macrocycle to move to station D counterclockwise, because the blue macrocycle blocks the clockwise direction. Heating the system to 100 ℃ resets stations A and B to their initial conformations. The red macrocycle present on station D moves to station A clockwise, and the blue macrocycle present on station C moves to station B counterclockwise. The macrocycles are thus again on the two most favorable stations, but their positions have been reversed. Applying a new cycle of conditions 1 → 2 → 3 will reset the system, and the macrocycles have both rotated counterclockwise around the larger macrocycle. Therefore, after several steps, the [3]catenane achieves a unidirectional 360 ° rotation.

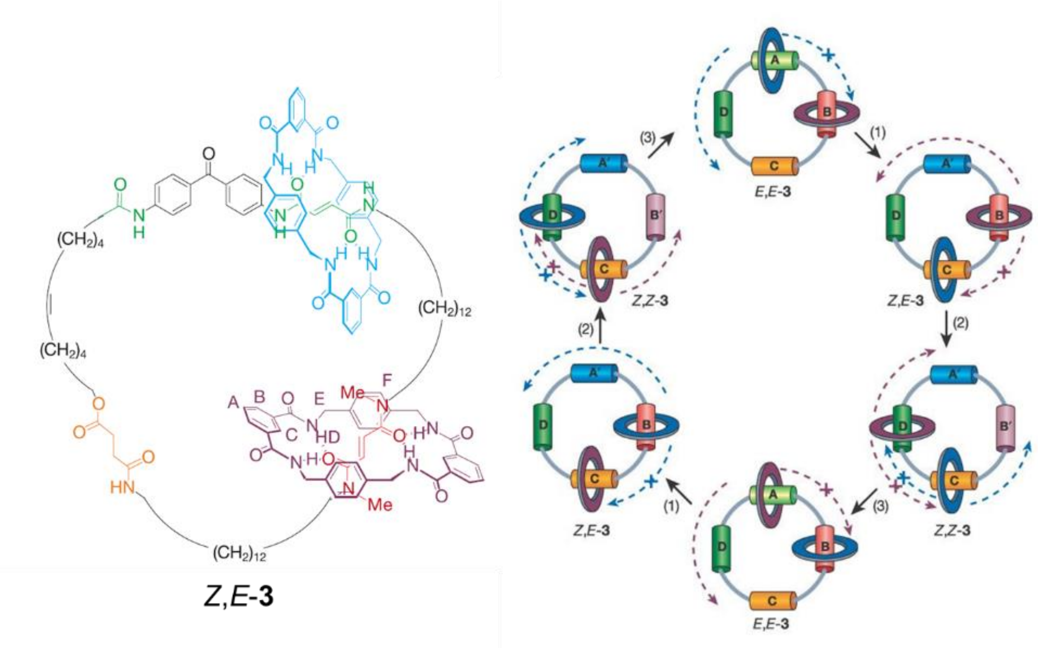

Figure 3. Chemical structure and the stimuli-induced unidirectional rotation in a four station [3] catenane: (1) 350 nm, CH_2Cl_2, 5 min, 67%; (2) 254 nm, CH_2Cl_2, 20 min, 50%; (3) heat, 100 ℃, $C_2H_2Cl_4$, 24h, ~100%; catalytic ethylenediamine, 50 ℃, 48 h, 65%; or catalytic Br_2, 400–670 nm, CH_2Cl_2, -78 ℃, 10 min, ~100%.

1.3 Rotaxanes

Rotaxanes are the other familly of famous mechanically interlocked molecules. They consist of linear guests and cyclic hosts bound together in a threaded shape through noncovalent interactions. Same as catenanes, the synthetic strategies to access catenanes were developed from statistical threading to template-directed synthesis.

In 1991, the Stoddart's group reported a bistable [2]rotaxane that consists of an axle with two binding stations threaded into a macrocycle (**Figure 4a**)[22]. The system composed a cyclobis(paraquat-p-phenylene) macrocycle (CBPQT^{4+}, blue box) shuttling between two identical hydroquinone stations placed a polyether axle termined by triisopropylsilyl groups used as stoppers to prevent dethreading. In this molecular shuttle, the blue box stops at the hydroquinone stations owing to a donor-acceptor interaction. When the blue box shuttles along the axle, the ^{1}H NMR signal of the hydroquinone stations split into two signals, indicating the blue box shares its position between the two hydroquinone stations. Because of the two identical stations on the axle, the proportion of bounded blue box is equally shared between them, and the speed of the shuttling motion is directed only by the temperature of the system.

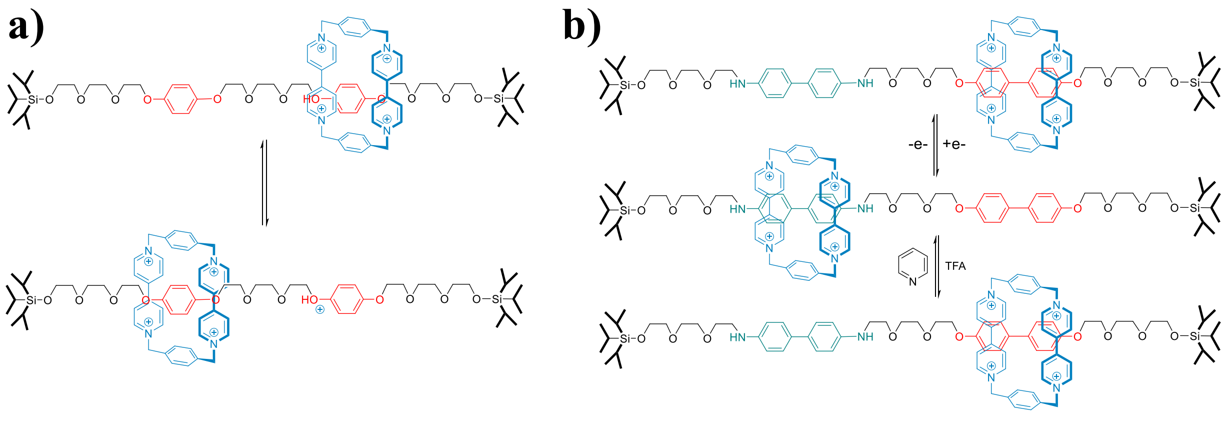

Figure 4. a) A symmetrical [2]rotaxane and b) an unsymmetrical [2]rotaxane reported by the Stoddart group.

An more advanced, that is unsymmetric [2]rotaxane, was described by the same group in 1994 (**Figure 4b**).[23] In this system, the linear axle contains both a benzidine group and a bisphenol group which act as two different donor stations capable of binding to the blue box macrocycle. Because the benzidine group behaves as a better donor than the bisphenol group, the blue box has a stronger binding constant when complexed with the benzidine unit. However, when the benzidine group is oxidized or protonated, the blue box shuttle moves toward the bisphenol station owing to the electrostatic repulsion force. Therefore, the blue box needs more energy to bind the benzidine station, pushing the ring to the energetically favored bisphenol station. Overall, it becomes possible to precisely determine the position of the ring over the thread by playing with external stimuli such as pH or redox potential.

Therefore, switchable rotaxanes have also become promising candidates for de design and synthesis of artificial molecular machines. The above works show that the molecular movements inside mechanically interlocked molecules can be efficiently controlled by modifying the axle and the ring correctly. A range of external stimuli such as chemicals, electricity, or light has been applied in these systems to control their relative motions, mostly under thermodynamic control. Beyond, chemists have recently tried to design artificial molecular pumps from rotaxanes, in particular for mimicking important processes to create gradients of chemicals in biology. In living systems, the out-of-equilibrium functioning of the cellular processes is highly dependent on the transportation of species across phospholipid membranes against a gradient of concentration, a process achieved by membrane-spanning carrier proteins using ATM as a source of energy. To mimic such natural transporters, chemists recently became interested in the development of minimal artificial molecular pumps, which can act against concentration gradients by pushing cargos from a low concentration region to a higher concentration one.

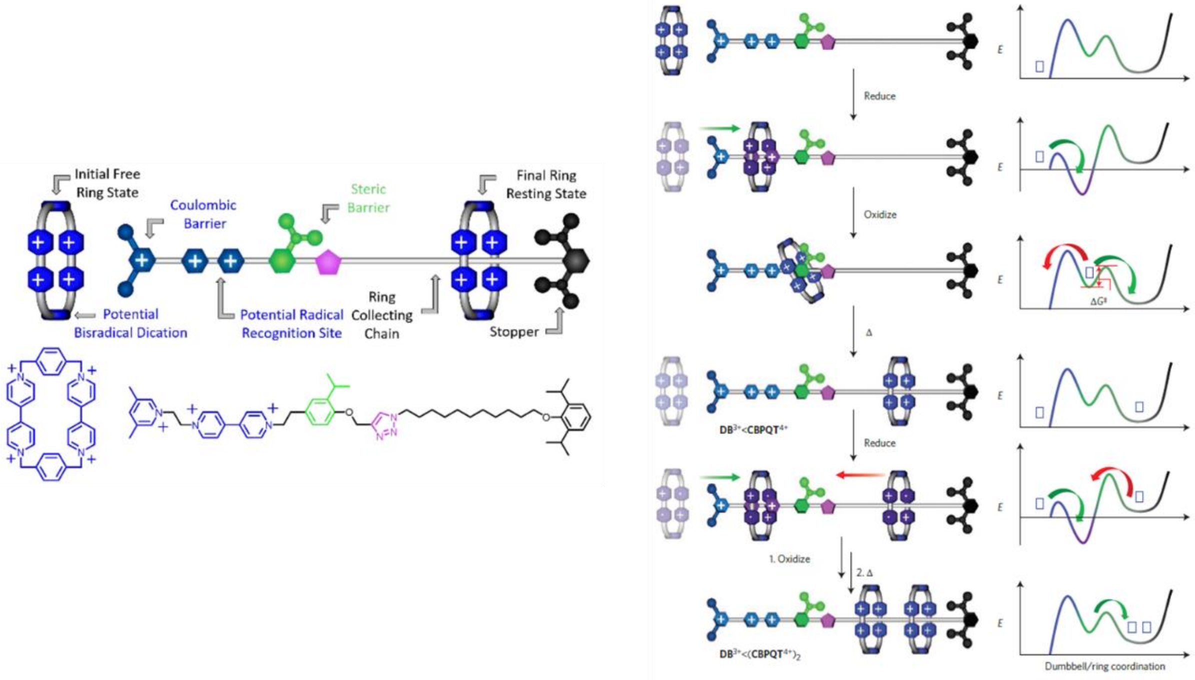

Figure 5. An artificial molecular pump.

Stoddart's group developed an ingenious artificial molecular pump in 2015 (**Figure 5**).[24] They designed and synthesized a dumbbell-shaped molecular pump that consists of a viologen recognition station, a 3,5-dimethylpyridinium as a Coulombic barrier, and an isopropyl phenyl unit as a steric speed bump. The isopropyl phenyl unit side was terminated with a bulky 2,6-diisopropyl phenol as a stopper. The redox pumping mechanism was based on a flashing energy ratchet mechanism. The first cycle of threading movements can happen between the axle and the blue box by electrochemical reduction, which enables the reduced CBPQT ring to pass over the 3,5-dimethylpyridinium owing to the radical-radical stabilizing interactions. Upon oxidation of the system, the Coulombic repulsion between the CBPQT^{4+} ring and the charged

4,4’-bipyridinium unit and 3,5-dimethylpyridinium units destabilized the complex. Consequently, the blue box overcomes the 2,6-diisopropyl phenol steric barrier and moves to the oligo ethylene chain. In the second cycle, the $CBPQT^{4+}$ ring was captured and reached in the ring collecting chain in the same mechanism as the first cycle. The number of cycles that can be achieved depends on the length of the chain. In this system, the molecular pump proved that driving the system away from equilibrium and can be operated repeatedly.

1.4 Light-driven rotary molecular motors

Among the various kinds of external stimuli to actuate molecular machines, light has numerous advantages because it does not produce wastes, because it can be remotely controlled, and because it can be precisely addressed in space and time. For example, by tuning the wavelength and intensity, light can be applied in a certain area with detailed power. Compared to light, it is more difficult for chemical reagents to be addressed in a specific location or concentration. One of the main problems with the use of light irradiation is the possible degradation of the molecular machines (or of the surrounding molecules) by phorodegradation. Improvements of chemical structures or special cares with irradiation conditions (such as freeze-thaw methods) should be often implemented.

1.4.1 First-generation molecular motors

The first example of a light-driven (rotary) molecular motor was reported by the group of Feringa in 1999 (**Figure 6**).[25]

This so-called “first generation” of molecular motors is composed of two identical halves connected by a central over-crowded alkene, which acts as the axis of motor rotation. Each half contains an additional methyl group as a stereogenic center, which is the crucial factor for the unidirectionality of the rotation step. The existence of the stereocenter prevents the molecule in a planar shape and causes a helicity inside the molecule. There should be four diastereoisomers that exist in natural conditions, but only *RR* and *SS* enantiomers can be obtained through the synthetic method employed. The stereocenter determined the conformation of the two halves. The methyl substituents at the stereocenter adopt an axial conformation to reduce the steric hindrance with another half part of the molecule. The steric hindrances between both the aromatic groups and the methyl substituents are at their minimum when the central over-crowded alkene are in the *trans*-configuration, the molecule here has the syn-fold conformation. Meanwhile, in the *cis*-configuration, the molecule shows the lowest energy when adopting the anti-fold conformation.

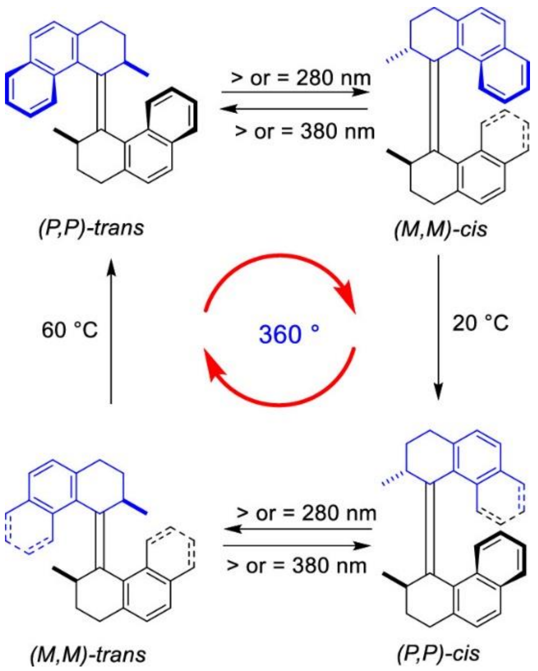

Figure 6. First-generation light-driven rotary molecular motor.

When irradiating the *trans*-configuration with UV light (λ = 280 nm), the motor molecule undergoes a (*P*, *P*)-*trans* to (*M*, *M*)-*cis* transformation. In the excited state, the central overcrowded alkene bond behaves more like a single bond and the rotation can be achieved. Owning to the steric hindrance between the two halves, the rotation is still limited and cannot finish the 360° rotation. Instead, a photoisomerization process takes place and results in the formation of the unstable *cis*-configuration. Under continuous irradiation, this photoisomerization state is reversible and result in a photostationary state between the *trans*-stable and *cis*-unstable.

The *trans*-*cis* photoisomerization around the central alkene bond leaves the methyl substituents in an equatorial conformation, which is an unfavorable state due to the steric hindrance. The strained configuration is released by a thermal helix inversion process. To finish this process, the aromatic parts of both halves need to slide past each other, which allows the methyl substituents to regain the thermally favorable axial conformation and contributing to the (*P*, *P*)-*cis* stable state.

The second photoisomerization takes place from (*P*, *P*)-*cis* stable state to (*M*, *M*)-*trans* unstable state, leaving the methyl substituent in an energetically unfavorable equatorial conformation. This process is a photo equilibrium and a photostationary state is reached. To release the steric hindrance, a thermal helix inversion process takes place and the methyl substituents regain the thermally favorable axial conformation. Hence, the molecule reached the (*P*, *P*)-*trans* stable state again. In sum, a 360° full rotation is achieved, and it can be iterated cyclicly with the same directionality. The whole rotation cycle is composed of two photo-isomerization steps (usually considered as fast) and two thermal helix inversion steps (usually considered as rate limiting).

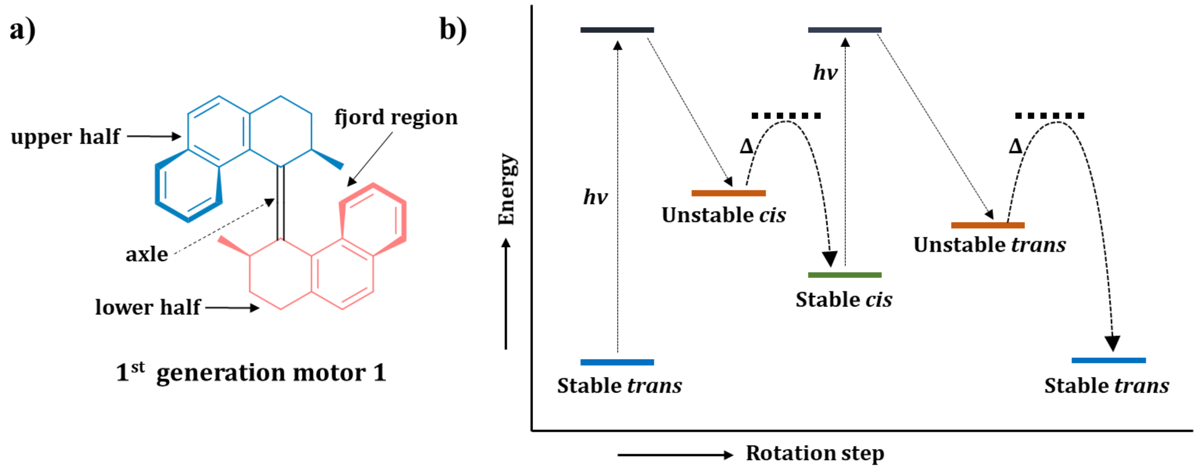

Figure 7. a) Chemical presentation of the first generation rotary molecular motor. b) General energy explanation of one whole rotary cycle.

The successful synthetic access to the first-generation of light rotary molecular motors opens the door for the construction of optical nanodevices which can convert light energy into mechanical work at molecular scale. Still, there are some limitations with such kinds of motors in order to perform useful tasks due to their slow rotation speed. The group of Feringa spent a lot of efforts to improve the rotation speed which can be achieved by playing on the thermal helix inversion by tuning its molecular structure.

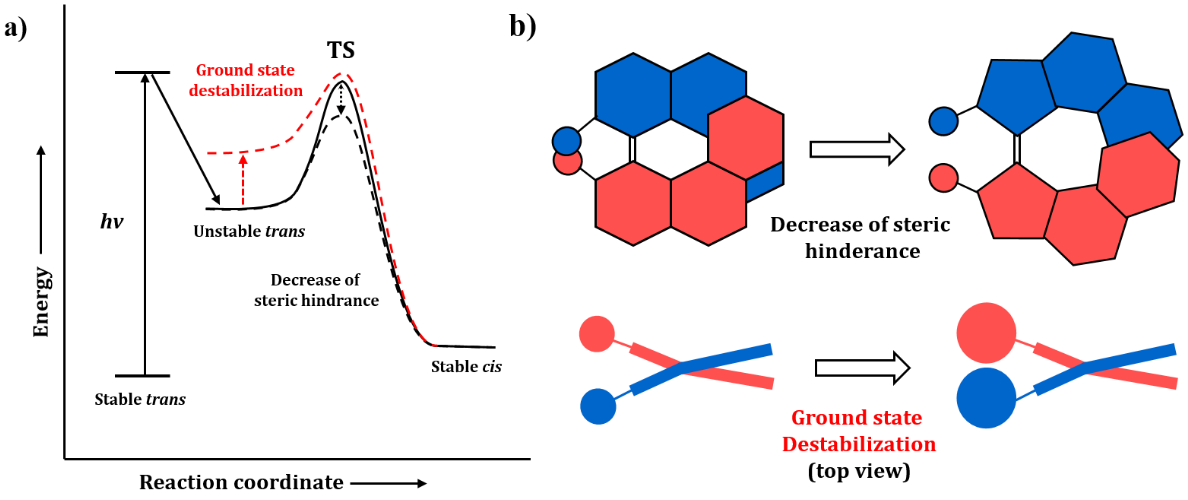

Figure 8. a) Simplified presentation of the energy profile describing how to increase the rotation speed by decreasing the steric hindrance in the fjord region and / or destabilizing the unstable state relative to the transition state. b) Schematic illustration of the structural features to accelerate the thermal helix inversion step following the energy profiles described in (a).

As mentioned above, the thermal helix inversion (THI) step determines the rotation rate of the cycle, and the steric hindrance of the *fjord* region (**Figure 7a**) was considered to be an important factor in affecting the THI. Therefore, lowering the Gibbs free energy of activation of this step was the dominant point for realizing a higher rotation speed. Increasing the energy of the unstable state relative to the transition state is a good method to lowering the Gibbs free energy of activation in the thermal helix inversion step. Hence, the size of the groups at the stereogenic center was studied, and a series of molecular motors with different structures were synthesized to investigate the influence of the substituents in the stereogenic position.

1.4.2 Second-generation molecular motors

The second-generation molecular motors is composed of two different halves connected by a central overcrowded bond. The stator is replaced by a tricyclic aromatic anthracene-type group, so only one stereogenic center remained in the rotor part.[26]

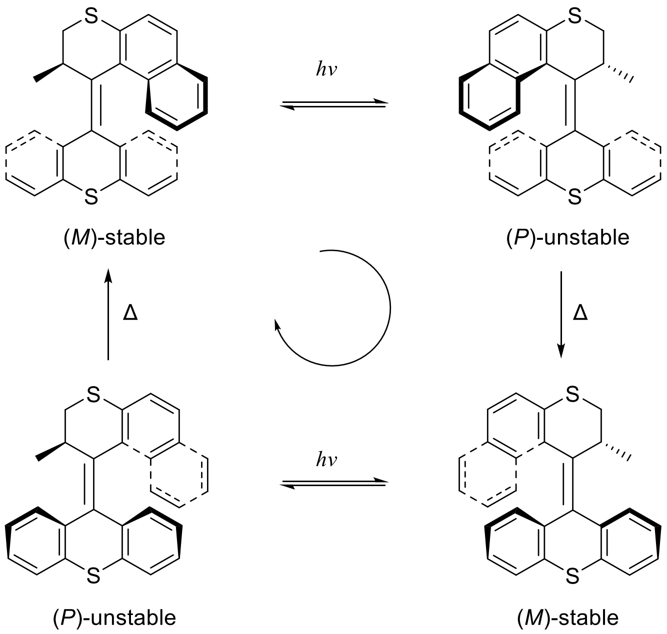

Figure 9. First-generation light-driven rotary molecular motor.

The rotation mechanism is similar to that of the first-generation motor (**Figure 9**). Firstly, a *trans-cis* photoisomerization occurred under the irradiation of UV light, resulting in the helicity change of the whole molecule and leaves it in a thermally unfavorable situation. The methyl substituent in the stereogenic center of this conformation stays in an equatorial orientation, which pushes it to the lower half part. To release this steric strain, the molecule undergoes a thermal helix inversion step subsequently and regenerates a thermal favorable axial orientation. Up to now, the molecule has reached a 180° rotation. After another photoisomerization step and thermal helix inversion, the molecule finishes a full rotation cycle.

Note that in the case of **Figure 9**, because of the symmetry of the bottom part, the energetic diagram can be described only by a 180° rotation, and that by spectroscopic techniques, only two species can be discriminated among the 4 steps of the full rotation cycle.

The unidirectional rotation process of the second-generation motor is dominated by the stereogenic center in the rotor part. Same to the first-generation motors, a series of second-generation motors with different structures were synthesized to study the rotation process (**Figure 10**).

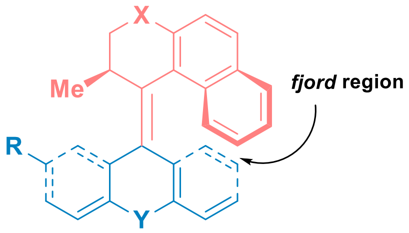

Motor	X	Y	R	k(20) [s^{-1}]	$\Delta^{\ddagger}G°$ [kJ mol^{-1}]	$t_{1/2}$(20°C) [h]
1	S	S	OMe	$1.04*10^{-6}$	105.2	184
2	S	S	H	$8.95*10^{-6}$	105.6	215
3	S	O	H	$7.32*10^{-6}$	100.5	26.3
4	S	$C(CH_3)_2$	H	$8.26*10^{-6}$	106.0	233
5	CH_2	S	H	$2.89*10^{-6}$	91.8	0.67
6	CH_2	$C(CH_3)_2$	H	$9.59*10^{-6}$	94.4	2.01
7	CH_2	CH=CH	H	$3.21*10^{-6}$	102.7	60.1

Figure 10. Kinetic parameters for the thermal helix inversion of selected second-generation motors with various bridge atoms **X** and **Y**

When both sides of the alkene central bond were six-membered rings, the motor appeared to have a slower rotation speed. The existence of the six-membered ring endows the molecule a flexible property and has several conformations that are in similar energy.[27] A series of molecular motors with different **X** or **Y** atoms at the heterocycles were synthesized to study the rotation speed. The rotation speed of the first second-generation molecular motor was found to be very slow. The Gibbs value for the thermal helix inversion step is up to 106 kJ/mol, resulting in an extremely long half-life time as high as 233 h. As the methods to lower the thermal helix inversion barrier for accelerating the speed in the first-generation motor, the same strategy was applied to the second-generation motor. The methods include reducing the steric hindrance in the *fjord* region and destabilizing the unstable state relative to the transition state.

Change of the atom in the **X** or **Y** position can change the $\Delta^{\ddagger}G°$ dramatically.[28] Changing the volume of the atoms in the **Y** position for a larger or a smaller one, the Gibbs free energy of activation will change and accelerate or decrease the corresponding rotation speed.

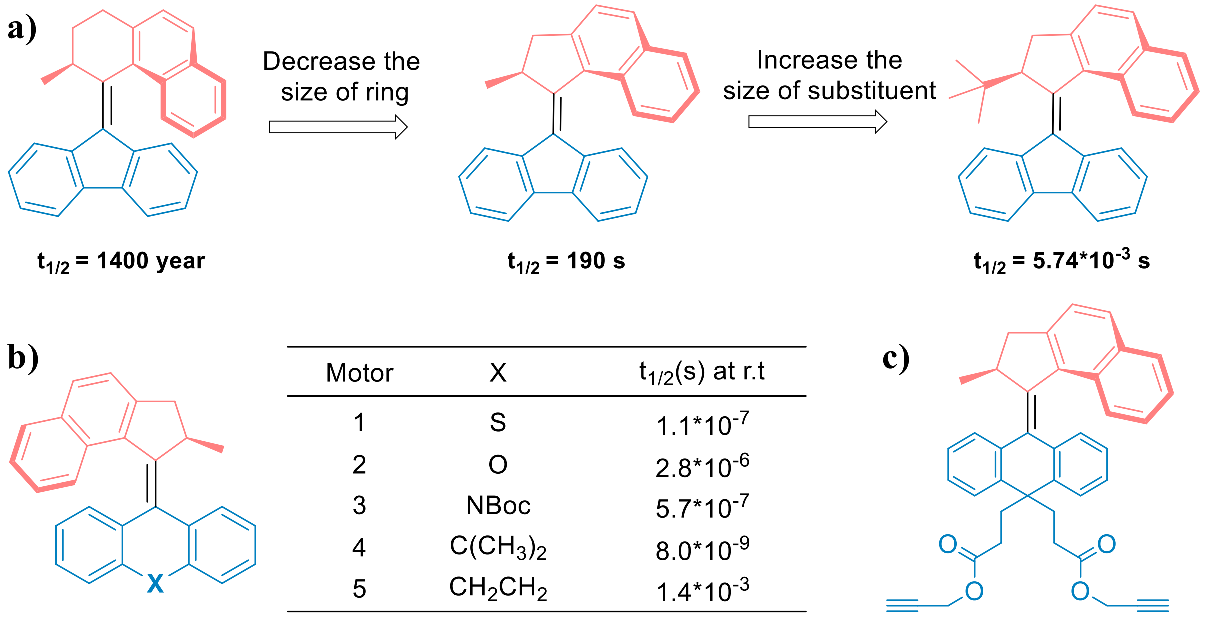

Motor	X	$t_{1/2}$(s) at r.t
1	S	1.1*10^{-7}
2	O	2.8*10^{-6}
3	NBoc	5.7*10^{-7}
4	$C(CH_3)_2$	8.0*10^{-9}
5	CH_2CH_2	1.4*10^{-3}

Figure 11. a). Increasing the rotation speed by decrease the ring size and increase the substituent size. b). Tuning the rotation speed by changing the **X** atom at the stator. c). The fastest rotary motor ever reported.

Another approach to reducing the steric hindrance is to change the six-membered ring in the upper part to a five-membered ring, the thermal helix inversion barrier was a dramatic decrease from 1400 years to 190 s (**Figure 11**).

In the biological world, the biological motors often need to reverse their rotation direction to perform opposite mechanical works[29]. To mimic this kind of behavior by an artificial molecular motor is an important stereochemical challenge.

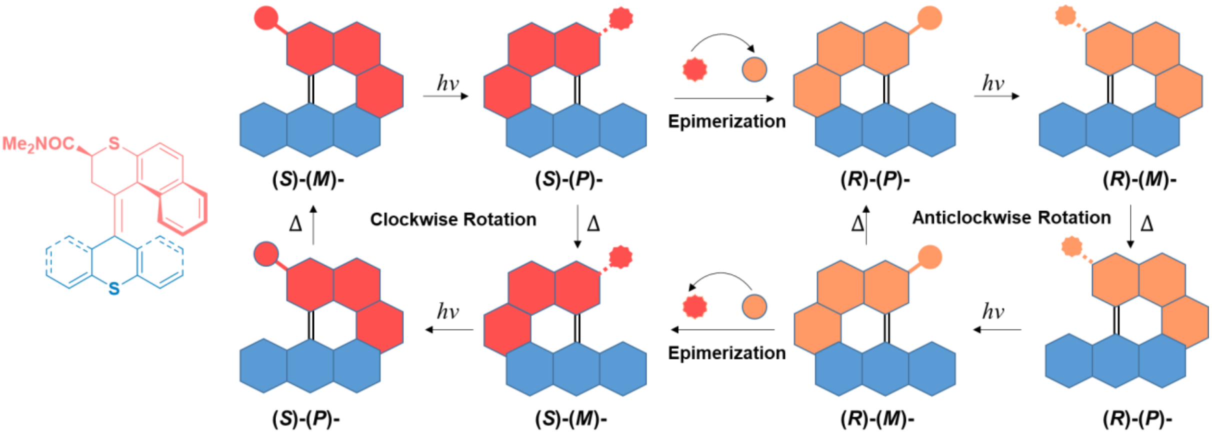

Figure 12. Chemical structure of the new motor and schematic presentation of clockwise and anticlockwise rotation process.

In 2010,[30] Feringa and co-workers reported a multilevel controllable molecular motor which can perform both clockwise and anticlockwise rotation, with the direction of photo-driven rotation being reversed by base-catalyzed epimerization (**Figure 12**). The unidirectionality is determined by the configuration at the stereogenic center, which provides the possibility to reverse the rotation direction from clockwise to anticlockwise by changing its chirality. To achieve this goal, base-catalyzed epimerization happened at the stereogenic center of the unstable isomer, which can be transformed to a stable isomer but in the opposite stereochemistry. In the design of this new motor, the electron-withdrawing group (EWG) was introduced to the stereogenic center at the 3’ position of the six-member ring at the upper part. The existence of EWG increases the acidity of the nearby proton and enhanced the selective deprotonation to promote epimerization.

The whole rotation process can be described as follows: the clockwise rotation starts from a photoinduced isomerization to transform (*S*)-(*M*)- to the unstable (*S*)-(*P*)- isomer, in which the EWG group is in a sterically disfavored pseudoaxial orientation. The less stable (*S*)-(*P*)-isomer could either convert into a stable (*S*)-(*M*)- state through a thermal helix inversion or undergo deprotonation to form an enolate by treatement with a base. The following protection results in the epimerization of the previous stereocenter to produce anther (*S*)-(*P*)- stable isomer in another enantiomer. An anticlockwise rotation occurrs from another photoinduced isomerization starting from the (*S*)-(*P*)- isomer. Therefore, upon the base-catalyzed epimerization of the stereogenic center, both the forward and backward rotation can be achieved in a single molecular motor molecule. The reversibility of the rotation direction of the motor paves the interest to develop new kinds of motor to perform relevant mechanical tasks.

1.4.3 Third-generation molecular motor

The intrinsic chirality of amino acids endows the biological molecular motors a controllable directionality, which is important for operating relevant mechanical tasks[31]. In biological systems, the rotation direction is determined by the point chirality transformed into helical chirality and chiral macromolecular assemblies. In synthetic molecular motors, the rotation direction is determined by the point chirality, as it controls the thermodynamical helix inversion step. In Feringa’s first and second-generation rotary molecular motors, the stereogenic center is one of the important factors to determine the unidirectionality of the rotation process. Compared with the first generation motor that needs two stereogenic centers for unidirectionality, the second generation motor only needs one stereogenic center. Therefore, it raised the question of whether a stereogenic center was essential for the unidirectional rotary? In previous studies, Leigh and co-workers found that in mechanically interlocked motors, when certain chemical steps can be applied to trigger rotation, the chirality is not essential to be contained in the molecule structure.[32-33] So it would be of fundamental interest to achieve a directional rotation in an achiral overcrowd rotary molecular motors.

The second-generation of rotary molecular motors inspired the construction of achiral molecular motor; this so-called "third-generation" of motors consists of meso derivatives comprising a single stereogenic center (*R* or *S* chirality) and a helical structure (*P* or *M* helicity) (**Figure 13**)[34]. The central (*R* or *S*) chirality of the motor determined the direction of the photo-induced rotation. The *M* helicity induces the clockwise rotation caused by repetitive photoisomerization and thermal helix inversion steps, while the clockwise rotary rotation is discovered in the *M*-helical structure. A single photoinduced *trans*-to-*cis* isomerization happened under the UV irradiation at -100 °C, producing a mixture of two different metastable isomers and the starting compound. Following thermal helix inversion at room temperature was happened in darkness to afford (r, *E*, *E*)- and (r, *Z*, *Z*)- isomers, finishing a half rotation cycle.

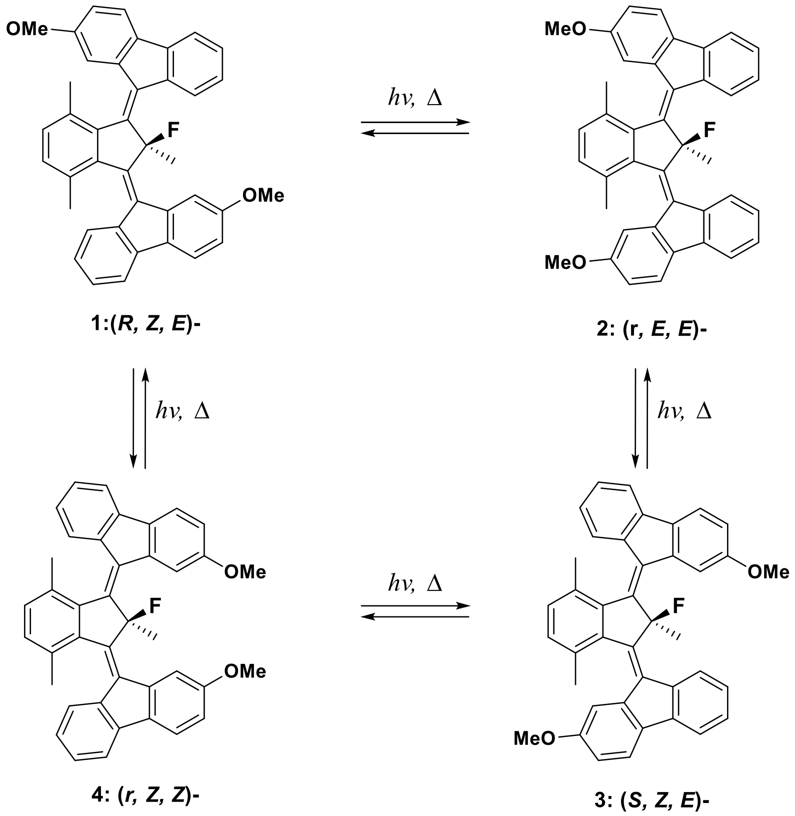

Figure 13. The rotational cycle of third-generation molecular motor happened in individual isomers.

1.4.4 Molecular motors based on Thioindigo and imines

Inspired by the studies on hemithioindigo switches, Dube and co-workers develop a novel light-activated molecular motor (**Figure 14**).[35] The new molecular motor comprises a thioindigo motif and a stilbene unit linked by a central alkene bond. By introducing two stereochemical components into the molecular structure, i.e. a stereocenter on the sulfur atom (*R* and *S* configurations) and a helical conformation (*P* and *M* helicites) around the alkene bond, the motor can achieve a full unidirectional rotation cycle. There are four different energetically (meta)stable states that were found. To have a clear explanation, only one isomer will be discussed here. Similar to Feringa's motor, this new system rotates around the alkene bond in four steps, including two photoisomerization steps and two thermal helix inversion steps. Under the irradiation of visible light, the *Z*-(*S*)-(*P*) is photoisomerized to *E*-(*S*)-(*M*), then convert into *E*-(*S*)-(*P*) upon a THI step. Further irradiation of the system transforms this compound in *Z*-(*S*)-(*M*), and Z-(*S*)-(*P*) is finally regenerated after THI. Unstable intermediates were confirmed by transient absorption measurements and high-level theoretical calculations. This hemithioindigo-based motor system can be opreated with visible light and is capable of kHz rotation speed at 20 °C, which is considered to be the fastest visible-light-driven artificial molecular motor to date.

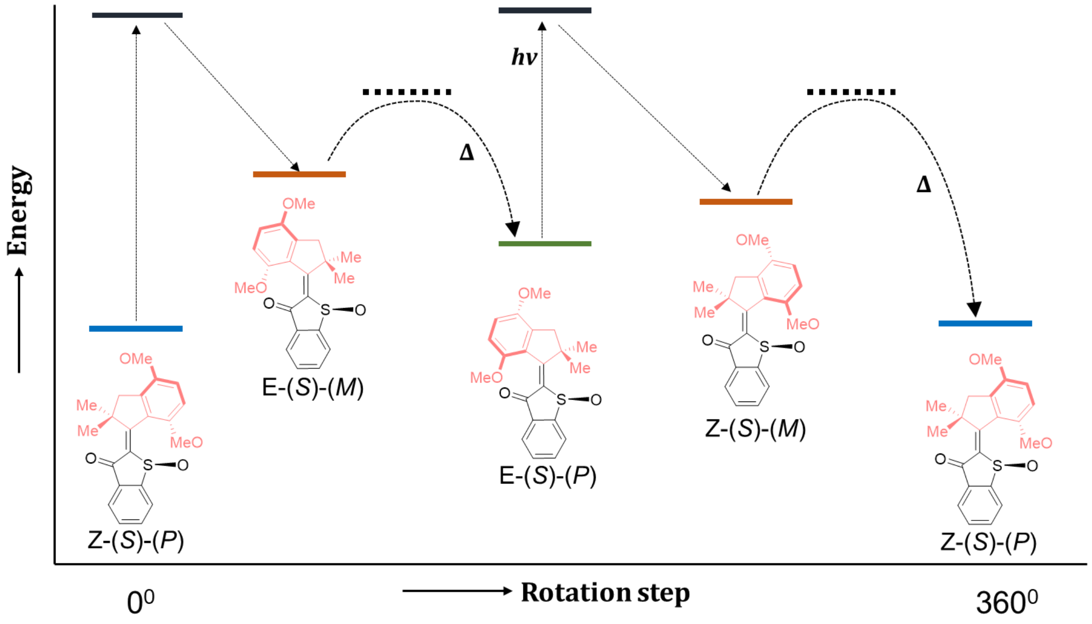

Figure 14. Simplified energy profile for the 360° visible light-powered unidirectional rotation of the hemithioindigo-based motor.

The imine bond is also a promising candidate to construct molecular motors, because it contains an unsymmetrically substituted C=N bond and can be present in *E* or *Z* isomers. Lehn and collaborators reported the first imine-based light-driven unidirectional rotary motor in 2014 (**Figure 15**).[36] The design of the molecular motor was based on the diaryl-N-alkyl imine, which could exhibit an *E*-*Z* isomerization at room temperature. Upon irradiation, the (*P*)-*cis* photoisomerized into *trans*-configuration through the rotation around the C=N double bond, leading to the formation of (*M*)-*trans* stereoisomer. The unstable state relaxes to a more stable state through a thermal helix inversion process. This step can happen because of the flexibility of the aromatic ring of the stator, which can flip out of the plane. Another half rotation around the C=N double bond leads to the formation of the unstable (*M*)-*cis* stereoisomer, and completes a full 360° rotation after the thermal helix inversion step.

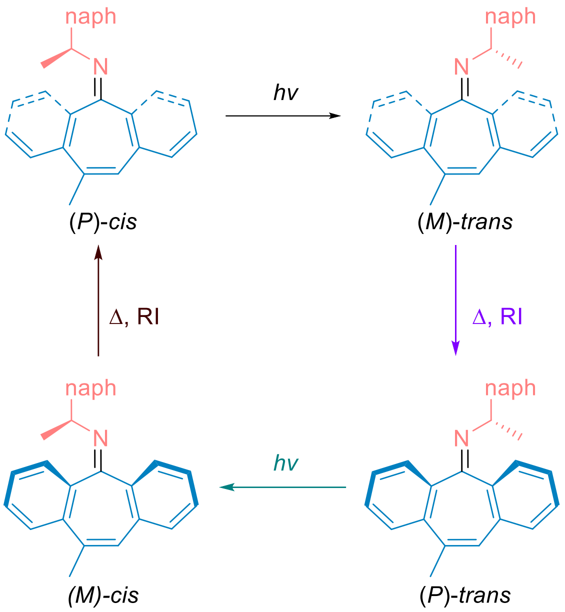

Figure 15. The unidirectional rotation process of the imine-based molecular motor.

1.5. Applications of Feringa's light-driven molecular motors

1.5.1 Construction of smart materials

Metal-organic frameworks (MOFs) have attracted huge interest in recent years. However, the combination of the molecular motor with MOFs has remained a challenge for a long time. Recently, Feringa and co-workers successfully inserted molecular motors into MOFs (**Figure 16**).[37] In this novel crystalline material, the light-driven rotary molecular motor was in a good position and can be activated in the solid-state. The molecular motor needs adequate space to perform the rotation functionality, so it is important to well organize the packing position of the units. In this 3D architecture, the motor units behave as organic linkers. The structure and dimensional positioning were demonstrated by a battery of experiments, such as X-ray analyses, Raman microscopy and polarized optical microscopy. The above experiments also proved the unencumbered unidirectional rotation in the solid framework, with a similar rotation speed to that was detected in the solution. The ingenious construction of motor-MOF not only enriches the MOF community but provides the possibility of creating dynamically controllable crystalline materials.

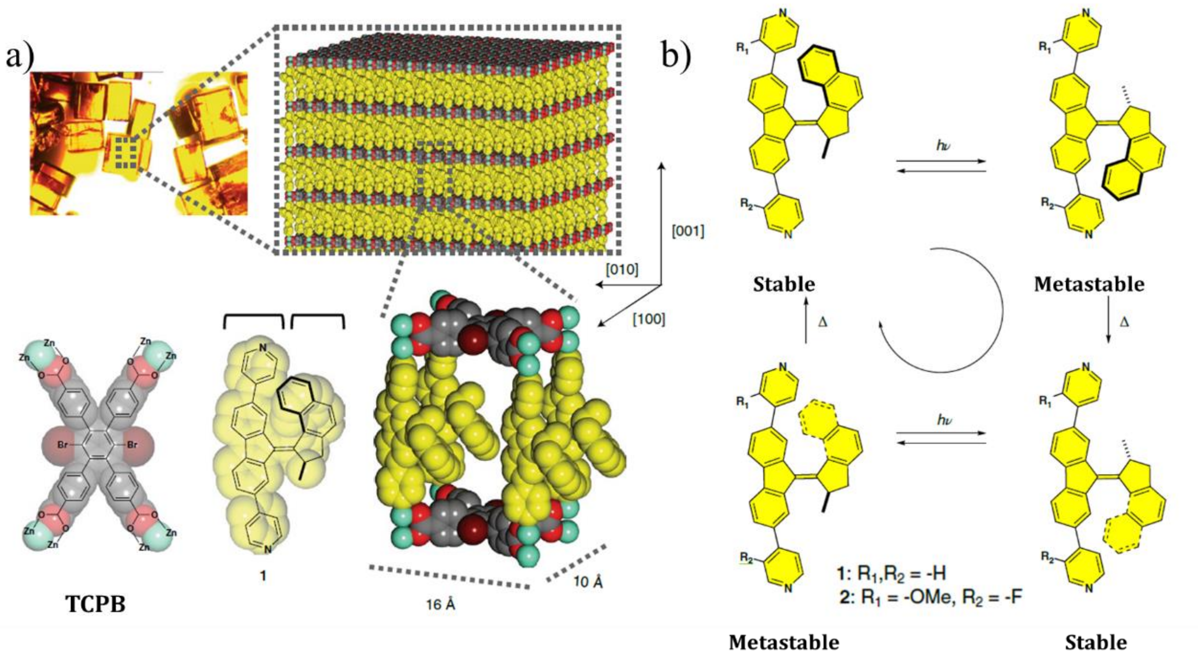

Figure 16. a) Schematic presentation of the design of the light-driven rotary molecular motor containing motor-MOF; b) The 360° unidirectional rotary cycle of the molecular motor.

The incorporation of the unidirectional rotary molecular motor in MOF opened up a new avenue for constructing functional solid materials. During the past decades, there are few solid materials based on photoswitch that have been reported. However, the large volume photoisomerization in the solid-state materials has several drawbacks, such as weaker light-penetration intensity and low isomerization efficiency because of the geometrical restriction. In 2020, Feringa and collaborators reported a photo-responsive porous switchable framework by integrating overcrowded alkene into a framework skeleton (**Figure 17**).[38] The required framework was constructed between tetra-*p*-bromo-phenylmethane and dibromo-appendant chiroptical switch through the Yamamoto cross-coupling reaction. The photochemical isomerization of the photoswitch in the solid framework was demonstrated by diffuse-reflectance UV-vis and Raman spectroscopies. Upon irradiation at 365nm or 470nm, red shift or blue shift was observed respectively, showing that the photoswitch exhibits wavelength-dependent isomerization reversibility in the solid state. When the material was exposed to 365nm, the color change was visible, which is consistent with the redshift of the absorption spectra. Furthermore, solid-state NMR studies of the photoswitch-containing framework proved that the existence of the photostationary state ratio of the chiroptical switch in the framework was as high as that in solution. Moreover, the gas absorption experiments were performed on the framework and found that can be modulated many cycles with light and heat. The reversibility can be attributed to the large percentage of photoisomerization in the materials. This finding provides new insights in the construction of novel responsive porous materials that can complete original tasks such as tunable size-based isolation methods.

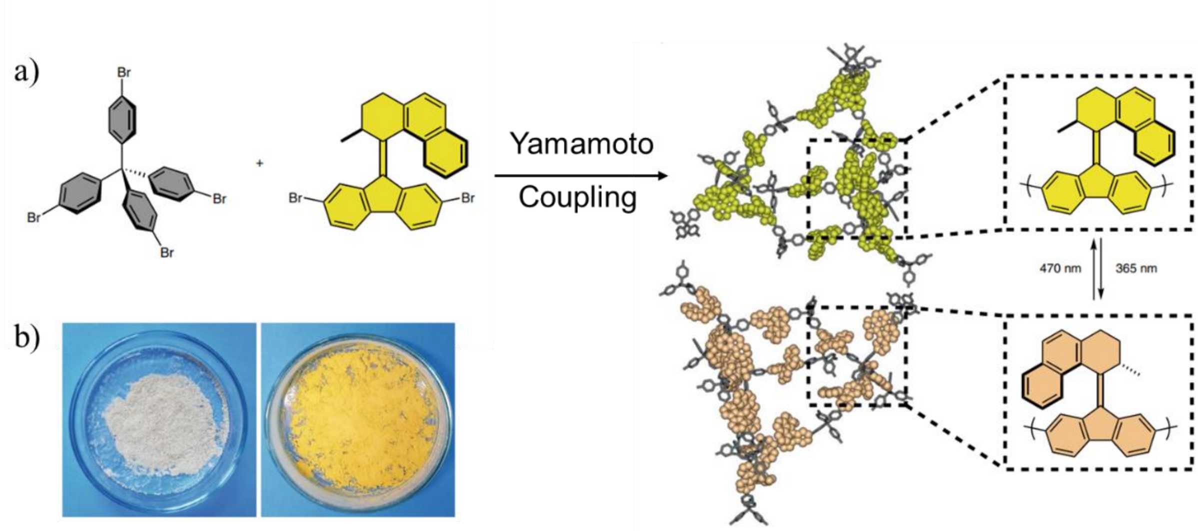

Figure 17. a) Schematic representation of the synthesis of the porous switchable framework and the light-induced isomerization of the molecular motor units. b) Photograph of the color change of the materials under UV irradiation at 365nm for half an hour. Before (left) and after (right) respectively.

1.5.2 On surfaces

In solution, molecules are constantly submitted to random Brownian movements in their environment, and to overcome this problem in the production of an efficient mechanical work, biological molecular motors such as kinesin or myosin are interfaced with fixed elements in space.[39,40] Inspired by biological motors, scientists endeavor to develop artificial molecular motors which can be linked to a surface covalently or by electrostatic interactions. In such configurations, the nanoscale actuation produced by single molecular switches or motors can be amplified to mechanical actuations at larger scale, and one can control for instance the wettability of surfaces or trigger molecular recognition or cargo transportation. These applications have huge potential interests for future technologies such as light-responsive biomaterials.

To illustrate and implement the interfacial approach described above, the construction of motorized nano cars of molecular size has become an area of interest. Tour and coworkers reported in 2005 the first artificial nanocar, a rectangular organic molecule with four fullerene molecules playing the role of rolling wheels.[41] Scanning tunneling microscopy (STM) technique was performed to study the isolated nanocars on a gold surface. Owing to the high adhesion force between the gold surface and the fullerene units, the experiments revealed the nanocar can keep stable on the surface up to 170 °C. At a higher degree (200 °C), both the translation motion and pivoting motion were observed. Obviously, these movements are not produced by a motorized action of the wheels and cannot be considered from the production of a mechanical work. In the following studies, Tour and coworkers synthesized and investigated a series of different nano cars.

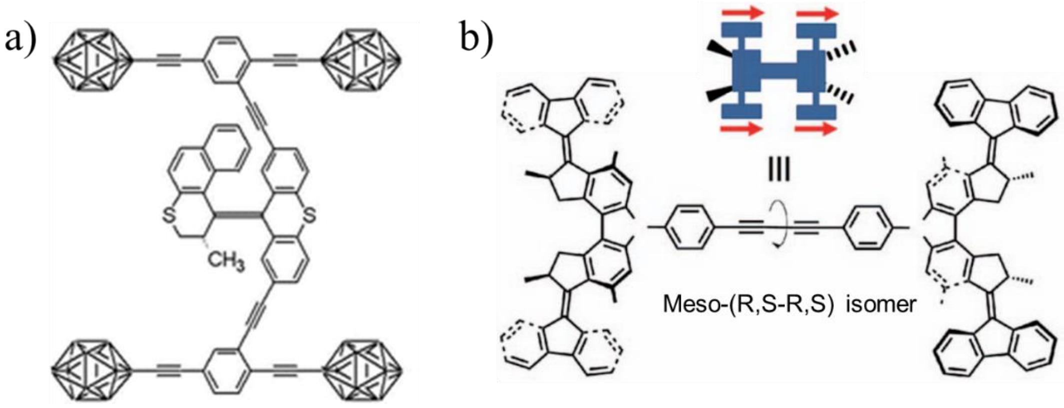

Figure 18. a) The motorized nano car reported by Tour et.al. b) The motor car reported by Feringa et.al.

In 2006, they reported the first motorized nano car (**Figure 18a**), an organic molecule with four *p*-carborane as the rolling wheel and a second-generation Feringa motor as the ‘engine’.[42] In 2011, they ungraded the 2006 invention by replacing the motor with an MHz rotating motor. In 2015 [43] and 2017 [44], they reported the fluorescent motorized nano car, consisting of four adamantane units as the rolling wheels, two Bodipy dyes in the axles, and a molecular motor in the center as the engine. Although most of these endeavors did not achieve the initial goal, their work provided tremendous experiences thoughts of molecule design and monitoring methods for future explorations.

The most prominent work in this area was achieved by Feringa and coworkers in 2011(**Figure 18b**).[45] They reported a nanocar that comprises four light-activated molecular motors as the rolling wheels, instead of the spherical molecule units. When this nanocar was put on a Cu(III) surface and when a STM tip was used to apply an electrical excitation to the molecular motor, the nanocar was proved to move forward due to the unidirectional rotation of the motors. The researchers found that though the excitation induced several isomers, only the *meso-(R,S-R,S)* isomer can achieve a linear translocation movement. All of the molecular motors in this isomer can rotate in the same direction, resulting in a paddlewheel-style movement. After ten excitations, the *meso-(R,S-R,S)* isomer nano car can finish a 6nm near-linear movement. The control experiments show also that when the motors are placed in the wrong position (or when having different geometries), the nanocar cannot perform a directional movement, but displays instead a random move across the surface. Although the rotation of the motor was activated by STM tip rather than light, this example has been the first example of translocation movement achieved by an artificial molecular motor. The design of this nano car also provides sights for developing manmade smart mechanical nanodevices.

Besides nanocars, lots of attempts have been launched toward the covalent linkage of molecular motors on surfaces. Surface functionalization provides possibilities of developing light stimuli-responsive systems in which interfacial properties can be modulated by the rotation of molecular motors. The commonly used surfaces to be functionalized usually include glass, quartz, and gold. Many types of molecular machines, and more particularly molecular motors, have been successfully covalently linked to these surfaces.

In 2005, Feringa and coworkers have successfully placed their molecular motors at the surface of gold nanoparticles (**Figure 19a**).[46] The bottom part of the motor was decorated with thiol terminated aliphatic chains, which can be covalently linked to the gold surface. The linkers were long enough to prevent hindering of the photoisomerization process, and the two link points can avoid the random rotation of the whole motor. The gold nanoparticle was chosen because it was small enough to use the typical investigation techniques such as NMR, UV-vis spectroscopies to study the motor rotations, other materials such as film cannot fulfill these requirements. When the motor was linked to the gold surface, it can keep the unidirectional rotation property (the $t_{1/2}$ of the THI is 12×10^3 s), though with a lower speed compared to its freedom state (the $t_{1/2}$ of the THI is 56×10^2 s). Latterly, they reported a similar system but with a slower motor and on a quartz surface.[47] Experiments show the motor can keep the unidirectional rotation property on the quartz surface. These examples push the research to more precise nanodevices that can perform rotation under stimuli.

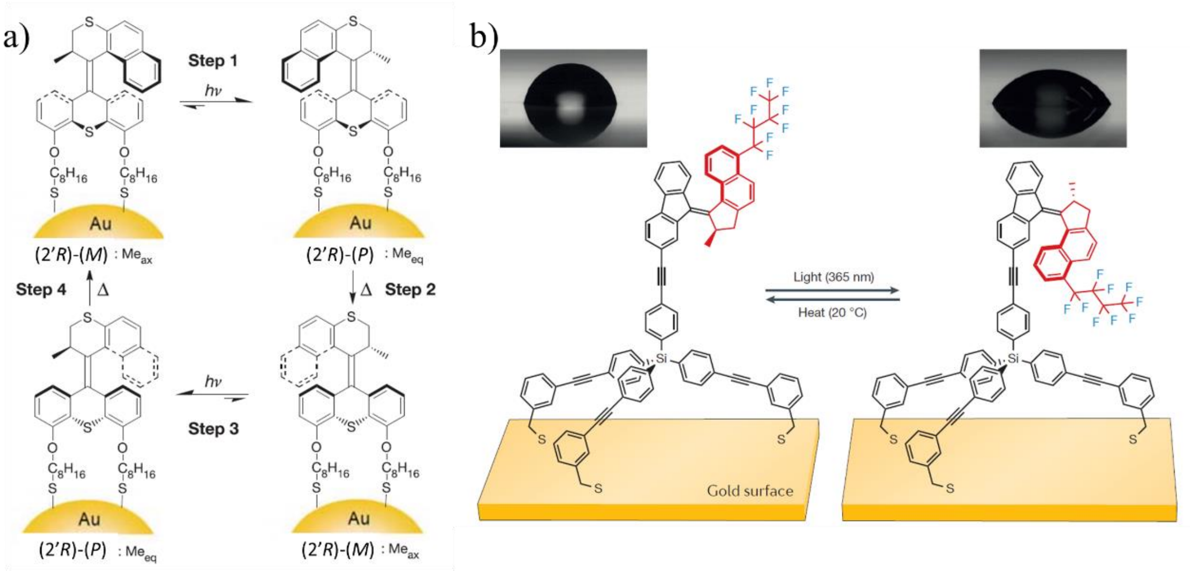

Figure 19. a) Molecular motor (azimuthal orientation) achieves a full rotation on a gold nanoparticle surface. b) Molecular motor (altitudinal orientation) on a gold surface, the surface shows different wettability in *trans*- (left) or *cis*- (right) state.

When the position of the motors can shift to a larger extent, it can be used to regulate the properties such as wettability or adhesion. Besides the examples described above involving motors with an azimuthal orientation, other examples involve their altitudinal orientation. The altitudinal orientation type molecular motor has high potentials to construct light-responsive surfaces owing to its large-scale structure changes.[48] In 2014, Feringa and coworkers reported an example that a molecular motor was grafted on a gold film surface (**Figure 19b**).[49] The motor was situated in an altitudinal position and can regulate the wettability of the gold surface through rotation. To reach this goal, the structure of the motor molecule was carefully designed and synthesized. The rotor part of the motor was linked with a perfluoro butyl hydrophobic chain to improve the wettability. The rigid tripod was linked to the stator because it can keep the motor away from the gold surface. Both *cis*- and *trans*- motor isomer was synthesized and investigated. NMR and UV-vis experiments found that motors at the gold surface have a similar unidirectional property to the free motors. The *cis*-isomer has a more hydrophilic property than the *trans*-isomer because the perfluoro butyl unit has a higher interaction with the water. The motor can achieve a *trans*-*cis* isomerization under light irradiation, hence, the wettability can be modulated by light in this system.

1.5.3 Chirality transfer

The chirality transfer at molecular scale has a huge potential in the areas of information storage, encryption or catalysis. In addition, amplified from the nanoscale to the macroscale, the chiral transfer can be used in the construction of stimuli-responsive materials. To achieve this goal, molecular motors were considered to be one of the best candidates because they can be operated in an ordered manner including photoisomerization and thermally induced transformations.

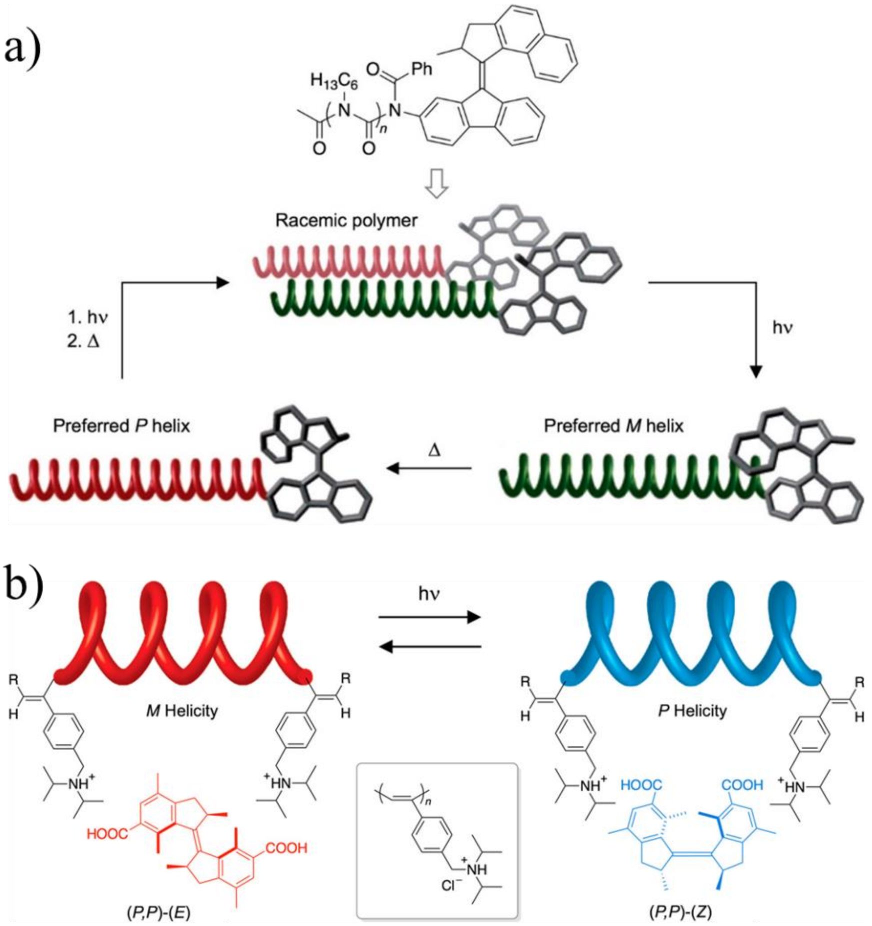

Figure 20. Schematic presentation of the photo-triggered helicity transformation of a polymer that linked to a second-generation molecular motor.

The first example of this area was demonstrated by Feringa and coworkers in 2007 (**Figure 20**).[50] They designed and synthesized a molecule with a poly(hexyl isocyanate) polymer linked to the stator of a first-generation molecular motor. In the stable *trans*-isomer form, the polymer motor conjugate was a racemic mixture, containing the same amount of left-handed and right-handed helices. Under UV irradiation, the stable *trans*-isomer photoisomerized to the unstable *cis*-isomer, and the *M*-helical polymer was formed. The following thermal helix inversion pushes the naphthalene units to the opposite side of the polymer chain, involving the formation of *P*-configuration polymer. When the motor finishes a full rotation cycle, the racemate mixture was obtained again. This example shows that the chirality of the motor can be transferred to the polymer upon rotation of the motor.

In another study, the same concept was applied in a water-soluble polymer.[51] Different from the former example, the molecular motor, in this case, was supramolecularly associated with the poly (phenylacetylene) polymer through hydrophobic and electrostatic interactions, rather than covalently linked to each other. Experiments show that the chirality of the motor can be transferred to the polymer. Therefore, the helicity conformation of the polymer unit can be regulated by light irradiation.

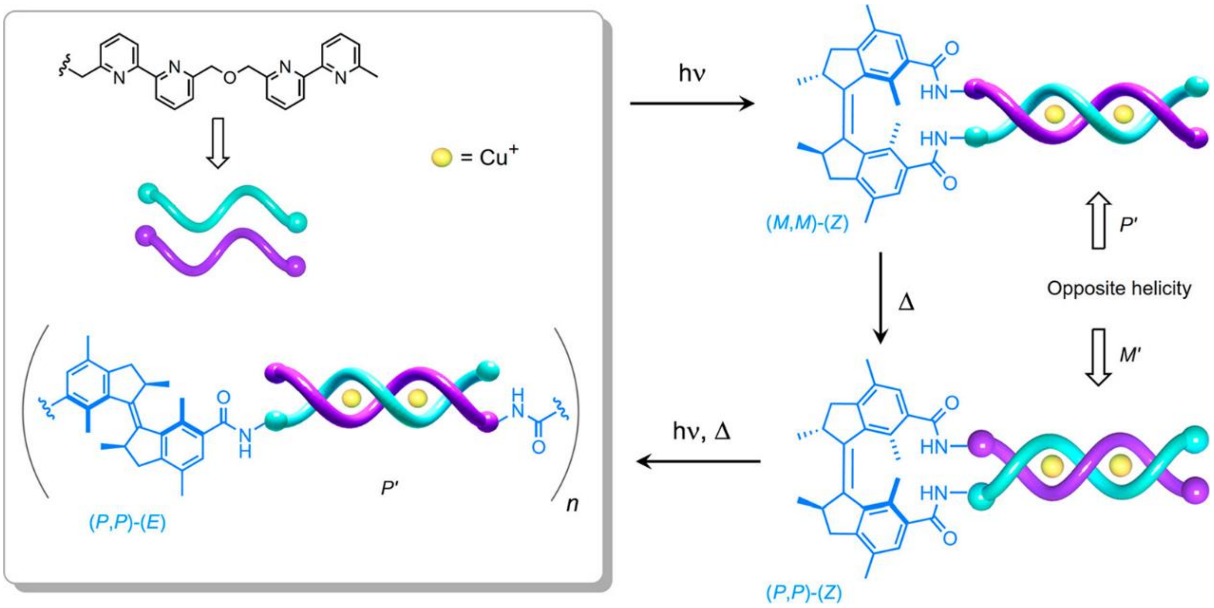

Figure 21. The structure of the bipyridine ligand functionalized motor molecule and schematic presentation of the photoswitching between the oligomer and double helicate.

In 2016, Feringa and coworkers reported a first-generation molecular motor in which both the stator and rotor were functionalized with oligo(bipyridine) ligand strands (**Figure 21**).[52] With the existence of Cu(I) ions, this ligand can self-assemble into double helicate complexes owing to the high binding affinities. When the motor was situated in the stable *trans*-isomer, the molecule can assemble into a *P'*-helicity oligomer in the presence of Cu (I) ions. Irradiating the system, the *trans*-isomer photo transformed into *cis*-isomer. The oligomer was disassembled and transformed into a *P'*-helicity monomeric intramolecular helicate. The following thermal helix inversion converts the helicate from *P'*-helicity to *M*'-helicity. The mechanism of this photoswitching transfer remained ambiguous, however, this light-regulate system opens the way for constructing smart materials and tuned catalysts.

Very recently, Qu and coworkers reported a molecular motor-based crown-ether-like macrocycle that has good stereoselectivity (**Figure 22**).[53] In this molecule, the rotor and stator part of the overcrowded alkane unit were linked together by an octaethylene glycol linker. The motorized macrocycle keeps the unidirectional rotation property of the motor unit and has a higher binding affinity with the ammonium unit through the host-guest interaction. Under UV irradiation, as the rotation of the motor, the macrocycle can bind chiral molecules selectively owing to the geometry changes of the structure.

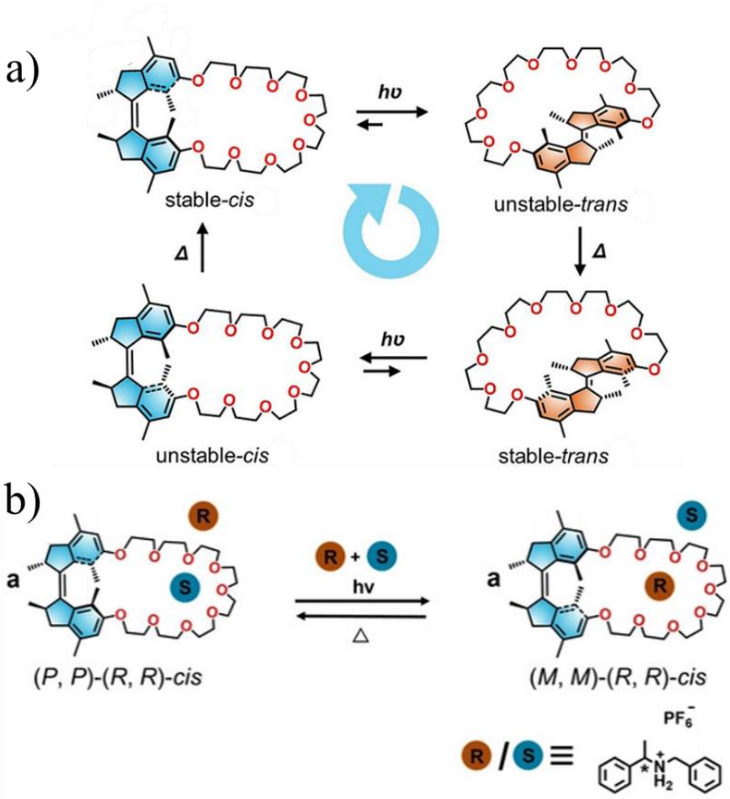

Figure 22. a) A full 360° rotation of the motorized macrocycle. b) Schematic presentation stereoselective guest recognization.

1.5.4 Use in catalysis

Catalysts play a key role in chemistry for their highly efficient and economic applications in the synthesis of molecules. In the biological world, the reactions catalyzed by enzymes show high selectivity and enhanced reactivity. To mimic the natural enzymatic catalytic behaviors, chemists have already developed huge amounts of artificial systems including stimuli-responsive catalysts. Not surprisingly, light-responsive rotary motors have become a popular candidate in this area owing to their remote and waste-free control ability. Here we will introduce some prominent works in this area.

In 2011, Feringa and coworkers demonstrated an example that can reversibly control both the catalysis reactivity and the absolute stereoselectivity by using a first-generation molecular motor scaffold (**Figure 23**).[54] The motor was decorated with a dimethylamino pyridine group at the rotor part and a thiourea catalytic group at the stator part that act as Brønsted base and hydrogen bond donor respectively. By integrating the motor and a catalytic function, a photoresponsive organocatalyst was formed. The catalyst was used in a Michael reaction by adding an aromatic thiol to 2-cyclohexen-1-one, to modulate the stereoselectivity and reaction rate. The experiment results show that different preferred chiral products were formed for different isomers of the motor. Under UV light irradiation, as the rotation of the molecular motor occurs, the two catalytic units have different distances and helical placements between them for each step of the rotation. The results show that three stable isomers in the rotation cycle give different products.

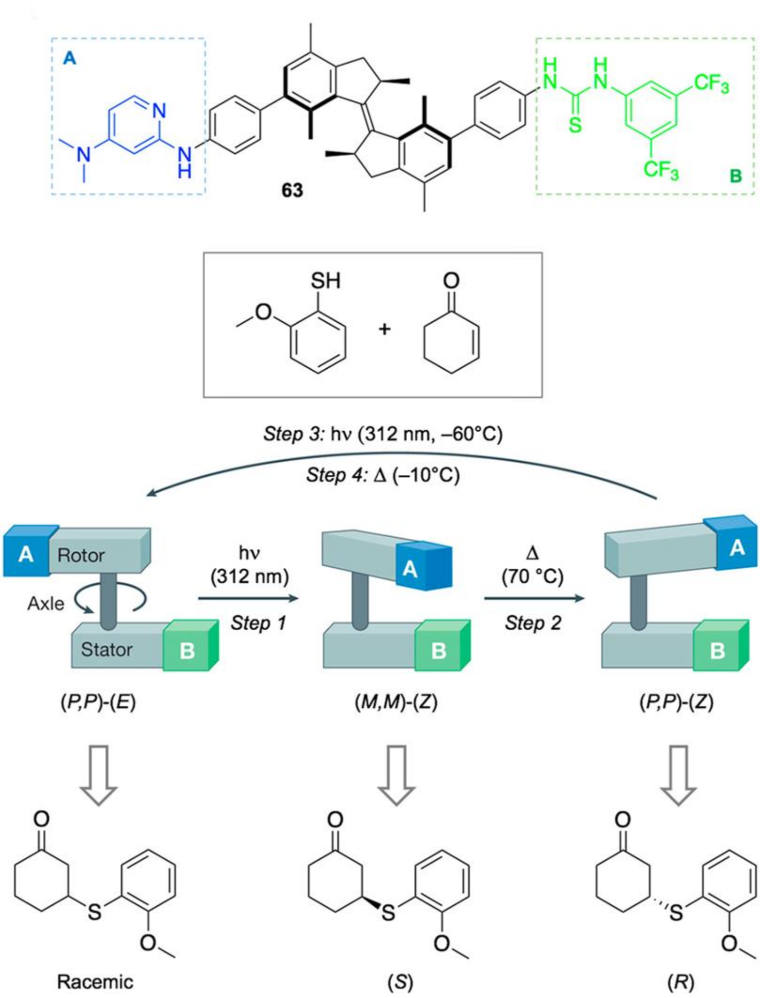

Figure 23. A molecular motor-based photoswitchable organocatalyst that can perform distinct yield and stereoselectivity reversibly and sequentially.[55]

When the (*P*, *P*)-*E* isomer was used as the catalyst, a racemic Michael addition product was acquired with a low yield and low conversion percentage. Irradiating the (*P*, *P*)-*E* isomer photoisomerized to the (*M*, *M*)-*Z* isomer, the two catalytic moieties migrated close to each other in a *M* helicity, the product yield was increased dramatically with a preferred (*S*)-product. When the DMAP and thiourea units changed to a *P* helicity from *M* helicity in the following thermal helix inversion, the *R* product was obtained with moderate enantioselectivity. At this point, a photo-responsive organocatalyst is achieved, as the yield and the stereoselectivity can be tuned in different steps of the rotation cycle.

Further, the application of the above photoresponsive organocatalyst has been expanded in a Henry reaction. However, both the activity and the stereoselectivity were found to be very low. By modifying the structure of the catalytic unit, the same group developed a new organocatalyst that can be used in Henry reaction with a good yield and excellent selectivity.[56] These examples show that only the catalyst subunits need to be modified corresponding to different organic reactions. The molecular motor scaffolds in these organocatalysts act as a regulator that could tune the relative position of the catalytic moieties.

1.5.5 Use in biological areas

Light-responsive units have been widely used in biological areas owing to their special properties such as remote control, non-harmful and waste-free characters. Feringa’s photoresponsive motor has been one of the most popular candidates in this context. The pioneering work to use Feringa’s molecular motor in the biological application was first achieved by Tour et co-workers.

In 2017, Tour and collaborators built several molecular motors containing recognition groups that can target specific cells, and they observed what happens when UV light is used to activate these compounds (**Figure 24**).[57] Note that Tour's laboratory has previously confirmed that when activated by UV light, the diffusion of the molecular rotor in solution can be enhanced.[58] These molecular motors need to rotate at a speed of two to three million revolutions per second (MHz) to overcome obstacles caused by nearby molecules and exceed natural Brownian motions. Although the mechanism of the motor activation-induced diffusion is still under investigation, these results can provide some insights to design the motorized nanomachines in solution.

These molecular motors developed by Tour in 2017, of only one nanometer wide, can be designed to target and penetrate the lipid bilayer membrane of cells in order to transport drugs or other cargo. They can also, when anchored into the bilayer and upon UV rotation, drill the cell membrane with a width of created holes of 8-10 nanometers, thereby killing the cell by provoking the leakage of their cytoplasm. These molecular motors can also be functionalized to improve their solubility and fluorescence tracking. Chemists have constructed a series of different molecular motors with different appendant groups, including molecules carrying molecular rotors of several different sizes. Peptide-carrying nanomachines were designed to target specific cells and to destroy them. They first successfully tested the ability of these molecular machines to open synthetic lipid bilayer membrane vesicles to allow dye-containing solutions to enter them. Next, they captured the dye-carrying molecular rotors inside the lipid bilayer membrane vesicles, activated them with ultraviolet light, and observed that the fluorescent dyes would fade, indicating that these molecular rotors had penetrated the lipid bilayer membrane vesicles. These researchers found that for molecular rotors, it takes at least one minute to pierce through the lipid bilayer membrane. In such a short period, cells are unlikely to be resistant to molecular machinery.

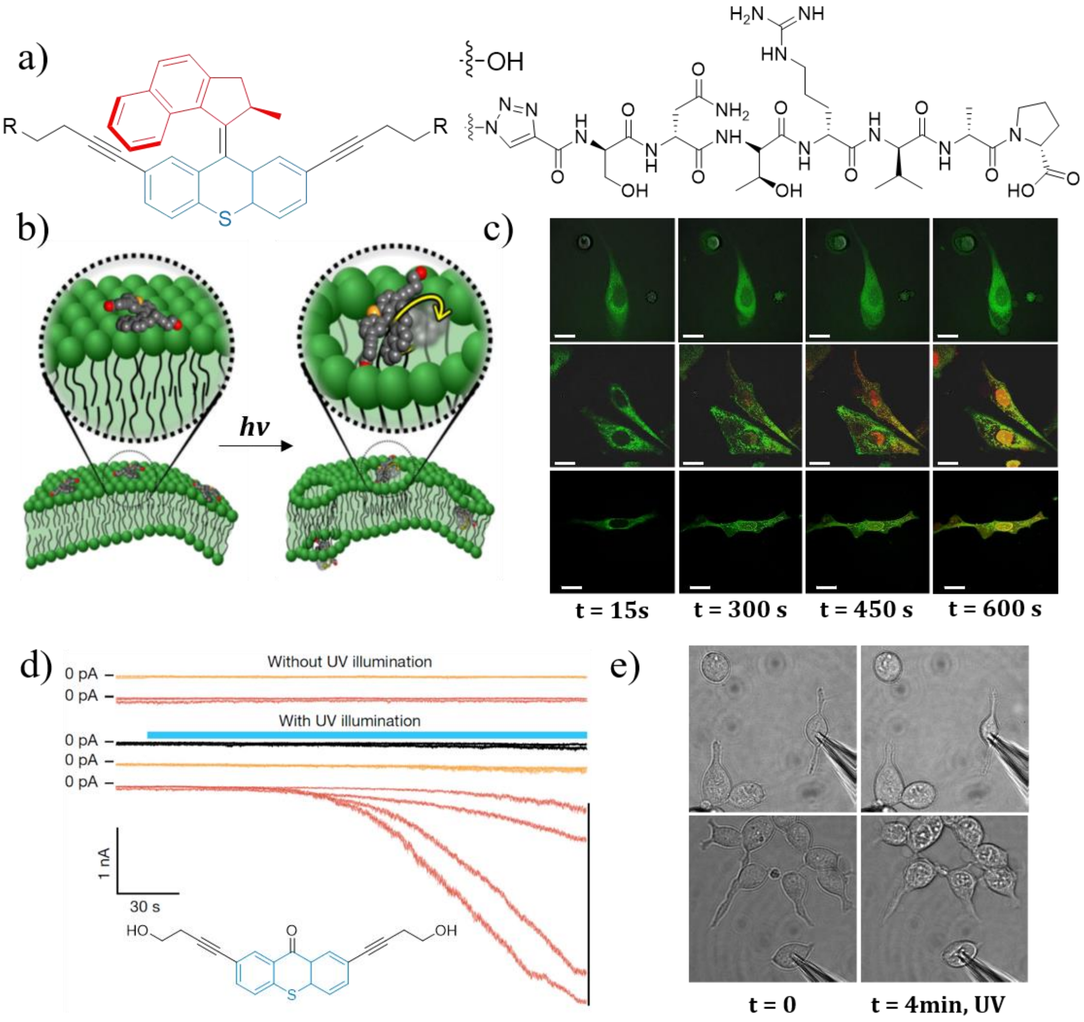

Figure 24. a) Chemical structure of the molecule motor that is used to open the membrane; b) Schematic presentation of the process of how the motor drilled into the lipid bilayer membrane; c) The cell experiments; d), e) Whole-cell patch-clamp experiments of the UV-triggered molecular motion on cells.

Researchers also tested these molecular motors in living cells, including human prostate cancer cells. Experiments confirmed that in the absence of UV light, they found specific cells and can stay on the surface of these target cells, but they could not punch holes in these cells. However, when triggered by UV light, these molecular rotors drill holes in the cell membrane quickly. The test molecular rotor designed to target prostate cancer cells penetrates their cell membrane from the outside and kills them within one to three minutes after activation. Researchers expect that nanomachines will help target cancers such as breast tumors and melanomas that are resistant to existing chemotherapy drugs. Once developed, this method may provide a potential step-change in non-invasive cancer treatment, and greatly improve patient survival and well-being globally. Smaller molecular rotors are more difficult to track, but it has been proven that when activated by UV light, they can better enter cells, destroy their cell membranes and kill them. According to these researchers, control molecules without a molecular rotor cannot kill cells after being irradiated with ultraviolet light. They expect that these molecular rotors may eventually be activated by near-infrared light, which will make this technology more suitable for in vivo treatment. Moreover, this will also establish a new simple and inexpensive photodynamic therapy pave the way to future biological applications.

Recently, our group in collaboration with the groups of Del Campo (at Leibniz Institute) and Garcia (at Georgia Tech) reported on the photo-regulation the cellular receptor by using the molecular rotary motors (**Figure 25**).[59] In the natural world, the biological motor protein can apply force on the cytoskeletal fibers. Inspired by this cellular mechanism, the authors demonstrated that the photoresponsive molecular motor can transfer the light energy source to mechanical forces at cell-matrix and cell-cell junctions. In the example, PEG_{5000} polymer chain functionalized molecular motor unit inserted between a bio-interface and a cell membrane receptor. UV irradiation triggered the rotation of the molecular motor, as a result, the polymer was twisted mechanically. Then, the elastic energy of the entangled motor polymer acts on the cell membrane receptors such as the integrins in the illuminated areas. T-cell activation and force-dependent focal adhesion maturation experiments revealed that the forces applied to the membranes have a physiologically relevant magnitude in the cell-friendly exposure environments. This technique opens the possibility of the light-rotary molecular motor regulating many functions of the living cell by mechanitransduction at the molecular scale.

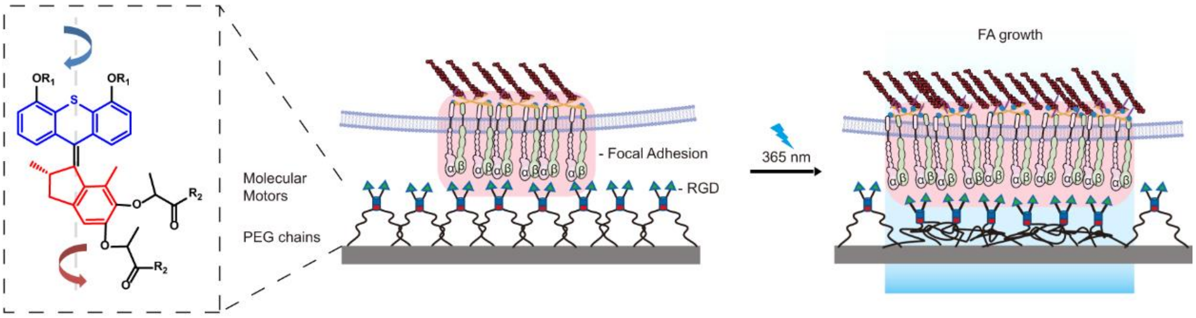

Figure 25. Schematic explanation of the molecular motor regulating the cellular receptor.

A very similar study has been reported by Feringa and co-workers recently[60], the major difference is the motor modulates the cell in a non-covalently (and non-specific) manner. The tetra-acid group functionalized light rotary molecular motor was immobilized on a glass surface through the electrostatic interaction. The tetradopal station can help the motor be fixed on the surface and avoid the uncontrollable Brownian motion and the free rotation of the motor itself, which have been proved in their previous reports[49]. A series of experiments proved that the rotation of the motor can convert the energy into controlled movements. The motion of the molecular can be used to tune the appendant protein layer and regulate the human bone marrowderived mesenchymal stem cells finally. This novel technique provides the possibility to control the cell by implementing the molecular motor on the membrane surface. Moreover, this work paves the way to biomaterials fabrication for clinical utilization.

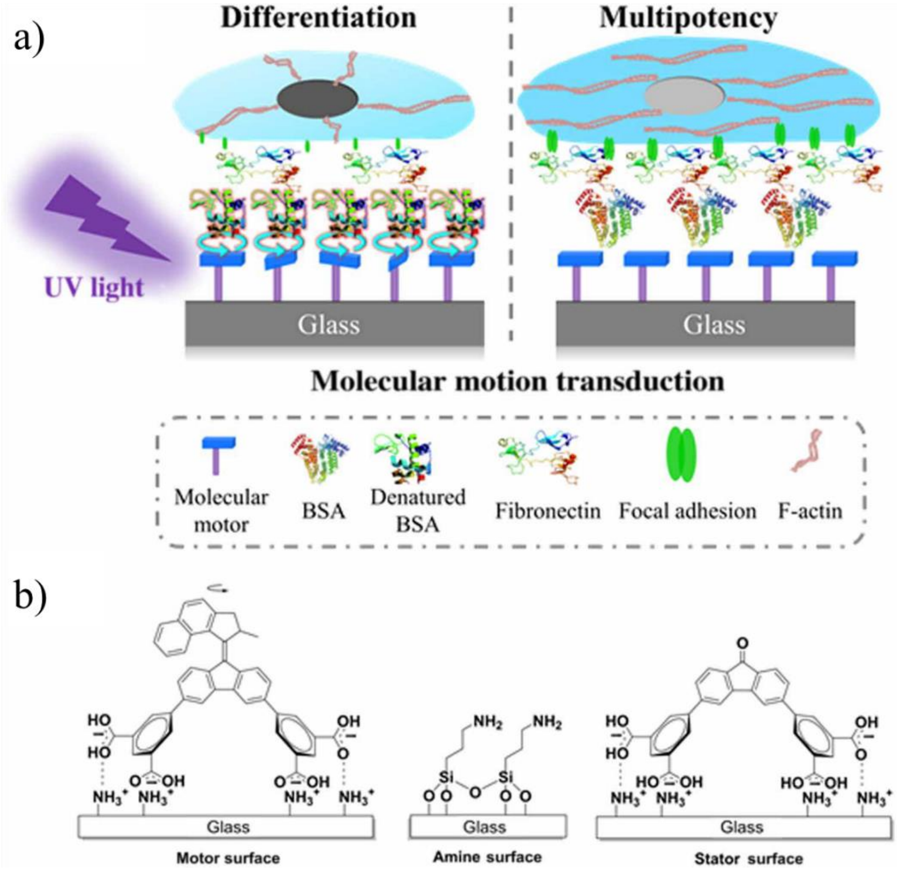

Figure 26. a) Schematic presentation of the molecular motor regulating the Hbm-MSCs. b). The structure of the molecular motors that grafted on the surfaces.

Scientists have achieved tremendous works during the past few decades in the areas of molecule machines. However, they are still many remaining challenges that need to be solved. Based on the pioneer's achievements, we believe that the study of molecule machines will be more and more fantastic in the future.

Chapter 2: Light-driven molecular motors boost the selective transport of alkali metal ions through phospholipid bilayers

We performed the ion transport experiments of this chapter by going directly in the laboratory of Prof. Mihail Barboiu, University of Montpellier.

2.1 Introduction

The separation of space (compartmentalization) by biological membranes is one of the basic elements of life. As the cell membrane maintains a cellular or subcellular environment, it needs to fulfill its mission by allowing the transport of ions or other polar molecules across the membrane.

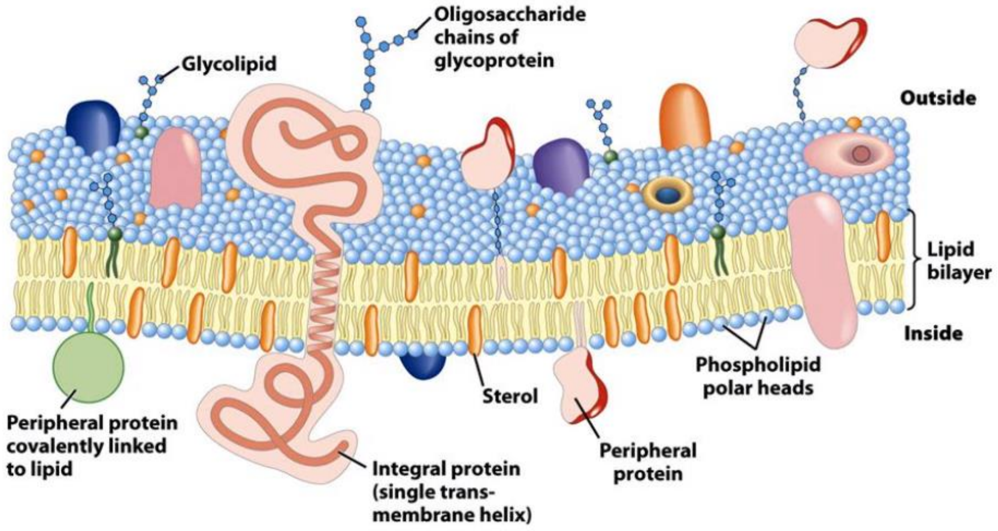

Figure 27. Schematic presentation of the biological membranes, which are heterogeneous lipid bilayers with proteins. The natural ion channels are large protein complexes consisting of a central channel portion that spans the membrane.

Under normal circumstances, the transport of ions across the membrane is completed by the species embedded in the phospholipid bilayer, which can be divided into active or passive transport. In natural organisms, transmembrane transport is usually done by transmembrane proteins. Transmembrane protein is a kind of protein that penetrates both ends of the cell membrane of the biological systems. Its function is to be used as a channel or carrier to reject or allow a specific substance to cross the biomembrane and enter the cell. At the same time, it also transports the discarded by-products from inside to outside.

Passive transportation is driven by the concentration gradient of ions both inside and outside the membrane, so the ion transporter such as ion carriers and channels facilitate the system toward thermodynamic equilibrium by exhaust the gradient. During active transport, the flow of ions needs to pass through the transporter protein against the concentration gradient, so the corresponding energy needs to be provided from the outside such as ATP hydrolysis. This type of ion transporter is called an ion pump, which operates far from equilibrium and can transform the input energy to the chemical potential between the transmembrane.

2.1.1 Natural Alkali Ion Transport

A variety of different ion channels exist in nature, which could selectively transport chloride, calcium, or proton, and we focus hereafter more particularly on such natural channels for alkali metal ions transportation. Indeed, our study of ion transport in this chapter will be performed using a light-driven molecular motor appended with an 18-crown-6 ether unit, which shows an excellent binding property for alkali metal ions, in particular potassium, and this is why we restricted our bibliographic introduction to this family.

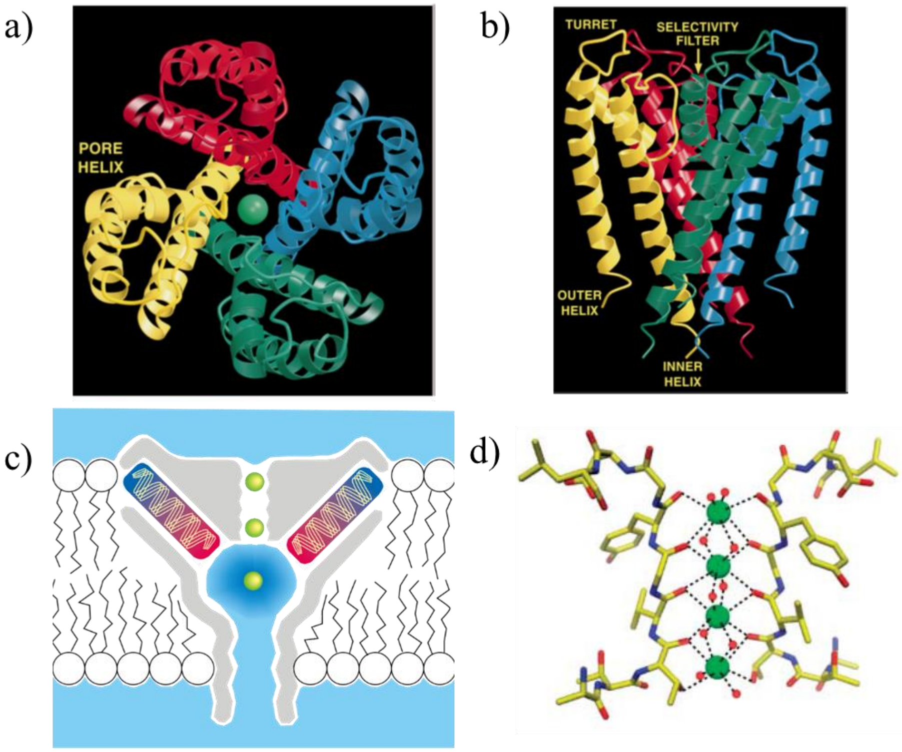

Figure 28 a) Stereoview of a ribbon representation illustrating the 3D fold of the KcsA tetramer from the extracellular side; b) perpendicular to that in (a); c) Schematic presentation of the K^+ ions across the channel; d) KcsA K^+ channel contains four potassium ions.

Potassium ion channels widely exist in the biological world as different types. They are composed of four identical protein subunits that interact with each other to form a symmetrical pore, as demonstrated by X-ray diffraction analysis. Such channels can be gated by various effectors, such as calcium dependant or voltage dependant potassium channels.

Notably, in 2003, Rod Mackinnon has been awarded the Nobel Prize for chemistry for his eminent contributions to this field. In 1998, Mackinnon and collaborators studied the K^+ channels of *streptomyces lividans* bacteria (KcsA K^+ channel)[61], which is a typical tetramer functional K^+ channel protein (**Figure 28**). The potassium channel forms a water-filled cavity cone and in this big cavity the electrostatic destabilization of the ions can be easily overcome, thus the potassium ion can be transported at a super high speed (~10^8 ions per second). The channel is around half-length of the pore and contains a selective filter which is around 12 Å. In this selective pore, four potassium ions are binded in a row. On each binding site, the potassium ions interact with the oxygen atoms from carbonyl groups of amino-acid residues. The size of the filter selectively screens for potassium ions, with an average distance of 2.84 Å between the potassium and the oxygen toms.

2.1.2 Artificial Alkali Ion Transport

Scientists have been committed to the development of artificial synthetic molecular devices used to regulate ion migration across membranes. Artificial molecular transporters have been developed to mimic natural ion transportation, which is a prosperous research area of supramolecular chemistry. The driving force of the research is the high basic scientific value and potential therapeutic application prospects such as in the treatment of cancer and cystic fibrosis. Achieving active transfers is potentially very interesting because it may also bring new energy conversion and storage methods, such as solar power generation and light-driven equipments.

Molecular machines have become one of the most promising candidates owing to their controlled movements. Recently, there have been reports of artificial transport molecules operating in homogeneous solutions, as well as transmembrane molecular machines based on biomolecules. However, the utilization of molecular machines that move between their different components has not been reported so far.

In 2018, Qu and co-workers designed, synthesized, and studied an artificial molecular machine that can passively transport K^+ ions in a bilayer membrane (**Figure 29**).[62,63] The transporter structure is a mechanically interlocked molecular shuttle, in which the ring and shaft components can slide relative to each other. The molecular shuttle is a very promising candidate molecule for the realization of passive transmembrane transport, owing to its advantages as follows; its special amphiphilic rod-like chemical structure is easy to insert perpendicularly into the double-layer membrane; the length of the shaft can be flexibly designed, and the thickness of the membrane can always be completely covered; the ring used to catch the “cargos” can be designed flexibly to fulfill its demand.

The investigated molecular shuttle was composed of an asymmetric chain guest and a crown ether host molecule. The symmetric chain contains two secondary ammonium units as the recognition site for the crown ether and a thiazolium unit behaves as an intermediate station in the shuttling process. The host molecule consists of two crown ethers with different sizes, a dibenzo-[24]crown-8 (DB24C8) with a larger cavity that can encircle the axil and a benzo[18]crown-6 (B18C6) whose cavity can bind the K$^+$ ions. The amphiphilic rotaxane can span across the lipid bilayer and function well, which was confirmed by molecular dynamics simulations and following experimental results. From a series of experiments, the results show that the molecular shuttle can transport the K$^+$ ions across the lipid bilayer membrane with high selectivity. The molecule shuttle reported here was a forerunner for designing further generation artificial molecule machines to operate in the lipid bilayer membrane environments. It will also enhance the relative knowledge of how molecule machines can be applied in biological areas in a controllable and repeatable method.

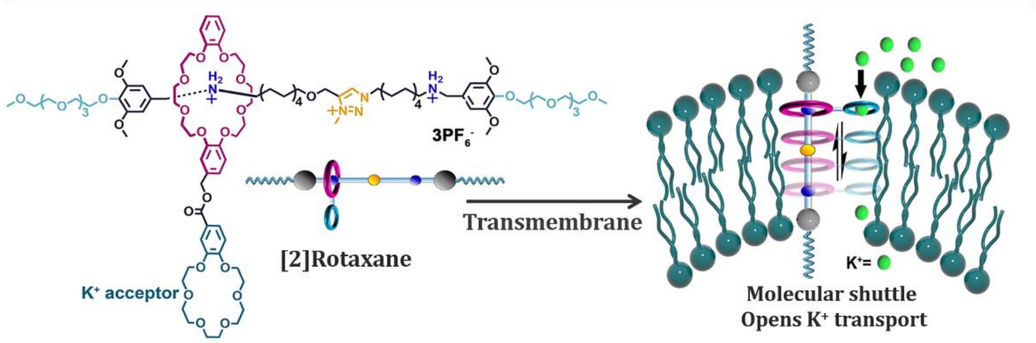

Figure 29 Chemical structure of the molecule shuttle transporter and the schematic presentation of how the transporter worked in the lipid bilayer membrane.

Though the former example enriches the ion transporter family, it depends on the stochastic Brownian motion to perform the transportation activity, which is very hard to control. The construction of stimuli-responsive transporter, especially photo-responsive ion transporters, has become a popular topic among membrane scientists. To address this aspect, the same group reported recently a light-operated molecular “cable car” for gated ion transport.[64] The structure of the molecular shuttle is similar to the previous one, the major difference is that an azobenzene unit was inserted into the chain part of the [2]rotaxane. The azobenzene would undergo *trans-cis* alternative conformational transformation under the UV light of 365 nm or 450 nm, respectively. Upon the photo-isomerization of the azobenzene unit, the length and shape of the amphiphilic molecular shuttle would be changed inside the lipid bilayers. The HPTS fluorescence-based LUVs assay and patch-clamp experiment revealed that the molecular shuttle has distinct transportation activity at different conformations. When in the *trans*-configuration, the molecular shuttle has a higher transportation activity than in the *cis*-configuration. This can be explained by the fact that the hindered *cis*-configuration of the azobenzene reduces the moving speed of the crown-ether macrocycle, resulting in a lower transportation activity of the “cable car”. Moreover, *in-situ* ON-OFF switching experiments show the transportation activity can be regulated by alternative irradiation with different UV wavelengths. The introduction of the photoresponsive azobenzene units provides new insights to fabricate novel artificial ion channels and biomimetic materials, and opens the possibility for future photo-therapeutic applications.

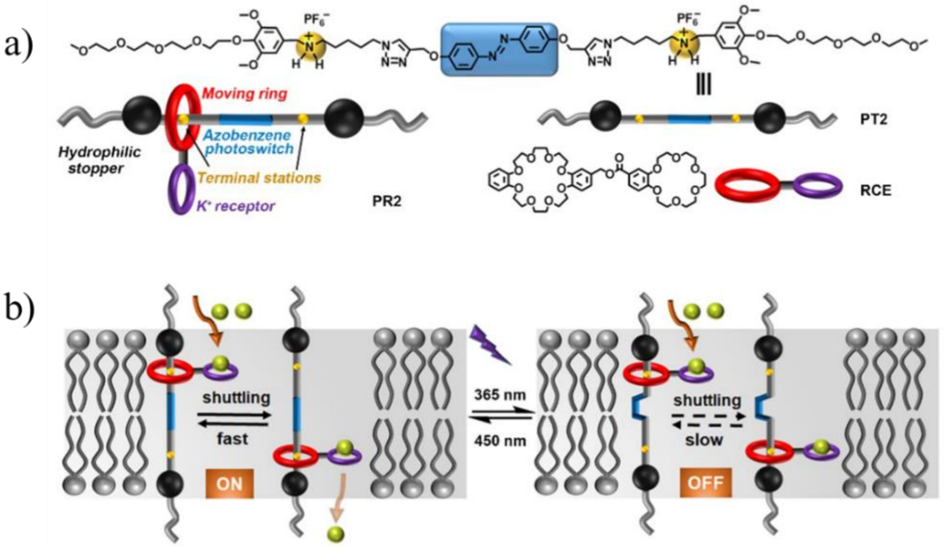

Figure 30. a) Chemical structure and schematic presentation of the azobenzene containing molecular shuttle. b) Schematic presentation of the proposed mechanism of the light-gated ion transportation across the lipid bilayer membrane.

In our doctoral own research work, we envisionned to use of light-responsive molecular motors to regulate ion alkali transportation for transmembrane applications. Our objective was to make use of the out-of-equilibrium roation of the motor to change the selectivity or the activity of an ion transporter. We were expecting that, conversely to the few previous examples involving molecular machines for ion transport, this change would not come from a configurational change of the actuating molecules, but realy from the continuously generated rotation under light irradiation. This possibility to perform such a task in the lipid bilayer membrane using an out-of-equilibrium regime would represent a real step forward in the fields of molecular machines on the one hand, and of ion channels on the other hand. In this section, we will discuss our efforts towards the implementation of such artificial molecular motors as ion transporters.

2.2 Synthesis of Ion Transporting Molecular motors

In this context, a series of molecular motors potentially relevant as molecular transporters have been designed and synthesized for different purposes.

2.2.1 Objectives and retrosynthesis

As discussed above for previous studies, Feringa's molecular motor was used to open membranes in biological systems. However, their implementation in the domain of ion transportation has still not been described in the literature, and we were wondering if light-driven rotary molecular motors could influence ion transportation across a lipid bilayer membrane. We suspected that under UV irradiation, by rotation of the motor inside the bilayer, the rate of transportation would be modulated, and we decided to probe this hypothesis by synthesizing motor-ion transporters conjugates such a **A**.

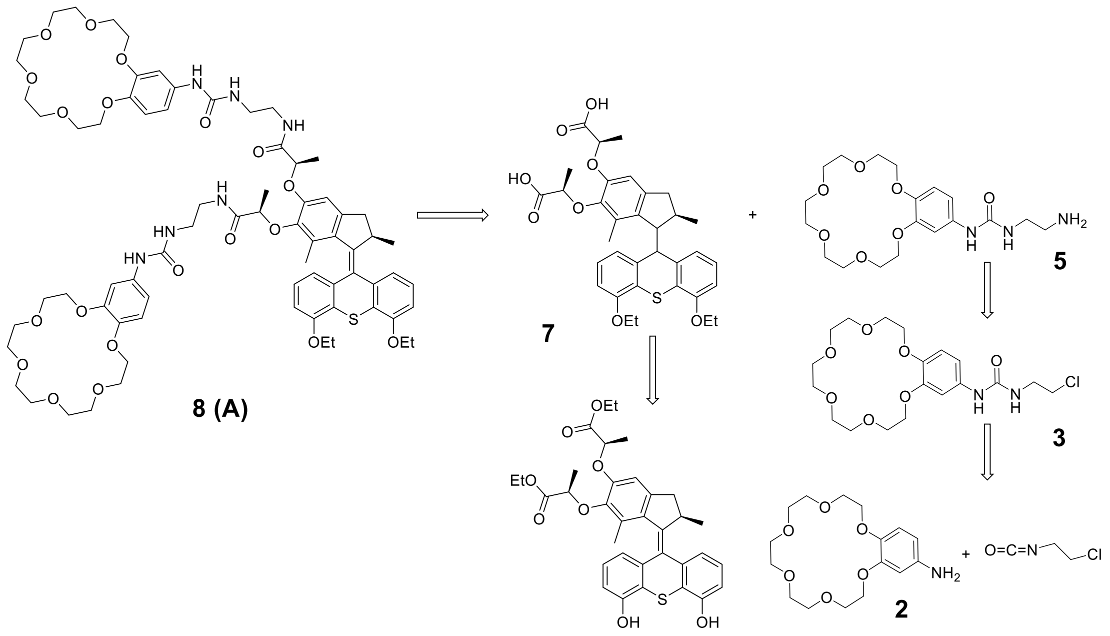

Figure 31 Retrosynthetic scheme of Compound **8 (A)**

The retrosynthetic strategy for molecular motor containing compound **A** is shown in **Figure 31**. This compound can be envisioned by a coupling reaction between bis-acid motor **7** and urea-bond amine crown-ether **5**. The urea-bond amine crown-ether can be envisioned by starting with 18-crown-6 amine **2** and 2-chloroethyl isocyanate. The bis-acid motor can be obtained after two steps: a substitution reaction between the bis-phenol motor and bromomethane, and saponification of the rotor part. This functionalized and optically pure molecular motor can be obtained on a gram scale as already described by our group.[65] The detailed synthesis of the molecular motor is described within the annexes in **Figure A1**, **Figure A2**, and **Figure A3**.

2.2.2 Synthesis of compound A

This work started with the synthesis of molecular motor **A** (**Figure 31**), which integrates a urea motif to potentially favor its supra-molecular self-assembly by hydrogen bonds within the phospholipid bilayer. Besides, it includes an 18-crown-6 ether as a macrocyclic unit, which is well-known to perfectly accommodate potassium cations in its center and to form sandwich-type complexes with rubidium cations. Motor **A** was prepared by coupling molecular motor bisacid **7** (**Figure 31**) and crown ether derivative **5**, which was synthesized as shown in **Figure 32**.

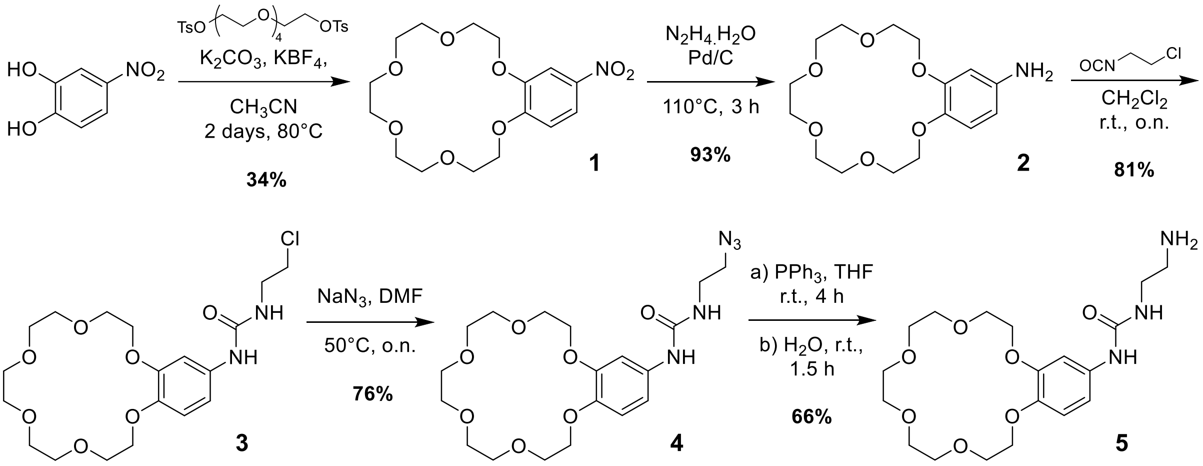

Figure 32. Synthesis of Compound **5**

To access derivative **5**, macrocycle **1** was first synthesized from commercially available 4-nitrocatechol and pentaethylene glycol di(*p*-toluenesulfonate) in the presence of templating potassium cations to favor macrocyclization. Further reduction of the nitro group with palladium on charcoal and hydrazine afforded compound **2**. Afer condensation of aniline **2** with 2-chloroethyl isocyanate, crown ether macrocycle **3** was obtained in reasonable yields. Subsequent nucleophilic substitution with sodium azide, and reduction of the azide to the amine using the Staudinger reaction, afforded compound **5** in good yields.

On the other hand (**Figure 33**), free phenol groups of the already reported molecular motor (**Figure A3**) were protected by nucleophilic substitutions with bromoethane to give compound **6**. Subsequent saponification of the two ethyl esters using sodium hydroxide in a mixture of

THF and methanol afforded motor bis-acid **7**.

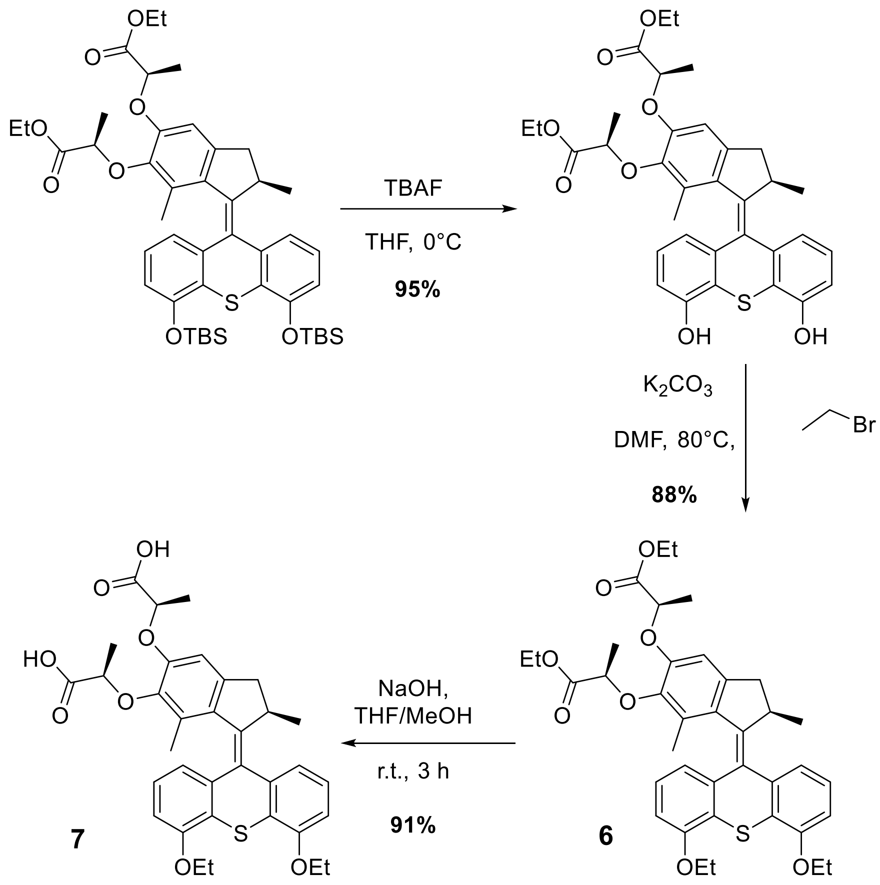

Figure 33. Synthesis of Compound **7**

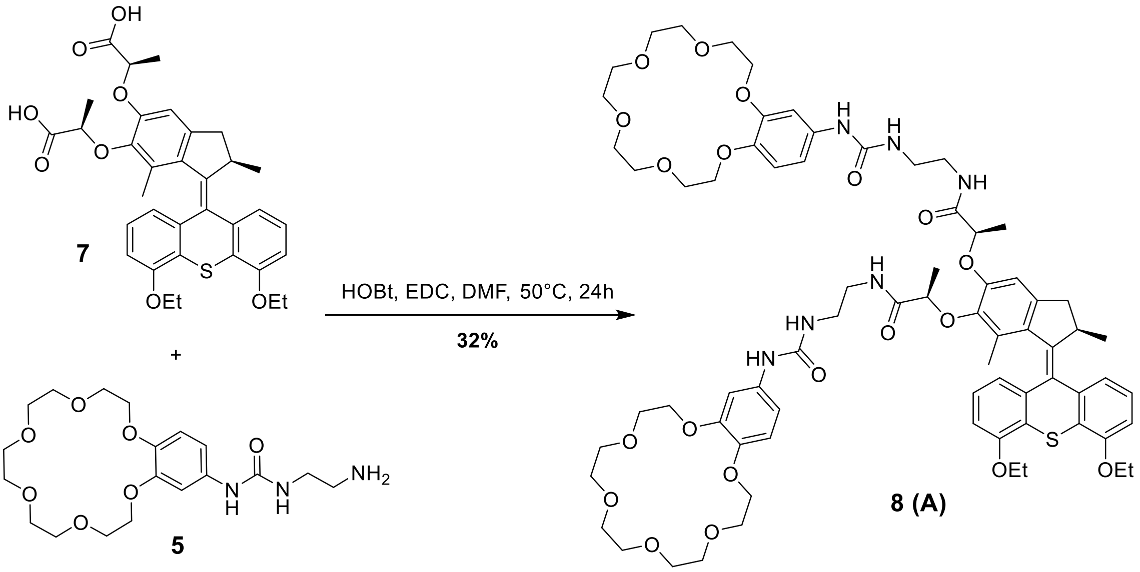

Figure 34. Synthesis of Compound **8** (**A**)

Finally, compound **8** (**A**) was obtained by an amide coupling reaction between amine **5** and bis-acid **7** using 1-Ethyl-3-(3-dimethyl aminopropyl)carbodiimide (EDC) and HOBt as reagents. This key compound was purified by preparative reverse-phase high-performance liquid chromatography (HPLC) and obtained as a yellow-brownish solid.

2.2.3 Synthesis of compound B

In addition, to better probe the influence of the rotation of molecular motor **A** on the ion transport properties upon light irradiation, we also synthesized episulfide **B** as a "control" molecule in which the central photo-actuating double bond of the motor is replaced by an episulfide moiety, thereby precluding any rotation upon light irradiation.

The synthetic route of compound **B** was similar to the one of compound **A**. Free phenol groups of already reported molecular episulfide were protected by nucleophilic substitutions with bromoethane to give the tetra ester episulfide compound **9**. Subsequent saponification of the two ethyl esters using sodium hydroxide in a mixture of THF and methanol afforded molecular motor **10**.

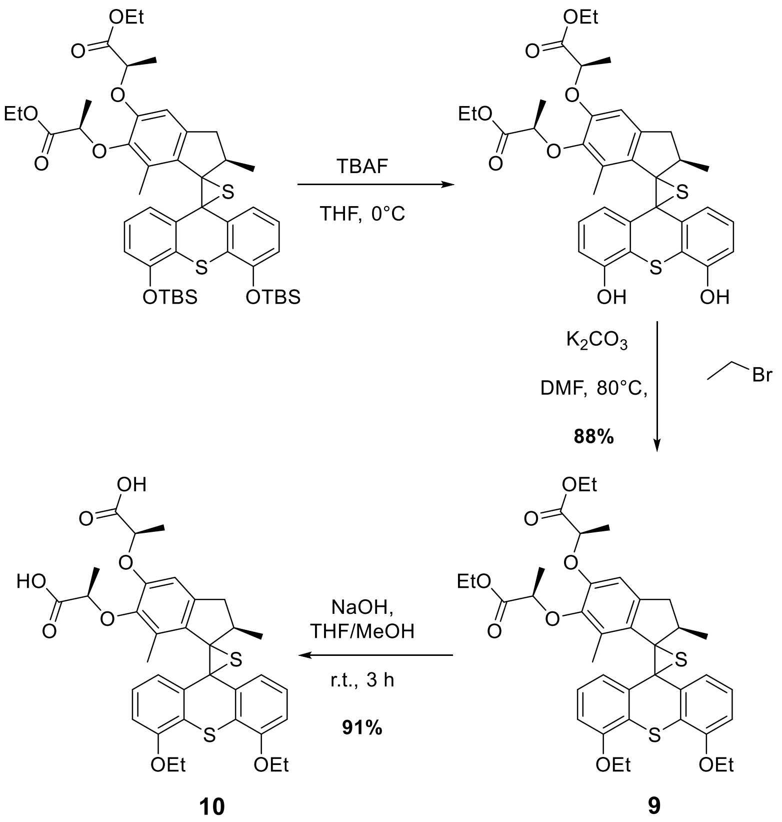

Figure 35. Synthesis of Compound **10**

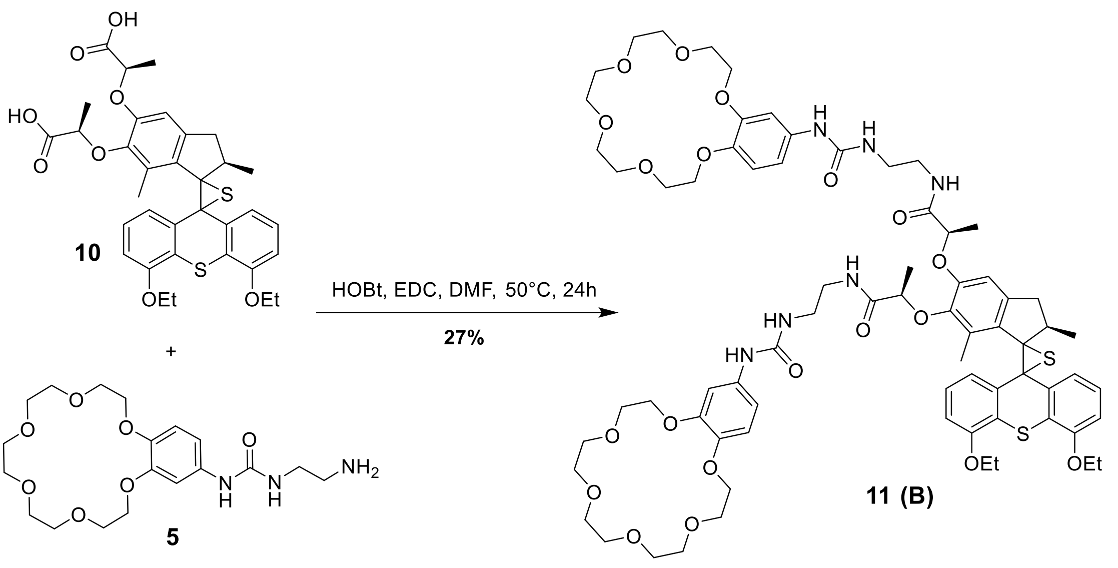

Figure 36. Synthesis of Compound **11 (B)**

Finally, compound **11(B)** was obtained by an amide coupling reaction between amine **5** and bis-acid **10** using 1-Ethyl-3-(3-dimethyl aminopropyl)carbodiimide (EDC) and HOBt as reagents. This reference compound was purified by preparative reverse-phase high-performance liquid chromatography (HPLC) and obtained as a yellow-brownish solid.

2.3.4 Synthesis of compound 17

The chemical structure of compound **16** is similar to that of compound **5**, the main difference is four pending short PEG chains were introduced in the upper part, instead of a crown ether macrocycle. The reason for the design of such a structure is to study the existence of crown ether is mandatory for ion transportation.

To access derivative **16**, compound **12** was first synthesized from commercially available 4-nitrocatechol and 2-(2-methoxyethoxy)ethyl 4-methylbenzene-1-sulfonate. Further reduction of the nitro group with palladium on charcoal and hydrazine afforded compound **13**. Then, condensation of aniline **13** with 2-chloroethyl isocyanate afforded crown ether macrocycle **14** in reasonable yields. Subsequent nucleophilic substitution with sodium azide to give compound **15**, and reduction of the azide to the amine using the Staudinger reaction, afforded compound **16** in good yields.

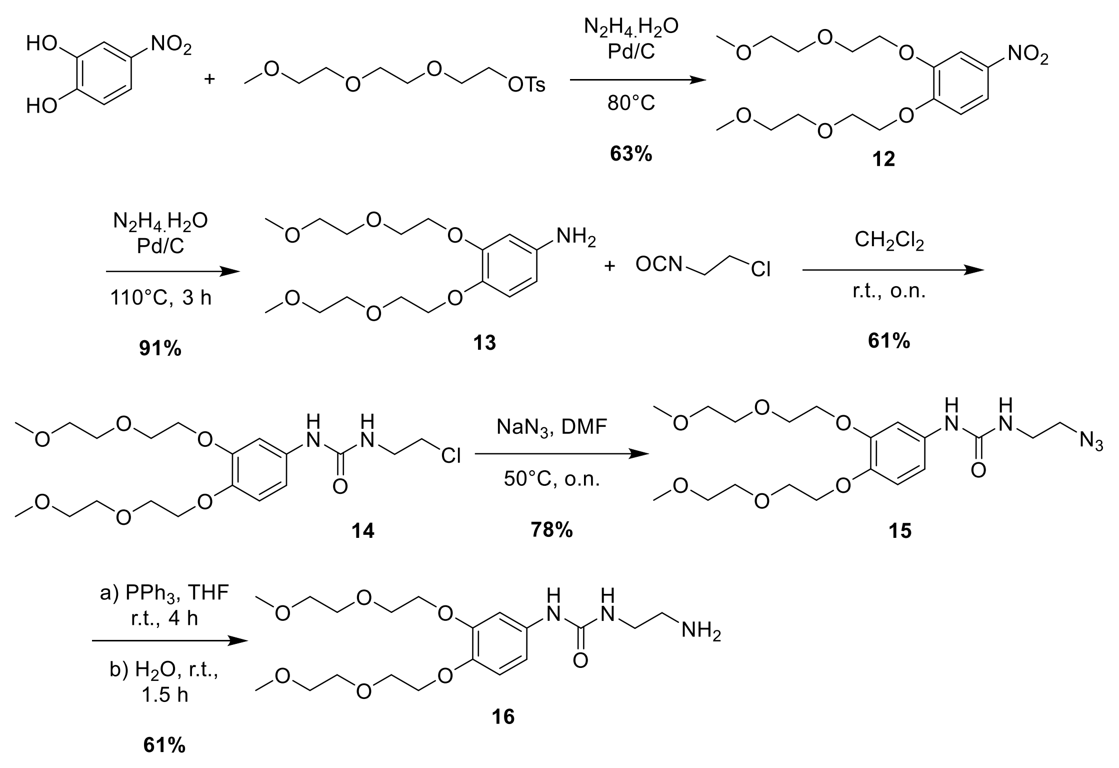

Figure 37. Synthesis of Compound **16**

Finally, compound **17** was obtained by an amide coupling reaction between amine compound **16** and bis-acid motor compound **7** using EDC and HOBt as reagents. This reference compound was purified by preparative reverse-phase high-performance liquid chromatography (HPLC).

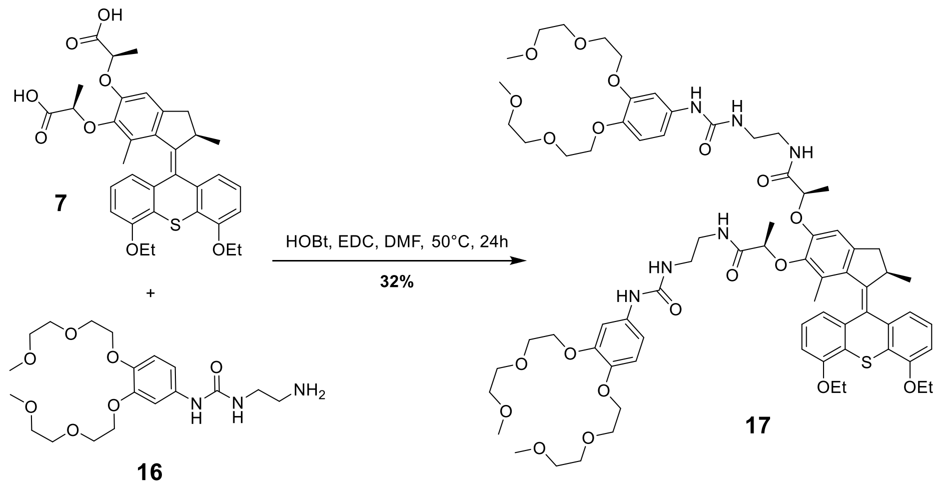

Figure 38. Synthesis of Compound **17**

2.3.5 Synthesis of compound D

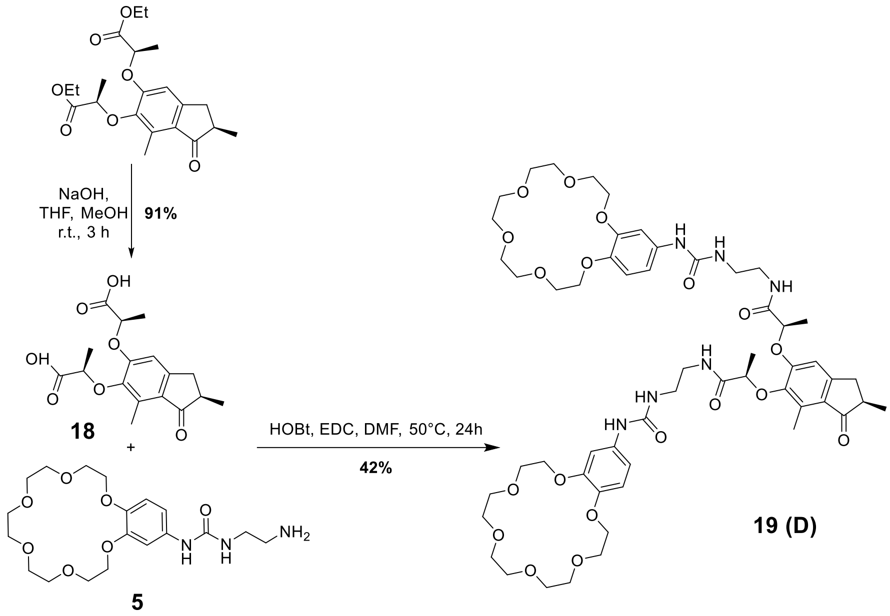

Figure 39. Synthesis of Compound **19** (**D**)

The intermediate compound of the rotor was saponified in sodium hydroxide solution to provide the bis-acid compound **18** in a quantitative yield. Amine coupling reactions between the two carboxylic acid and compound **5** with EDC and HOBt as reagents, yielded compound **19**. This reference compound was purified by preparative reverse-phase high-performance liquid chromatography (HPLC).

2.3.6 Synthesis of compound E

Free phenol groups of the already reported molecular motor compound were protected by nucleophilic substitutions with propargyl bromide to give the motor compound **20**. Subsequent saponification of the two ethyl esters using sodium hydroxide in a mixture of THF and methanol afforded bis acid molecular motor **21**. Excess of oxalyl chloride was added to compound **21** in dichloromethane with the catalysis of the DMF, in order to form the acyl chloride intermediate. Subsequently, the addition of propargylamine gave the tetra-alkyne compound **22** a yield of 90% over two steps.

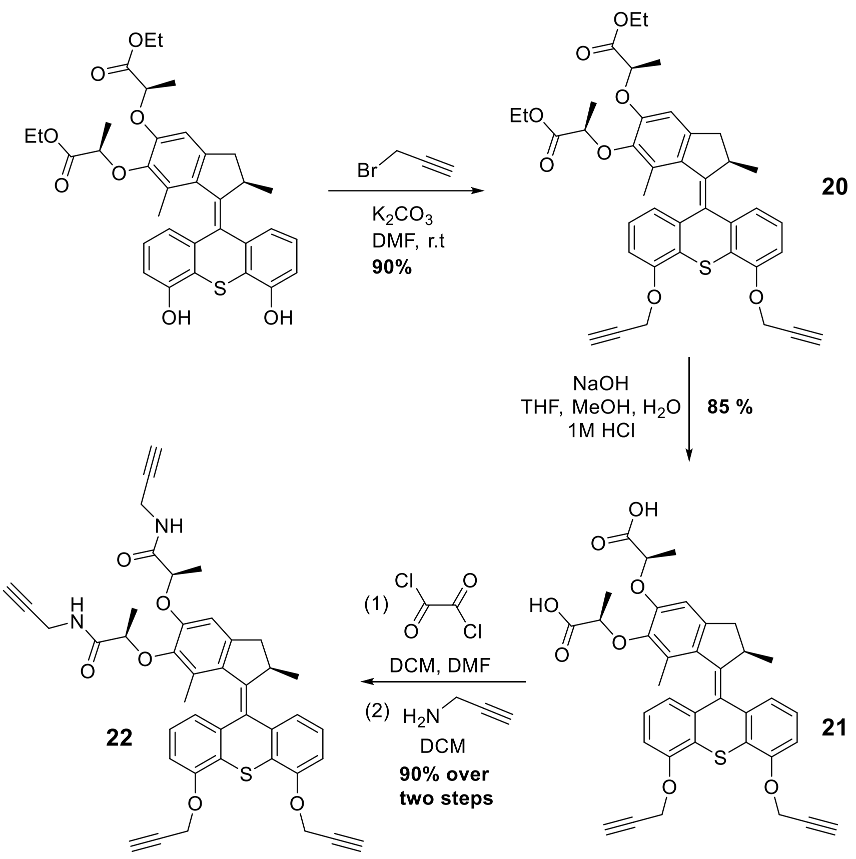

Figure 40. Synthesis of tetra-alkyne motor Compound **22**

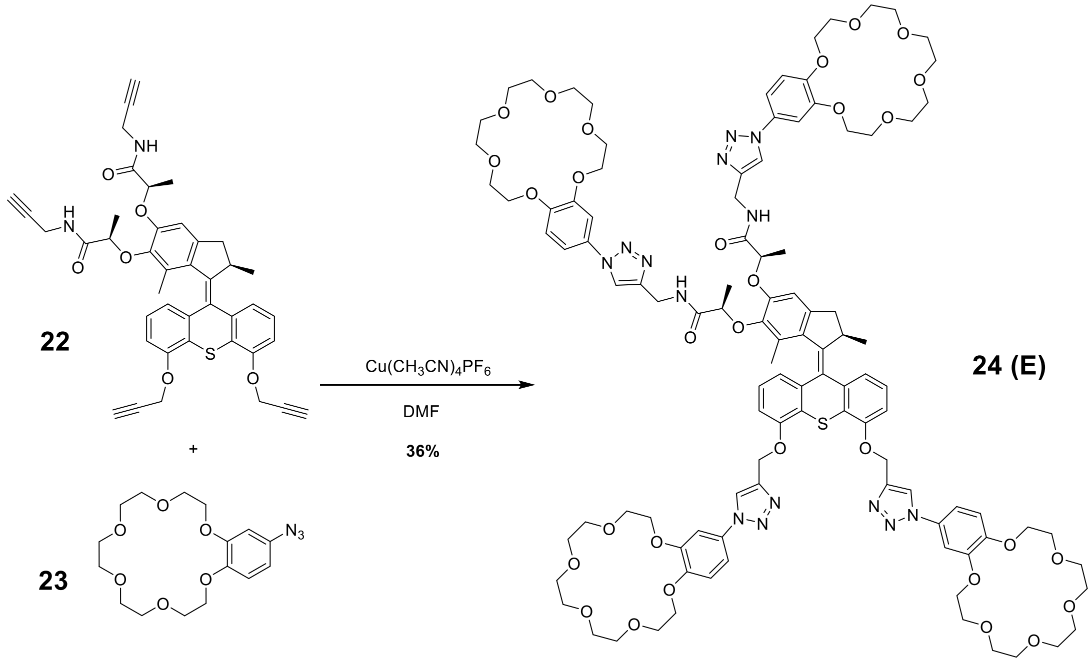

Figure 41. Synthesis of tetra-click motor compound **24 (E)**

Tetra-alkyne **22** was reacted with azide crown ether **23** under microwaves with tetrakis(acetonitrile) copper(I) hexafluorophosphate reagents to form the final molecular motor **24 (E)** through click reaction. This compound was purified by preparative reverse-phase high-performance liquid chromatography (HPLC).

2.3.7 Synthesis of compound F

Free phenol groups of the already reported molecular motor were protected by nucleophilic substitutions with ethyl bromoacetate to give the tetra-ester motor compound **25**. Subsequent saponification of the four ethyl esters using sodium hydroxide in a mixture of THF and methanol afforded tetra-acid molecular motor **26** as a green solid with a yield of 85%.

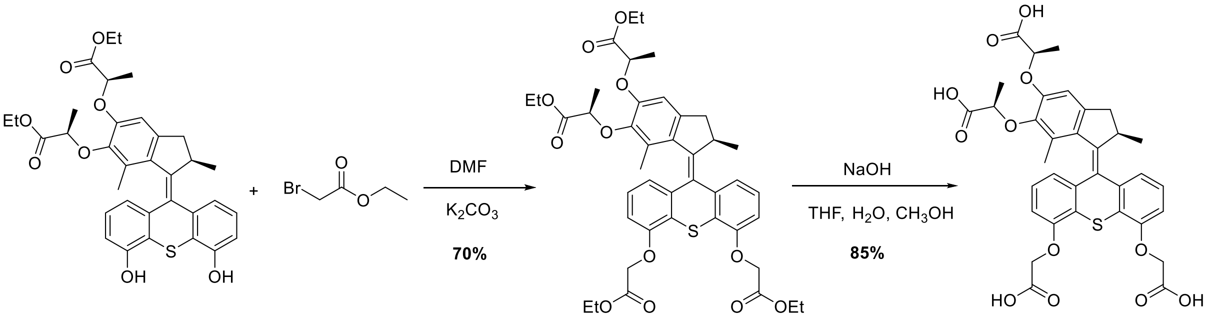

25

26

Figure 42. Synthesis of tetra-acid motor compound **26**

Finally, compound **27 (F)** was obtained by an amide coupling reaction between amine **5** and tetra-acid compound **26** using EDC and HOBt as reagents. This tetra macrocycle-containing compound was purified by preparative reverse-phase high-performance liquid chromatography (HPLC) as a yellow-brownish solid.

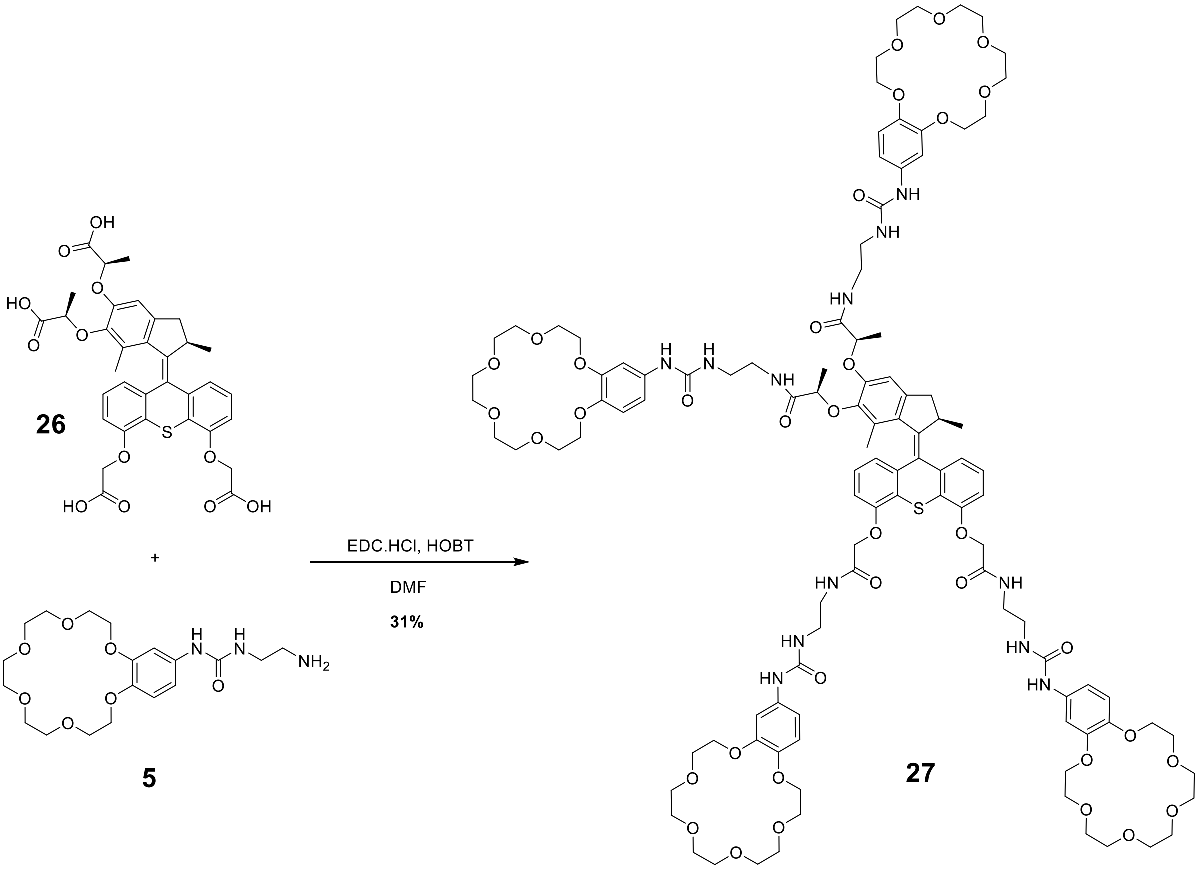

Figure 43. Synthesis of tetra-urea motor compound **27 (F)**

2.3 Study of the molecular motor rotation process

After obtaining this series of molecular motors, we wanted to study their unidirectional rotation process. Although motors of the same family (without macrocycles) have been investigated by Dr. Quand Li from our group, we wanted to synthesize a dissymmetric motor derived from motor **A** for the reasons described hereafter.

2.3.1 Dissymmetric motor C

Owning to the superfast rotation speed of the molecular motor (theoretically up to the MHz), it is consequently hard to trap the unstable helical state obtained by the photochemical isomerization step. Usually, very low temperatures are required to visualize the unstable helix, but with motors containing many polar groups such as **A**, the solvents used are not liquid at such temperatures. One can however expect to see the stable cis and tans isomers, but again, regarding the symmetry of the stator in motor **A**, no difference can be expected. Therefore, the NMR, UV, and even CD signals appear similar for a fast rotation under light irradiation, and it cannot be proven by spectroscopy. Therefore, we synthesized a dissymmetric molecular motor in the lower part, from which the two stable helices can be differentiated by spectroscopy.

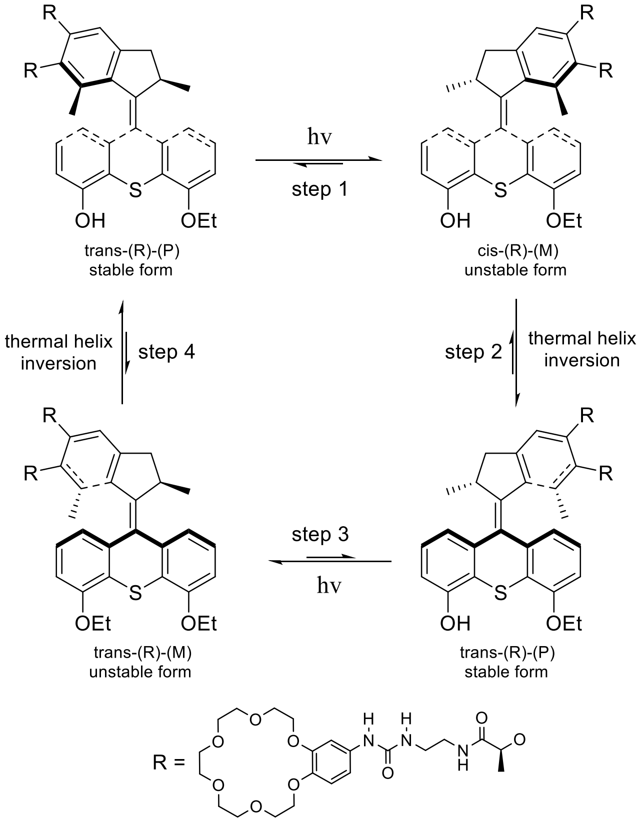

Figure 44. Proposed mechanism of the rotation cycle of the asymmetric molecular motor **C**

Because of the difficulty in separating the intermediate compounds, we used a "one-pot" synthesis to get this dissymmetric motor. In the first step, the free phenol groups of the molecular motor were protected by nucleophilic substitutions with bromoethane (**Figure 45**). The bromomethane was added (0.5 eq.) to afford the mono-substituted intermediate compound **28**. After a saponification reaction, the bis-acid mono-substituted compound **29** was obtained. The polarity of these two mixed mono-substituted intermediate compounds was close to each other, so they were used for the next step without purification. Finally, the asymmetric motor compound **30** was obtained by an amide coupling reaction between amine **5** and mono-substituted bis-acid motor compound **29** using EDC and HOBt as reagents, and the two configurational isomers can be separated by reverse column chromatography.

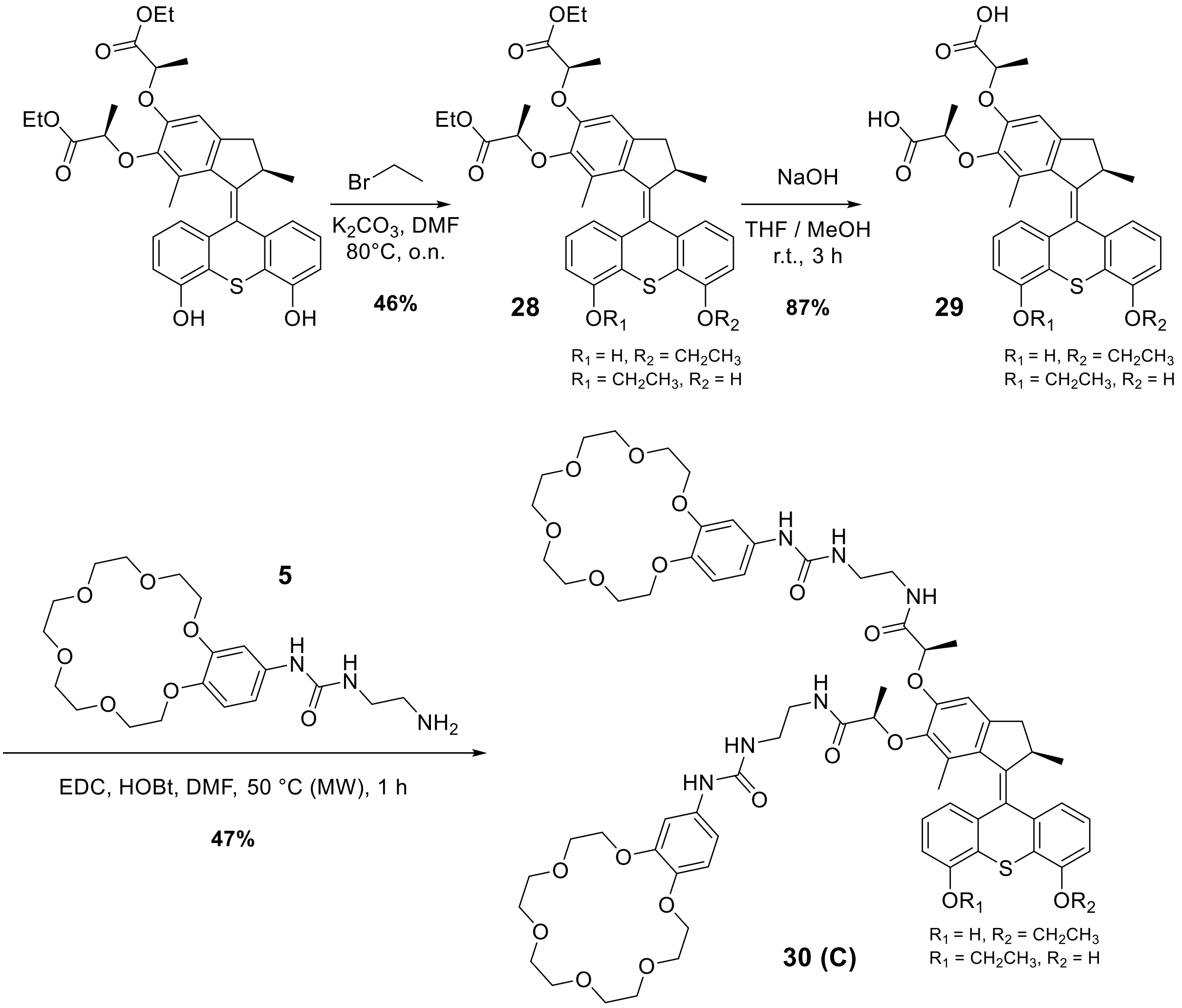

Figure 45. Synthetic route of the asymmetric motor compound **30**

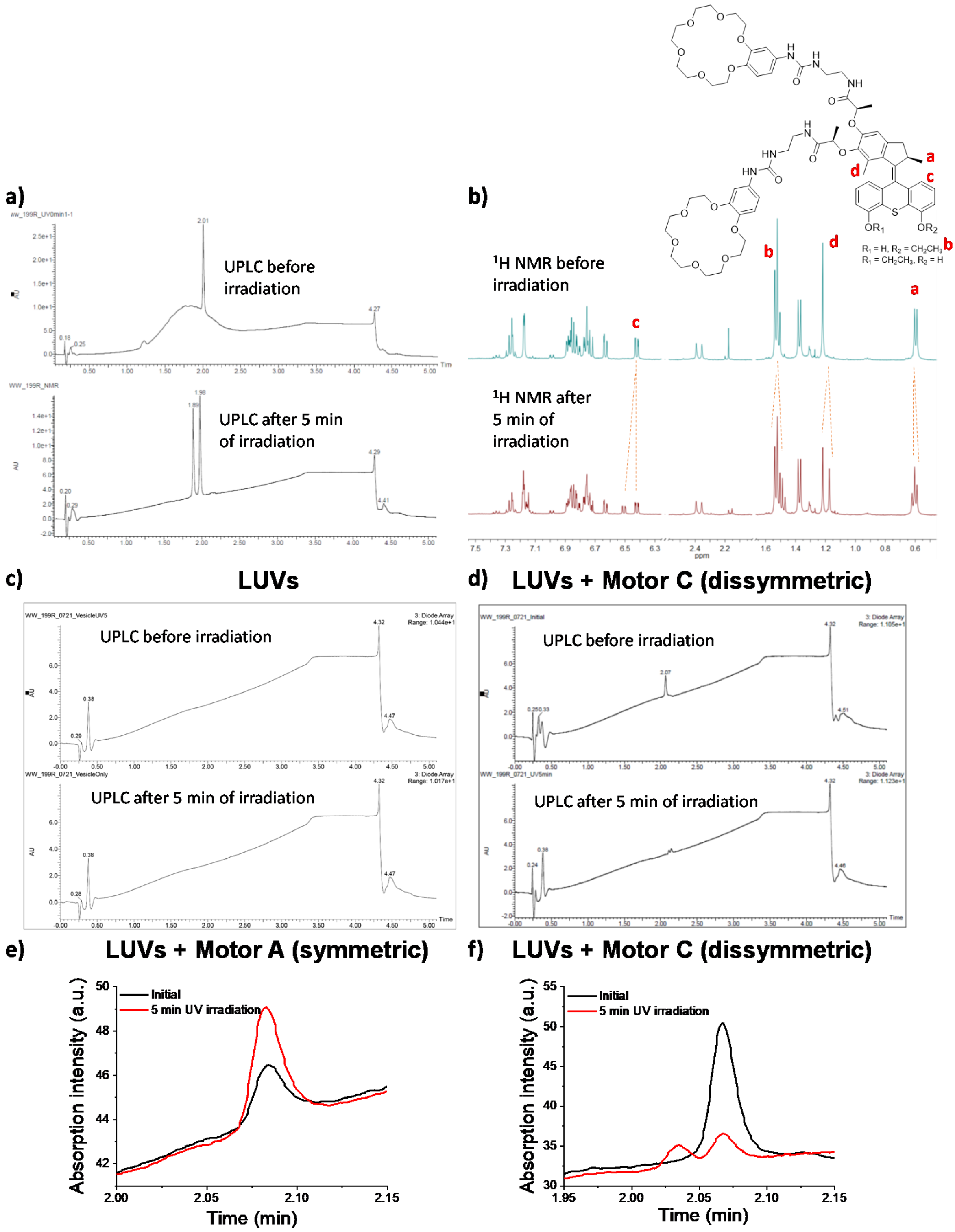

Figure 46. a) UPLC traces recorded for dissymmetric motor **C** before irradiation (top) and after 5 minutes irradiation (bottom); b) ^{1}H NMR spectra (400 MHz, CD_3OD) recorded for dissymmetric motor **C** before irradiation (top) and after 5 minutes irradiation (bottom) with the assignment of some signals of interest; c-d) UPLC traces recorded for c) LUVs alone and d) a mixture of LUVs and dissymmetric motor **C** before irradiation (top) and after 5 minutes irradiation (bottom); e-f) Portion of the UPLC traces recorded for e) a mixture of LUVs and motor **A** and d) a mixture of LUVs and dissymmetric motor **C** before irradiation (black) and after 5 minutes irradiation (red). Experiments (d-f) were performed in the conditions of the HPTS assay at a concentration of CA = 100 M.

If we cannot precisely assign the *cis* and *trans* configuration of these two isomers, both gave distinct spectroscopic signatures. Satisfyingly, when a single isomer was irradiated by UV light, a mixture of the two isomers was obtained, as proved by ^{1}H NMR and UPLC-MS analyzes. From **Figure 46** one can see that after one of the isomers was irradiated at UV light for 5 minutes, a mixture of the two isomers was formed. Furtherly, the UPLC-MS technique shows that one of the isomers can split into two isomers after being irradiated at UV light for 5 minutes (**Figure 46a**). We also perform the UPLC-MS both of compounds **A** and **C** in the same conditions with the HPTS fluorescence test. From **Figure 46e**, we can see that the peak of compound **A** remains a single peak after being irradiated at UV light for 5 minutes. However, for the dissymmetric motor **C**, one of the isomers will split into two isomers after being irradiated at UV light for 5 minutes (**Figure 46 d,f**). These results indirectly demonstrated that the rotation of the motor is indeed occurs under UV light at room temperature.

2.3.2 UV-vis and CD spectra of compound A

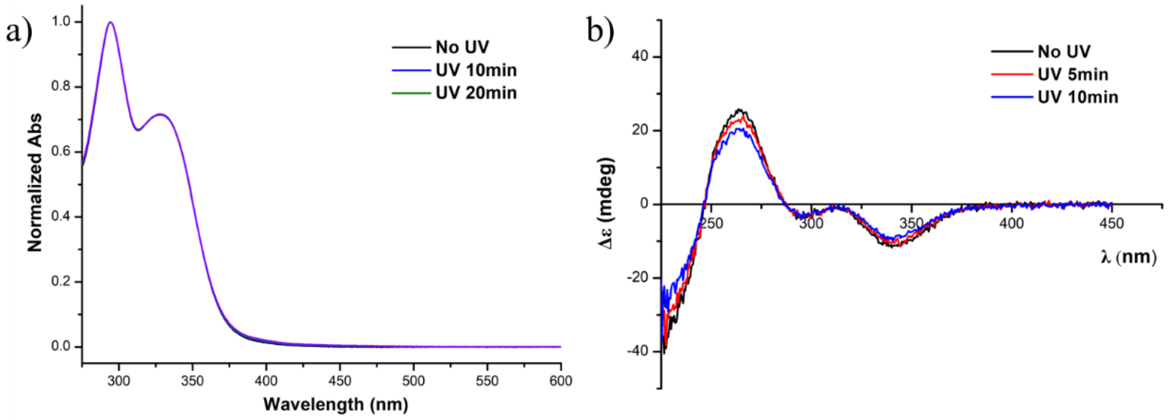

Figure 47. a) UV-vis absorption spectrum of compound **A** ($3.3*10^{-5}$ M) under UV irradiation (λ_{irr} = 365 nm) for different times. b) CD spectrum of the compound **A** ($3.3*10^{-5}$ M) after different irradiation times. Solvent: Acetonitrile.

Compound **A** was characterized by UV-vis at a concentration of $3.3 * 10^{-5}$ M in acetonitrile. Before irradiation, the absorption spectra has two feature peaks at 295 nm and 330 nm (**Figure 47a**). Under UV irradiation at 365 nm, no change was observed in the spectra. The results revealed that there is no unstable state which can be observed under these conditions.

CD spectra experiments were also performed at the same condition to detect the rotation of the molecular motors (**Figure 47b**). Both with UV irradiation or without UV irradiation, no change in shape or intensity of the CD signal was observed in these conditions.

The UV-vis test was also performed in the vesicle containing aqueous solutions. As **Figure 48** shows, before the UV irradiation, the absorption spectra have two feature peaks at 295 nm and 330 nm, which were similar to that observed in acetonitrile. Under UV irradiation at 365 nm for 10 minutes, there was again no change was observed in the spectra. The results revealed that there is no unstable state that can be observed when the motor was inserted into the lipid bilayer membranes.

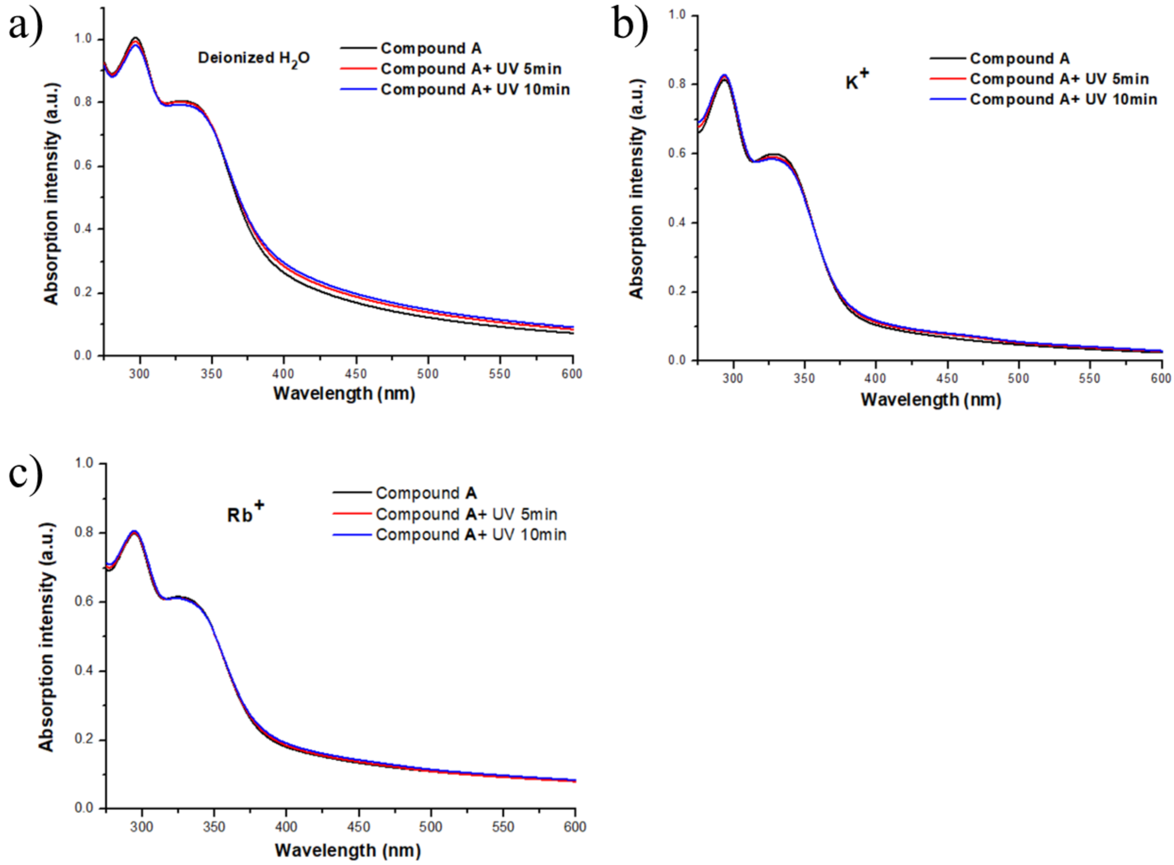

Figure 48. UV-vis absorption spectrum of compound **A** (3.3 * 10^{-5} M) under UV irradiation (λ_{irr} = 365 nm) for different times. Solvents: a) Deionized water (2840 μL); b) KCl PBS solution (2840 μL); c) RbCl PBS solution (2840 μL);+ Vesicle(150μL)+ Compound A DMSO solution (10μL).

Overall, the combination of the ^{1}H NMR, UPLC, UV, and CD experiments reveal that the rotation of motor **A** occurs, and that the unstable states cannot be observed at room temperature, which therefore implies that this rotation is very fast in these conditions (including in the phospholipid bilayers).

2.4 Ion transport Experiments.

2.4.1 HPTS fluorescence assay

The transport of alkali metal ions through lipid bilayers in the presence of molecular motor **A** was monitored by an HPTS fluorescence assay on Large Unilamellar Vesicles (LUV) of phosphatidylcholine. In this assay (**Figure 49**), the fluorescent probe HPTS (8-hydroxypyrene-1,3,6-trisulfonic acid, pKa = 7.2), which in its protonated and deprotonated states exhibits two different absorption wavelengths (450 and 405 nm respectively), is used as a pH probe inside the LUV to indirectly measure the transport of alkali cations M^+. After the introduction of **A** within the bilayer, the addition of sodium hydroxide solution to the extravascular medium creates a pH gradient of approximately one unit compared to the intravesicular medium. Because of the presence of **A**, this gradient can then be compensated by cation/proton antiport or by metal-cation/hydroxide co-transport. By monitoring the relative fluorescence intensity (I_{450}/I_{405}) of the HPTS probe, one can measure an increase of the intravesicular pH which reflects the alkali cation transport across the membrane.

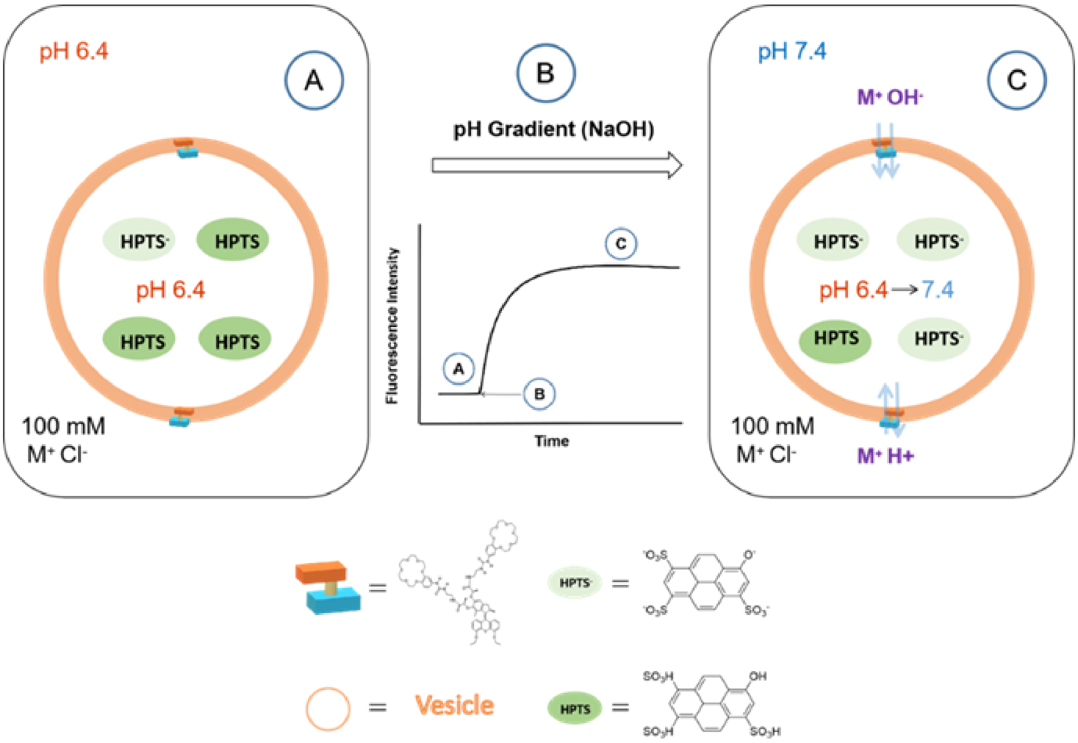

Figure 49. a) Schematic representation of the HPTS fluorescence assay implemented here to study the transport of alkali metal cations through phospholipid bilayer membranes incorporating molecular motor **A**.

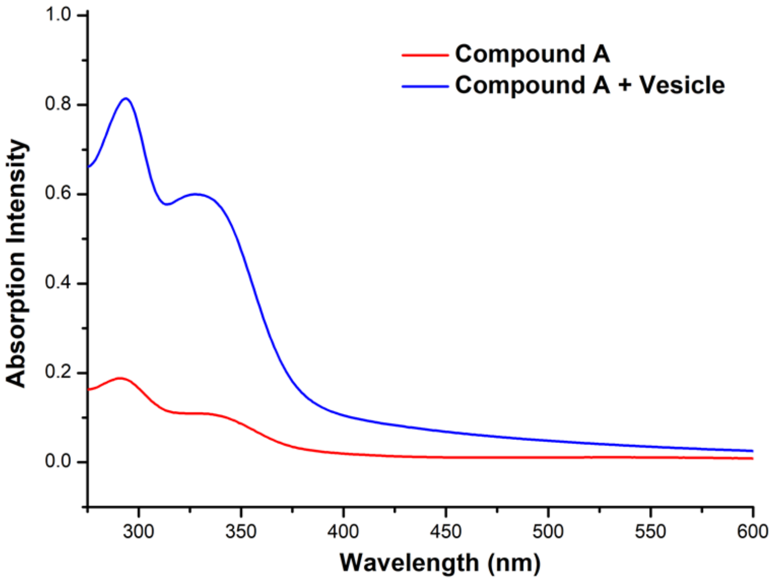

Figure 50. UV-Vis spectra of motor **A** (c = 33 μM)) in a KCl / PBS medium, in the presence (blue) or the absence (red) of LUVs.

Preliminary to this experiment, we probed the solubility of molecular motor **A** into Egg yolk L-a-phosphatidylcholine (EYPC) LUVs by UV-Vis spectroscopy. The linearity of the Beer-Lambert law was verified in the presence of the LUVs, and we determined an extinction coefficient = 1.44 * 10^4 L.mol^{-1}.cm^{-1} in the conditions of the assay. The linearity of the Beer-Lambert relationship and the determination of the extinction coefficient were given by the titration experiment presented in **Figure 51**.

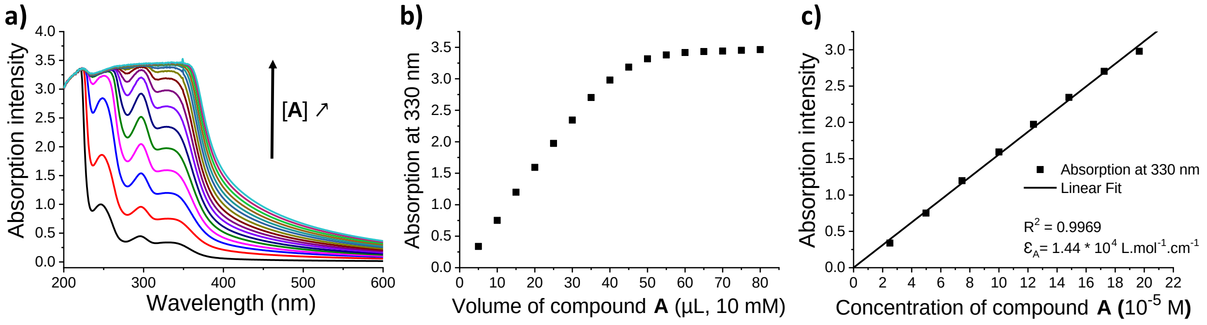

Figure 51. a) Evolution of the absorption intensity for increasing concentration of motor **A** (from 2.5 to 38.6 * 10^{-5} M) in KCl PBS solution (2840 μL) + Vesicle(150μL); b) Evolution of the absorption at 300 nm for increasing volume of compound A starting from a mother solution of 10 mM; c) Evolution of the absorption intensity at 300 nm for increasing concentrations of compound **A** and determination of the extinction coefficient by linear fitting of the data.

In a quartz cuvette, 2840 μL of a solution of 100 mM KCl (or RbCl) in PBS buffer and 150 μL EYPC vesicle were added. This solution was used to record the baseline by UV-Vis spectroscopy. 10 μL of a 10 mM DMSO solution of compound **A** was then added (leading to a 3.3 * 10^{-5} M solution of compound **A**). **Figure 50** shows that for the same concentration of **A**

($3.3 * 10^{-5}$ M) in a KCl / Phosphate-buffered saline (PBS) solution, the absorption spectrum of the motor increases its intensity by more than 4 times in the presence of LUVs, indicating that most of the motor is present within the phospholipid bilayers during the HPTS fluorescence assay.

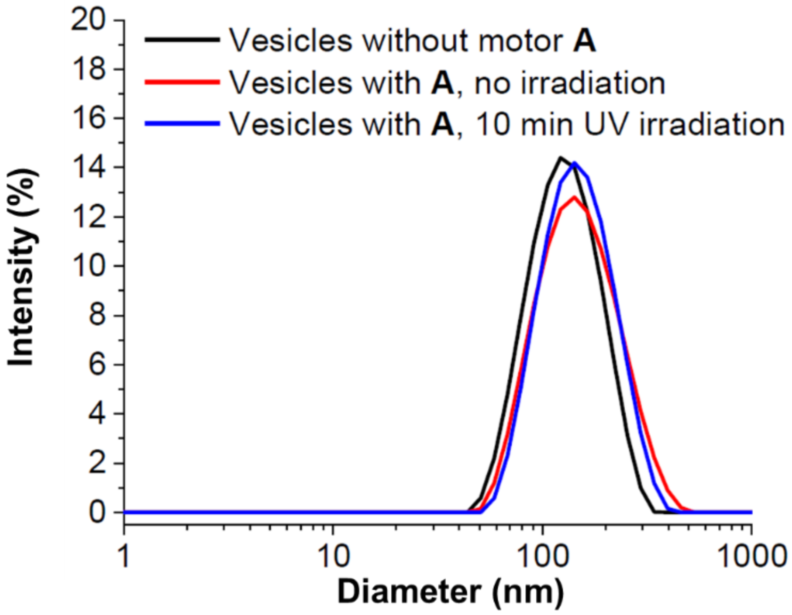

Figure 52. Distributions of hydrodynamic diameters were measured for a solution of vesicles without motors (black), with motors but no irradiation (red) and with motors and after 10 minutes irradiations with UV light (blue).

In addition, we measured by dynamic light scattering (DLS) the size of the vesicles, which show similar diameters of 100 nm with and without molecular motors. We also probed as a control experiment that the typical UV irradiation used in this entire study (365 nm, 7.5 mW/cm^{-2}, for 10 min) of the vesicles loaded with motors does not alter their integrity neither their size.

2.4.2 HPTS fluorescence test of compounds A & B

With this preliminary information, we evaluated the transport activities of Na^+, K^+ and Rb^+ cations with increasing concentrations of compound **A** within bilayer membranes and in the presence of continuous, partial and no UV light irradiation at 365 nm. EYPC LUVs (100 nm diameter) were filled with HPTS and 100 mM NaCl in a phosphate buffer solution (10 mM, pH 6.4). The liposomes were then suspended in an external phosphate buffer solution (10 mM, pH 6.4) containing 100 mM of either NaCl, KCl or RbCl. After addition of 20 µL of a stock solution of molecular motor A in DMSO (2-10 mM), the effective concentration of A was in the range of 20-100 µM. A pH gradient was generated upon external addition of NaOH, and the internal pH change (i.e. inside the liposome) was monitored by the change in fluorescence of HPTS.

For each batch of experiments, control experiments were recorded in the absence of **A** (with and without UV irradiation), to evaluate if ionic diffusion through the lipids bilayer might be affected by UV irradiation, that is by rotation of the molecular motor.

In all the experiments performed, we confirmed the negligible transport of alkali ions in the absence of **A**, independently of the UV irradiation of the vesicles. Importantly, without UV irradiation and in the presence of **A**, a strong increase of transport activity was measured compared to the control experiment without **A** (**Figure 53 a-c**, blue and black curves, respectively).

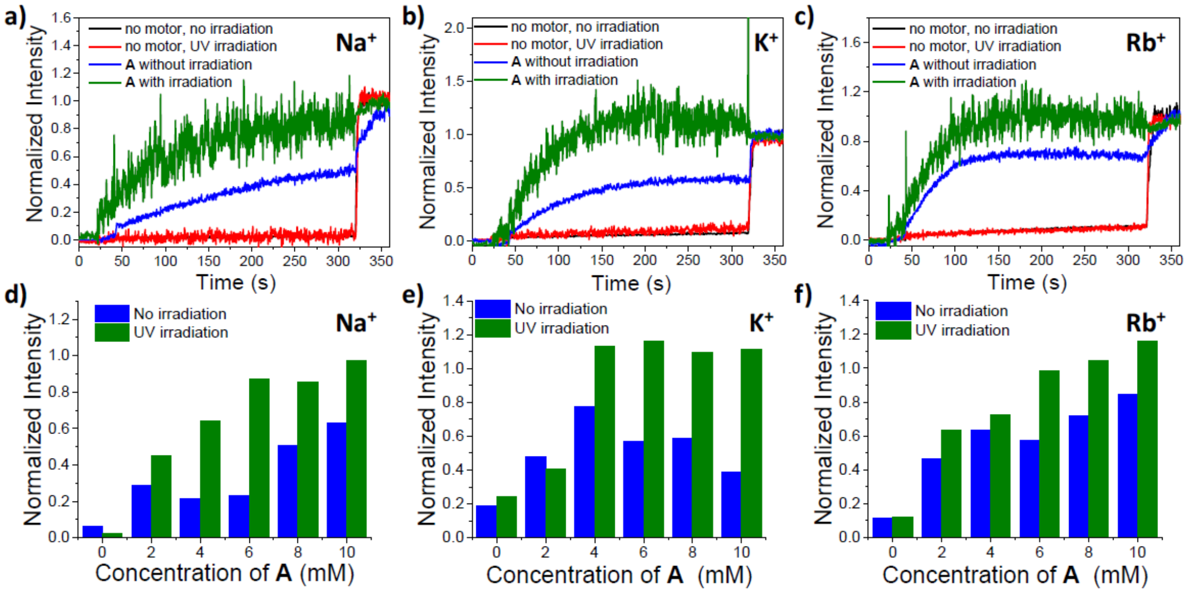

Figure 53. a-c) Evolution of the fractional cation transport activity as a function of time for a) Na^+, b) K^+ and c) Rb^+ cations in the absence of molecular motor **A** and without (black) or with (red) UV irradiation (365 nm, 7.5 mW.cm^{-2}, for 330 s); and in the presence of an 80 µM of molecular motor **A** and without (blue) or with (green) UV irradiation (365 nm for 330 s); d-f) Evolution of the fractional cation transport activity as a function of the concentration of molecular motor **A** in the bilayer membrane at 300 s for d) Na+, e) K+ and f) Rb+ without (blue) and with (green) UV irradiation. Internal composition of LUV is 100 mM NaCl, 10 mM phosphate buffer at pH 6.4 and HPTS 10 µM. External compositions are 100 mM of a,d) NaCl, b,e) KCl or c,f) RbCl in 10 mM phosphate buffer at pH 6.4.

Variations of the fractional ion transport profiles were also shown to depend on the nature of the alkali cation present on the outer shell of the vesicle (see for instance at a concentration of 80 µM in **A**, the effect on the transport of NaCl (**Figure 53a**), KCl (**Figure 53b**) and RbCl (**Figure 53c**), with the following relative rates of transport $Rb^+>K^+>Na^+$). In addition, when evaluating the transport activity in the dark with increasing concentration of **A** (**Figure 53 d-f**, black bars), one can evidence that compound **A** forms aggregated ion-channels towards cations and Hill coefficients were determined for these three metal ions (see **Figure 54**). The Hill coefficients are n>1 for all cations, meaning that more than one active molecule of **A** is used to generate channels with a high degree of cooperativity for the selective transport of cations.

To calculate EC50 and Hill coefficient n, we used the fractional activity Y. Y was calculated for each curve using the normalized value of I_{460}/I_{403} (just before lysis of the vesicles), from 0 (ratio for the blank) to 1 (highest ratio obtained, i.e. a plateau). We expressed Y as a function of time, and we performed fittings using a 2-parameter equation, which is, Hill equation: Y=1/(1+ (EC50/[C])n).

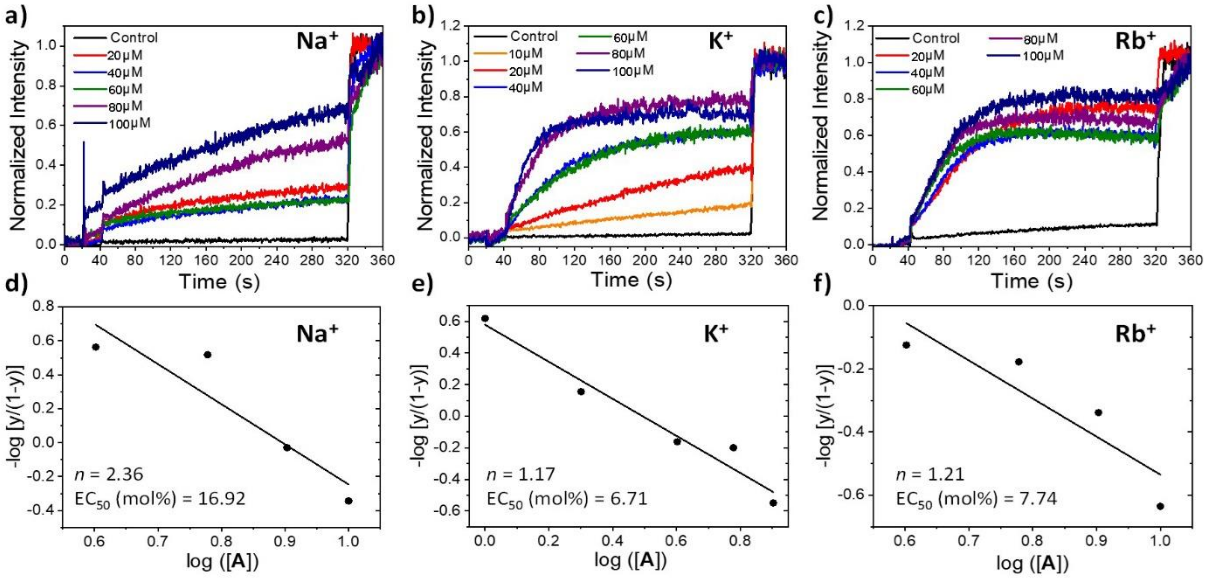

Figure 54. a-c) Evolution of the fractional ion transport activity as a function of time for a) Na^+, b) K^+ and c) Rb^+ in the absence of UV light and without motor (black), and upon continuous UV irradiation and for different concentration of motor A: 10 µM (orange), 20 µM (red), 40 µM (blue), 60 µM (green), 80 µM (purple) and 100 µM (dark blue); d-f) and according to the sequential UV irradiation process (blue); d-e) Hill plots for d) Na^+, e) K^+ and f) Rb^+ transport with motor A. EC50 values are expressed as mol% (% molar of compound/lipid needed to obtain 50% ion transport activity) and n is the Hill coefficient.

The use of benzo-18-crown-6 as a cationic recognition site in the bilayer membrane induces adaptive transport behaviors for compound **A** with selectivity for K^+ at low and medium concentrations (0-40 µM), which then evolves for Rb^+ cations at high concentrations (60-100 µM). Although the exact translocation mechanism of the cations remains difficult to precisely describe at this stage, we know from previous studies that macrocyclic compounds recognize the fittest cations *via* an equatorial binding, whereas a selective sandwich macrocyclic recognition occurs to completely surround the bigger cations. This has been systematically rationalized for ion-specific chromatography[66], membrane[67] and sensing[68,69] polymeric materials. This behavior is reminiscent with the spatial positioning of the carbonyl moieties, perfectly replacing the hydration sphere of K^+ cations within the active gate of KcsA K^+ natural channel[61]. In the present case, it is therefore highly possible that the cations translocate through self-assembled macrocyclic cation-binding aggregates involving proximal macrocycles that may create dynamic pores within the membrane environment.

We then probed with the same HPTS assay the effect of UV irradiation, and therefore indirectly the effect of molecular motor rotation, on the transport activity of Na^+, K^+, and Rb^+ (**Figure 53** a-c, green curves). Satisfyingly, experiments under UV light revealed a very different picture from the results obtained in the dark. Fractional activity increases in all cases in the presence of UV light, and with the strongest improvement of 400% was observed for Na^+ in the presence of **A** at a concentration of 60 μM. Because, in all cases, the fractional activity is at least one order of magnitude higher than the one observed under UV irradiation but in the absence of **A**, one can postulate that this increase is the result of a mechanically activated transport mechanism. Selectivity of transport is also observed under light irradiation, with for instance $SK^+/Na^+= 1.8$ at a concentration of 40 μM in **A**. This preference for K^+ cations decreases in favor of Rb^+ cations at higher concentrations and $SRb^+/K^+ = 2$, following the same trend already observed without light irradiation. Overall, the general trend observed in these experiments corresponds to a strong acceleration of the transport process in the presence of light irradiation, while preserving selectivity aspects between the different ions as a function of the concentration in **A**.

We also studied if this intriguing light-activated transport is the result of an irreversible triggered process, or of a reversible process requiring a continuous irradiation to function. To probe this behavior, we performed sequential irradiation experiments (see protocol of irradiation described in **Figure 55a**) with the same HPTS assay and with a 40 μM concentration in **A**. The alternation of UV irradiation and dark periods shows that higher transport rates were observed for the 3 metal ions that the overall intensity of the transport is reduced by the presence of light-off periods (**Figure 55 b-d**). One can even notice that by just lighting the system at the beginning of the transport for only 70s (**Figure 55 e-g**) or 40s (**Figure 55 f**), the accelerated transport rate drops immediately when switching off the light, and reaches a transport regime which is comparable with the "no light" reference experiment (**Figure 55 a-c**).

To clarify whether the mechanism involved in the acceleration of the ion transport was related to a configurational or conformational switch of molecule **A**, or rather to its out-of-equilibrium rotational motion, we performed a series of 4 control experiments (*i-iv*). *i*) We first studied the influence of UV irradiation on control episulfide **B (Figure 36)** in which the central photo-actuating double bond of the motor is replaced by an episulfide moiety, thereby precluding any rotation upon light irradiation. **Figure 55** h-j show the results for Na^+, K^+, and Rb^+ cations respectively, and unambiguously indicate that there is no enhancement of transport generated by locked motor **B**, thereby strongly suggesting that the rotation motion of **A** is essential to boost the ion transport. *ii*) To verify this rotation hypothesis, we recorded UV and

CD spectra of motor **A** in the precise conditions of the fluorescent assay (that is in the presence of the LUVs and K^+ ions).

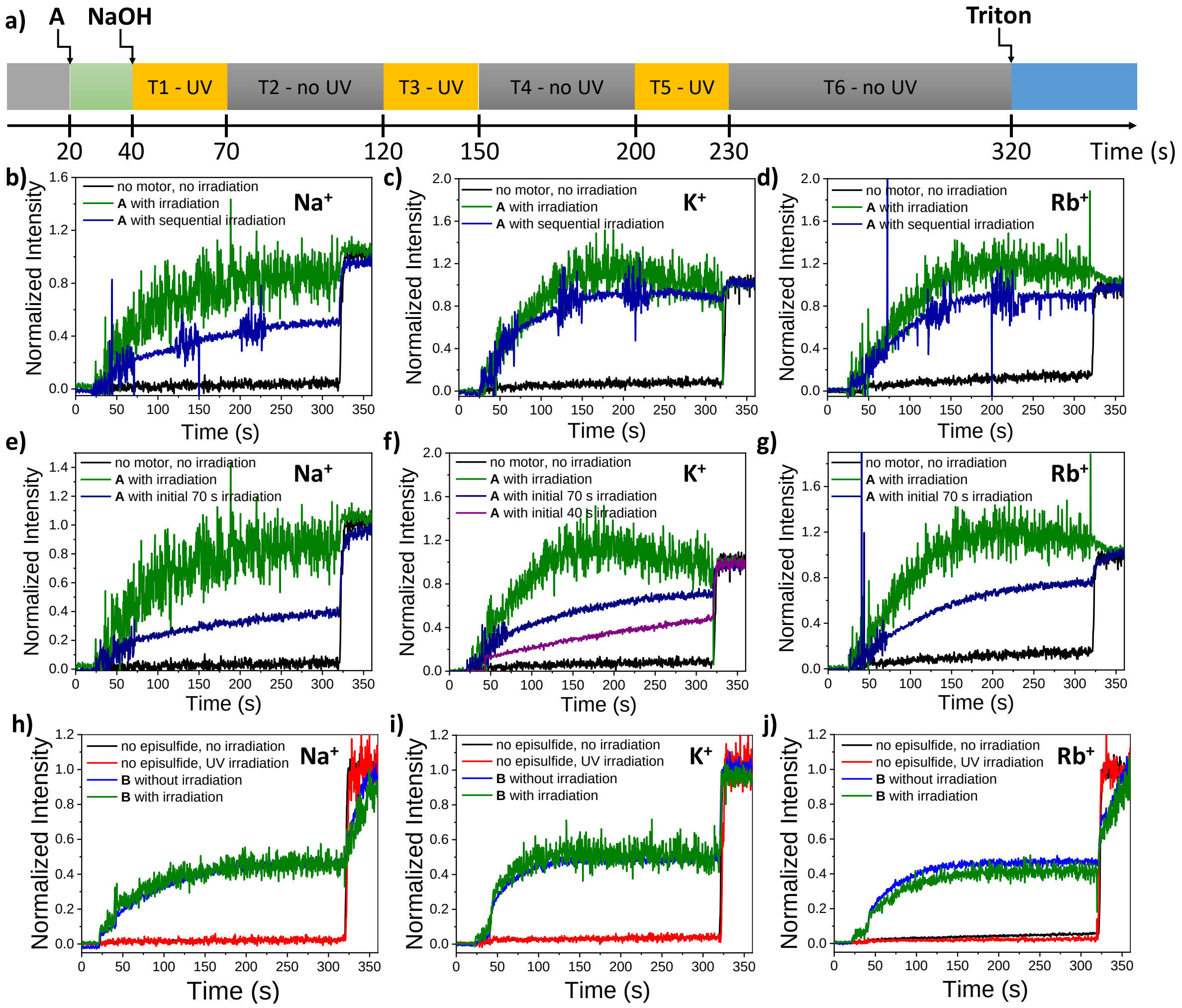

Figure 55. a) Sequential UV irradiation protocol over 360 s for ion transport experiments: at 20 s, addition of compound **A**; no UV irradiation from 20 to 40 s; UV irradiation at 365 nm from 40 to 70 s (T1), 120 to 150 s (T3), and 200 to 230 s (T5); no UV irradiation from 70 to 120 s (T2), 150 to 200 s (T4), and 230 to 320 s (T6); b-d) Evolution of the fractional ion transport activity (C_A = 40 µM) as a function of time for b) Na^+, c) K^+ and d) Rb^+ in the absence of UV light (black), upon continuous UV irradiation (red) and according to the sequential UV irradiation process (blue); e-g) Evolution of the fractional ion transport activity (C_A = 40 µM) as a function of time for e) Na+, f) K^+ and g) Rb^+ in the absence of UV light (black), upon continuous UV irradiation (red), according to an initial 70-second UV irradiation process (blue) and according to the initial 40-second UV irradiation process (purple); h-i) Evolution of the fractional ion transport activity as a function of time for h) Na^+, i) K^+ and j) Rb^+ in the absence of UV light and of episulfide (black), in the presence of UV light but without episulfide (red), in the presence of episulfide **B** but without UV irradiation (blue), and in the presence of episulfide **B** along with UV irradiation (green), with C_B = 100 M.

As shown in **Figure 47**, no change was observed after 5 or 10 minutes of UV irradiation, indicating the absence of another isomer of **A** in the system. In particular, the presence of the unstable helix form of **A** should be visible if its lifetime was long enough. This control experiment therefore shows that either the motor is not turning, or that it is turning too fast to detect the unstable helix (as it is the case for this type of second-generation rotary motors with MHz frequencies due to a low activation energy of thermal helix inversion in solution). iii) To probe whether the rotation indeed takes place in the phospholipid membrane, we synthesized a dissymmetric motor **C**, having in its bottom part a phenol group and an ethoxy group (instead of two ethoxy groups in **A**). This structure allows to differentiate between the *E*/*Z* isomers by ^{1}H NMR, and even to separate them by preparative HPLC (**Figure 46**). By isolating one isomer of **C** and by irradiating it in the LUVs and in the presence of K$^+$ ions, we proved the formation of the other configurational isomer resulting from *E*/*Z* photoisomerization, and therefore the rotation of the motor (**Figure 46**). iv) As a last control experiment, we performed the HPTS assay with variable intensities of UV light, showing that the rate of the transport increases with more powerful irradiations (with a saturation effect above 7.5 mW.cm^{-2}), thus strongly suggesting that the speed of the rotation is related to the transport efficiency (**Figure 56 a-b**).

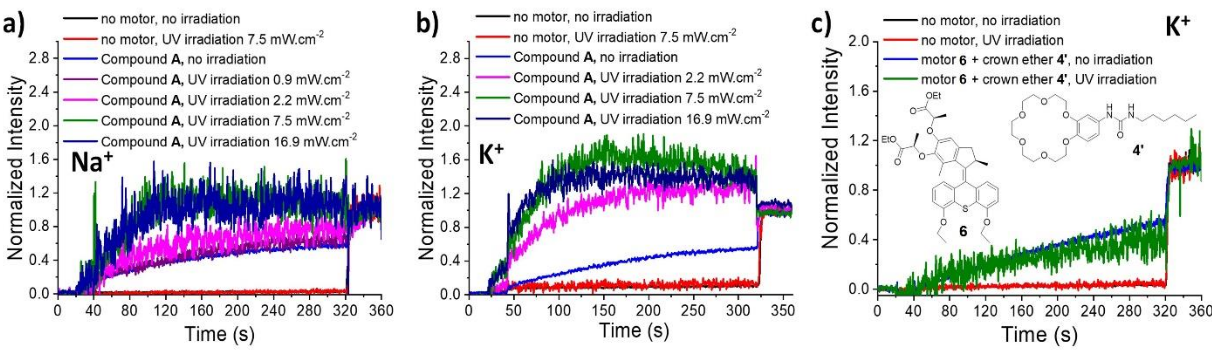

Figure 56. a-b) Evolution of the fractional ion transport activity (C_A = 40 µM) as a function of time for a) Na$^+$, and b) K$^+$ in the absence of UV light (blue), and for different UV irradiation intensities 0.9 mW.cm^{-2} (purple), 2.2 mW.cm^{-2} (pink), 7.5 mW.cm^{-2} (green) and 16.9 mW.cm^{-2} (dark blue), traces in black and red corresponds to measurements performed in the absence of motor and in the absence of UV light (black) or with a UV irradiation intensity of 7.5 mW.cm^{-2} (red); c) Evolution of the fractional ion transport activity as a function of time for K$^+$ in the absence of UV light and of motor (black), in the presence of UV light but without motor (red), in the presence of motor 2 and crown ether 4' but without UV irradiation (blue), and in the presence of motor 2 and crown ether 4' along with UV irradiation (green), with $C_2 = C_{4'}$ = 60 µM.

To understand the importance of the chemical structure of **A** in boosting the ion transport, we performed a second set of 3 control experiments (*i*-*iii*). *i*) First of all, we probed the importance of the macrocycle in channeling potassium ions by performing the fluorescent assay with motor **6** alone (which not contain crown ethers). No transport was observed both in the dark and under UV irradiation, which indicates in addition that no drilling of the phospholipid membrane by the motor takes place in these conditions (**Figure 57**). *ii*) Then, we performed the same experiment but with adding crown ether **5'** in addition of motor **6** (**Figure 56c**). The compound **5'** has been reported in the previous literature[70], which shows excellent K$^+$ ion transportation properties. In that case, a modest transport of K$^+$ ions was measured in the dark, and with no acceleration under UV irradiation, which indicates the necessity to link covalently the crown part and the motor part to benefit from its mechanical actuations. *iii*) We also performed an experiment with motor **F** containing 4 macrocycles (see **Figure 60**). No transport was observed in the dark or with light irradiation, possibly because of a too high steric hindrance of the molecular structure avoiding the formation of ion channels.

The below are some other control experiments, whose results proved the correct design of compound **A**.

a) Free motor 6

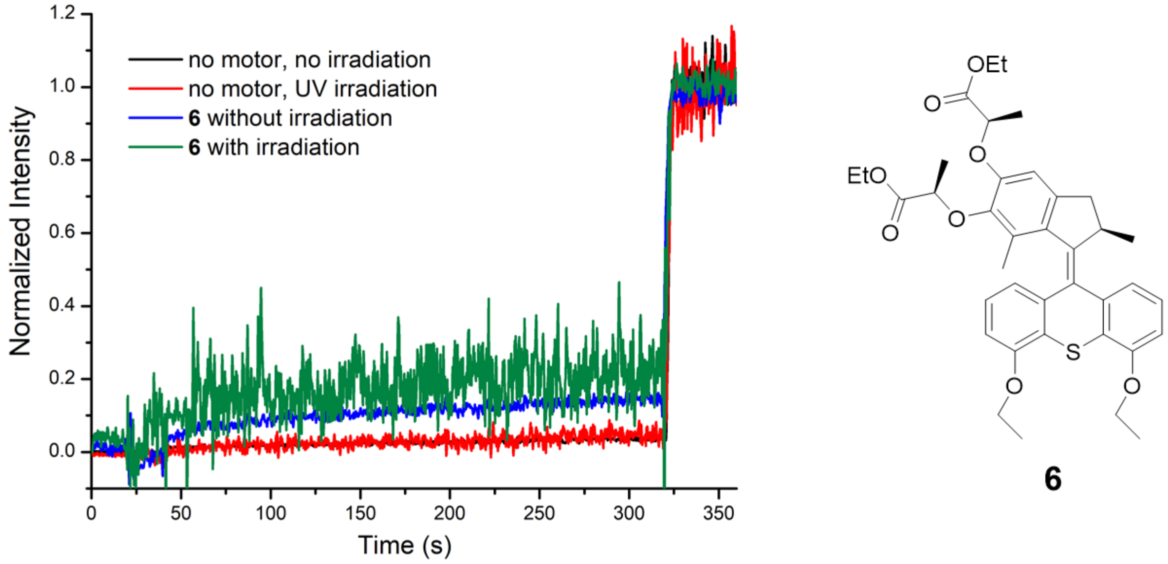

Figure 57. Evolution of the fractional cation transport activity as a function of time for K$^+$ cations in the absence of molecular motor **6** and without (black) or with (red) UV irradiation (365 nm, 7.5 mW.cm^{-2}, for 330 s); and in the presence of a 5 mM of molecular motor **6** and without (blue) or with (green) UV irradiation (365 nm for 330 s); Internal composition of LUV is 100 mM NaCl, 10 mM phosphate buffer at pH 6.4 and HPTS 10 M. External compositions are 100 mM KCl 10 mM phosphate buffer at pH 6.4.

To investigate if the existence of crown ether macrocycle is essential for the formation of the ion channel and the photoresponsive ion transportation, a free motor **6** without macrocycle was used for the test. As shown in **Figure 57**, the transportation activity can be negligible when no UV light was applied. Under UV irradiation, the transportation activity shows no enhancement, which was quite different from the macrocycle containing motor compound. This experiment shows that the two crown ether units are essential for both ion channel formation and photoresponsive ion transportation.

b) Compound D

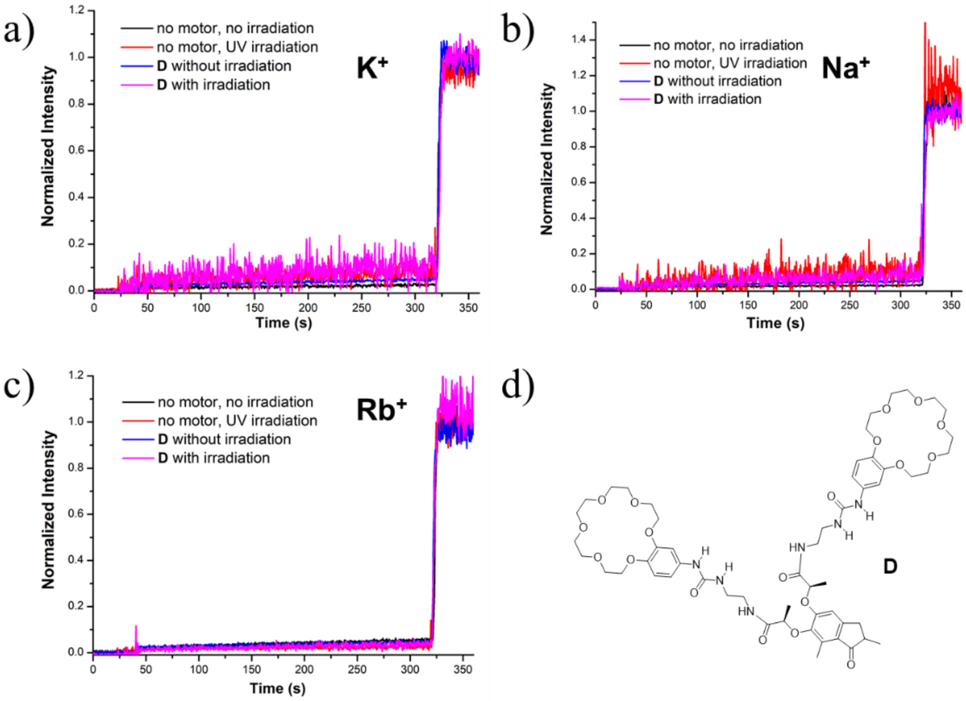

Figure 58. Evolution of the fractional cation transport activity as a function of time for Na^+, K^+ and Rb^+ cations in the absence of molecular motor **D** and without (black) or with (red) UV irradiation (365 nm, 7.5 $mW.cm^{-2}$, for 330 s); and in the presence of a 10 mM of molecular motor **D** and without (blue) or with (pink) UV irradiation (365 nm for 330 s); Internal composition of LUV is 100 mM NaCl, 10 mM phosphate buffer at pH 6.4 and HPTS 10 M. External compositions are 100 mM of NaCl, KCl or RbCl in 10 mM phosphate buffer at pH 6.4.

The concept of the design of molecular motor **D** was inspired by reported literature[58], to study the function of the molecular motors in the ion transportation process. The structure of compound **D (Figure 58d)** was similar to compound **A**, the major difference is instead of a molecular motor as the central core, only a rotor unit was functionalized. The HPTS fluorescence assay experiments (**Figure 58 a-c**) show with the presence of compound **D**, no ion transportation process happen, both with UV irradiation and without UV irradiation. The absence of molecular motor can be explained why no transportation behavior occurred. Though compound **D** contains two 18-crown-6 ether macrocycles, which was considered to be a very useful unit to transport alkali ions such as K^+ or Rb^+, the results show an unexpected result. Moreover, the existence of urea-bond was believed to play an important role in the formation of supramolecular assembly aggregated structures, the results revealed no ion channel was formed inside the lipid bilayers. Together with previous experiments of molecular motor compound **A** and episulfide compound **B**, the results of compound **D** strongly proved the correctness of the molecular structure of compound **A**. As we described, compound **A** contains a hydrophobic molecular motor, which promotes the compounds to be absorbed into the phospholipid bilayer.

c) Compound E

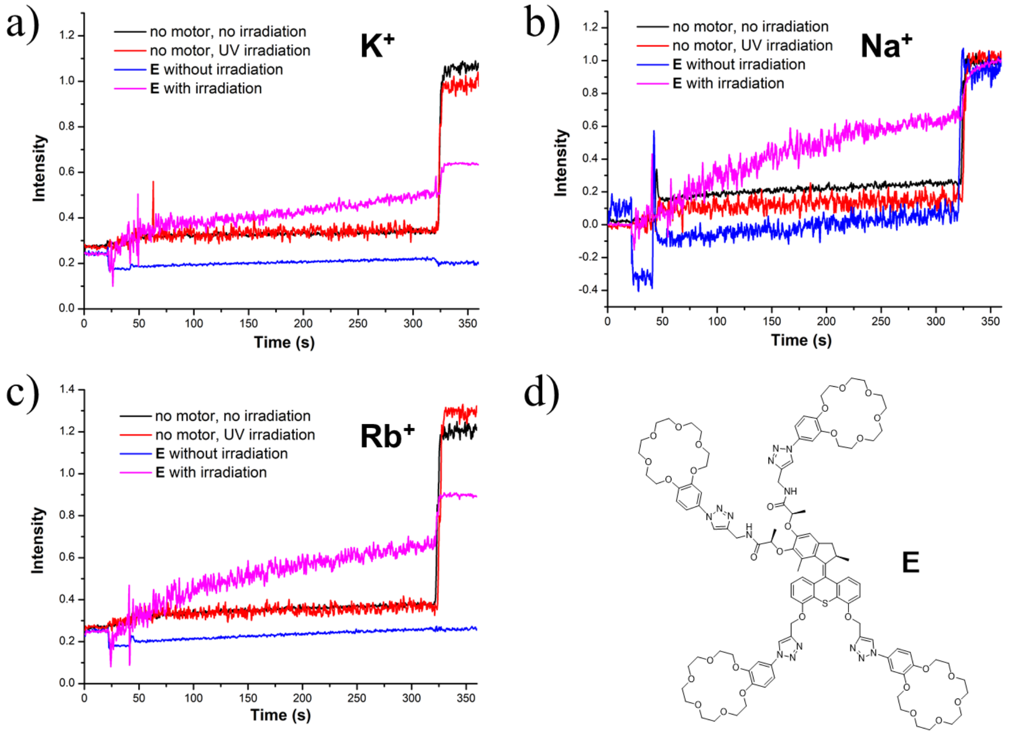

Figure 59. Evolution of the fractional cation transport activity as a function of time for Na^+, K^+ and Rb^+ cations in the absence of molecular motor **E** and without (black) or with (red) UV irradiation (365 nm, 7.5 mW.cm^{-2}, for 330 s); and in the presence of a 100 μM of molecular motor **E** and without (blue) or with (pink) UV irradiation (365 nm for 330 s); Internal composition of LUV is 100 mM NaCl, 10 mM phosphate buffer at pH 6.4 and HPTS 10 M. External compositions are 100 mM of NaCl, KCl or RbCl in 10 mM phosphate buffer at pH 6.4.

Unlike the previous molecules, compound **E (Figure 59d)** contains four crown ether macrocycles, both the rotor and stator parts of the molecular rotor were functionalized. The crown ether macrocycle and the molecular motor core were connected through the Huisgen 1,3-dipolar cycloaddition. HPTS fluorescence experiments (**Figure 59 a-c**) show that there is no transportation without UV irradiation, which illustrates the molecule cannot self-assemble into the ion channel. This result also proved that although the crown-ether unit was necessary for the formation of the ion channel, but cannot promise the formation of the ion channel. Moreover, under UV light, both of the three kinds of alkali ions show a transportation activity, which proves that the rotation of the molecular motor attributes the photoresponsive ion transport.

d) Compound F

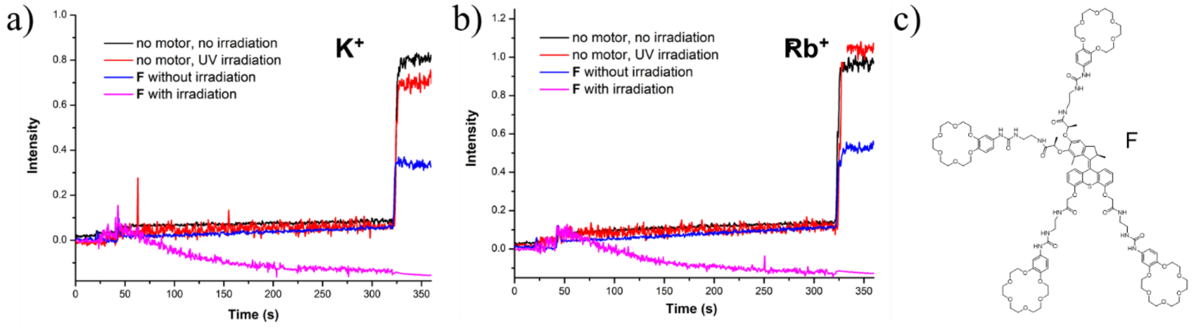

Figure 60. Evolution of the fractional cation transport activity as a function of time for K$^+$ and Rb$^+$ cations in the absence of molecular motor **F** and without (black) or with (red) UV irradiation (365 nm, 7.5 mW.cm^{-2}, for 330 s); and in the presence of a 100 μM of molecular motor **F** and without (blue) or with (pink) UV irradiation (365 nm for 330 s); Internal composition of LUV is 100 mM NaCl, 10 mM phosphate buffer at pH 6.4 and HPTS 10 M. External compositions are 100 mM of KCl or RbCl in 10 mM phosphate buffer at pH 6.4.

The structure of compound **F (Figure 60d)** was similar to compound **E**, the main difference is the crown-ether macrocycle was linked to the central molecular motor central core by the amine coupling reaction, which is similar to compound **A**. The existence of the four urea-bond endow the compound **F** with higher association constants, assuming the molecules will assembly into a well-organized supramolecular structure through the hydrogen bonding interactions. As described in previous compounds, compound **F** was used to perform the HPTS fluorescence assay experiments (**Figure 60 a-c**). The experiments shown, with the presence of compound **F**, ion transportation behavior did not happen. This revealed the existence of the macrocycle cannot permit the formation of ion channels. This can be explained that maybe some aggregated assembly was formed, but they are not proper and suitable enough for ion transportations. The formed supramolecular aggregation structures are disorganized and disordered. Then the same HPTS assay experiments on the effect of UV irradiation were performed. Surprisingly, experiments under UV light revealed a very different picture from the results obtained in compound **A**. Though the results are quite weird, they also proved the correctness of the structure design of compound **A**. Moreover, the unexpected results also proved the existence of molecule motor can not permit improved ion transportation activity under UV light irradiation.

All the controlled experiments by the previous reference compounds prove that both the molecule motor and the crown ether unit were essential for the formation of the ion channel. These two fundamental elements should be covalently connected. The UV can enhance the transportation activity for some of their motor-containing molecules but does not influence others. The hydrophobicity of the molecular motor is very important for transportation. The above experiments prove the correctness of the molecule design.

2.4.3 Single-channel planar bilayer experiments

To obtain supplementary evidence on the ion translocation mechanism through macrocyclic superstructures, we performed a set of conductance experiments with potassium cations. For that, we used the planar lipid bilayer clamp technique[71] in a symmetrical 1M KCl bath solution as an electrolyte, with or without UV irradiation (see experimental part for detailed procedures). After the addition of compound **A**, the transport activity is rather slow to initiate, often requiring 20 min before detecting any onset of activity, which suggests that time is required to self-assemble the channel structure (**Figure 61a**). When active, at a concentration of 80 μM in **A**, transitions between opened and closed states are observed, describing long events (1-2 s) without UV irradiation. These events become shorter (<0.5 s) with UV irradiation, and with an average opened state conductance around 200 pS (multi-level conductance type).

The activity without UV irradiation (**Figure 61a**) suggests the formation of unstable single channels with an erratic activity produced as periodic and occasional bursts and possibly arising from unstable pores.[72] In the present case, evaluation of the overall conductance of the open states is more likely related to dynamic exchanges between channel components rather than copies of a single channel[73]. These open state events are highly amplified under UV irradiation (**Figure 61b**), and therefore supposing by the mechanical rotation of molecular motor **A**. Their orderly flow toward one direction creates a dynamic charge distribution along the channel, which can certainly be stimulated if a strong electric field is applied. Thus, this multiple conductance behavior is intrinsically related to a type of ‘supramolecular polymorphism’ while the cation translocation is related to the dynamics of the crown-ether aggregates within bilayers. In addition, despite the presence of local signal variability due to dynamic behaviors of the lipid bilayers under combined UV irradiation/mechanical motor motions, the presence of open and close states under light irradiation in the patch-clamp experiment, as well as the ion selectivity revealed by the HPTS assay, strongly discard the possibility of a transport mechanism resulting from the drilling of the membrane.

I-V plots in **Figure 61c** also show a linear variation (i.e., ohmic behavior) at low potential, while at the higher potential they become asymmetric, suggesting that channels of **A** can be triggered at high positive voltage. The ionic conductance values (γK^+) are 0.45 ± 0.04 nS (without UV irradiation, blue data) and 0.95 ± 0.1 nS (with UV irradiation, red data) for the positive currents and 0.24 ± 0.02 nS (without UV irradiation) and 0.35 ± 0.05 nS (with UV irradiation) for the negative current. The ion transport conductances present a 100% increase upon UV irradiation compared to the same experiment in the dark, a value similar to the one previously observed with HPTS assays (**Figure 53e**).

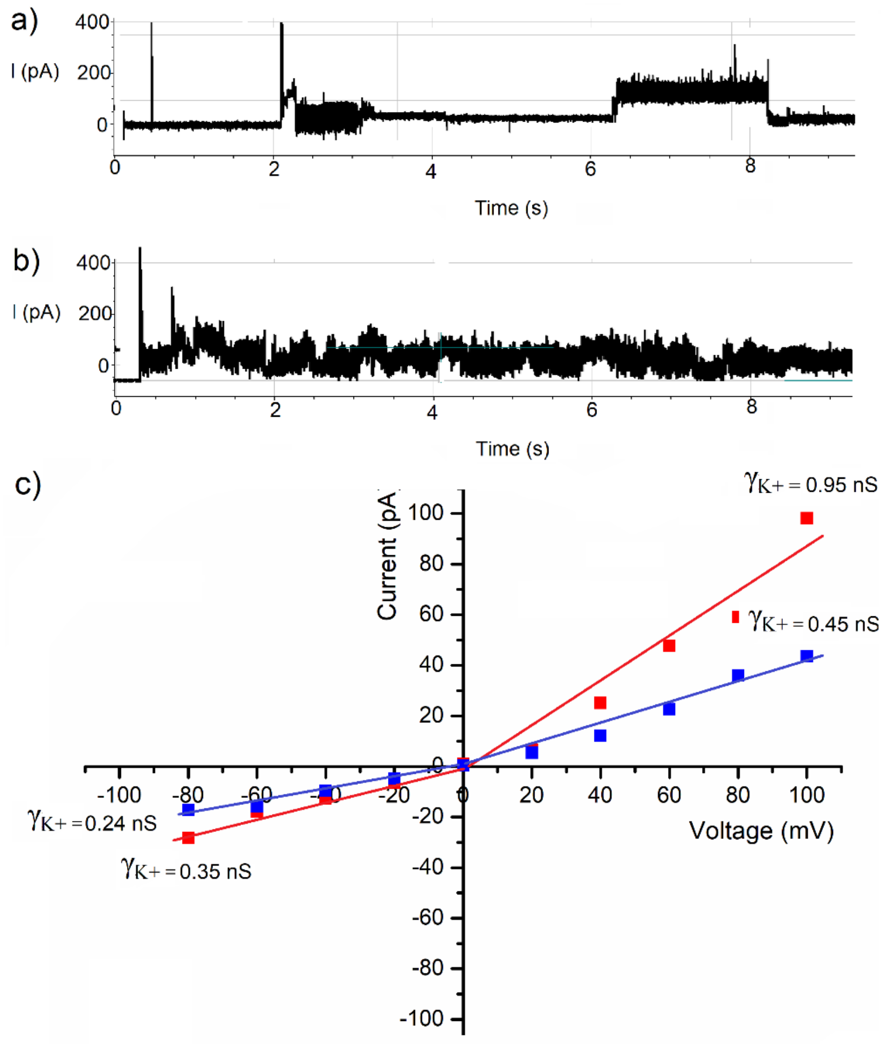

Figure 61. a) Typical evolution of the membrane activity measured by single-channel planar bilayer experiments involving motor **A** a) without UV and b) under UV irradiation (Cis/trans 1M KCl, diphytanoylphosphati-dylcholine (diPhyPC), 8 mM **A**, +100 mV). b) I-V plots for channels made of compound **A** recorded with UV (red) and without UV (blue) irradiation.

Further comparison of the two sets of perfectly fitted current versus voltage curves indicates that channels of **A** present an interesting rectification behavior, as confirmed by the different conductance values determined at negative and positive potentials. Such rectification behaviours are reminiscent with a specific dipolar orientation of the asymmetric superstructures of compound A within the membrane bilayer (see also CD spectra in **Figure 47b**).[74]

2.5 Conclusion

In summary, we have designed intriguing ion channels constructs based on 18-crown-6 macrocycles conjugated with light-driven rotary molecular motors. Such channels show selective transport of alkali cations through phospholipid bilayers in the dark. Further, their transport activity strongly increases – up to 400% – under UV irradiation. To rationalize this effect, one can propose that the actuation dynamics of the molecular motor provides energy to the ion channel in the form of mechanical deformations and vibrations,[75] or in the form of local heating by energy dissipation. This adds to the surrounding thermal energy and helps crossing the activation barrier necessary to translocate ions between macrocycles along the artificial pore. This first observation of a selective and accelerated cation transport provided by an artificial molecular motor is of importance for the field of molecular machines where such applications are highly expected. The experiments performed in this study strongly suggest that the continuous out-of-equilibrium[76] rotation of molecular motor **A** is responsible for boosting the ion transport activity, which is a fundamentally different functioning principle when compared to molecular switches which can change ion conductivity by adopting different configurations/conformations as a function of their states. These results are also of particular interest for the development of new regulated transport mechanisms making use of responsive artificial channels. This motional activation gives to the channels an increase in performance from the point of view of mass transfer. They can adapt dynamic transient superstructures which are ion selective and permeable. In addition, for the particular case of the patch-clamp experiment, this study demonstrates the intriguing coupling between mechanical forces with electrical signaling, a phenomenon at the core of very important pathogenic mechanisms in biology, such as those involved in neurodegenerative diseases.[77]

Chapter 3: Actuation of molecular motor-based gels

Special thanks to Alexis, Damien, Joachim, Xuyang for sharing their precious motor precursors with me.

3.1 Systems with covalently linked molecular motor units

The incorporation of molecular machines into polymer networks has attracted huge attention in recent years due to their promising application to gather and enlarge motion from the nanoscale to the macroscale. Prominent examples in this topic are the mechanically interlocked linear polymers constructed through the head-to-tail linkage of the bi-functionalized [*c*2] daisy chain rotaxane heterodimers.[78,79] [*c*2] daisy chains are a kind of mechanically interlocked molecule first introduced by Sauvage and co-workers, with a unique double-threaded topology which confers to these molecules the ability to contract and extend at molecular scale upon external stimuli (such as pH or redox potential).

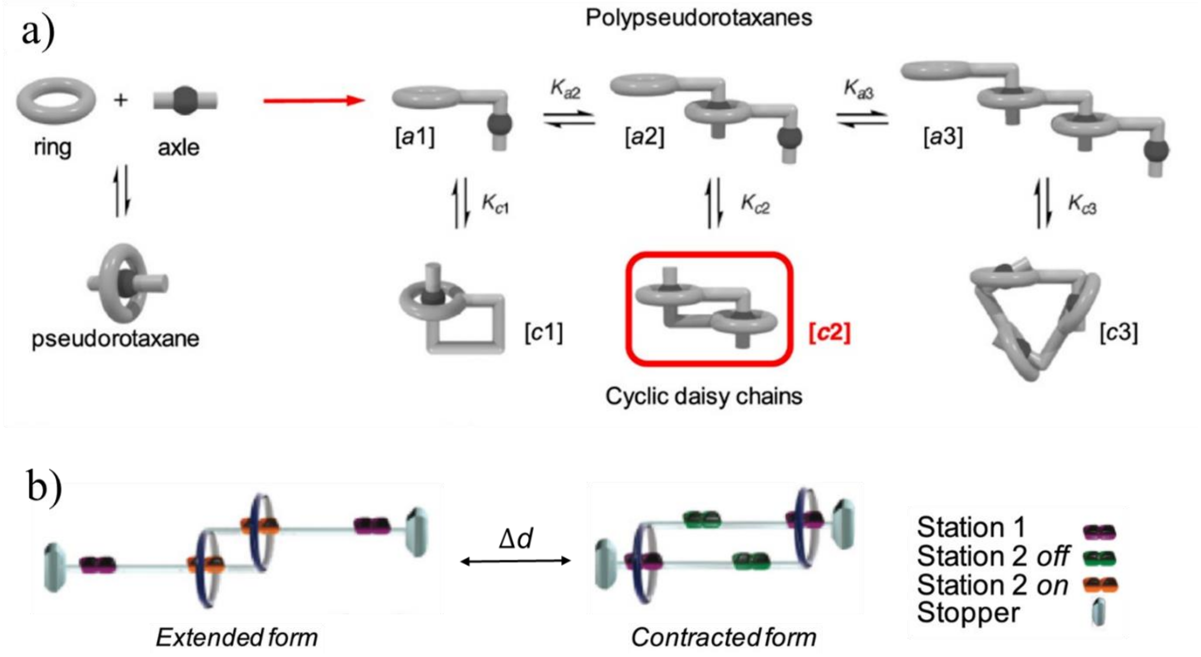

Figure 62. Schematic representation of a) the construction of a [c2]daisy chain); b) of a bistable [c2]daisy chain rotaxane in its extended and contracted forms[80].

Our group reported the first example about the pH-responsive collective motion derived from polymerized [*c*2] daisy chains. The ends of the [*c*2] daisy chain monomer were terminated with two terpyridine groups, which were responsible for the formation of supermolecular polymers when adding Zn^{2+} or Fe^{2+} ions through octahedral coordination between two ligands. Through several scattering experiments (using light and neutrons), the bistable [*c*2] daisy chain rotaxane polymers were shown to actuate by a global micrometric contraction along a single polymer chain. Further, in 2016, our group demonstrated the possibility to aggregate such single-chain supermolecular polymer produce dynamic mesoscale structures which can contract and extend while changing their morphologies (**Figure 63**).[81] In that case, the monomer was a pH-switchable [*c*2] daisy chain terminated with two 2,6-diacetylamino pyridine units, which can self-assemble in supramolecular muscle-like polymers through complementary hydrogen-bonding interaction with a bis-uracil motif as a rigid linker. The interaction between the complementary monomers was revealed by ^{1}H-NMR experiments. The remarkable morphological transformation between the contracted state and expanded state was observed through the TEM and AFM macroscopic techniques， as well as by light and neutron scattering techniques.

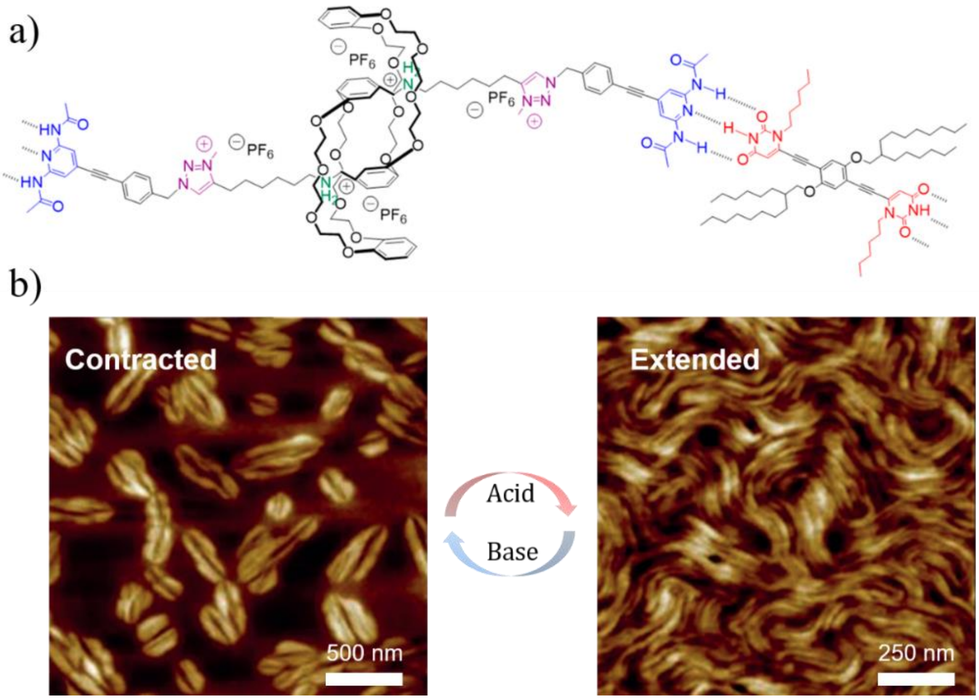

Figure 63. a) The chemical structure of the acid-base responsible [*c*2] daisy chain monomer terminated with 2,6-diacetylamino pyridine motif. The terminated unit can be polymerized with a bis-uracil linker. b) AFM images of the coffee-bean-shaped pattern and the entangled fibers of the contracted or extended states, respectively.

Besides the conformation variations that occur in single-chain polymers and in their self-assemblies, scientists also make efforts to explore collective motion up to the macroscopic scale. One of the strategies is, through supramolecular methods, to entangle single fibers or their bundles into larger networks. On this point, our group reported a 2-ureido-4[1H]-pyrimidinone (Upy) terminated acid-base bistable [*c*2] daisy chain rotaxane (**Figure 64**).[82] The Upy units can form H-bonds dimers in organic solvents such as chloroform or toluene with high association constants, and therefore bis-Upy derivatives can undergo supramolecular polymerization. In addition, Upy dimers can interact between them by π-π stacking interactions, providing the single chain polymers of rotaxanes with the possibility to produce non-covalent polymer networks. In this example, under UV irradiation at 365nm, the 2-nitrobenzyl-protected UPy-terminated [*c*2] daisy chain rotaxanes undergo photocleavage in toluene, releasing the unprotected UPy group which dimerizes through hydrogen bonding interaction, resulting in the formation of single chains supramolecular polymers with a degree of polymerization in 22 in the contracted state. In the extended state, the lesser steric hindrance at the vicinity of the Upy dimers allows for their π-π stacking and subsequent physical crosslinks induce a sol-gel transition. The gel-sol states can be reversible switched upon protonation or deprotonation of the [*c*2] daisy chains.

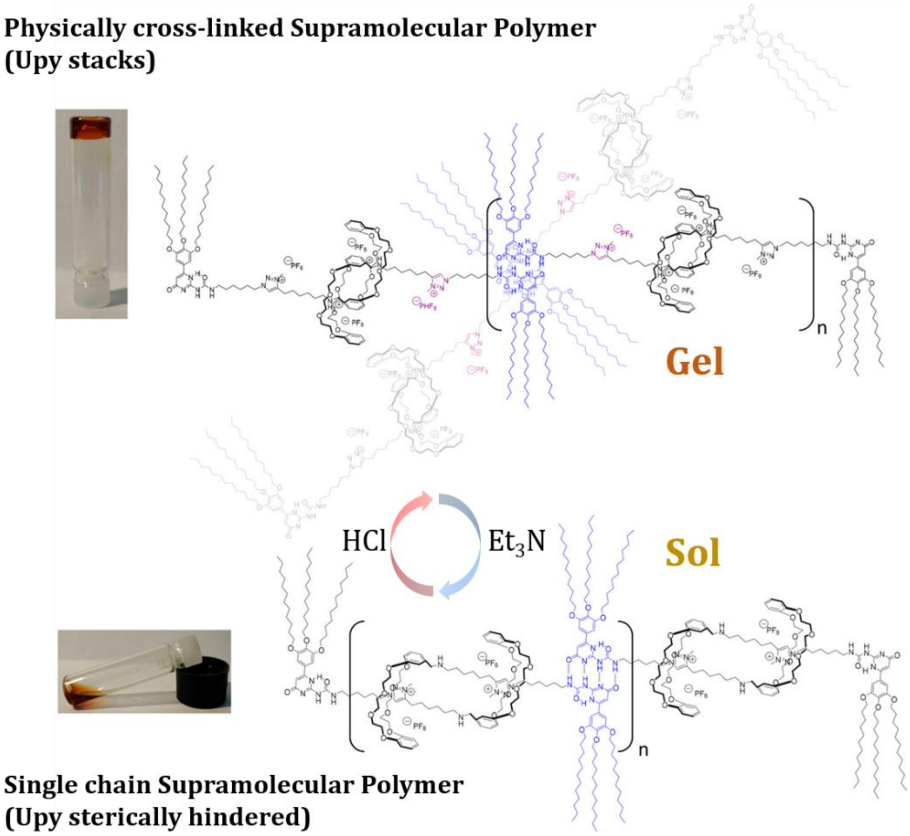

Figure 64. The [c2]dasiy chain rotaxane-based supramolecular polymers. The gel-sol transition was observed with the addition of HCl or Et_3N respectively.

Another method to achieve collective motion of rotaxanes consists in their covalent reticulation into chemical polymer gels, as our group reported in 2017.[83] By integrating the [*c*2]daisy chain with the oligo (ethylene glycol) through the azide-alkyne click reaction, a covalently chemical gel was obtained (**Figure 65**). By immersing these gels into the basic solutions or acidic solutions, the volume of the gel can be contracted or extended. Compared to the original state, the maximum contraction of the gel volume could be ~60%. The contract-expand process can be repeated several times and shows excellent reversibility. High-resolution magic angle spinning ^{1}H NMR, and neutron scattering experiments proved the macroscopic volume change caused by the controlled motion of the [*c*2] daisy chains polymers. Along with the previous studies, one can definitely consider that macroscopic motion can be achieved by the collective actuation of tiny molecular machines when properly integrated within polymer materials.

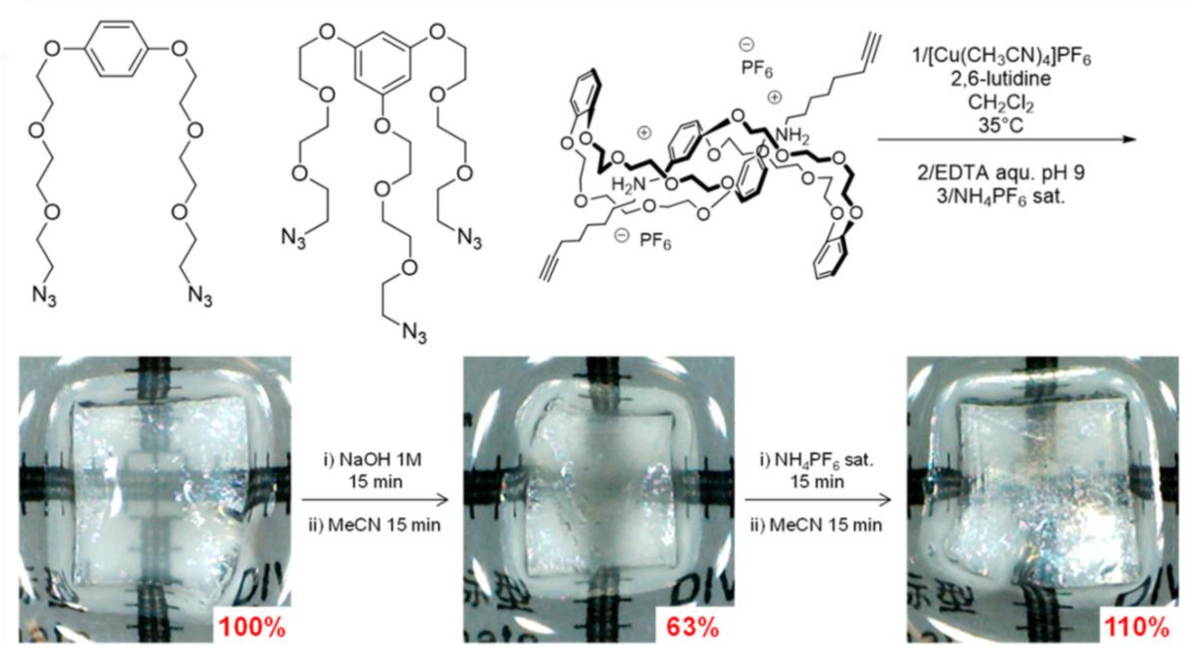

Figure 65. Construction of the covalently linked chemical gel which should contraction-expansion reversibility in the basic or acidic solutions respectively.

Harada and co-workers also developed photo-responsive actuated hydrogels and xerogels constructed from [*c*2] daisy chain rotaxane compounds (**Figure 66**).[84] Taking another macrocycle that the well-known crown-ether as the host molecule, they synthesized a new-type interpenetrated [*c*2] daisy chain by choosing the α-cyclodextrin (α-CD) unit. Through the polycondensation reaction between the α-CD [*c*2] daisy chain and the tetra-armed poly(ethylene glycol), both dry and wet types of actuators were obtained, named [*c*2]AzoCD2 hydrogel and [*c*2]AzoCD2 xerogel, respectively. The cuboid hydrogel was prepared to study the contraction and expansion properties.

Under UV irradiation, the azobenzene units undergo *cis*-*trans* photoisomerization and slide away from the α-CD macrocycle, resulting in the shrinkage of the [*c*2]AzoCD2 hydrogel volume. The volume of the contracted azo hydrogel can be recovered when the gel was exposed to visible light. Furtherly, photo actuation of the hydrogel and xerogel was studied. [*c*2]AzoCD2 hydrogel bends towards the UV light source and recovers to the initial state under visible light.

Both of the two phenomena can be explained as the conformational change of the azobenzene, the water in the hydrogel was discharged. The azobenzene unit of the light source part preferentially absorbed the UV light and easier undergo the contraction behavior, causing the flex of the [*c*2]AzoCD2 hydrogel string. The dry [*c*2]AzoCD2 xerogel was obtained from the icy hydrogel after a freeze-drying technique. Compare to the bending speed of the [*c*2]AzoCD2 hydrogel requires ~3 h to bend 7.2°, the [*c*2]AzoCD2 xerogel just need 1s, which was 10800 times faster than that of the wet-type actuator. The xerogel cannot achieve the light-responsive back and forth motion, while the hydrogel owns excellent reversibility by varying the UV and visible light.

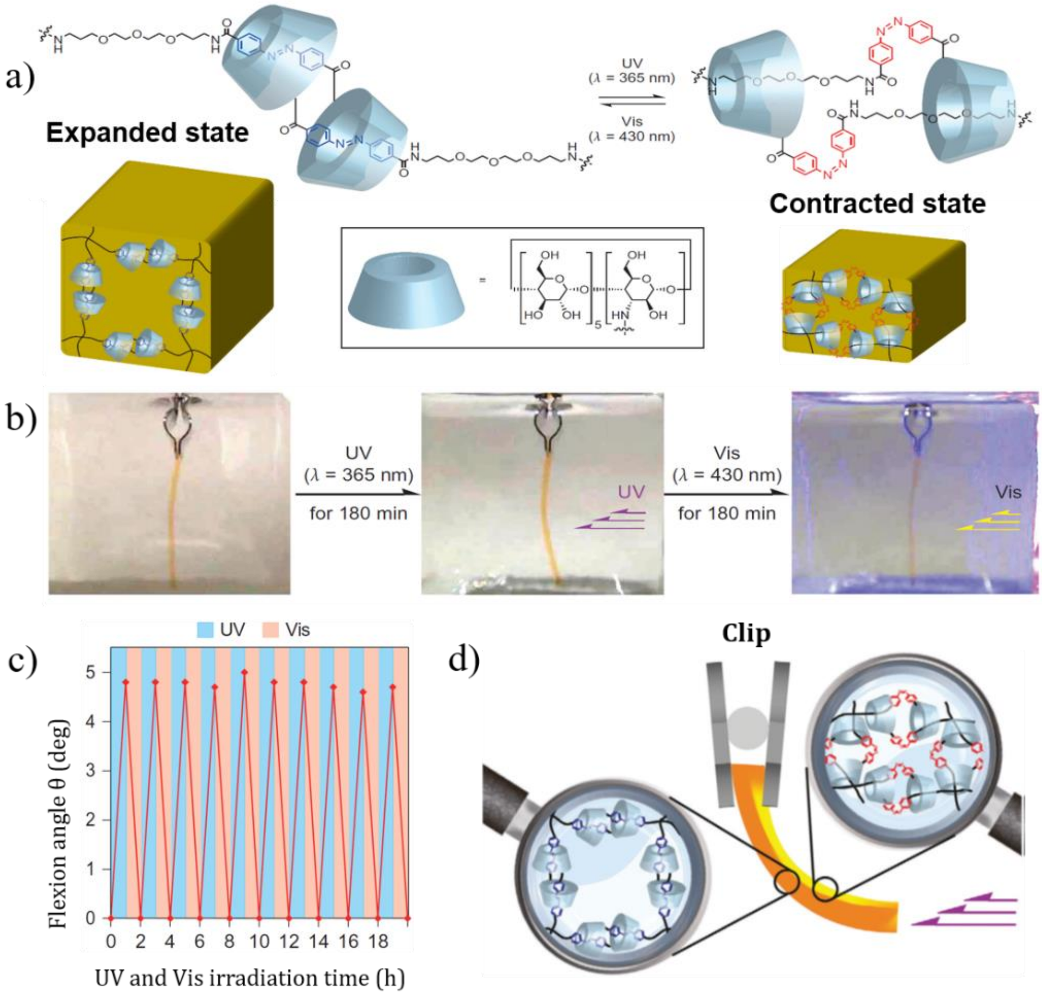

Figure 66. a) Chemical structure of the light-responsive αCD-based [*c*2]daisy chain rotaxane motif used to construct the gel and the schematic presentation of the cuboid hydrogel. b) Photo-responsive actuation of the [*c*2]AzoCD$_2$ hydrogel under UV and visible irradiation. c) Reversible control of the [*c*2]AzoCD2 hydrogel by varying with UV and visible light. d) Schematic presentation of the bending mechanism of the [*c*2]AzoCD$_2$ hydrogel.

In 2018, the same group reported a similar system base on the stilbene (Sti) unit rather than the azobenzene unit, both wet and dry gel was obtained.[85] Two kinds of gels can achieve rapid and large deformations upon the irradiation of UV light, due to the photoisomerization property of the Sti moiety. Both of actuation and contraction behaviors of the stilbene-based gel are much faster than those of the azobenzene-based [*c*2]daisy chain materials.

Dithienylethenes have attracted wide attention among a variety of photochromic molecular switches due to their promising application for constructing novel materials such as optoelectronic devices. Alternatively irradiated by UV or visible light, diarylethenes undergo a reversible photocyclization reaction (through 6π electrons) between a colorless open form and a colored closed form. Photoresponsive switch embedded polymers have proved to be efficient responsive materials, and in particular dithienylethene switches allow for reversible control of materials properties under the diverse regulation of different wavelengths of light.

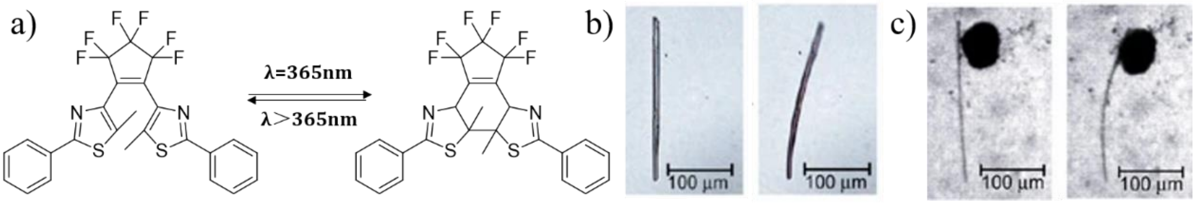

Figure 67. (a). Chemical structures of the open- and closed-ring isomers of the dithienylethene compound. (b). Before and after UV irradiation of the crystalline rod. (c). Movement of a gold micro-particle (the black spot).

One of the crucial applications of the dithienylethene switch was achieved by Irie and coworkers[86] in 2007 (**Figure 67**). By using 1,2-bis(thienyl) perfluorocyclopentene motif, a rod-like crystal was constructed which can achieve bending under the irradiation with ultraviolet light, with the bending direction towards the incident light. Moreover, during the bending of the rod-like crystal, the force was large enough to move a gold micro-particle (the black spot) which is 90 times heavier than the weight of the crystal.

Feringa’s molecular motors were also shown to achieve collective motion at a larger scale. For instance, Feringa and coworkers reported a hierarchical biomimetic supramolecular system by using light-responsive molecular motors (**Figure 68**).[87] They carefully designed an amphiphilic molecular motor with a hydrophobic dodecyl chain at the rotor part and two water-soluble carboxyl groups at the stator part. This amphiphilic molecule can self-assemble into nanofibers in water, and with a water content in the materiel as high as 95%. When the nanofibers are added to a $CaCl_2$ aqueous solution, the disordered nanofibers transform into unidirectionally aligned noddle-like strings, and both of the morphologies were confirmed by scanning electronic microscopy (SEM). Under UV irradiation, the supramolecular string was shown to bend to the light source. This example is the first direct observation of the hierarchical molecular motor-based supramolecular system constructed through non-covalent interactions.

The bending process of the string is relatively fast at large scale, going from the initial state of 0° to the maximum flexion state of 90° within one minute. Then, the saturated 90° bent string was heat at 50 °C in the dark and recovered to its original conformation with 3 hours. The same string was able to perform a second actuation, with a maximum bending angle of 45°. The poor reproducibility was attributed to the high temperature necessary to achieve the thermal helix inversion, and which can also cause the partial damaging of the supramolecular assembly. Photo-actuation was also performed in the air, and in that case, the gelified noodles can lift a 0.4 mg piece of paper during the irradiation process with a saturated angle of 45°. The mechanical work made by the string actuation process was calculated to be 0.05 μJ. Note that in this case, the Feringa's motor is used as a bistable unit and that its rotation does not involve the motion. The actuation is controlled by the configurational / conformational change of the motor, which is therefore acting as a switch.

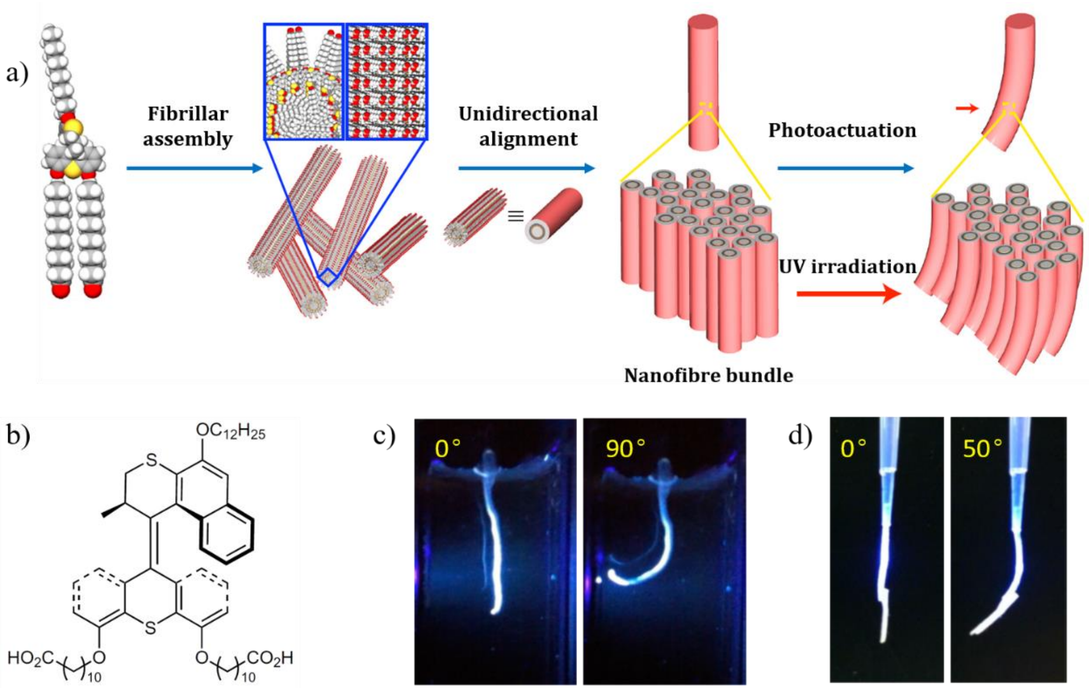

Figure 68. a). Schematic representation of the hierarchical self-assembly and photo actuation of the amphiphilic molecular motor-based nanofibers and buddles used to construct the macroscopic strings. b). Structure of the photoresponsive molecular motor. c) Photographic snapshots of a supramolecular string in the water. The UV irradiation from the left and string bends towards the light source from 0° to 90° within 60 s. d) Photographs of the photo-actuation of the string upon UV irradiation in the air with 0.4 mg paper as weight appendant.

In fact, the first integration of Feringa's motors in polymer network was reported by our group in 2015, and in that case, the actuation of the motors was proved to really function through continuous rotation of the machine. We integrated a functionalized second-generation molecular motor into a polymeric network to generate active chemical gel (**Figure 69**).[88] The key motor compound was obtained by decorating the rotor part with two azide-terminated poly(ethylene glycol) polymer chains, and the stator part with two alkyne-terminated oligomeric ethylene glycol chains.

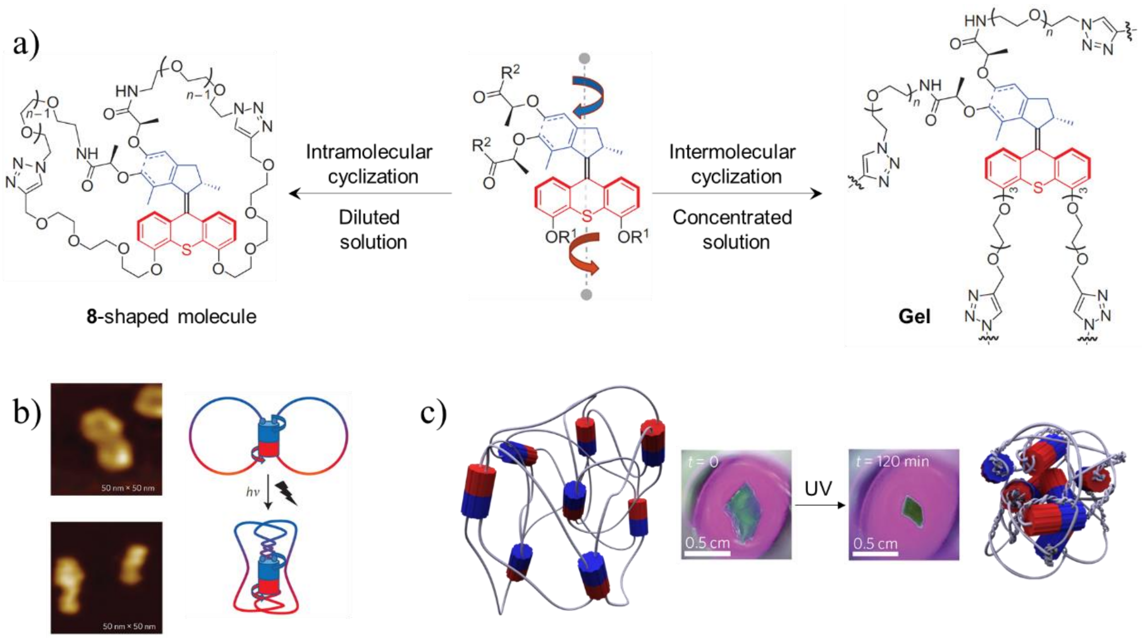

Figure 69. a) Chemical structures of the molecular motor, the 8-shape macromolecule and the polymeric gel. b) AFM images of the 8-shape molecule before (top) and after (bottom) UV irradiation. c) Images of the gel before (left) and after (right) UV irradiation.

The head-to-tail intramolecular double cyclization of the motor compound under diluted conditions resulted in the formation of ‘8’-shaped macromolecules. Under UV irradiation, the rotation of the 8 shape macromolecule results in a wound structure, which was revealed by the AFM images and X-ray scattering experiments. At higher concentration, the intermolecular click reaction was achieved and resulted in the formation of a chemical crosslinks, as the polymer chains link to other motors by the triazole units and the molecular motors behave as the reticulating units. This polymer network can form a gel in toluene (10 %w/w). The structure of the gel was characterized by SAXS and AFM techniques. Under UV light irradiation, a small piece of gel was found to contract macroscopically by 80% of its original volume. This observation was attributed to the rotation of the molecular motor, by inducing new entanglements in the network through the twisting of pairs of polymer chains and leading to the contraction of the gel. This explanation was consistent with the study of the 8-shaped motor macromolecule. This work which was the first example of macroscopic response from molecular motors also highlighted the possibility of constructing energy storage materials from molecular machines.

In this early example, because of the unidirectional rotation of the motor, the contraction of the materials is irreversible and, to make the system reversible, our group described an advanced version in 2017 (**Figure 70**).[89] By incorporating the molecular motors together with a dithienylethene photoswitch in a mixed polymer system, the switch can act as an energy dissipating unit named as a “modulator”, which can release the torsion of the polymer chains caused by the rotation of the motor. This switch was found to be ring-closed when absorbing light at around 300 nm and ring-opened at 530 nm. Therefore, by irradiating the system at 300 nm to close the ring of the modulator, and at 365 nm to induce the rotation of the motor, one can observe the contraction of the gel. Then, when the contracted gel was exposed to visible light at 530 nm, causing the openness of the modulator ring, the free rotation along with the single bond of the modulator release the torsion energy in the system until reaches the thermodynamic equilibrium in the expanded state. Therefore, the gel system accomplishes a full contraction and release cycle under distinct wavelengths of irradiation.

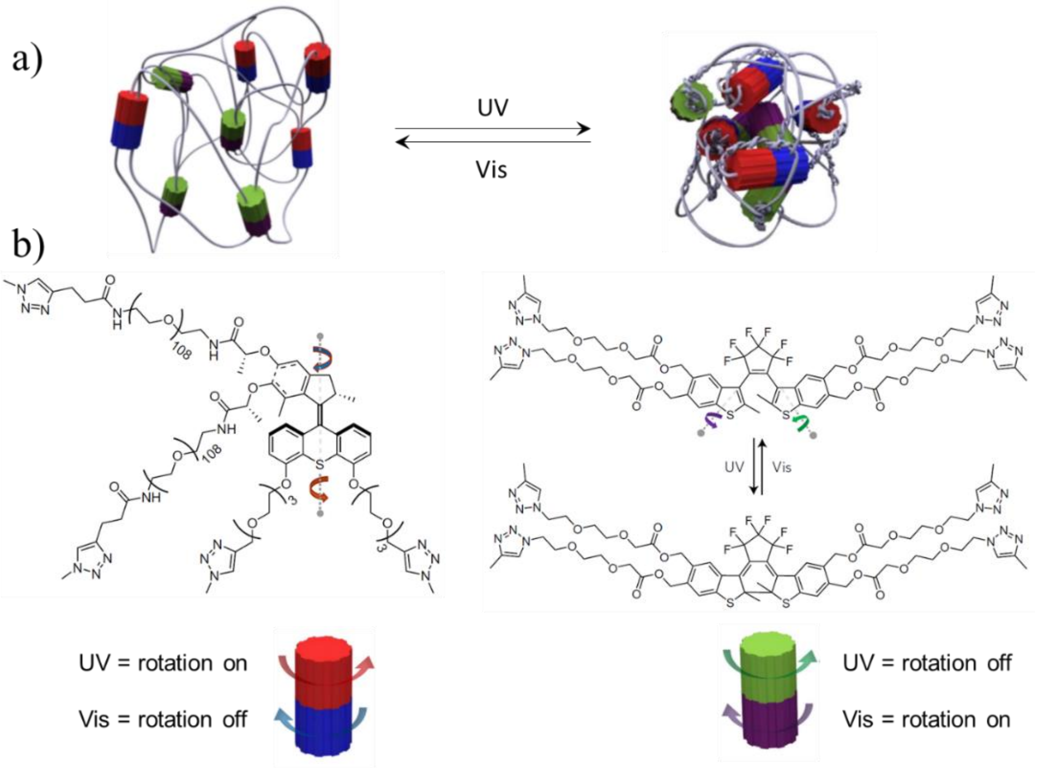

Figure 70. a) Schematic presentation of the contraction and release process. b) Chemical structure of the motor and diarylethene switch used to construct the gel.

As seen in this introduction, not only [*c*2] daisy chain molecules or other switches working at thermodynamic equilibrium can be used to produce macroscopic movement. Real molecular motors functioning out of thermodynamic equilibrium can also be integrated in polymer networks to produce motions. However, the contraction and expansion processes obtained with our polymer-motor conjugates were fully isotropic, and could not be exploited easily as actuators. In that direction, the objective of our work in this part of the PhD was to achieve a bending motion from self-standing motorized materials, and to possibly measure their actuation capacity, for instance in lifting a weight.

3.2 Synthesis of the compounds

3.2.1. Retrosynthesis

In the construction of the motor-containing polymeric gel, the efficient click reaction was chosen because of its high yield even in difficult reaction conditions – such as here within molds to cast films of defined thicknesses. In the previous studies, we functionalized the molecular motor with PEG polymer chains before crosslinking, an approach which proved efficient contraction of the resulting gel under UV irradiation. However, the purification of the motor-polymer conjugate unit was a bit difficult, requiring the HPLC method or reverse-phase column due to the polymer's high polarity. To improve the facility and time of preparation of the motorized gel, we have first improved the method by coupling the motor units and the PEG polymer chains at the last step, that is during the formation of the gel. First, four azide-terminated TEG (short triethylenglycol) chains were attached to the molecular motor, which behaves as reticulating units in the three-dimensional polymeric network. Then, bis-alkyne terminated PEG chains were synthesized and "clicked" with the tetraazide motor to produce the chemical network. In this strategy, both the tetra-azide motor units and the bis-alkyne terminated PEG chain can be easily accessed on large scale.

a) Non-reversible gel

More specifically, the unreversible gel was constructed between the tetra-azide molecular motor unit **35** and the bi-alkyne PEG polymer **32** with a ratio of 1:2 through the efficient click reaction. The tetra-azide motor compound can be obtained from the bis-acid motor compound **34** and amine-TEG-azide linker. The bis-acid motor compound **34** was obtained by functionalization of the lower part of the bisphenol motor and subsequently saponification of the upper part.

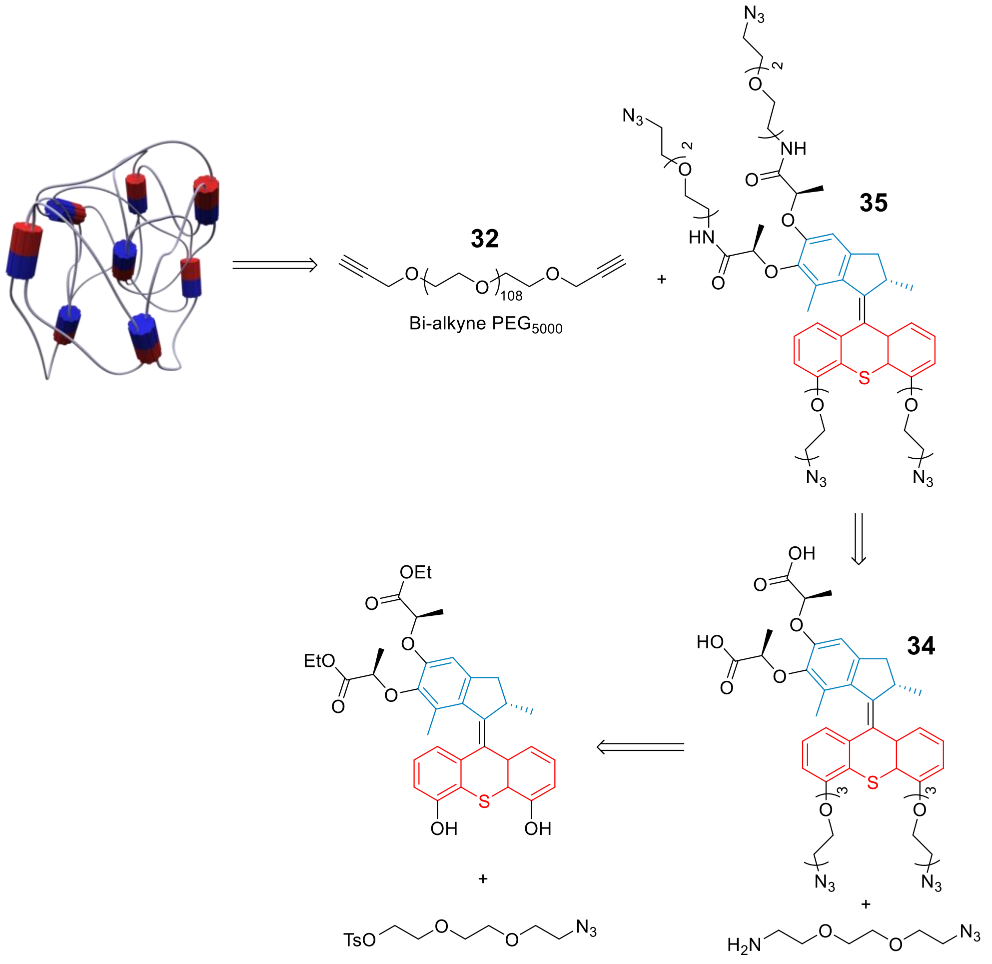

Figure 71. Retrosynthetic scheme for the unreversible gel.

b) Reversible gel

As we introduced previously, the diarylethene switch was chosen to be a good candidate as a modulating unit. Under UV irradiation, the diarylethene compound can form a ring closed state through electrocylisation. When exposed to visible light, the closed ring can switch back to its original open state. Hence, when being irradiated with UV light, the elastic energy will be stored in the contracted gel. When the UV irradiation is stopped and being exposed to visible light, the stored elastic energy will be released as the uncoiling of the network.

Similar to the construction of the non-reversible gel, the reversible gel was obtained by integrating the modulator into the network. Similar to the tetra-azide motor compound, the modulator compound also has four tetra-azide units. Therefore, the ratio of the components, the (motor+modulator)-tetraazide: PEG-di-alkyne polymer should be kept at 1:2. However, the proportions of the motor and modulator inside the material can be varied. The modulator **44** was synthesized after 9 steps from 4-bromo-2-methylthiophene. The tetra-azide compound **44** can be obtained from the tetra alcohol compound **43**, which can be obtained from the intermediate compound **41** and perfluorocyclepentene. Compound **41** was synthesized after four steps including 6-electron electrocyclisation, bromination, reduction, and protection of the terminal alcohol group. Bis-alkyne compound **37** can be accessed by bromination and a Heck reaction from the commercially available compound 4-bromo-2-methylthiophene.

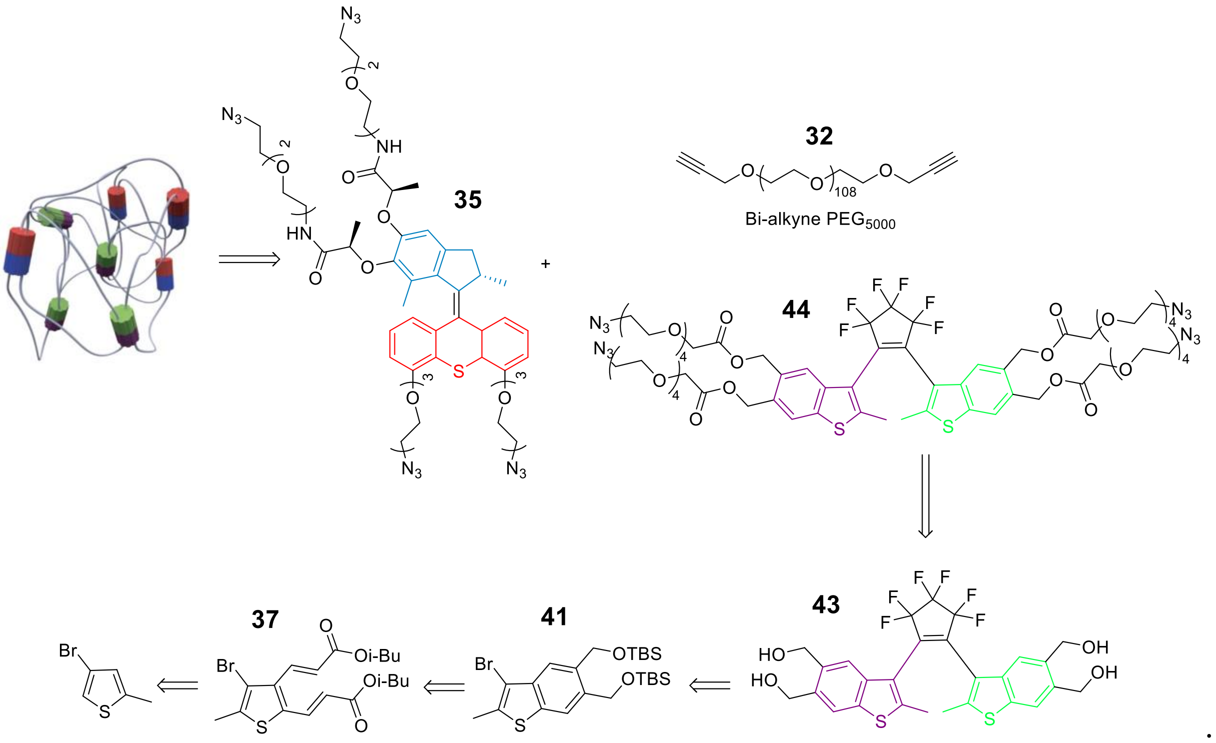

Figure 72. Retrosynthetic scheme for reversible gel.

3.2.1 Synthesis of tetra-azide motor

As we discussed before, the tetra-azide motor unit **35** was selected to construct the gel owing to its facile preparation. The tetra-azide motor **35** can be accessed from the bisphenol compound after four steps.

Firstly, the bisphenol compound was reacted with azide group terminated the tri-ethylene glycol tosylate chain to give motor compound **33**. After the saponification of the ester to give the bis-acid motor compound **34** with a high yield. This bis-acid motor was reacted with amine-azide triethylene glycol tosylate chain to afford the tetra-azide substituted molecular motor compound **35** as a yellow oil.

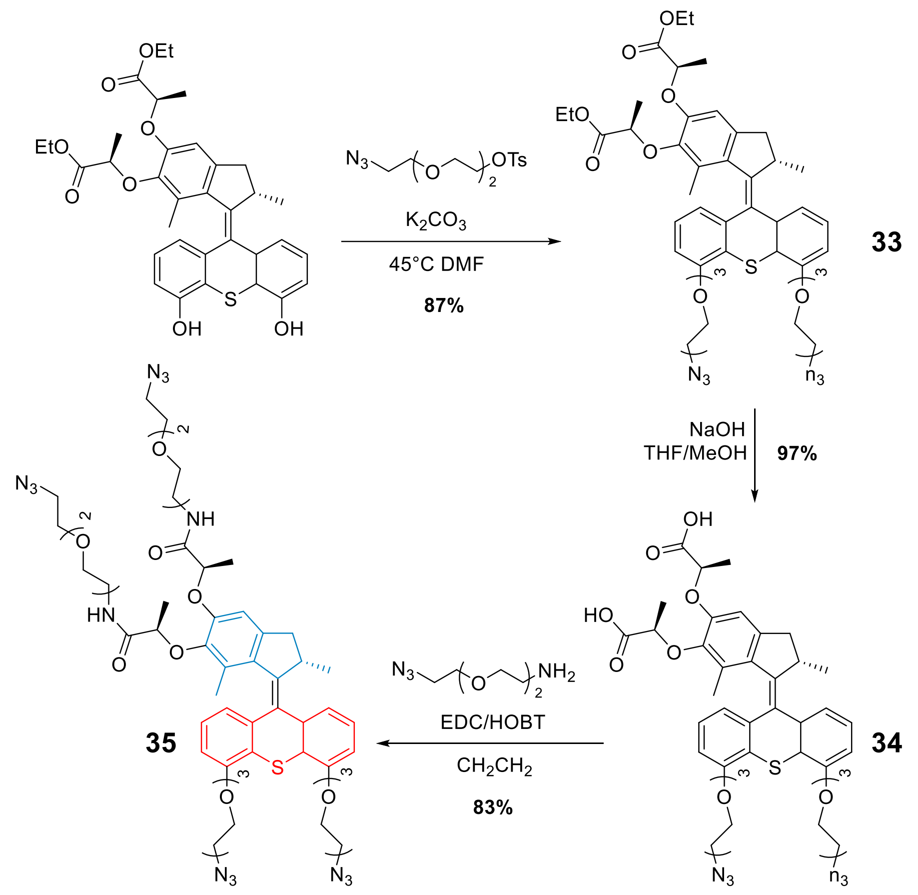

Figure 73. Synthesis of the tetra-azide motor **35**.

3.2.2 Synthesis and study of tetraazide modulator

The synthesis of the modulator was first developed by Dr. Justin T. Foy, a former post-doctor in our group. The novel modulator was obtained after nine steps of the following optimized synthesis (**Figure 74**). The commercially available 4-bromo-2-methylthiophene was mono brominated by N-bromosuccinimide (NBS) to give compound **36** at a yield of 91%. After a Heck reaction obtained from reported literature,[90] compound **36** was reacted with isobutyl acrylate to form compound **37** as a colorless liquid with a yield of 88%. An intramolecular electrocyclization occurs in compound **37** to give a cyclized intermediate, followed by the dehydrogenation with 2,3-dichloro-5,6-dicyano-1,4-benzoquinone (DDQ) to afford the aromatized compound **38** with a yield of 59%.

Compound **38** was then mono-brominated with liquid bromine to give compound **39** with a yield of 81%. After a reduction reaction with diisobutylaluminium hydride (DIBAL-H), the bis-alcohol compound **40** was obtained with a yield of 70% as a white solid. The bis-alcohol was protected by the TBS group to give compound **41** as a white solid. The dithienylethene switch was synthesized through an adapted protocol from the literature. [91] Compound **41** was first transformed into an organolithium intermediate compound with the existence of lithium, and underwent elimination after the addition of perfluorocycloalkenes to afford the dithienylethene switch **42**. Then, **42** was deprotected by acid alcohol solution to give compound **43** as a light yellow solid, the total yield of the two steps was 45%.

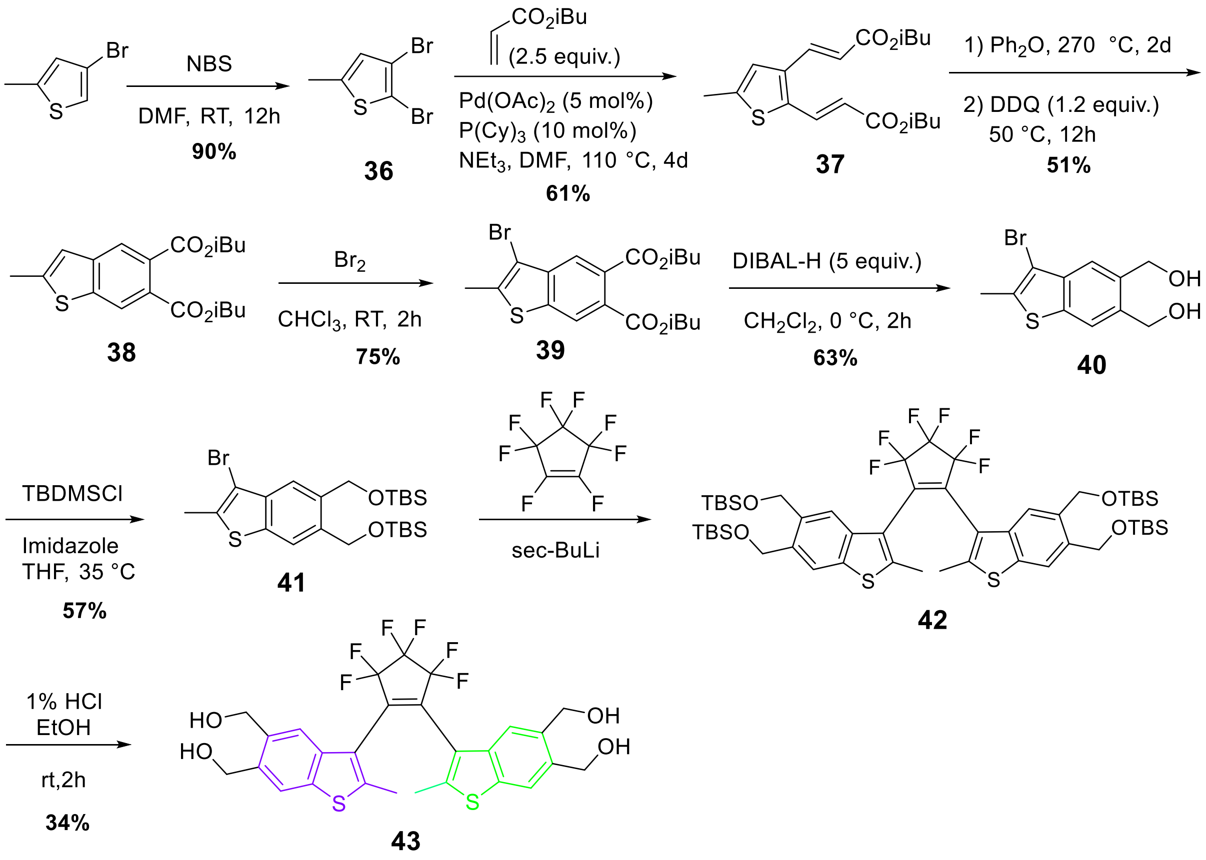

Figure 74. Synthesis of the dithienylethene switch **43.**

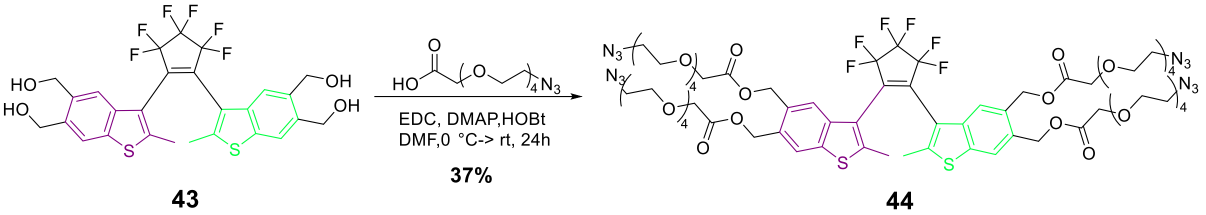

Figure 75. Synthesis of tetraazide dithienylethene switch **44.**

Finally, after an esterification reaction between the tetra alcohol modulator **43** and the 14-

azido-3,6,9,12-tetraoxatetradecan-1-oic acid, the tetrazaide dithienylethene switch **44** was obtained as a colorless liquid (37% yield).

3.3 Surface functionalization

The successfully achieved collective motion at the macroscopic scale has inspired us to explore further applications, such as object transportation, weight lifting or other mechanical work. Such complex anisotropic motions would require to differenciate between different zones of the gel. Therefore, we first planned to dessymetrize the gel material by coating the mechanically active polymer on the surface of an inactive polymer. We envisaged that, with the contraction of the motor gel, the inactive polymer will be bend.

3.3.1 Chemical functionalization

To coat the gel at the surface of the inactive polymer, the primary condition is that the surface should be (covalently) linked with the motor gel. In this case, an azide group terminated linker was used to functionalize the surface. In detail, polydimethylsiloxane (PDMS) coated glassine sheet (64 cm^2) was treated with low-pressure plasmas (7.2 W) for 120 s for demethylation. Directly after this manipulation, (11-azidooctyl)trimethoxysilane (200.1 mg) in THF (12 mL) with 42 µL of water and 4 µL of concentrated HCl. This solution was added to 30 mL of cyclohexane and the demethylated-PDMS coated sheet was immersed in this solution overnight. The sheet was recovered and washed with cyclohexane. The remaining solutions were concentrated to recover the extra (11-azidooctyl)trimethoxysilane. Weighing it allowed us to estimate that 80.4 mg were functionalized on the surface (average of ~ 4.6 $mmol/cm^2$).

3.3.2 Test of the surface functionalization by contact angle

To get information about the functionalization quality of the surface, we used the contact angle method. In theory, before the plasma treatment, the surface of the PDMS coated glassine polymer should be hydrophobic and it would become hydrophilic after demethylation by plasma treatment. To immerse the demethylated-PDMS coated glassine polymer to (the linker) containing solution. After surface functionalization by the linker (11-azidooctyl)trimethoxysilane, the polymer surface should become hydrophobic. Subsequently, after immersion in the di-alkyne peg polymer solution, the surface should become hydrophilic once again.

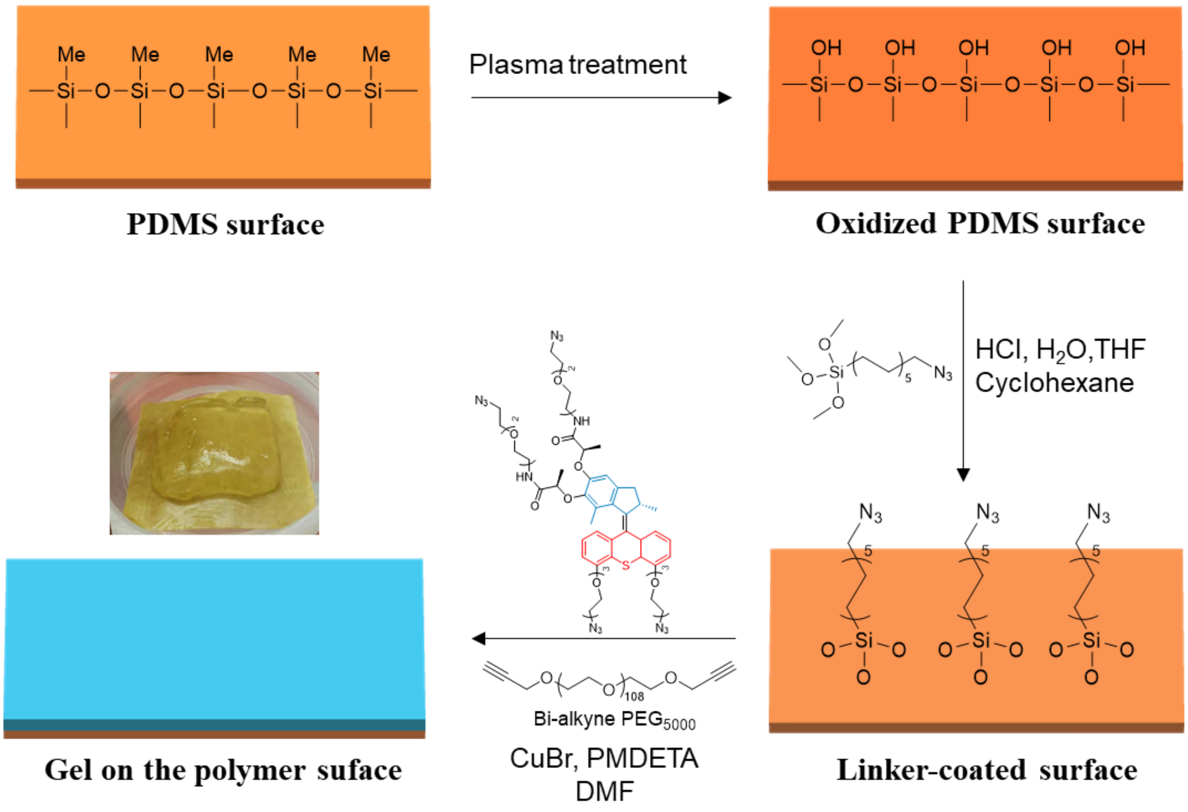

Figure 76. Schematic presentation of the functionalization process.

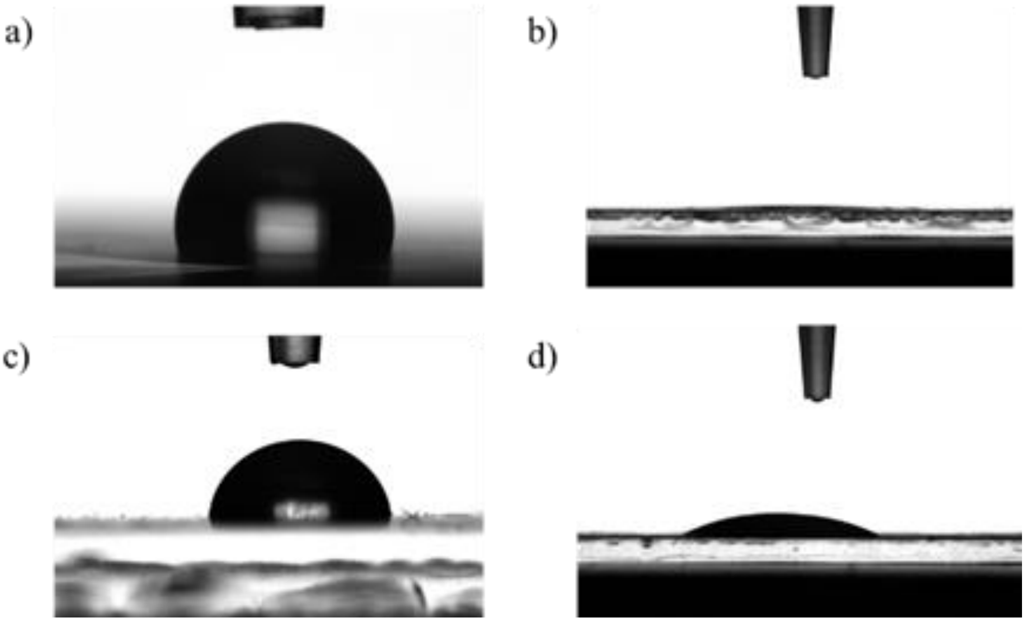

Figure 77. Contact angle test of different steps of the surface functionalization. a) The glassine polymer before plasma treatment, shows a hydrophobic property; b) After plasma treatment, the surface becomes hydrophilic; c) After the surface is coated with siloxane azide, it becomes hydrophobic again. d) After siloxane azide reacted with di-alkyne PEG polymer, the surface becomes hydrophilic.

To prove our hyperthesis, contact angle experiments were performed at each step of the functionalization (**Figure** 77). To eliminate the error and prove the homogeneity of the functionalization, we propose to test a series of experiments in a matrix (3 * 4 droplets). If all the droplets show the same property, it means that the surface treatment or functionalization was homogenous. Satisfyingly, the contact angle experiments all show the same properties as our hypothesis, which means the surface functionalization was expected to be of good quality.

3.4 Preparation of devices: photoresponsive motor gel on surfaces and as self-standing materials

Based on the chemistry described above, we prepared a series of surfaces with the objective to demonstrate anisotropic photoresponsive actuation.

3.4.1 Motor polymer at surface (Gel 1)

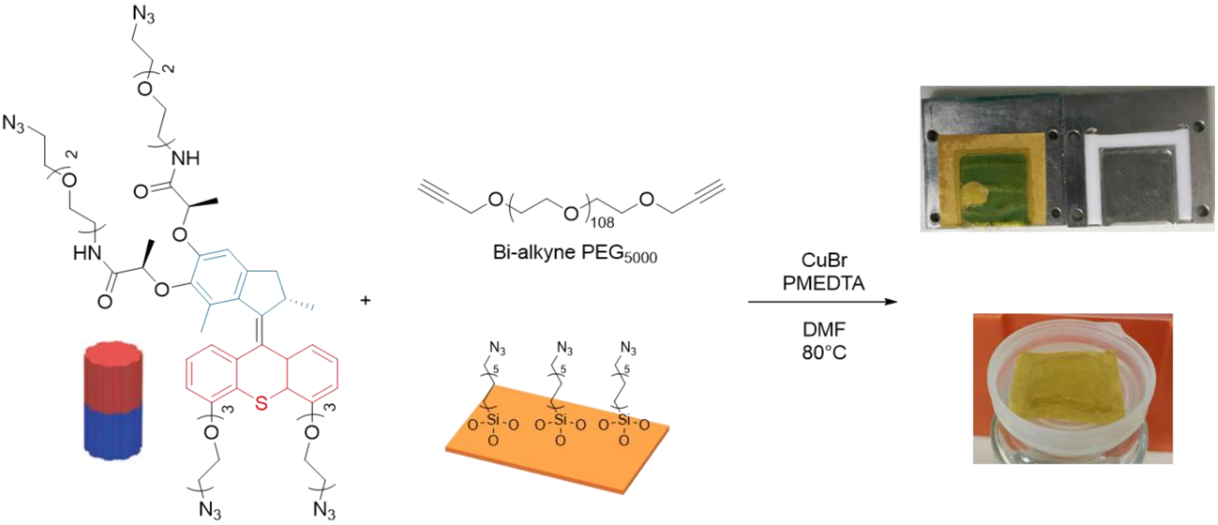

Figure 78. Coating the active motor gel on an inactive polymer surface. The right photograph is the gel before (up) and after (down) being washed by EDTA solution.

A slice of ~ 9 cm^2 of the functionalized surface was placed in the side of the cavity of a rheology mold. In a vial was prepared a solution of bi-alkyne PEG compound **32** (47.65 mg) in DMF (160 µL). Then another solution of tetra-azide compound **35** (5 mg), CuBr (8 eq.) and PMDETA (8 eq.) in DMF (40 µL – V_{PMDTA}) was added into the first one. This mixture was then transferred into the mold using a pipette. The mold was then heated up to 80 °C in a sand path for 30 min and cooled down to room temperature for another 30 min. The formed gel was washed by immersion in an EDTA solution until the blue color was fade. Then the transparent gel (**Gel 1**) was immersed in deionized water.

3.4.2 Self-standing motor polymer (Gel 2)

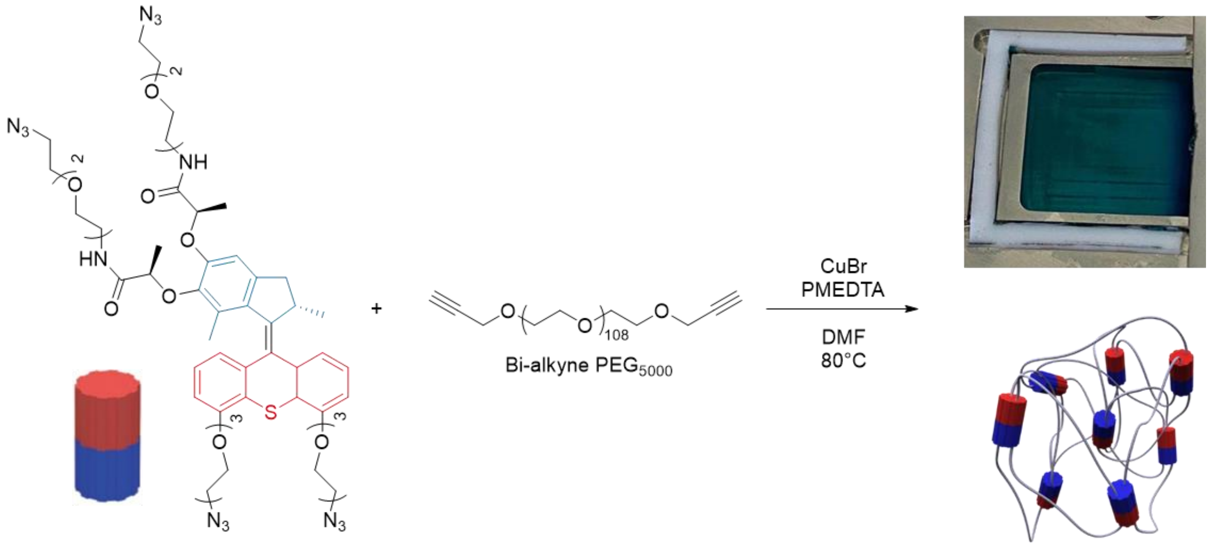

Figure 79. Construction of self-standing films of motor-gel from the tetra-azide motor **32** and bi-alkyne Peg polymer compound **32**. On the right is the photograph of the formed gel and the schematic presentation of the gel structure.

A solution of copper bromide (5.6 mg, 4×10^{-2} mmol) and PMDTA (8.2 µL, 4×10^{-2} mmol) in DMF (400 µL) was added to a mixture of compounds tetraazide motor compound **35** (5.8 mg, 4.9×10^{-3} mmol) and bis-alkyne PEG compound **32** (55 mg, 9.82×10^{-3} mmol) in DMF (400 µL) and homogenized before being pipetted into a 2mm thick mold and heated to 80 °C for 30 min. The device was then allowed to cool for 1 h and produced a blue gel (**Gel-2mm**) that was washed by immersion in a saturated aq. EDTA solution, and then in deionized water to yield a clear, colorless **Gel 2** ($2 \times 2 \times 0.2$ cm^3). This gel formed in DMF can be then transferred to a series of solvents including but not limited to Acetonitrile, Toluene, Water, and Methanol.

3.5 Study the bending behavior of the gel string

3.5.1 Photoresponsive actuation of the molecular motor hydrogel

In this part, we will study the actuation property of the motor gel. Under UV irradiation, the rotation of the light-rotary molecular motor leads to the contraction of the gel that is exposed to the light, while the opposite side of the gel will remain its original shape. The collapse of the activated part of the gel contributes to the whole shape change, the so-called bending behavior (**Figure 80**). By studying different parameters, one can determine which factors influence the bending behavior of the actuation process. Moreover, one can expect to load weight on these actuators to evaluate how much work the gel can produce, or even roughly calculated how much work can be done by a single molecular motor. The parameters that can be changed include light intensity, the distance between the beam and the gel surface, the concentration of materials (PEG and motor units) used to construct the gel, the length of the piece of gel used to perform the experiments, the different weights to be loaded, etc. The results to be analyzed include the time used to actuate different weights, the maximum angle that can be achieved by the actuator and the height by which the weight can be lifted.

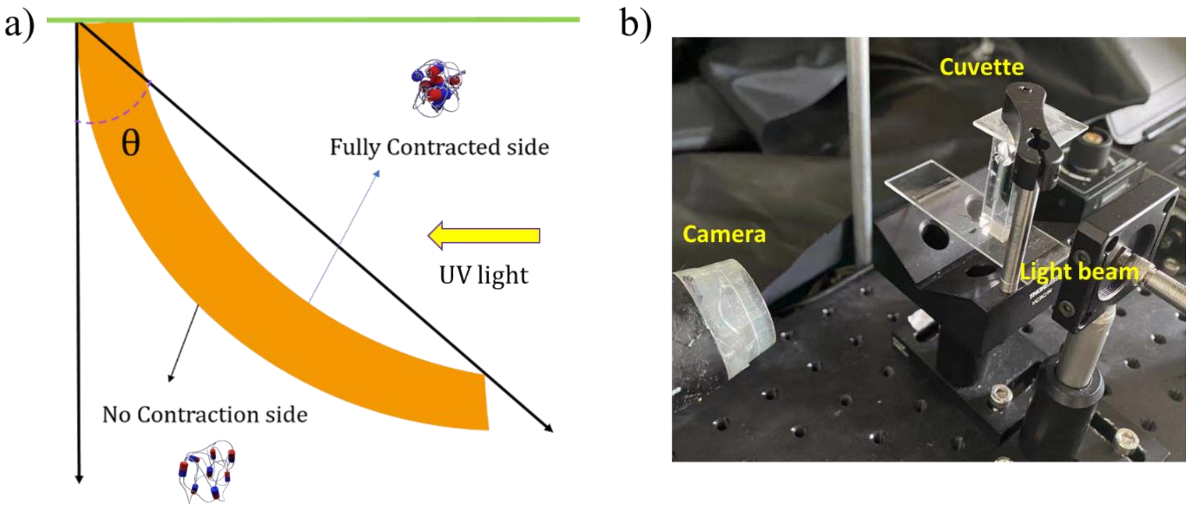

Figure 80. a) Schematic presentation of the bending mechanism of the molecular motor hydrogel upon photoirradiation coming from the right-hand side. Ultraviolet light decreases the volume of the exposed surface of the molecular motor hydrogel, but the volume of the non-irradiated side remains in the original relaxed state. The strain between the exposed and unexposed areas results in bending. b) The set-up is used to monitor the gel bending process.

The gel actuation process was monitored in an optical irradiation setup (**Figure 80b**). The piece of gel (15 × 5 × 2 mm^3) was immersed in a cuvette full of solvent, which was degassed before the irradiation. At the top of the cuvette, a clamp was fixed which can catch the gel string. The cuvette was covered by a coverslip with the help of grease. The light beam was placed in the front of the gel surface, and the camera was placed at the side view of the cuvette. Finally, the whole system was covered by a black cloth, to prevent the perturbation of the room light.

a) Motor polymer at the surface (Gel 1)

Our initial hypothesis is that by coating the motor hydrogel on the surface of the inactive polymer surface. Irradiating by UV light, as the contraction of the gel, causing the bending of the polymer. The bending experiment was performed both in toluene and deionized water (**Figure 82**). When the experiment was performed in the toluene (**Figure 82a**), we can see that after 6 hours of UV irradiation, the polymer (**Gel 1**) bent towards the light source. However, the motor gel was decomposed and dissolved at the end of the test, which was not what we expected. Further, the same experiment was performed in deionized water. As **Figure 81b** shown, under UV irradiation for 6 hours, the gel achieved a bending behavior. However, the gel strip was disconnected from the surface, which can be attributed to the low quality of functionalization in deionized water gel. Though the result was not fulfilling our hypothesis, this phenomenon inspired us to do something depending on the self-standing motor polymer (**Gel 2**).

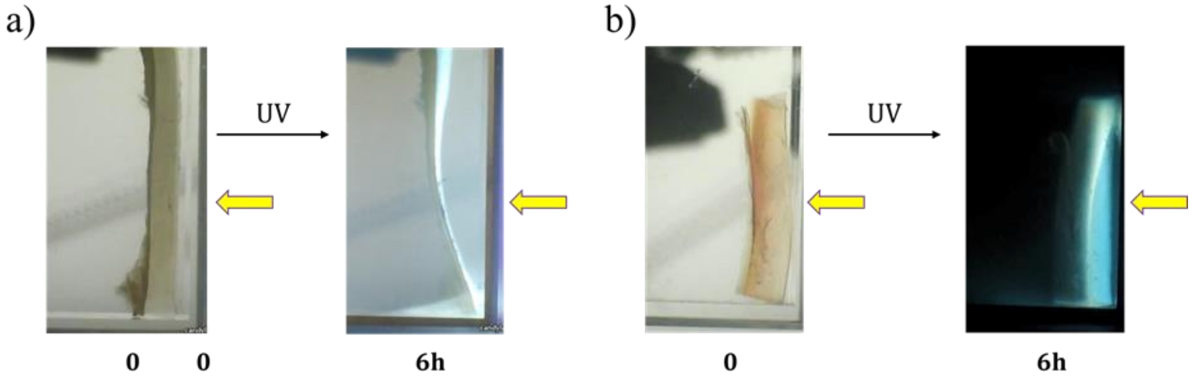

Figure 81. Photographs of the molecular motor surface gel irradiated with UV irradiation in toluene (a) and deionized water (b), the surface string bends to the right.

b) Self-standing motor polymer (Gel 2)

The successfully bending of the dangling gel push our research interest towards the self-standing gel (**Gel 2, Figure 79**). Therefore, we perform the **Gel 2** actuation experiments as we described in **Figure 80**. Because of the excellent property in water, the gels used in the following test were all performed in degassed deionized water.

The relationship between the bending direction of the string and the UV light (λ = 365 nm) was performed and studied. The molecular motor actuator ($15 \times 5 \times 2$ mm^3) was immersed in full degassed deionized water. The molecular motor gel string bends towards the light upon UV irradiation. **Figure 82** shows the flexion angle θ of the motor gel irradiated with UV light. Initially, the motor gel did not start bending before 60 minutes. This can be explained by the molecular motor need enough time to activate the coiling of the reticulating network (which means that the first twists are not efficient for macroscopic contractions). When the motor unit reaches the most tensioned state, the volume of the gel starts to contract. This means the contraction from the nanoscale has been amplified to a macroscale. The flexion angle θ reached the maximum angle after ~5h of UV irradiation and can keep the shape without UV irradiation for a very long time (over one week). The rotation speed was calculated to be 0.3° / min.

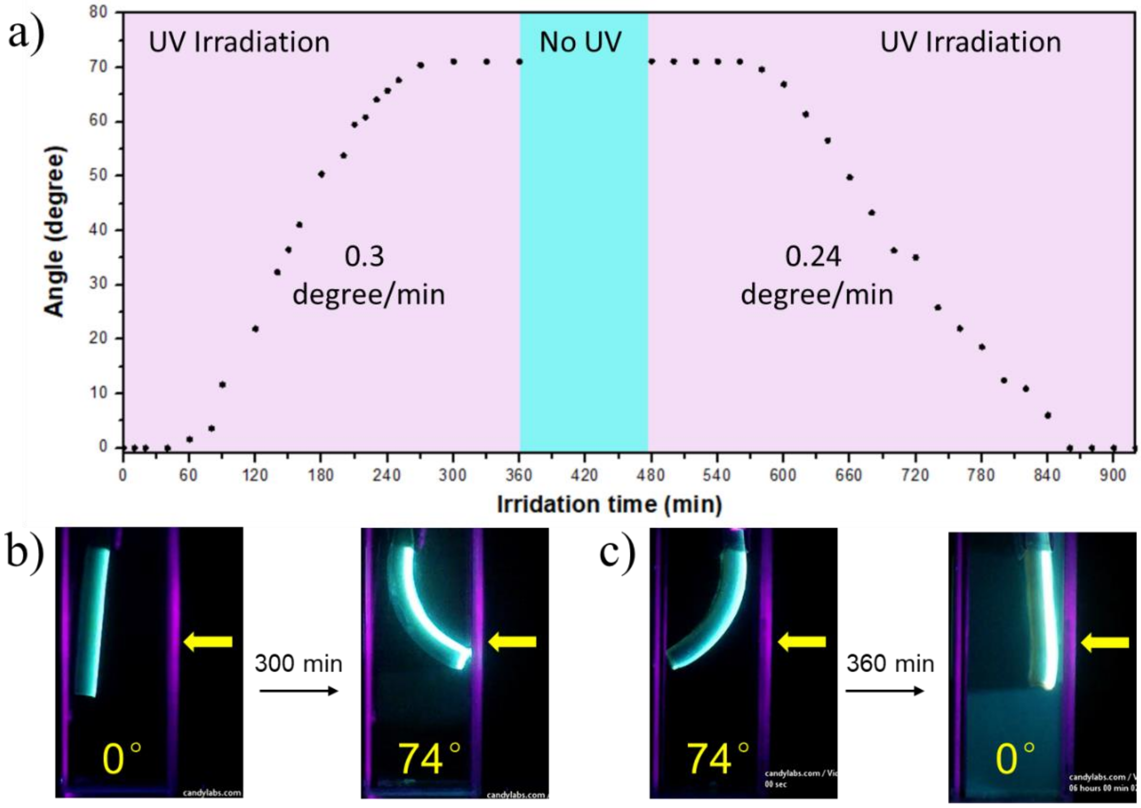

Figure 82. a) Plot of flexion angle θ versus irradiation time of the molecular motor **Gel 2**. Purple, blue areas denote UV irradiation and dark storage without light exposure, respectively. Flexion angle θ was measured from snapshots; b.c) Photographs of the molecular motor reticulating hydrogel irradiated with UV irradiation, the molecular motor hydrogel string bends to the right;

When the bending got the maximum angle, we irradiated the opposite side with UV light. Same as the first time, the gel bending towards the UV light again. Owning to the high tension of the contracted gel, the speed of the opposite bending process is slightly slower than the first time (0.24 °/min). Interestingly, the gel can be brought back to its initial straight shape. However, because the motor-peg reticulating network was fully coiled, it cannot continue bending towards the opposite side though under light irradiation, showing the non-reversibility of the process (due to the unidirectional rotation of the motor).

3.5.2 The factors that influence the bending behavior

The actuation of the gel can be influenced by a series of factors. To get the optimum condition is good for us to know best how the bending process was achieved.

Here, we have studied how factors such as light intensity, length of the gel string, and the loading weight influence the result of the bending process.

a. Light intensity

We know from previous experiments performed in our group that both in solution and the gel state, the light intensity strongly affects the rotation speed of the molecular motor although it is commonly accepted that the THI is the rate-limiting step of the rotation process. Therefore, we probed if light intensity can affect the gel anisotropic actuation process.

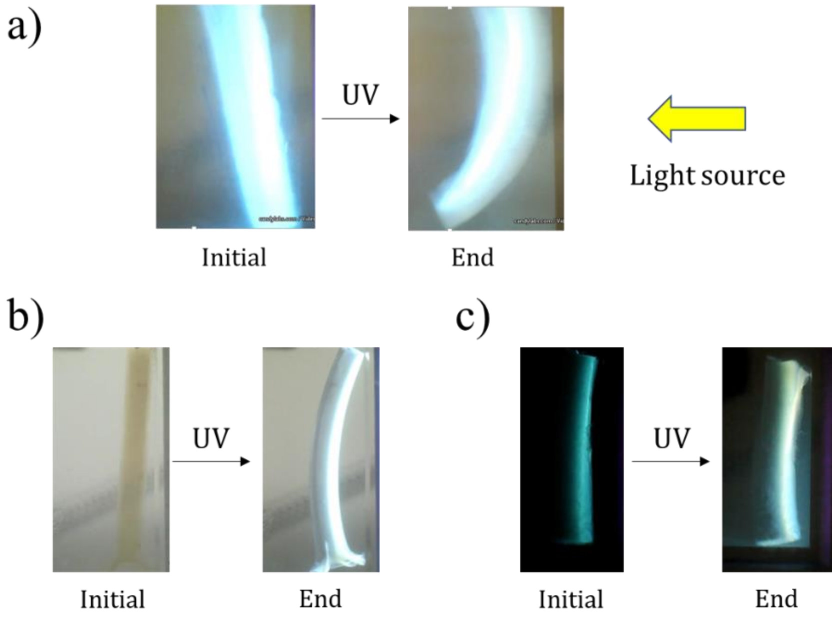

Figure 83. Gel 2 immersed in the a) deionized water and b) toluene, UV light 20 mW/cm^2; c) **Gel 2** immersed in deionized water, UV light 6.5 mW/cm^2. All the light sources came from the right side of the gel. All the gel was irradiated for 5 hours.

From **Figure 83** one can see the bending behavior of different light intensities or in different solvents. In **Figure 83a**, after being exposed to the light source for 5 hours, the gel in water bends towards the opposite direction from light, which is quite different from our initial hypothesis. In **Figure 83b**, the gel in toluene bends toward the light source under the same light intensity in **Figure 83a**. We found that the gel in water under UV light intensity of 20.0 mW/cm^2 was emitting fluorescence over its full thickness, while the gel in toluene was being penetrated only over its half-thickness. This means that in water at his light power, all the motors of the gel are activated and the bending direction becomes hard to control. These results are consistent with our initial hypothesis, which has been described in **Figure 80**. To further prove our hypothesis, we placed the gel in weaker light intensity of 6.5 mW/cm^2. From **Figure 83c**, one can see that the UV light penetrates half-length of the gel and the gel can bend towards the light source.

Further, the bending behavior of **Gel 2** under different light intensities was performed systematically in water. The gels used in the experiments came from the same batch of gel. As

Figure 84 shows, as the light intensity increases, the bending speed of the gel is enhanced. When the gel was exposed with a light intensity of 1.6 mW/cm^2, the flexion angle reached 9.2° after 230 mins (0.04 ° /min). When the light intensity increased to 6.5 mW/cm^2, the flexion angle can be reached to 51.9° after being irradiated for 270 mins (0.19 °/min). Continuing to increase the light intensity to 13 mW/cm^2, the gel can be actuated much faster; 43.2° after 100 mins (0.43°/min). When the light intensity reaches 19.8 mW/cm^2, the gel can reached a flexion angle of 45.9° (0.46°/min). These results show that the light intensity indeed influences the bending behaviors of the gel, including bending speed and maximum flexion angle.

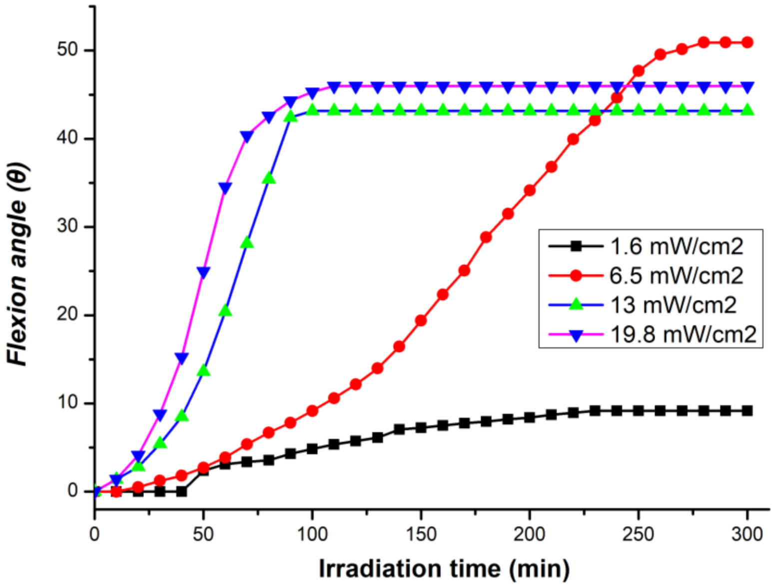

Figure 84. The relationship between the flexion angle and irradiation time under different light intensities.

b. Length of the gel string

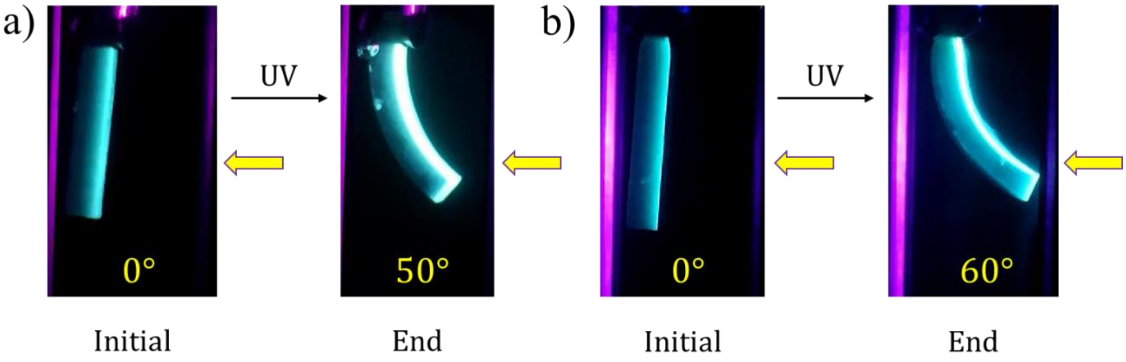

Figure 85. Two gel string from the same batch of gel was studied, with lengths of 1.2 cm and 1.5 cm respectively. The light source from the right side of the gel with an intensity of 6.5 mW/cm^2.

The length of the piece of gel was also being investigated. At first, we think that the length of the gel would affect the bending angle. To solve our hypothesis, we perform two experiments with different lengths of the gel. The two gel string was from the same batch of gel, to eliminate other possible factors.

From **Figure 85b**, we can see that the gel (1.5 cm) reached its maximum bending angle of 60° after 6 hours of UV irradiation. To reduce the length of the gel from 1.5 cm to 1.2 cm **(Figure 85a**), the irradiation experiment was performed under the same conditions. After 6 hours of irradiation, the gel bending angle reaches the saturated state and reaches a angle of 50°. Therefore, the length of the gel did affect the bending angle of the gel, which is geometrically conceivable as the net differences of surface change between the two faces of the gel is greater for greater surfaces. .

c. Weight lifting experiments

The motor can achieve a huge gel contraction under UV light irradiation, as demonstrated in previous publications. However, the extraction of directional work such as by achieving weight lifting was not yet demonstrated. With our new gel strings, we were able to perform weight lifting experiments.

From **Figure 86**, we can see that with the attachment of weights at the end of the gel, the string still has an excellent gel actuation process under UV irradiation. As the weight increases, the gel shows a slower speed and smaller bending angle. This means the weight influence the gel actuation.

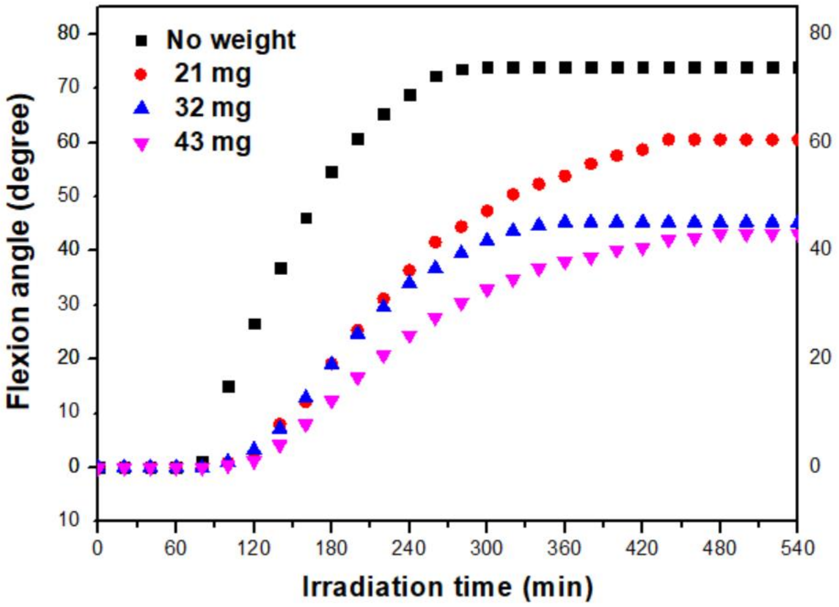

Figure 86. The relationship between flexion angle and irradiation time with different weights.

The results are detailed concluded in:

Gel	Flexion angle θ	Actuation speed	Lift-up height	Work
Gel2	74°	0.3 °/min	0.4 cm	-
Gel2+21 mg	61°	0.178 °/min	0.4 cm	0.84 μJ
Gel2+32 mg	45°	0.168 °/min	0.4 cm	1.28 μJ
Gel2+43 mg	43°	0.108 °/min	0.2 cm	0.86 μJ

Table 1. Flexion angle θ, Actuation speed, the maximum lift-up weight, and the work done by the actuation process with different weights.

As **Table 1** shown, when the weight reached a number, the height of the lift-up would be reduced, and as a result, the work done by the gel actuation can be calculated.

3.5.3 Analysis of work during weight lifting experiment

The work of the lift-up process was calculated by the formula：

$$W = mgh$$

m, the mass of the weight (center of the mass); g, acceleration due to gravity; h, the distance of the weight that has been lifted vertically.

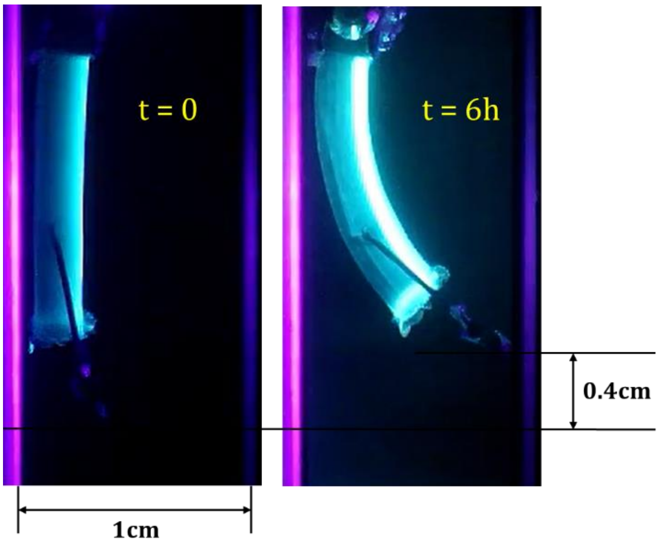

Figure 87. Photographs of the photo-actuation of the **Gel 2** string upon UV irradiation in the water with 32 mg weight as weight appendant.

As **Figure 87** shown, a **Gel 2** string with a 33mg weight terminated can be lifted with a height of 0.4 cm.

Therefore, the work during the weight lifting experiment can be calculated as:

W = mgh

$=32\ (\mathrm{mg}) * 10\ (\mathrm{m/s}^2) * 0.4\ (\mathrm{cm})$

$=32*10^{-6}\ (\mathrm{kg}) * 10\ (\mathrm{m/s}^2) * 0.4*10^{-2}\ (\mathrm{m})$

$=1.28\ \mu\mathrm{J}$

The motors used to fabricate the string (15 × 5 × 2 mm^3) were calculated to be 1.06 µmol. In our experiment, only half of the thickness of the gel has been actuated. Hence, the number of motors used to perform the actuation process was calculated to be 0.53 µmol. In this case, the work achieved by per mol can be calculated as:

$$\frac{1.28\ \mu J}{0.53\ \mu mol} = 2.42\ J/mol$$

So, in the weight lifting experiments, every mol motor can perform 2.42 J work.

As we introduced in the introduction (**Figure 68**), the group of Feringa has reported a similar work before.[87] In their work, the gel was constructed in a supramolecular manner. To prove the advantage of our work, here we make a comparison with their work.

	Maximum work	Maximum weight	Motor concentration
a. This work	1.28 J	43 mg	5.3 mM
b. Feringa's work	0.05 J	0.4 mg	50 mM
Ratio a/b	25.6 times	108 times	0.1

Table 2. Comparison between this work with Feringa's work.

As **Table 2** show, the maximum work measured in our system is 25.6 times higher than the the work produced in the system of Feringa involving switching motors. More interesting, this work can lift 43 mg weight, which is 108 times higher than Feringa's work.[87] Besides these advantages, compared with Feringa's gel, the gel used in our work is much more easily prepared, which is much more efficient and less time-consuming.

3.6 Integrating the “modulator” into motor gel

3.6.1 Studying the close-open property of the “modulator”

The molecular study of the modulator unit has been performed in our previous research. A series of experiments such as X-ray crystallography, ^{1}H NMR spectroscopy, and density functional theory (DFT) were used to prove the kinetic efficiency of rotation and the possibility to be used as an elastic release. Here we repeat the UV-vis experiments of the tetra azide modulator **44** to prove its specific absorption wavelength.

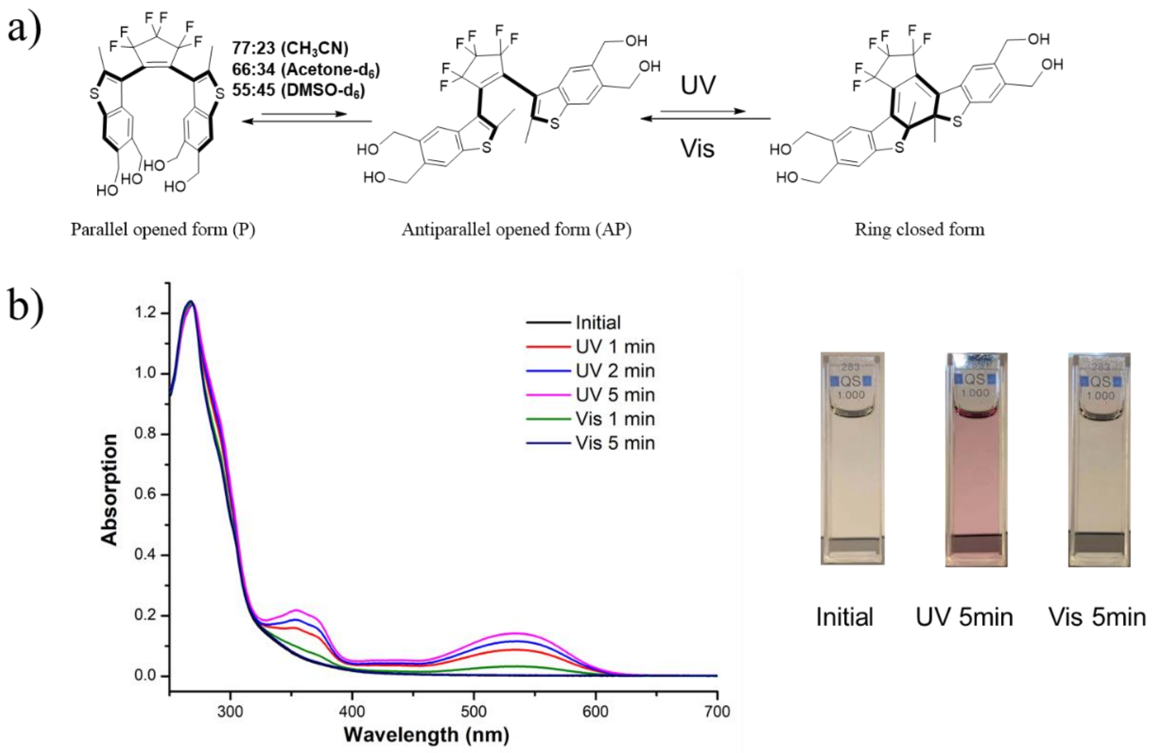

Figure 88. a) In the opened form, the dithienylethene **43** has two formed, a parallel and an antiparallel form keep an equilibrium by the rotation of two C-C single bonds. Under UV irradiation, the open form will be transformed to the ring-closed form. b) UV-vis absorption spectra of dithienylethene compound **44** in solution (c = 2 × 10^{-4} M in CH_3CN) after different times of irradiation with ultraviolet and visible light; the absorption at 530 nm is characteristic of the closed-form and results in the purple color of the solution.

As **Figure 88b** shows, the ring closed form of the modulator was confirmed by the emergence of the characteristic purple color with a maximum absorption band at 530nm under the UV (312 nm) irradiation. Then under visible light irradiation, the color transformed into transparent, which proves the re-opening of the closed ring. Therefore, the modulator compound can be dual controlled with the irradiation of UV (312 nm) light or visible light.

3.6.2 Preparation of modulator + motor gel

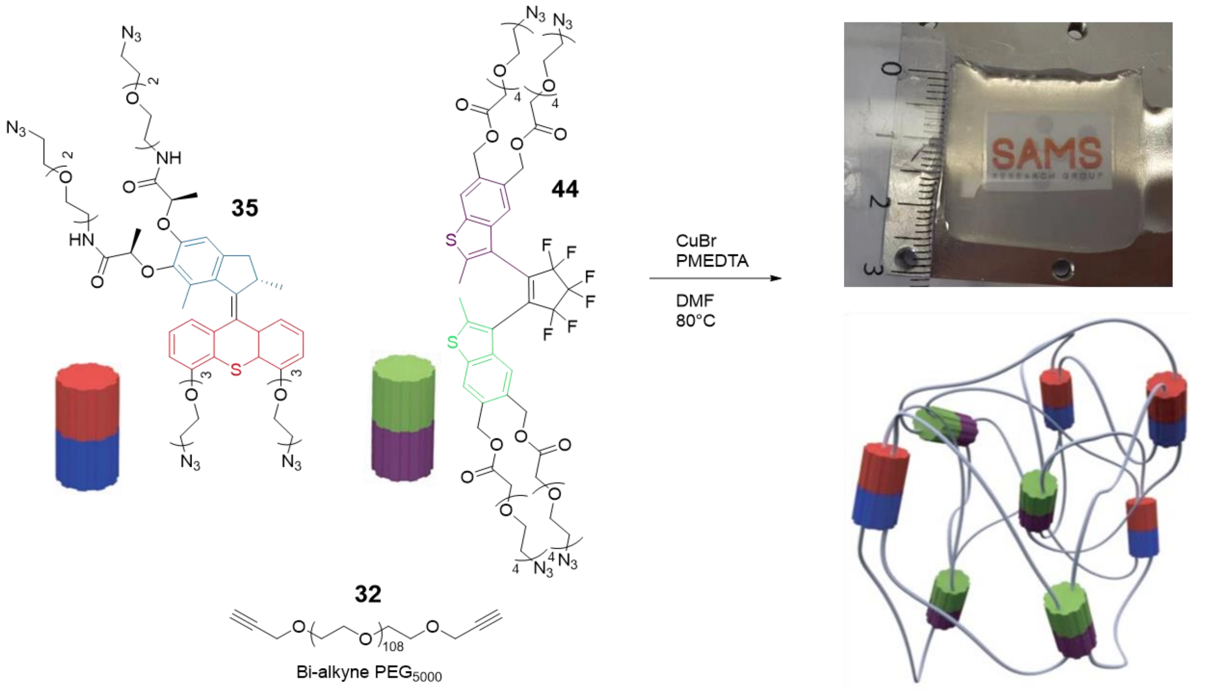

Figure 89. Scheme presentation and chemical structure of motor/modulator gel by click reaction in DMF.

A solution of copper bromide (5.6 mg, 4×10^{-2} mmol) and PMDETA (8.2 µL, 4×10^{-2} mmol) in DMF (400 µL) was added to a mixture of compounds tetraazide motor **35** (2.9 mg, 2.45 × 10^{-3} mmol), tetraazide modulator **44** (4 mg, 2.45 × 10^{-3} mmol) and bis-alkyne peg polymer **32** (55 mg, 9.82 × 10^{-3} mmol) in DMF (160 µL) and homogenized before being pipetted into a 2 mm thickness mold and heated to 80 °C for 30 min. The device was then allowed to cool for 1 h and produced a blue gel that was washed by immersion in saturated aq. EDTA solution, deionized water to yield a clear, colorless gel (2 × 2 × 0.2 cm^3).

Gel	Motor **35**	Modulator **44**	Peg-alkyne-polymer **32**
Gel 3	0.9	0.1	2
Gel 4	0.75	0.25	2
Gel 5	0.5	0.5	2

Table 3. Compositions and labels of the gels were obtained using the conditions described in **Figure 89** and for different ratios of monomers.

3.6.3 The actuation of the motor + modulator gel

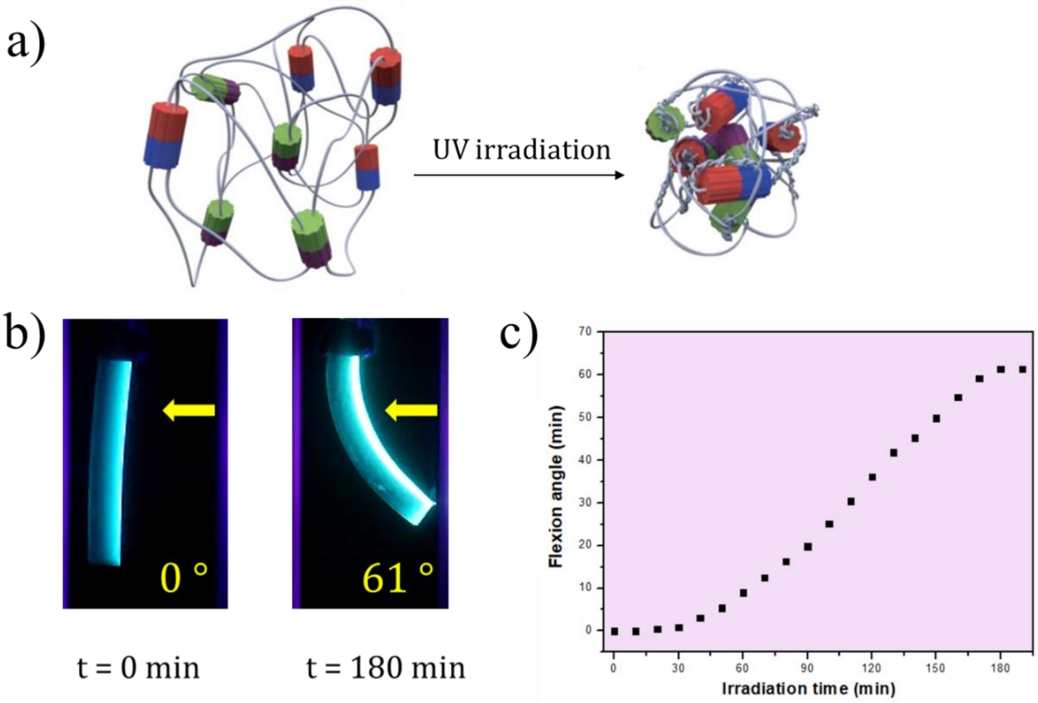

Figure 90. a) Schematic presentation of the contractile motor+modulator gel under UV irradiation. b) Photographic snapshots of **Gel3** in the water. The UV irradiation from the right and string bends towards the light source from 0° to 61° within 180 min. c) Plot of flexion angle θ versus irradiation time of the motor + modulator **Gel3**.

Gel 3 was used to perform the irradiation experiment. Under UV (365 nm) irradiation, the gel string can achieve the maximum bending angle of 61°. It should be noted that, in this experiment, the modulator was in the open form because there is no UV (312 nm) was applied. The reason why the gel can achieve the bending with an opened form modulator subunit can be explained by that the amount of motor unit in **Gel 3** is far more excess than the modulator unit (motor: modulator = 9:1). The coiling speed caused by the motor is bigger than the release speed caused by the modulator, therefore, the system is pushed far from equilibrium which results in the bending of the gel string.

This result is very interesting in itself, as it confirms the possibility to actuate self-standing materials using our motor-actuator approach. To fully take advantage of this advanced molecular system, a fully reversible bending in both directions by sequential UV irradiations should be demonstrated. This is the purpose of ongoing experiments.

3.7 Conclusion

The work present here shows unprecedented results compared to other systems described so far. Indeed, the actuation of the gels presented here has been achieved by using the out-of-equilibrium functioning of molecular motors as compared with previous examples using molecular switches changing their configurations or conformations at thermodynamic equilibrium. In particular, the determination of the work produced by the motors in weight lifting experiments shows high values of hundred times compared to Feringa's work. In addition, the possibility to design macroscopically out-of-equilibrium systems in the motor and motor-modulator systems enriches the fundamental functioning principles of actuating materials known so far.

We are currently finalizing this work for publication by refining the data already obtained, in particular by implementing a number of control experiments and in getting more precise values of the work and power delivered by the system as a function of parameters such as light intensity, the thickness of the material, or percentage of the modulator used as well as dual light control in this latter reversible – fully out-of-equilibrium – system.

Conclusion and perspectives

The emerging field of artificial molecular machines has gained huge attraction owing to its unique potential to control mechanical actuation and work at nanoscale. Feringa's light rotary molecular motors have become one of the most important dynamic objects in this large family because they are light responsive, with evident non-invasive and remote control advantages, and because they can, in principle, produce a continuous work on their environement (even if only a very few number of practical examples have been effectively implemented so far). In this thesis manuscript, I described the advances I achieved on two main topics related to molecular motor-based applications during my PhD, and which evidence and exploit these two main assets.

In chapter two, I reported the molecular motor boosted ion transportation across a lipid bilayer membrane. Although a series of artificial molecular machines such as molecular shuttle and azobenzene-based molecules have been applied in this area, ion transport based on out-of-equilibrium molecular motors has not been reported so far in the literature. The careful design and synthesis of molecular motors combined with two 18-crown-6 macrocycles were instrumental in this success. This relatively hydrophobic molecules can be inserted into the phospholipid bilayers in which the crown-ethers can self-assemble into ion channels, which demonstrated selective transport for alkali metal ions. When UV light was applied to the system, the transportation rate can be strongly boosted (up to 400%) while keeping its selectivity. Based on HPTS fluorescence assays, on Patch-clamp measurements, and on a number of control experiments, this boosting effect was attributed to the continuous rotation of the molecular motors, a mechanism totally different to those involving molecular switches based on configurational / conformational changes of the actuators at thermodynamic equilibrium. This work is the first artificial molecular motor-based ion transporter to date, and I anticipate that it will have an important fundamental impact in the field of molecular machines, with potential applications in the field of molecular transport.

Besides the utilization at the nanoscale, artificial molecular motors have also been recently applied in the macroscopic world. The successful construction of molecular motor-polymer conjugates pave the way to cross lengthscales and design truly active out-of-equilibrium materials. In chapter three, based on contractile gels containing rotary motors, I achieved a step further in this direction by finding ways to transform this contraction into macroscopic actuations. Under UV light, pieces of gels can be anisotropically bent toward the light source at an important angle and generate a work. By placing a weight at the bottom of the piece of gel, the weight can be successfully lift-up during upon irradiation and the work produced –

coming again from the out-of-equilibrium actuation of the motor – can reach much higher values compared to the other system existing so far in the literature. Moreover, a molecular ‘modulator’ has been successfully combined into the motor gel, in order to tune the gel actuation process and to make it fully reversible and reprocessable. The first experiments show that such a motor-modulator system still can maintain the initial bending property, and experiments on back and forth actuation are currently ongoing. If successful, a full determination of the work and power produced in both series will be performed to complement this study before publication.

Experimental Part

General procedures

I. Solvents and Chemical Reagents

All reactions were performed with dry solvents under an atmosphere of argon unless otherwise indicated. All reagents and solvents were purchased at the highest commercial quality and used without further purification unless otherwise noted. Dry solvents were obtained using a double-column SolvTech purification system. Water was deionized by using a milli-gradient system (Millipore, Molsheim, France). Microwave reactions were carried out with a single-mode cavity Discover Microwave Synthesizer (CEM corporation, NC, USA), producing continuous irradiation at 2455 MHz and equipped with a simultaneous air-cooling system. Yields refer to purified spectroscopically (^{1}H NMR) homogeneous materials. Bases for coupling reactions (Cs_2CO_3, K_2CO_3, NaO*t*Bu) were dried under vacuum at 180°C for 24 h and then stored in a desiccator.

II. Chromatographic Methods

Thin Layer Chromatographies (TLC) were performed on TLC silica on aluminum foils (Silica Gel/UV254, Aldrich). In most cases, irradiation using a *Bioblock VL-4C* UV-Lamp (6W, 254 nm and/or 365 nm) was used as well as *p-anisaldehyde and Ce-molybdate stainings* were used for visualization. *Preparative Adsorption Flash Column Chromatographies* were performed using silica gel (60 Å, 230–400 mesh, 40–63 µm, Sigma-Aldrich). *Ultra Performance Liquid Chromatographies coupled to Mass Spectrometry* (UPLC-MS) were carried out on a *Waters Acquity UPLC-SQD* apparatus equipped with a PDA detector (190-500 nm, 80 Hz), a SQD mass spectrometer, using a reverse-phase column (Waters, BEH C18 1.7 µm, 2.1mm x 50 mm), and the MassLynx 4.1 –XP software with a gradient (water-acetonitrile + 0.1% formic acid) as eluent. *Preparative High Performance Liquid Chromatographies coupled to Mass Spectrometry* (HPLC-MS) were carried out on a *Waters AutoPurify* system equipped with a UV detector (275 nm) and a 3100 mass spectrometer, using a reverse-phase column(Waters, SunFire Prep C18 or XBridge Prep C18, 5.0µm, 19 mm x 150 mm) running with a gradient (water-methanol+ 0.05% NH_3 for XBridge Prep C18 and water-methanol+ 0.1% Formic acid for SunFire Prep C18) as eluent and the MassLynx 4.1 –XP software.

III. Analytical Methods and Instruments

a. Nuclear Magnetic Resonance (NMR)

^{1}H NMR and ^{13}C NMR spectra were recorded either on a Bruker Avance III HD 500 MHz spectrometer equipped with a CPPBBO «Prodigy» cryo-probe at 298K or on a Bruker Avance III HD 400 MHz spectrometer equipped with a BBFO probe at 298K.

The spectra were internally referenced to the residual solvent peaks ($CDCl_3$: 7.26 ppm, Toluene-d_8: 7.09, 7.01, 6.97 and 2.08 ppm, CD_3OD: 3.31 ppm, CD_3CN: 1.94 ppm, DMSO-d_6: 2.50 ppm and D_2O: 4.80 ppm for ^{1}H spectrum, and $CDCl_3$: 77.16 ppm, Toluene-d_8: 137.48, 128.87, 127.96, 125.13 and 20.43 ppm, CD_3OD:49.00 ppm, CD_3CN: 118.26 and 1.32 ppm and DMSO-d_6: 39.52 ppm for ^{13}C spectrum). For ^{1}H NMR assignments, the chemical shifts are given in ppm. Coupling constants *J* are given in Hz. Peaks are described as singlet (s), doublet (d), triplet (t), quartet (q), multiplet (m) and broad (br).

b. Mass Spectrometry

Electrospray Mass Spectrometry (ESI-MS) were recorded using a Waters SQD mass spectrometer either by direct injection or after chromatography. *High-Resolution Mass Spectrometry* (HRMS) was performed on a microTOF-Q instrument from Bruker. *Matrix-Assisted Laser Desorption/Ionization* (MALDI) was performed on an Autoflex apparatus (Bruker). The sample matrix was dithranol dissolved in high purity CH_2Cl_2 and the sample solvent either in CH_2Cl_2 or DMF. Results were calibrated against a peptide calibration standard (Bruker) prepared in a mixture of CH_3CN and 0.1% TFA in ultra-pure water in a volume ratio of 1:2 and spotted with a 1,8-Diazabicyclo[5.4.0]undec-7ene (DBU) matrix in the same solvent system.

c. Optical Spectroscopies

UV-Vis-NIR spectra were recorded either on a Varian Cary 5000 apparatus from Agilent Technologies (for far NIR region measurements or temperature dependant measurements) or on a Lambda 25 spectrometer from Perkin Elmer.

d. Dynamic Light Scattering (DLS) Experiments

Dynamic light scattering was recorded on a Zetasizer Nano from Malvern Instruments Ltd.

UK).

e. Contact Angle Measurements

Measurements were performed on a GBX Digidrop apparatus.

f. Formation of Liposomes for HPTS Fluorescence Assay

Egg yolk L-α-phosphatidylcholine (EYPC chloroform solution, 1.2 mL, 30 mg, 39 mmol) was dissolved in 1.2 mL of MeOH (2.4 mL total volume), the solution was slowly evaporated under reduced pressure and the resulting thin film was dried overnight under high vacuum. The lipid film was hydrated in 0.6 mL of phosphate buffer (10 mM sodium phosphate, pH = 6.4, 100 mM NaCl) containing 10 µM HPTS (pyranine, 8-hydroxypyrene-1,3,6-trisulfonic acid trisodium salt) for at least 60 minutes. After hydration, this suspension was submitted to 7 freeze-thaw cycles (liquid nitrogen and water at room temperature). This large multilamellar liposome suspension (0.4 mL) was submitted to high-pressure extrusion at room temperature (21 extrusions through a 0.1 µm polycarbonate membrane afforded a suspension of LUVs with an average diameter of 100 nm as determined by DLS, Zetasizer Nano, Malvern Instruments Ltd., UK). The LUV suspension was separated from extravesicular dye by size exclusion chromatography (SEC) (stationary phase: Sephadex G-50, mobile phase: phosphate buffer) and diluted to 4.2 mL with the same phosphate buffer to give a stock solution with a lipid concentration of 3.66 mM (assuming 100% of lipid was incorporated into liposomes).

IV. Methods to Study Ion Transport through Lipid Bilayer Membranes

Various techniques have been developed to study ion transport properties, and are still undergoing. Among these techniques, the fluorescence and planar bilayer conductance method have been the most frequently used. Besides, calorimetric assays, NMR spectroscopy, or ion-selective electrodes are also very popular. Here, we focus on the fluorescence and bilayer conductance methods, which are the methods used in our systems.

a. HPTS Fluorescence Assay for Cation Transport Experiments

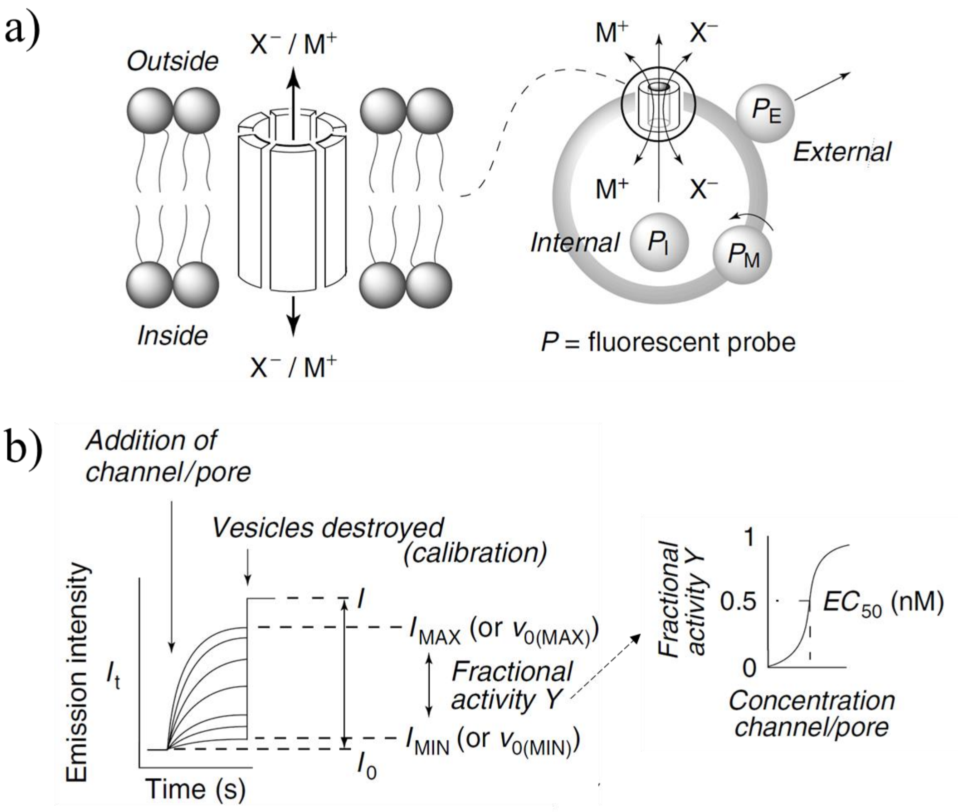

Figure 91. Schematic representation of the HPTS fluorescent assay (a) and analysis (b) of the vesicle flux experiments. Adapter from reference [92]

Fluorescence spectroscopic techniques are the most commonly used to characterize artificial ion channels or pores, for their ability to detect ions in real-time and without destroying the vesicles. Large unilamellar vesicles are labeled with fluorescent probes, both intravesicular and extravesicular or membrane-bounded. A series of internal fluorescence probes have been invented to determine the transport activity, the representative one is the pH-sensitive pyranine dye 8-hydroxypyrene-1,3,6-trisulfonic acid (HPTS).

HPTS is a pH-sensitive fluorophore with pKa = 7.3, it shows distinct absorption wavelength (450 nm and 405 nm respectively) in its protonated state and deprotonated state. The two different excitation maxima allow the ratiometric exploration of pH variation in channel fluorescence experiments. Activity of the artificial ion channels is determined in the HPTS assay by the subsequently applied pH gradient (around one unit) caused by sodium hydroxide. To alleviate the external pH change, the existence of an ion channel could speed up the internal pH vesicle by improving both proton efflux or OH^- influx.

The fluorescence emission of HPTS in response to the addition of artificial ion channels to the vesicles is generally measured as a function of time at different concentrations. The change of the fluorescence intensity was used to determine the transportation activity. To adjust the dose-response, emission I_∞ of free fluorophores is obtained at the end of each fluorescence experiment by destroying the vesicles, usually achieved by adding a detergent such as Triton X-100.

i.Without UV irradiation

100 μL of HPTS-loaded vesicles, prepared according to the previously described protocol (3.66 mM stock solution), were suspended in 1.85 mL of buffer (10 mM PBS, pH = 6.4 containing 100 mM of either RbCl, NaCl or KCl)and placed into a quartz fluorimetric cell. The emission of HPTS at 510 nm was monitored using two excitation wavelengths (403 and 460 nm)simultaneously. During the experiment, 20 μL of a 0-10 mM DMSO solution of compound **A**or **B** was added at t = 20 s after the start of the experiment, followed by an injection of 29 μL of a 0.5 M aqueous NaOH solution att = 40 s. The addition of the NaOH solution resulted in a pH increase of approximately 1 pH unit in the extra vesicular buffer. Maximal possible changes in dye emission were obtained at t = 320 s by lysis of the liposomes with detergent (40 μL of 5% aqueous Triton X100). The experiment was ended at t = 360 s. The final transport trace was obtained as a ratio of the emission intensities monitored at 460 nm and 403 nm and normalized to 100% of transport.

ii.With UV irradiation

The procedure with UV irradiation is almost similar to the one without UV irradiation. The main difference consists in an irradiation of the fluorimetric cell with UV light from t = 20 s to t =320 s. The wavelength of the UV light is 365 nm and the power of the UV light is 7.5 mW/cm^2. (M365FP1-365 nm, 9.8 mW (Min) Fiber-Coupled LED, 1400 mA, SMA, Thorlabs).

The optical fiber was fixed on the top of the cuvette which was placed inside the fluorescence spectrometer at a 2 cm distance from the solution.

b. Voltage Clamp

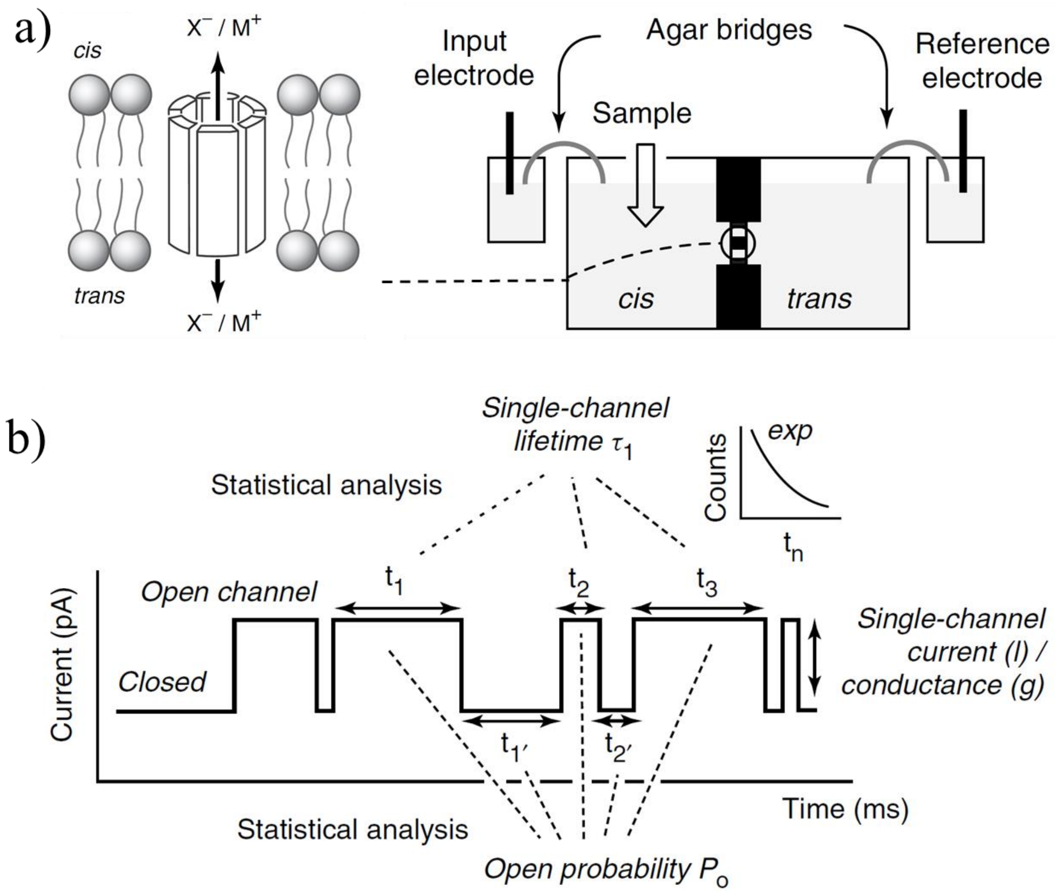

Figure 92. a) Schematic presentation of the voltage clamp experiment; **b)** Analysis of the single-channel recordings.

A model BC-535A bilayer clamp (Warner Instrument Corp.) was used for planar bilayer experiments. All data were hardware filtered at 1 kHz (8-pole Bessel filter), digitized (Axon 1440a) and recorded in a survey mode using the Gap-free protocol and processed (ClampEx and ClampFit 10.3.1.5). Chambers were made of Delrin holding a polystyrene cup with an aperture of 250 µm. The lipid was phosphatidylcholine (PC) (Avanti Polar lipids). A stock solution (400 µL) of 25 mg·mL-1 lipid in CHCl$_3$was dried under nitrogen gas for 1.5 hours and then resuspended in decane(400 µL.)The electrolyte used was 1 M KCl in 10 mM HEPES, 10 mM TRIS (pH was adjusted via pH meter from Hersteller-Prüfzertifikat, model: MU6100H, serial no. 19051681). The aperture was initially prepared with 2 µL of decane/lipid and excess solvent could be removed by gently blowing N$_2$ gas over the aperture. The cup was then placed into the electrolyte-filled holding cell, consisting of 5 mL and 3 mL chambers, and salt bridges (KCl/Agar) and electrodes (Ag/AgCl) were attached. Bilayers were formed by brushing another

4-8 μL of decane/lipid over the aperture and were monitored for stability, capacitance and resistance for at least 40 minutes before a solution of compounds **A** or **B** was added (10 mM solution in DMSO, 10-30 μL altogether). Bilayers were tested repeatedly for capacitance and resistance with different applied potentials (-200 mV to 200 mV).

For planar bilayer lipid clamp assay performed under UV irradiation, the UV lamp (power of 7.5 mW/cm^2) was placed on the top of the chambers, with a distance between the optical fiber and the chamber of about 2 cm.

c. Data analysis for the HPTS fluorescence assay for cation transport experiments

First-order initial rate constant was calculated from the slopes of the plot of ln ($[H^+]$in-$[H^+]$out) versus time, where $[H^+]$in and $[H^+]$out corresponds to the intravesicular and extravesicular proton concentrations, respectively. The $[H^+]$out was assumed to remain constant during the whole experiment (pH = 7.4), while $[H^+]$in values were calculated for each point from HPTS emission intensities using the following equation:

$$\mathrm{pH} = 1.1684 \times \log\left(\frac{I450}{I405}\right) + 6.9807,$$

where I_{460} is the absolute emission intensity with excitation at 460 nm and I_{403} is the absolute emission intensity with excitation at 403 nm.

The normalized pH has been calculated as follows:

$$\mathrm{pH_{norm}} = \frac{\mathrm{pH{-}pH\ initial}}{\mathrm{pH\ final{-}pH\ initial}}$$

where initial and final pH are pH at t = 0 s and at the end of the experiment, respectively.

V. Organic Synthesis and analyses

Compound 1

4-nitrobenzo-18-crown-6

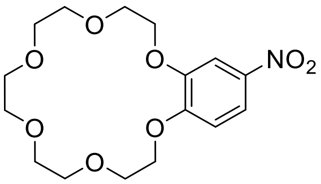

1

A suspension of finely ground K_2CO_3 (3.32 g, 23.98 mmol) and KBF_4 (1.46 g, 11.60 mmol) in CH_3CN (150 mL) was heated to reflux under vigorous stirring. A solution of 4-nitrocatechol (1.20 g, 7.74 mmol) and penta(ethylene glycol) ditosylate (5.10 g, 9.28 mmol) in CH_3CN (150 mL) was added dropwise over 12 hours to this suspension and the reaction mixture was stirred under reflux for another 3 days. After that time, the suspension was filtered through celite with dichloromethane (200 mL) and the solvents were removed under reduced pressure. Then, water (200 mL) was added and the mixture was extracted with dichloromethane (4 × 200 mL). The organic phase was washed with brine (200 mL) and subsequently dried over anhydrous Na_2SO_4, followed by filtration and evaporation under reduced pressure. Further purification by column chromatography (SiO_2, Methanol: CH_2Cl_2 = 1:100 → 1:25) provided compound **5** (0.94 g, 34%) as a yellow powder.

^{1}H NMR ($CDCl_3$, 400 MHz, 298 K): δ (ppm) = 7.88 (dd, J_1 = 8.9 Hz, J_2 = 2.6 Hz, 1H), 7.73 (d, J = 2.6 Hz, 1H), 6.88 (d, J = 8.9 Hz, 1H), 4.25 – 4.21 (m, 4H), 3.97 – 3.92 (m, 4H), 3.78 – 3.75 (m, 4H), 3.72 – 3.69 (m, 4H), 3.68 (s, 4H);

^{1}H NMR (DMSO-d_6, 400 MHz, 298 K): δ (ppm) = 7.87 (dd, J_1 = 9.0 Hz, J_2 = 2.7 Hz, 1H), 7.71 (d, J = 2.7 Hz, 1H), 7.15 (d, J = 9.0 Hz, 1H), 4.23 – 4.17 (m, 4H), 3.77 – 3.74 (m, 4H), 3.60 – 3.55 (m, 4H), 3.54 – 3.50 (m, 4H), 3.50 (s, 4H);

^{13}C NMR (DMSO-d_6, 100 MHz, 298 K): δ (ppm) = 154.2, 148.0, 140.8, 118.0, 111.8, 107. 3, 70.2, 70.0, 69.8, 69.0, 68.7, 68.5, 68.5;

ESI-MS: m/z calculated for $C_{16}H_{24}NO_8$ 358.1496 $[M+H]^+$; found 358.2061.

Compound 2

4'-Aminobenzo-18-crown-6

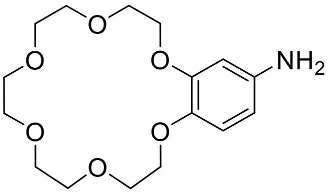

2

A solution of 4-nitrobenzo-18-crown-6 (0.40 g, 1.12 mmol) and 10% Pd/C (30 mg) in 1,4-dioxane (10 mL) was heated to reflux. Hydrazine hydrate (3 mL) was then added dropwise and the reaction was stirred at reflux for another 3h. After cooling to room temperature, the reaction mixture was filtered off through celite. Celite was washed with DCM (15 mL) and the solvent was removed under reduced pressure to provide compound **2** (341 mg, 93%) as a pale yellow oil. The compound was clean enough to be used as such in the following step.

^{1}H NMR ($CDCl_3$, 400 MHz, 298 K): δ (ppm) = 6.62 (d, J = 8.5 Hz, 1H), 6.25 (d, J = 2.5 Hz, 1H), 6.06 (dd, J_1 = 8.4 Hz, J_2 = 2.5 Hz, 1H), 3.97 – 3.93 (m, 2H), 3.91 – 3.88 (m, 2H), 3.74 – 3.70 (m, 2H), 3.69 – 3.66 (m, 2H), 3.59 – 3.51 (m, 8H), 3.51 (s, 4H);

^{1}H NMR (DMSO-d_6, 400 MHz, 298 K): δ (ppm) = 6.62 (d, J = 8.5 Hz, 1H), 6.25 (d, J = 2.5 Hz, 1H), 6.06 (dd, J_1 = 8.4 Hz, J_2 = 2.5 Hz, 1H), 3.97 – 3.93 (m, 2H), 3.91 – 3.88 (m, 2H), 3.74 – 3.70 (m, 2H), 3.69 – 3.66 (m, 2H), 3.59 – 3.51 (m, 8H), 3.51 (s, 4H);

^{13}C NMR (DMSO-d_6, 101 MHz, 298 K): δ (ppm) = 149.3, 143.6, 139.4, 115.9, 105.8, 101.1, 70.0, 70.0, 69.9, 69.3, 69.2, 69.1, 67.8;

ESI-MS: m/z calculated for $C_{16}H_{25}NO_6$ [M]+: 328.1755. Found: 328.2037.

Compound 3

3-(2-chloroethyl)-1-(2,3,5,6,8,9,11,12,14,15-decahydro-1,4,7,10,13,16-benzohexaoxacyclooctadecin-18-yl)urea

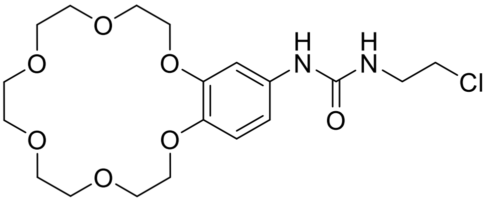

3

Compound **2** (280 mg, 0.86 mmol) and 2-chloroethyl isocyanate (135.4 mg, 110 µL, 1.28 mmol) were dissolved in dichloromethane (5 mL). The mixture was stirred overnight at room temperature. After this time, the resulting solution was poured into deionized water (20 mL) and extracted twice with dichloromethane (2 × 20 mL). The organic phase was washed twice with brine (2 × 50 mL) and then dried over anhydrous Na_2SO_4. The organic solvents were evaporated under reduced pressure. The resulting crude residue was purified by column chromatography (SiO_2, CH_2Cl_2: MeOH: NEt_3 = 100: 2: 1) providing compound **7** (299.9 mg, 81%) as a dark red liquid.

^{1}H NMR ($CDCl_3$, 500 MHz, 298 K): δ (ppm) = 8.42 (s, 1H), 7.15 (d, J = 2.2 Hz, 1H), 6.86 (dd, J_1 = 8.7 Hz, J_2 = 2.3 Hz, 1H), 6.65 (d, J = 8.7 Hz, 1H), 6.49 (brt, J = 5.1 Hz, 1H), 4.04 – 3.99 (m, 4H), 3.84 – 3.82 (m, 2H), 3.78 – 3.76 (m, 2H), 3.72 – 3.62 (m, 12 H), 3.55 (t, J = 5.9 Hz, 2H), 3.49 (t, J = 5.7 Hz, 2H);

^{13}C NMR ($CDCl_3$, 125 MHz, 298 K): δ (ppm) = 156.4, 148.3, 143.2, 134.3, 114.3, 111.8, 105.7, 70.4, 70.3, 70.3, 69.6, 69.4, 68.9, 68.1, 43.9, 41.8;

HRMS (ESI$^+$): m/z calculated for $C_{19}H_{29}N_2O_7ClLi$ $[M+Li]^+$ 439.1818, Found: 439.1817.

Compound 4

3-(2-azidoethyl)-1-(2,3,5,6,8,9,11,12,14,15-decahydro-1,4,7,10,13,16-benzohexaoxacyclooctadecin-18-yl)urea

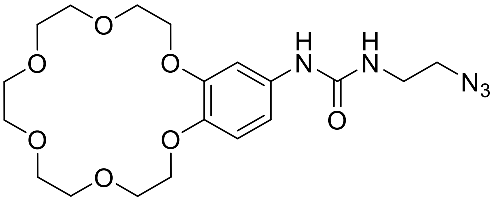

4

To a solution of compound **3** (280 mg, 0.65 mmol) in DMF (4 mL) was added sodium azide (63.1 mg, 0.97 mmol). The reaction mixture was stirred overnight at 50 °C. After cooling down to room temperature, the reaction mixture was extracted twice with dichloromethane (2 × 15 mL) and the combined organic phases were dried over anhydrous Na_2SO_4 and evaporated under reduced pressure. Further purification of the crude residue by column chromatography (SiO_2, CH_2Cl_2: MeOH: NEt_3 = 100: 2: 1) provided compound **4** (216 mg, 76%) as a brown-red solid.

^{1}H NMR ($CDCl_3$, 400 MHz, 298 K): δ (ppm) = 8.53 (s, 1H), 7.16 (d, J = 2.3 Hz, 1H), 6.74 (dd, J_1 = 8.6 Hz, J_2 = 2.3 Hz, 1H), 6.60 (d, J = 8.7 Hz, 1H), 6.51 (brt, J = 5.4 Hz, 1H), 3.99 – 3.95 (m, 4H), 3.77 – 3.71 (m, 4H), 3.63 – 3.53 (m, 12H), 3.30 – 3.24 (m, 4H);

^{13}C NMR ($CDCl_3$, 125 MHz, 298 K): δ (ppm) = 156.3, 148.6, 143.3, 134.3, 114.4, 111.0, 105.6, 70.2 (x 2), 70.1, 69.4, 69.2, 69.0, 68.1, 51.2, 39.0;

HRMS (ESI$^+$): m/z calculated for $C_{19}H_{29}N_5O_7$ $[M+H]^+$ 440.2145, Found: 440.2139.

Compound 5

3-(2-aminoethyl)-1-(2,3,5,6,8,9,11,12,14,15-decahydro-1,4,7,10,13,16-benzohexaoxacyclooctadecin-18-yl)urea

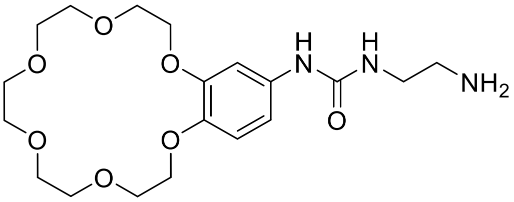

5

A solution of compound **4** (200 mg, 0.46 mmol) and triphenylphosphine (239 mg, 0.91 mmol) in THF (10 mL) was stirred at room temperature for 4 hours. Deionized water (1 mL) was then added and stirring was continued for 1.5 hours. After concentration under reduced pressure, the residue was dissolved with water (20 mL) and the aqueous phase was extracted twice with dichloromethane (2× 20 mL). Further evaporation of the aqueous phase under reduced pressure provided compound **5** (124 mg, 66%) as a light yellow solid.

^{1}H NMR (D_2O, 400 MHz, 298 K): δ (ppm) = 7.01 (d, J = 12.0 Hz, 1H), 7.01 (s, 1H), 6.84 (dd, J_1 = 8.6 Hz, J_2 = 2.3 Hz, 1H), 4.23 (t, J = 6.1 Hz, 4H), 3.94 – 3.91 (m, 4H), 3.77 – 3.72 (m, 12H), 3.39 (t, J = 5.9 Hz, 2H), 3.00 (t, J = 59 Hz, 2H);

^{13}C NMR (D_2O, 100 MHz, 298 K): δ (ppm) = 158.4, 147.2, 143.7, 131.7, 114.0, 112.5, 107.0, 69.7, 69.7, 69.6, 69.4, 68.7, 68.6, 67.4, 67.2, 40.4, 40.2;

HRMS (ESI$^+$): m/z calculated for $C_{19}H_{31}N_3O_7Li$ $[M+Li]^+$ 420.2317, Found: 420.2314.

Compound 6

ethyl 2-{[(2R)-3-(4,5-diethoxy-9H-thioxanthen-9-ylidene)-6-[(1-ethoxy-1-oxopropan-2-yl)oxy]-2,4-dimethyl-2,3-dihydro-1H-inden-5-yl]oxy}propanoate

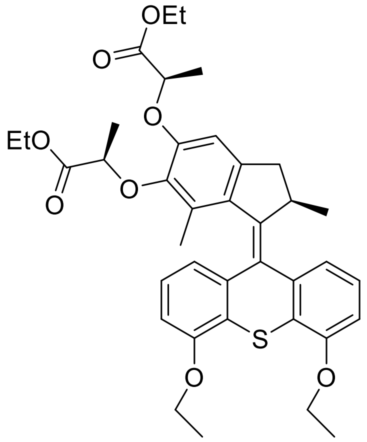

6

To a solution of the bisphenol motor compound (200 mg, 0.33 mmol) and ethyl bromide (108 mg, 74 μL, 0.99 mmol) in DMF (10 mL) was added anhydrous K_2CO_3 (137 mg, 0.99 mmol). The reaction mixture was stirred overnight at 80°C. After this time, the reaction mixture was filtered and the collected residue was washed with dichloromethane (20 mL). After concentration under reduced pressure, water (200 mL) was added to the crude product and the mixture was extracted with dichloromethane 3 times (3 × 20 mL). The combined organic phase was washed with brine (50 mL) and subsequently dried over anhydrous Na_2SO_4 and then concentrated under reduced pressure. Further purification of the crude residue by column chromatography (SiO_2, cyclohexane / EtOAc: 50:1→10:1) provided compound **6** (192 mg, 88%) as a yellow liquid.

^{1}H NMR ($CDCl_3$, 400 MHz, 298 K): δ (ppm) = 7.30 (d, J = 7.4 Hz, 1H), 7.20 (dd, $J_1 = J_2$ = 7.9 Hz, 1H), 6.95 (dd, $J_1 = J_2$ = 7.9 Hz, 1H), 6.72 (dd, J_1 = 8.1 Hz, J_2 = 0.8 Hz, 1H), 6.66 (dd, $J_1 = J_2$ = 7.9 Hz, 2H), 6.59 (s, 1H), 4.77 (q, J = 6.8 Hz, 1H), 4.49 (q, J = 6.8 Hz, 1H), 4.29 – 4.05 (m, 9H), 3.33 (dd, J_1 = 14.8 Hz, J_2 = 6.3 Hz, 1H), 2.33 (d, J = 14.9 Hz, 1H), 1.62 (d, J = 6.8 Hz, 3H), 1.54 – 1.48 (m, 9H), 1.28 (t, J = 7.1 Hz, 3H), 1.27 (t, J = 7.1 Hz, 3H), 1.18 (s, 3H), 0.62 (d, J = 6.7 Hz, 3H);

^{13}C NMR ($CDCl_3$, 100 MHz, 298 K): δ (ppm) = 172.6, 172.2, 155.9, 155.5, 150.2, 145.7, 144.8, 142.3, 141.6, 138.1, 133.6, 131.1, 127.9, 126.8, 126.4, 124.6, 124.3, 120.5, 119.9, 109.0, 108.6, 108.2, 77.3, 73.0, 64.6, 64.5, 61.2, 60.7, 39.6, 38.2, 27.0 (2C), 19.0, 18.8, 18.5, 14.9, 14.9, 14.6, 14.2, 14.2;

HRMS (ESI$^+$): m/z calculated for $C_{38}H_{44}O_8SNa$ $[M+Na]^+$ 683.2655, Found: 683.2682.

Compound 7

2-{[(2R)-6-(1-carboxyethoxy)-3-(4,5-diethoxy-9H-thioxanthen-9-ylidene)-2,4-dimethyl-2,3-dihydro-1H-inden-5-yl]oxy}propanoic acid

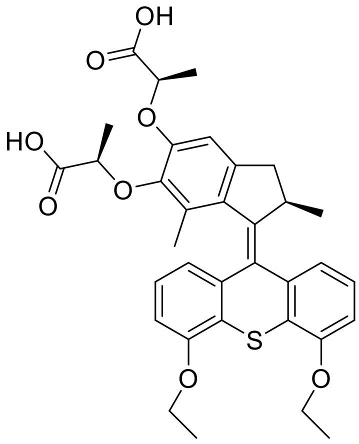

7

To a solution of compound **6** (45 mg, 68.1μmmol) in a 1:1 mixture of THF and methanol (3 mL / 3 mL) was added a NaOH solution (40 mg in 2 mL of deionized water). The reaction mixture was stirred at room temperature for three hours and then quenched with 1 M HCl (1 mL) at 0°C. The mixture was extracted twice with dichloromethane (2 × 20 mL), the combined organic phase was dried over anhydrous Na$_2$SO$_4$ and then concentrated under reduced pressure, providing compound **7** (37.5 mg, 91%) as a light green solid, which was pure enough to be used as such in the next step.

^{1}H NMR (CDCl$_3$, 400 MHz, 298 K): δ (ppm) = 7.29 (d, J = 7.5 Hz, 1H), 7.20 (dd, J_1 = J_2 = 7.9 Hz, 1H), 6.95 (dd, J_1 = J_2 = 7.9 Hz, 1H), 6.73 (d, J = 8.1 Hz, 1H), 6.70 – 6.66 (m, 2H), 6.63 (dd, J_1 = 7.7 Hz, J_2 = 1.0 Hz, 1H), 4.87 (q, J = 6.9 Hz, 1H), 4.67 (q, J = 7.0 Hz, 1H), 4.23 – 4.03 (m, 5H), 3.33 (dd, J_1 = 15.0 Hz, J_2 = 6.2 Hz, 1H), 2.34 (d, J = 15.1 Hz, 1H), 1.66 (d, J = 6.8 Hz, 3H), 11.52 (t, J = 7.0 Hz, 3H), 1.50 (t, J = 6.9 Hz, 3H), 1.45 (d, J = 7.0 Hz, 3H), 1.19 (s, 3H), 0.63 (d, J = 6.7 Hz, 3H);

^{13}C NMR (CDCl$_3$, 100 MHz, 298 K): δ (ppm) = 176.9, 176.2, 155.9, 155.5, 149.0, 145.2, 144.0, 142.8, 141.3, 137.9, 134.3, 130.9, 128.5, 127.0, 126.4, 124.6, 124.2, 120.4, 119.8, 109.4, 109.2, 108.6, 76.9, 73.2, 64.6, 64.5, 39.6, 38.1, 18.9, 18.3, 18.1, 14. 9, 14.8, 14.6;

HRMS (ESI$^+$): m/z calculated for C$_{34}$H$_{36}$O$_8$SNa [M+Na]$^+$ 627.2029, Found: 627.2047.

Compound 8

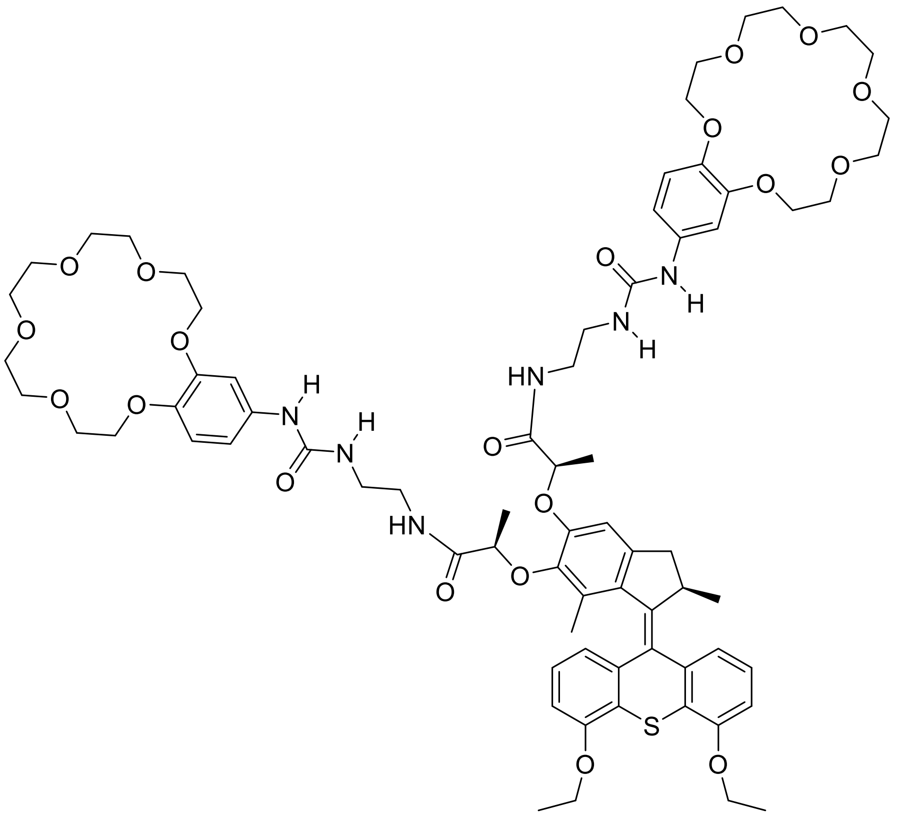

8

To a solution of compound **5** (7.0 mg, 11.6 µmol) and compound **7** (11.5 mg, 24.8 µmol) in DMF (1 mL) was added successively Hydroxybenzotriazole (HOBt) (12.5 mg, 92.6 µmol) and 1-Ethyl-3-(3-dimethylaminopropyl) carbodiimide (EDC) (17.8 mg, 92.6 µmol). The reaction mixture was heated in the microwave oven (Power 200W, 50 °C) for 1 hour. After removal of DMF under reduced pressure, the crude residue was dissolved with dichloromethane (20 mL), the organic phase was extracted with H_2O (20 mL) and the aqueous phase was further washed twice with dichloromethane (2 × 20 mL). The combined organic phase was dried over anhydrous Na_2SO_4 and concentrated under reduced pressure. Further purification by reverse-phase HPLC provided compound **8** (5.0 mg, 32 %) as a yellow solid.

^{1}H NMR ($CDCl_3$, 400 MHz, 298 K): δ (ppm) = 7.80 (d, *J*=12 Hz, 2H), 7.69 (s, 2H), 7.69 (t, *J*=8 Hz, 1H), 7.30 (t, *J*=8 Hz, 1H), 7.22 (t, *J*=8 Hz, 1H), 7.08 (d, *J*=8 Hz, 2H), 6.86 (t, *J*=8 Hz, 1H), 6.78-6.70 (m, 6H), 6.61 (t, *J*=8 Hz, 2H), 6.07 (s, *2*H), 4.67 (q, *J*=8 Hz, 1H), 4.59 (q, *J*=8 Hz, 1H), 4.22-4.12 (m, 5H), 4.06 (d, *J*=4 Hz, 8H), 3.87-3.83 (m, 8H), 3.72-3.66 (m, 24H), 3.43-3.33 (m, 9H), 2.49 (s, 1H), 2.35 (d, *J*=16 Hz, 1H), 1.54-1.47 (m, 9H), 1.31 (d, *J*=8 Hz, 3H), 1.18 (s, 3H), 0.63 (d, *J*=12 Hz, 3H).

^{1}H NMR (CD_3OD, 400 MHz, 298 K): δ (ppm) = 8.33 – 8.27 (brs, 1H) 7.26 (s, 1H), 7.25 (d, *J*

= 3.0 Hz, 1H), 7.10 – 7.06 (m, 2H), 6.86 – 6.67 (m, 9H), 6.48 (dd, J_1 = 7.6 Hz, J_2 = 0.9 Hz, 1H), 4.73 (q, J = 6.7 Hz, 1H), 4.44 (q, J = 6.8 Hz, 1H), 4.23 – 3.98 (m, 13H), 3.82 – 3.72 (m, 8H), 3.70 – 3.57 (m, 28H), 3.42 – 3.33 (m, 5H), 2.33 (d, J = 15.2 Hz, 1H), 1.53 – 1.40 (m, 9H), 1.35 (d, J = 6.8 Hz, 3H), 1.18 (s, 3H), 0.57 (d, J = 6.7 Hz, 3H);

^{13}C NMR (CD$_3$OD, 100 MHz, 298 K): δ = 176.0, 175.1, 158.6, 157.3, 156.8, 150.8, 150.3, 150.3, 146.8, 145.7, 145.7, 145.5, 144.0, 142.9, 139.3, 135.0, 135.0, 134.8, 131.3, 129.6, 128.1, 127.9, 126.1, 125.3, 121.5, 121.0, 115.8, 115.7, 113.4, 110.4, 110.1, 109.9, 108.0, 107.9, 79.9, 76.2, 71.7, 71.6, 71.5, 70.8, 70.6, 70.6, 70.4, 69.8, 69.7, 65.7, 41.0, 40.8, 40.6, 40.3, 39.3, 28.0, 19.6, 19.5, 19.3, 15.3, 15.3;

HRMS (ESI$^+$): m/z calculated for $C_{72}H_{94}N_6O_{20}SNa$ [M+Na]$^+$ 1417.6168; found: 1417.6185.

Compound 9

ethyl 2-[(2R)-4'',5''-diethoxy-6-[(1-ethoxy-1-oxopropan-2-yl)oxy]-2,7-dimethyl-2,3-dihydrodispiro[indene-1,2'-thiirane-3',9''-thioxanthen]-5-yloxy]pro

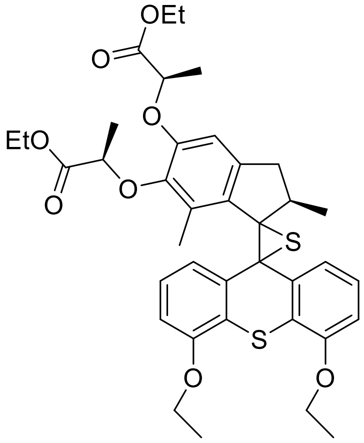

9

To a solution of bis-phenol episulfide compound (50.0 mg, 78.5 µmmol) and ethyl bromide (18.8 mg, 12 µL, 0.17 mmol) in DMF (6 mL) was added anhydrous K_2CO_3 (22.0 mg, 0.17 mmol). The reaction mixture was stirred overnight at 80°C. After this time, the reaction mixture was filtered and the collected residue was washed with dichloromethane (20 mL). After concentration under reduced pressure, water (200 mL) was added to the crude product and the mixture was extracted with dichloromethane 3 times (3 × 20 mL). The combined organic phase was washed with brine (50 mL) and subsequently dried over anhydrous Na_2SO_4 and then concentrated under reduced pressure. Further purification of the crude residue by column chromatography (SiO_2, cyclohexane / EtOAc: 50:1→10:1) provided compound **9** (50.0 mg, 92%) as a yellow liquid.

^{1}H NMR (CDCl$_3$, 400 MHz, 298 K): δ (ppm) = 7.37 (dd, J_1 = 7.8 Hz, J_2 = 1.1 Hz, 1H), 7.23 (dd, J_1 = 7.8 Hz, J_2 = 1.3 Hz, 1H), 7.17 (dd, J_1 = J_2 = 7.9 Hz, 1H), 7.08 (dd, J_1 = J_2 = 7.9 Hz, 1H), 6.76 (dd, J_1 = 8.0 Hz, J_2 = 1.2 Hz, 1H), 6.64 (dd, J_1 = 8.2 Hz, J_2 = 1.0 Hz, 1H), 6.34 (s, 1H), 4.64 (q, J = 6.8 Hz, 1H), 4.28 – 3.90 (m, 9H), 3.17 (dd, J_1 = 14.9 Hz, J_2 = 6.4 Hz, 1H), 2.11 (s, 3H), 2.07 (d, J = 15.0 Hz, 1H), 1.52 (d, J = 6.8 Hz, 3H), 1.47 (t, J = 7.0 Hz, 3H), 1.37 (t, J = 7.0 Hz, 3H), 1.36 (d, J = 6.8 Hz, 3H), 1.30 (t, J = 7.1 Hz, 4H), 1.20 (t, J = 7.1 Hz, 3H), 0.94 (d, J = 6.9 Hz, 3H);

^{13}C NMR (CDCl$_3$, 100 MHz, 298 K): δ (ppm) = 172.5, 172.1, 154.8, 154.6, 149.6, 144.4, 140.2, 139.6, 135.9, 131.4, 128.9, 126.4, 125.8, 125.3, 125.0, 123.0, 121.1, 110.3, 109.9, 109.0, 73.1, 71.2, 64.8, 64.7, 61.7, 61.1, 60.7, 41.0, 37.7, 26.9, 21.2, 18.5, 18.3, 14.8, 14.7, 14.2, 14.2, 12.4;

HRMS (ESI$^+$): m/z calculated for $C_{38}H_{44}O_8S_2Na$ [M+Na]$^+$ 715.2375; found: 715.2401.

Compound 10

2-[(2R)-6-(1-carboxyethoxy)-4'',5''-diethoxy-2,7-dimethyl-2,3-dihydrodispiro[indene-1,2'-thiirane-3',9''-thioxanthen]-5-yloxy]propanoic acid

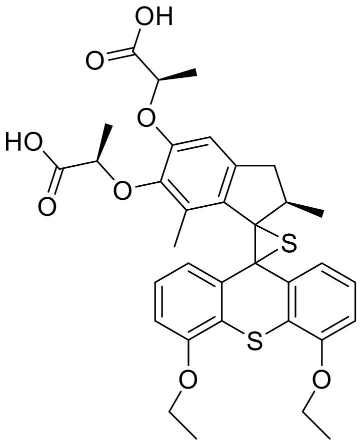

10

To a solution of compound **9** (50 mg, 72 µmol) in a 1:1 mixture of THF and methanol (3 mL / 3 mL) was added a NaOH solution (40 mg in 2 mL of deionized water). The reaction mixture was stirred at room temperature for three hours and then quenched with 1 M HCl (1 mL) at 0°C. The mixture was extracted twice with dichloromethane (2 × 20 mL), the combined organic phase was dried over anhydrous Na_2SO_4 and then concentrated under reduced pressure, providing compound **10** (44.0 mg, 95%) as a light green solid, which was pure enough to be used as such in the next step.

^{1}H NMR (CDCl$_3$, 400 MHz, 298 K): δ (ppm) = 7.29 (d, J = 7.5 Hz, 1H), 7.20 (dd, J_1 = J_2 =

7.9 Hz, 1H), 6.95 (dd, $J_1 = J_2 = 7.9$ Hz, 1H), 6.73 (d, $J = 8.1$ Hz, 1H), 6.70 – 6.66 (m, 2H), 6.63 (dd, $J_1 = 7.7$ Hz, $J_2 = 1.0$ Hz, 1H), 4.87 (q, $J = 6.9$ Hz, 1H), 4.67 (q, $J = 7.0$ Hz, 1H), 4.23 – 4.03 (m, 5H), 3.33 (dd, $J_1 = 15.0$ Hz, $J_2 = 6.2$ Hz, 1H), 2.34 (d, $J = 15.1$ Hz, 1H), 1.66 (d, $J = 6.8$ Hz, 3H), 11.52 (t, $J = 7.0$ Hz, 3H), 1.50 (t, $J = 6.9$ Hz, 3H), 1.45 (d, $J = 7.0$ Hz, 3H), 1.19 (s, 3H), 0.63 (d, $J = 6.7$ Hz, 3H);

^{13}C NMR ($CDCl_3$, 100 MHz, 298 K): δ (ppm) = 207.47, 177.32, 176.45, 154.65, 154.56, 148.03, 144.81, 140.79, 139.53, 135.66, 131.41, 130.37, 126.61, 126.01, 125.07, 125.00, 123.06, 120.98, 111.81, 110.81, 109.83, 77.55, 77.26, 73.81, 70.75, 65.00, 64.66, 61.76, 40.96, 37.45, 30.96, 21.22, 18.32, 17.36, 14.84, 14.71, 12.42;

ESI-MS: m/z calculated for $C_{34}H_{37}O_8S_2$ $[M+H]^+$ 637.1924, Found: 637.4510.

Compound 11

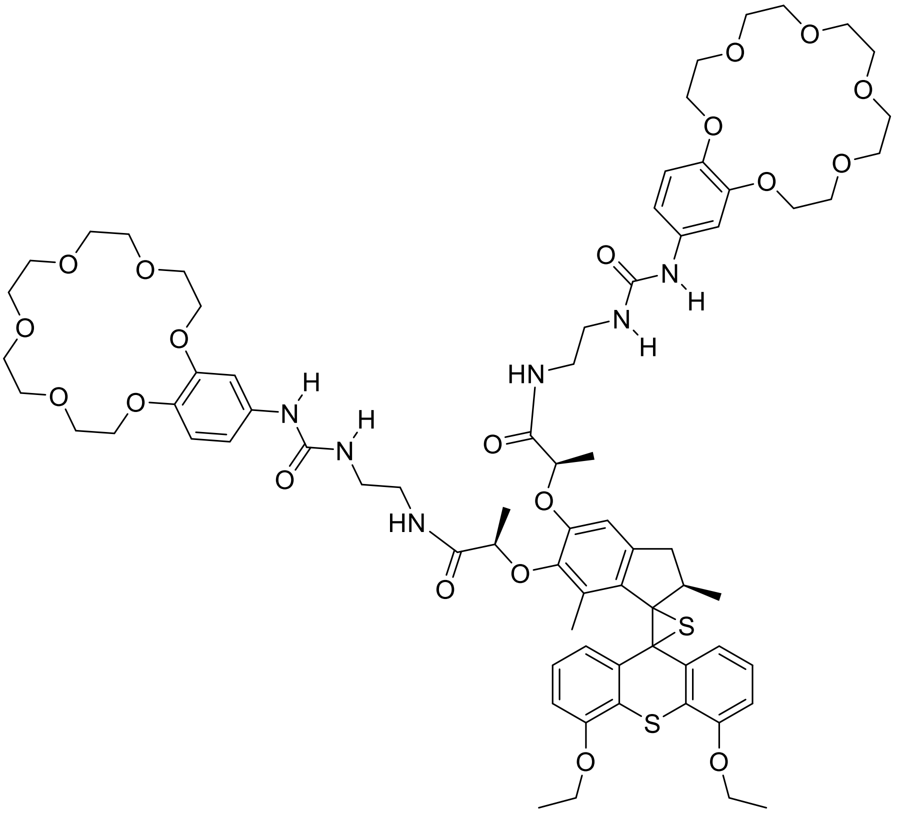

11 (B)

To a solution of compound 11(32.9 mg, 79.5 μmol) and compound **5** (2.03 mg, 36.1 μmol) in DMF (2 mL), was added HOBt (19.5 mg, 144.5 μmol) and EDC (27.7 mg, 144.5 μmol). The reaction mixture was heated in the microwave oven (Power 200W, 50 °C) for 1 hour. After removal of DMF under reduced pressure, the crude residue was dissolved with dichloromethane (20 mL), the organic phase was extracted with H_2O (20 mL) and the aqueous phase was further washed twice with dichloromethane (2 × 20 mL). The combined organic phase was dried over anhydrous Na_2SO_4 and concentrated under reduced pressure. Further purification by reverse-phase HPLC provided compound **B** (14.0 mg, 27 %) as a yellow solid.

^{1}H NMR ($CDCl_3$, 400 MHz, 298 K): δ = 7.66 (brs, 1H), 7.61 (brs, 1H), 7.50 (brs, 1H), 7.34 (dd, J_1 = 7.7 Hz, J_2 = 0.9 Hz, 1H), 7.22 (dd, J_1 = 7.8 Hz, J_2 = 1.6 Hz, 1H), 7.18 (dd, J_1 = J_2 = 7.7 Hz, 1H), 7.10 (brs, 1H), 7.02 (dd, J_1 = J_2 = 7.9 Hz, 2H), 6.78 (dd, J_1 = 7.7 Hz, J_2 = 1.6 Hz, 1H), 6.73 – 6.67 (m, 3H), 6.60 – 6.56 (m, 2H), 6.50 (s, 1H), 5.69 (brs, 1H), 5.15 (brs, 1H), 4.55 (q, J = 6.7 Hz, 1H), 4.48 (q, J = 6.7 Hz, 1H), 4.22 – 4.02 (m, 10H), 3.98 – 3.81 (m, 10H), 3.76 – 3.63 (m, 26H), 3.51 – 3.41 (m, 1H), 3.39 – 3.18 (m, 8H), 3.17 – 3.07 (m, 1H), 2.13 (s, 3H), 2.08 (d, J = 15.7 Hz, 3H), 1.48 (d, J = 7.0 Hz, 3H), 1.38 (d, J = 6.6 Hz, 3H), 1.35 – 1.30 (m, 1H), 1.28 (t, J = 7.0 Hz, 3H), 1.21 (d, J = 6.8 Hz, 3H), 0.93 (d, J = 6.9 Hz, 3H);

^{13}C NMR ($CDCl_3$, 100 MHz, 298 K): δ = 173.4, 172.7, 157.2, 156.6, 154.9, 154.7, 149.3, 149.2, 148.2, 144.3, 142.9, 141.5, 139.6, 135.9, 133.6, 133.1, 131.6, 126.7, 126.1, 125.2, 125.0, 122.9, 121.0, 115.0, 113.3, 112.3, 110.5, 110.0, 106.8, 77.3, 71.1, 70.7, 70.7, 70.7, 70.6, 70.6, 70.6, 69.8, 69.6, 69.6, 69.5, 68.8, 68.7, 64.8, 61.8, 53.5, 41.3, 40.7, 39.3, 37.6, 21.1, 18.3, 18.0, 14.9, 14.8, 12.7;

HRMS (ESI$^+$): m/z calculated for $C_{72}H_{94}N_6O_{20}S_2Li$ $[M+Li]^+$ 1433.6120; found: 1433.6144

Compound 12

({3,4-bis[2-(2-methoxyethoxy)ethoxy]phenyl}nitroso)oxidanide

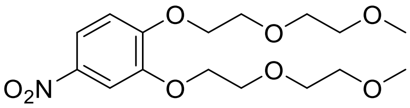

12

To a round bottom flask, 2-(2-Methoxyethoxy)ethyl 4-methyl benzenesulfonate (1.35 g, 4.93 mmol), 4-nitropyrocatechol (0.35 g, 2.24 mmol), and anhydrous potassium carbonate (1.86 g, 13.45 mmol) were dissolved in DMF (10 mL), and the mixture was stirred at 80°C for overnight. After this time, DMF was evaporated under reduced pressure. The residue was washed with deionized water (20 mL) and extract by dichloromethane two times (2 × 20 mL). The organic phases were combined and dried over anhydrous Na_2SO_4. After removal of the organic solvent, the crude product was purified by column chromatography (SiO_2, CH_2Cl_2: MeOH = 50: 1) to give compound **12** as a yellow liquid (0.69 g, 1.91 mmol, 86% yield).

^{1}H NMR ($CDCl_3$, 400 MHz, 298K): δ (ppm) = 7.90 (dd, J_1 = 4.0 Hz, J_2 = 8.0 Hz, 1H), 7.82

(d, *J* = 4.0 Hz, 1H), 6.95 (d, *J* = 8.0 Hz, 1H), 4.29-4.25 (m, 4H), 3.94-3.91 (m, 4H), 3.76-3.74 (m, 4H), 3.60-3.57 (m, 4H), 3.40 (s, 6H);

^{13}C NMR ($CDCl_3$, 100 MHz, 298K): δ (ppm) = 154.41, 148.45, 141.51, 118.05, 111.84, 109.00, 71.99, 71.97, 70.95, 70.90, 69.52, 69.39, 69.16, 68.97, 59.10;

ESI-MS: calculated for $C_{16}H_{26}NO_8$ $[M+H]^+$ 360.17, Found: 360.57.

Compound 13

3,4-bis[2-(2-methoxyethoxy)ethoxy]aniline

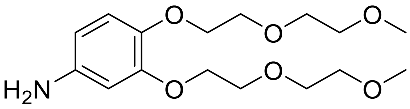

13

A solution of compound **12** (400 mg, 1.11 mmol) and 10% Pd/C (300 mg) in 1,4-dioxane (15 mL) was heated to reflux. Then hydrazine hydrate (5 mL) was added dropwise, and the reaction was kept refluxing for another 3h. After cooling to room temperature, the remaining insoluble catalyst was filtered off and the solvent was removed under reduced pressure to provide compound **13** (333 mg, 1.01 mmol 91% yield) as a yellow oil, which was pure enough to be used without further purification.

^{1}H NMR ($CDCl_3$, 400 MHz, 298K): δ (ppm) = 6.77 (d, *J* = 8.0 Hz, 1H), 6.33 (d, *J* = 2.8 Hz, 1H), 6.23 (dd, J_1 = 8.4 Hz, J_2 = 2.8 Hz 1H), 4.14-4.08 (m, 4H), 3.87-3.80 (m, 4H), 3.74-3.71 (m, 4H), 3.59-3.56 (m, 4H), 3.40 (s, 6H);

^{13}C NMR ($CDCl_3$, 100 MHz, 298K): δ (ppm) = 150.23, 141.59, 141.57, 118.07, 107.55, 103.17, 71.98, 70.71, 70.61, 70.28, 70.01, 69.74, 68.56, 59.06;

ESI-MS: calculated for $C_{16}H_{28}NO_6$ $[M+H]^+$ 330.19, Found: 330.57.

Compound 14

1-{3,4-bis[2-(2-methoxyethoxy)ethoxy]phenyl}-3-(2-chloroethyl)urea

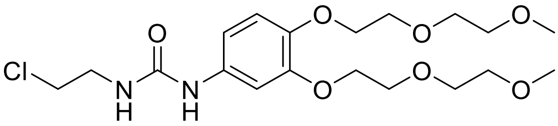

14

Compound **13** (100 mg, 0.3 mmol) and 2-chloroethyl isocyanate (135.4 mg, 38.85 μL, 0.46 mmol) were dissolved in dichloromethane (5 mL). The mixture was stirred under an argon atmosphere at room temperature overnight. After this time, the resulting solution was poured into deionized water (20 mL) and extracted with dichloromethane two times (2 × 20 mL). The organic phase was washed with brine twice (2 × 50 mL). After drying over anhydrous Na_2SO_4, the organic solvents were evaporated under reduced pressure. Then the crude product was purified by silica column chromatography (CH_2Cl_2: MeOH: TEA = 100: 2: 1) to provide compound **14** (86 mg, 65% yield) as a light red liquid.

^{1}H NMR ($CDCl_3$, 400 MHz, 298K): δ (ppm) = 7.36 (s, 1H), 7.04 (d, *J* = 2.0 Hz, 1H), 6.75 (d, *J* = 8.4 Hz, 1H), 6.72 (dd, J_1 = 8.6 Hz, J_2 = 2.2 Hz, 1H), 5.85 (s, 1H), 4.11-4.06 (m, 4H), 3.82 (t, *J* = 4.6 Hz, 4H), 3.73-3.70 (m, 4H), 3.62-3.56 (m, 8H), 3.38 (s, 6H).

^{13}C NMR ($CDCl_3$, 100 MHz, 298K): δ (ppm) = 156.09, 149.18, 144.59, 133.27, 115.72, 113.11, 107.69, 71.93, 71.92, 70.61, 70.57, 69.81, 69.62, 69.37, 68.42, 58.98, 58.95, 44.64, 41.92.

ESI-MS: calculated for $C_{19}H_{32}ClN_2O_7$ $[M+H]^+$ 435.19, Found: 435.61.

Compound 15

3-(2-azidoethyl)-1-{3,4-bis[2-(2-methoxyethoxy)ethoxy]phenyl}urea

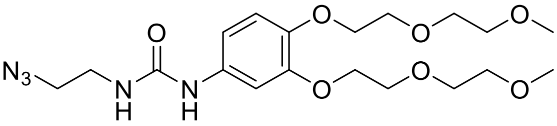

15

To a solution of compound **14** (200 mg, 0.46 mmol) in DMF (5 mL) was added sodium azide (45 mg, 0.69 mmol). The reaction was stirred at 50 °C overnight. The reaction was extracted by dichloromethane two times (2 × 15 mL) and the combined organic solvent was dried over anhydrous Na_2SO_4 and evaporated under vacuum. The crude product was purified by silica cplumn chromatography (CH_2Cl_2: MeOH: NEt_3 = 100: 2: 1) to give compound **15** (158 mg, 0.36 mmol, 78% yield) as a brown-red solid.

^{1}H NMR ($CDCl_3$, 400 MHz, 298 K): δ (ppm) = 6.94 (d, *J* = 2.0 Hz, 1H), 6.84 (d, *J* = 8.4 Hz, 1H), 6.75 (dd, J_1 = 8.6 Hz, J_2 = 2.2 Hz, 1H), 6.47 (s, 1H), 5.16 (s, 1H), 4.15-4.12 (m, 4H), 3.86-3.83 (m, 4H), 3.73-3.71 (m, 4H), 3.58-3.55 (m, 4H), 3.45-3.40 (m, 4H), 3.39 (s, 3H), 3.38 (s, 3H);

ESI-MS: calculated for $C_{19}H_{32}N_5O_7$ $[M+H]^+$ 442.23, Found: 442.61.

Compound 16

3-(2-aminoethyl)-1-{3,4-bis[2-(2-methoxyethoxy)ethoxy]phenyl}urea

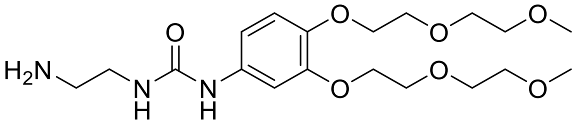

16

Compound **15** (20 mg, 0.045 mmol) and triphenylphosphine (29.7 mg, 0.11 mmol) were dissolved in THF (5 mL). The mixture was stirred at room temperature for four hours, then deionized water (1 mL) was added and the reaction was continued for half an hour. After evaporation of the organic solvents, the residue was dissolved with water (20 mL) and extracted by dichloromethane two times (2× 20 mL). The target compound would be dissolved in water while other impurities would be dissolved in dichloromethane. Further evaporation of water under vacuum provided compound **16** (11.5 mg, 0.03 mmol, 61% yield) as a light yellow solid.

^{1}H NMR (D_2O, 400 MHz, 298 K): δ (ppm) = 7.01 (brs, 1H), 6.96 (dd, J_1 = 8.8 Hz, J_2 = 2.4 Hz, 1H), 6.82 (d, J = 8.8 Hz, 1H), 4.15 (brs, 4H), 3.86-3.83 (m, 4H), 3.72-3.69 (m, 4H), 3.61-3.59 (m, 4H), 3.39 (t, J = 6.0 Hz, 2H), 3.35 (s, 6H), 3.02 (t, J = 5.8 Hz, 2H);

^{13}C NMR (D_2O, 100 MHz, 298 K): δ (ppm) = 158.44, 147.82, 144.19, 132.18, 114.85, 114.79, 108.65, 70.95, 69.58, 69.54, 69.02, 68.93, 68.46, 68.00, 58.02, 40.01, 38.45;

ESI-MS: calculated for $C_{19}H_{34}N_3O_7$ $[M+H]^+$ 416.24, Found: 416.41.

Compound 17

(2R)-N-{2-[({3,4-bis[2-(2-methoxyethoxy)ethoxy]phenyl}carbamoyl)amino]ethyl}-2-{[(2R)-6-[(1R)-1-({2-[({3,4-bis[2-(2-methoxyethoxy)ethoxy]phenyl}carbam

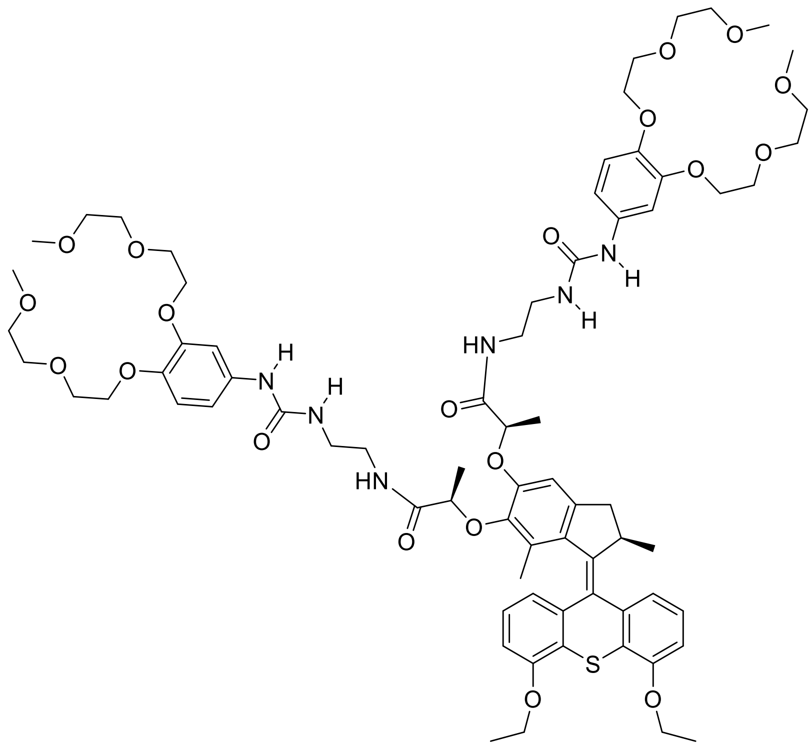

17

To a solution of compound **7** (5.0 mg, 79.5 µmol) and compound **16** (10.3 mg, 24.81 µmol) in DMF (2 mL) was added HOBt (8.9 mg, 66.15 µmol) and EDC (12.68 mg, 66.15 µmol). The reaction mixture was heated in the microwave oven (Power 200W, 50 °C) for 1 hour. After removal of DMF under reduced pressure, the crude residue was dissolved with dichloromethane (20 mL), the organic phase was extracted with H_2O (20 mL) and the aqueous phase was further washed twice with dichloromethane (2 × 20 mL). The combined organic phase was dried over anhydrous Na_2SO_4 and concentrated under reduced pressure. Further purification by reverse-phase HPLC provided compound **17** (3 mg, 26 %) as a yellow solid.

^{1}H NMR ($CDCl_3$, 400 MHz, 298 K): δ (ppm) = 7.63 (s, 1H), 7.55-7.45 (brm, 3H), 7.29 (d, *J* = 7.6 Hz, 1H), 7.21 (dd, $J_1 = J_2$ =7.6 Hz, 1H), 7.07 (s, 1H), 7.02 (s, 1H), 6.90 (dd, $J_1 = J_2$ = 7.6 Hz, 1H), 6.80-6.74 (m, 4H), 6.72 (brd, *J* = 4.8 Hz, 2H), 6.64 (d, *J* = 8.0 Hz, 1H), 6.58 (d, *J* = 7.6 Hz, 1H), 5.81 (s, 1H), 5.74 (s, 1H), 4.69-4.65 (brs, 2H), 4.09 (br, 13H), 3.83-3.79 (m, 7H), 3.70-3.68 (m, 7H), 3.56-3.54 (m, 9H), 3.37-3.57 (m, 18H), 2.35 (d, *J* = 15.2 Hz, 1H), 1.53-1.47 (m, 9H), 1.28-1.26 (d, *J* = 6.8 Hz, 3H), 1.16 (s, 3H), 0.61(d, *J* = 6.4 Hz, 3H);

^{13}C NMR ($CDCl_3$, 100 MHz, 298 K): δ (ppm) = 173.93, 173.13, 156.81, 155.93, 155.47, 149.23, 148.30, 145.13, 144.47, 143.39, 142.99, 141.29, 137.85, 135.01, 133.66, 130.89, 128.81, 127.12, 126.49, 124.55, 124.18, 120.15, 119.81, 115.93, 112.50, 111.70, 109.19, 108.70, 107.30, 75.94, 71.94, 70.62, 70.58, 69.83, 69.65, 69.46, 68.56, 64.58, 59.05, 58.99, 53.46, 40.16, 39.41, 39.31, 39.23, 38.20, 29.76, 18.96, 18.88, 18.43, 14.91, 14.85, 14.72;

ESI-MS: m/z calculated for $C_{72}H_{99}N_6O_{20}S_2$ $[M+H^+]^+$:1399.6557; found: 1400.14.

Compound 18

2-{[(2R)-6-(1-carboxyethoxy)-2,7-dimethyl-1-oxo-2,3-dihydro-1H-inden-5-yl]oxy}propanoic acid

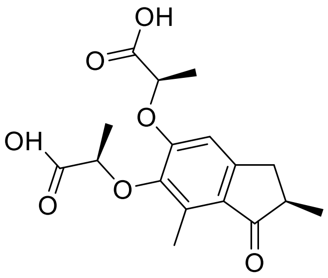

18

To a solution of rotor **A10** [65] (80 mg, 0.2 mmol) in a 1:1 mixture of THF and methanol (3 mL / 3 mL) was added a NaOH solution (40 mg in 2 mL of deionized water). The reaction mixture was stirred at room temperature for three hours and then quenched with 1 M HCl (1 mL) at 0 °C. The mixture was extracted twice with dichloromethane (2 × 20 mL), the combined organic phase was dried over anhydrous Na_2SO_4 and then concentrated under reduced pressure, providing compound **18** (62 mg, 91%) as a light green solid, which was pure enough to be used as such in the next step.

ESI-MS: calculated for $C_{16}H_{21}O_7$ $[M+H]^+$ 337.13, Found: 337.23.

Compound 19

N-(2-{[(2,3,5,6,8,9,11,12,14,15-decahydro-1,4,7,10,13,16-benzohexaoxacyclooctadecin-18-yl)carbamoyl]amino}ethyl)-2-{[(2R)-6-{1-[(2-{[(2,3,5,6,8,9,11,1

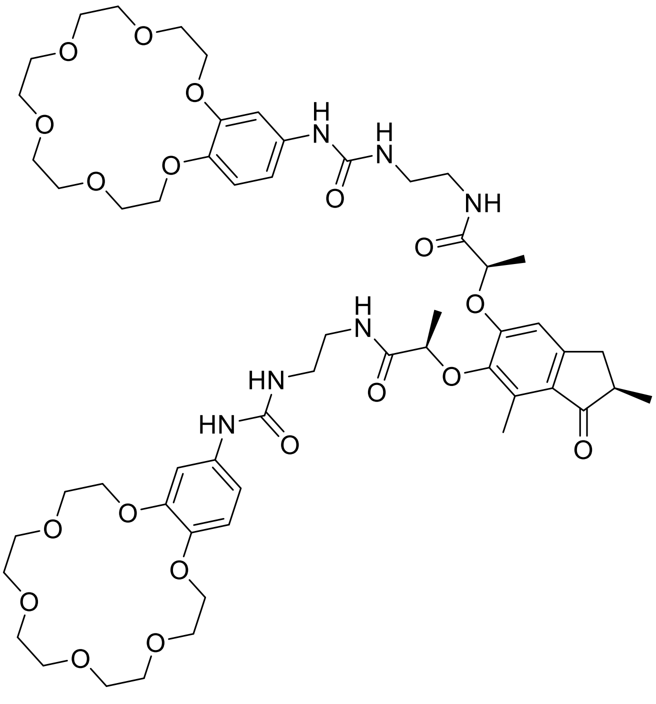

19

To a solution of compound **18** (12.0 mg, 35.68 µmol) and compound **5** (32.0 mg, 78.49 µmol) in DMF (3 mL), was added HOBt (19.3 mg, 0.14 mmol) and EDC (22.2 mg, 0.14 mol). The reaction mixture was heated in the microwave oven (Power 200W, 50 °C) for 1 hour. After removal of DMF under reduced pressure, the crude residue was dissolved with dichloromethane (20 mL), the organic phase was extracted with H_2O (20 mL) and the aqueous phase was further washed twice with dichloromethane (2 × 20 mL). The combined organic phase was dried over anhydrous Na_2SO_4 and concentrated under reduced pressure. Further purification by reverse-phase HPLC provided compound **19** (17 mg, 42 %) as a yellow solid.

^{1}H NMR ($CDCl_3$, 400 MHz, 298K): δ (ppm) = 8.17 (s, 1H), 7.78 (s, 1H), 7.53 (s, 1H), 7.48 - 7.44 (m, 1H), 6.94 (1H), 6.88 (d, *J* = 2.0 Hz, 1H), 6.63 - 6.53 (m, 4H), 6.09 (s, 1H), 5.79 (s, 1H), 4.70 - 4.61 (m, 1H), 4.47 (d, *J* = 6.7 Hz, 1H) 4.10 - 3.97 (m, 6H), 3.93-3.59 (m, 3H), 3.43 - 3.10 (m, 9H), 2.61 - 2.46 (m, 3H), 2.39 (t, *J* = 11.4 Hz, 3H), 1.52 (d, *J* = 4.57 Hz, 3H), 1.43 (t, *J* = 6.8 Hz, 3H), 1.24 - 1.19 (m, 3H);

^{13}C NMR ($CDCl_3$, 100 MHz, 298K): δ (ppm) = 208.97, 172.99, 172.07, 157.28, 154.66, 151.81, 148.86, 144.48, 132.66, 128.00, 117.97, 114.47, 110.28, 107.91, 79.32, 75.51, 70.66, 70.58, 70.53, 70.43, 70.37, 70.31, 70.25, 69.67, 69.60, 69.39, 69.24, 53.46, 42.67, 40.71, 38.89, 34.40, 19.03, 18.61, 16.67, 16.32, 14.90, 11.48.

ESI-MS: calculated for $C_{55}H_{79}N_6O_{18}$ $[M+H]^+$ 1127.54, Found: 1128.06.

Compound 20

Ethyl 2-{[(2R)-3-[4,5-bis(prop-2-yn-1-yloxy)-9H-thioxanthen-9-ylidene]-6-[(1-ethoxy -1-oxopropan-2-yl)oxy]-2,4-dimethyl-2,3-dihydro-1H-inden-5-yl]oxy}p

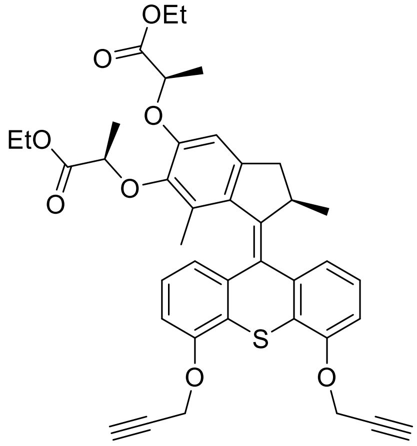

20

To a solution of the bis-phenol motor **(*R*)-A14** [65] (35 mg, 0.058 mmol) and propargyl bromide (20.7 mg, ~15 µL, 0.17 mmol) in anhydrous DMF (3 mL) was added anhydrous K_2CO_3 (24 mg, 0.17 mmol). The reaction mixture was stirred at room temperature overnight. After evaporating the solvent, the crude product was purified through column chromatography (SiO_2, n-hexane / EtOAc 50/1-> 10/1) to give compound **20** (36.3 mg, 92 % yield) as a yellow solid.

^{1}H NMR ($CDCl_3$, 400 MHz, 298K): δ (ppm) = 7.36 (d, J = 7.6 Hz, 1H), 7.24 (dd, $J_1 = J_2$ =8.0 Hz, 1H), 7.00 (dd, $J_1 = J_2$ = 8.0 Hz, 1H), 6.93 (dd, J_1 =8.0 Hz, J_2 = 0.8 Hz, 1H), 6.86 (dd, J_1 = 8.2 Hz, J_2 = 1.0 Hz, 2H), 6.71 (dd, J_1 =7.6 Hz, J_2 = 1.0 Hz, 4H), 6.57 (s, 1H), 4.88-4.75 (m, 5H), 4.49 (q, J = 6.8 Hz, 1H), 4.27-4.08 (m, 5H), 3.33 (dd, J_1 = 14.9 Hz, J_2 = 6.2 Hz, 1H), 2.53 (t, J = 2.7 Hz, 1H), 2.52 (t, J = 2.7 Hz, 1H), 2.34 (d, J = 15.0 Hz, 2H), 1.61 (d, J = 8.0 Hz, 3H), 1.53 (d, J = 6.8 Hz, 3H), 1.29-1.23 (m, 6H), 1.18 (s, 3H), 0.62 (d, J = 6.7 Hz, 3H);

^{13}C NMR ($CDCl_3$, 100 MHz, 298K): δ (ppm) =172.54, 172.15, 154.70, 154.31, 150.36, 146.22, 144.94, 142.43, 142.14, 138.68, 133.29, 131.09, 127.49, 126.94, 126.55, 125.24, 124.73, 121.64, 121.02, 109.34, 109.74, 108.26, 78.72, 78.64, 76.06, 76.03, 72.97, 61.28, 60.77, 56.95, 56.79, 39.66, 38.25, 19.08, 18.88, 18.58, 14.69, 14.34, 14.23;

ESI-MS: calculated for $C_{40}H_{40}O_8S$ $[M+H]^+$ 681.25, Found: 681.67.

Compound 21

2-{[(2R)-1-[4,5-bis(prop-2-yn-1-yloxy)-9H-thioxanthen-9-ylidene]-6-(1-carboxyethoxy)-2,7-

dimethyl-2,3-dihydro-1H-inden-5-yl]oxy}propanoic acid

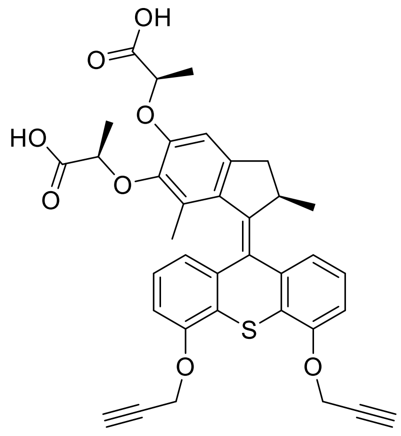

21

To a solution of compound **20** (36.3 mg, 0.05mmol) in THF/MeOH (3 mL/3mL) was added a NaOH (21.3 mg, 0.53mmol) solution (in 2 mL H_2O). The mixture was stirred at room temperature for 3 hours and then quenched with 1 M HCl (1 mL) at 0 °C. After evaporating the organic solvents, the mixture was extracted by dichloromethane 3 times (3 × 20 mL). The organic phase was dried over anhydrous Na_2SO_4 and further evaporated under reduced pressure to provide compound **21** (28.3 mg, 85 % yield) as a light yellow solid.

^{1}H NMR ($CDCl_3$, 400 MHz, 298K): δ (ppm) = 9.95 (s, 2H), 7.35 (d, J = 7.7 Hz, 1H), 7.24 (dd, J = 7.9 Hz, 1H), 6.99 (dd, J = 7.9 Hz, 1H), 6.99 (dd, J = 7.9 Hz, 1H), 6.87 (dd, J_1 = 8.2 Hz, J_2 = 0.8 Hz, 1H), 6.70-6.68 (m, 2H), 4.89-4.78 (m, 5H), 4.64 (q, J = 7.0 Hz, 1H), 4.15-4.07 (m, 1H), 3.33 (dd, J_1 = 15.1 Hz, J_2 = 6.2 Hz, 1H), 2.53 (t, J = 2.5 Hz, 1H), 2.52 (t, J = 2.5 Hz, 1H), 2.34 (d, J = 15.2 Hz, 1H), 1.66 (d, J = 6.8 Hz, 3H), 1.45 (d, J = 7.0 Hz, 3H), 1.18 (s, 3H), 0.63 (d, J = 6.7 Hz, 3H).

ESI-MS: calculated for $C_{36}H_{32}O_8S$ $[M+H]^+$ 625.19, Found: 625.62.

Compound 22

2-{[(2R)-1-[4,5-bis(prop-2-yn-1-yloxy)-9H-thioxanthen-9-ylidene]-2,7-dimethyl-6-{1-[(prop-2-yn-1-yl)carbamoyl]ethoxy}-2,3-dihydro-1H-inden-5-yl]oxy}-N

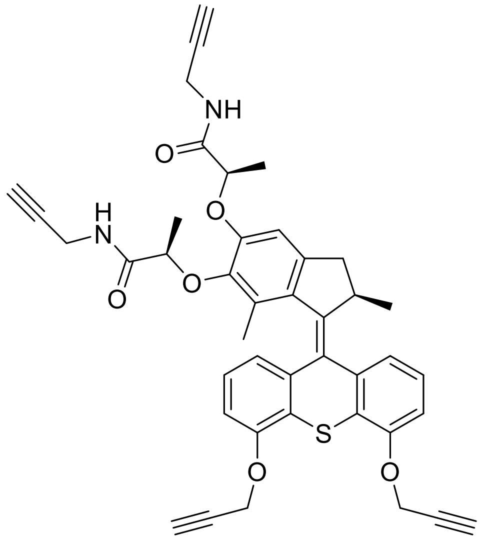

22

To a solution of compound **21** (28.3 mg, 0.045 mmol) in dichloromethane (2 mL), was added an excess of oxalyl dichloride (0.1 mL) and DMF (catalytic amount). The reaction mixture was then stirred at 45 °C for half an hour. Further evaporation of the solvents provided an intermediate product which was used directly in the next step.

To a solution of the intermediate compound (29.9 mg, 0.045 mmol) in dichloromethane (2 mL) was added propargylamine (30 μL, 0.45 mmol). As the propargylamine was added, the reaction forms lots of bubbles in the bottle. The reaction mixture was stirred at room temperature for 12 hours. After evaporation of the solvents, the crude product was purified through a column chromatography (SiO_2, CH_2Cl_2: MeOH = 50:1) to give a yellow solid 28.5 mg (90% yield).

^{1}H NMR ($CDCl_3$, 400 MHz, 298K): δ (ppm) = 7.38 (d, *J* = 7.5 Hz, 1H), 7.27 (d, *J* = 8.0 Hz, 1H), 7.15 (t, *J* = 5.4 Hz, 1H), 7.03 (dd, *J* = 7.9 Hz, 1H), 6.96 (dd, *J* = 8.1, 0.8 Hz, 1H), 6.90 (dd, *J* = 8.2, 1.1 Hz, 1H), 6.71 (dd, *J* = 7.6, 1.1 Hz, 1H), 6.66 (s, 1H), 6.65 (s, 1H), 4.91 - 4.80 (m, 4H), 4.69 (q, *J* = 6.8 Hz, 1H), 4.46 (q, *J* = 6.8 Hz, 1H), 4.23 - 4.06 (m, 5H), 3.37 (dd, *J* = 14.9, 6.3 Hz, 1H), 2.55 (t, *J* = 2.7 Hz, 1H), 2.53 (t, *J* = 2.7 Hz, 1H), 2.39 (d, *J* = 15.2 Hz, 1H), 2.28 (t, *J* = 2.6 Hz, 1H), 2.26 (t, *J* = 2.6 Hz, 1H), 1.62 (d, *J* = 6.8 Hz, 3H), 1.45 (s, 2H), 1.35 (d, *J* = 6.9 Hz, 3H), 1.31 - 1.25 (m, 4H), 1.17 (s, 3H), 0.65 (d, *J* = 6.7 Hz, 3H).

^{13}C NMR ($CDCl_3$, 101 MHz, 298K): δ (ppm) = δ 172.29, 171.60, 154.72, 154.24, 149.36, 145.65, 143.14, 142.84, 141.80, 138.24, 134.19, 130.69, 128.16, 126.70, 126.66, 125.31, 124.39, 121.31, 120.75, 110.40, 109.74, 108.69, 79.50, 79.04, 78.55, 78.41, 77.78, 77.24, 76.13, 76.02, 75.91, 71.99, 71.95, 60.42, 56.83, 56.70, 39.59, 38.12, 30.96, 29.01, 28.78, 21.08, 18.94, 18.84, 18.35, 14.84, 14.22.

ESI-MS: calculated for $C_{42}H_{36}N_2O_6S$ $[M+H]^+$ 699.25, Found: 699.74.

Compound 23

18-azido-2,3,5,6,8,9,11,12,14,15-decahydro-1,4,7,10,13,16
benzohexaoxacyclooctadecine

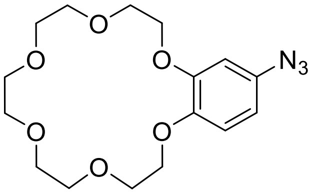

23

In a round-bottom flask equipped with a magnetic stirring bar, compound **2** (475 mg, 1.45 mmol) was dissolved with HCl (6N, 3 mL) in an ice bath. $NaNO_2$ (150.2 mg, 2.18 mmol) dissolved in water (3 mL) was then added dropwise. The reaction mixture was stirred for 30 min. Then, sodium azide (283 mg, 4.35 mmol) dissolved in water (50 mL) was added dropwise. After addition, the reaction mixture was stirred for another 3 hours at room temperature. Then, the mixture was extracted with ethyl acetate (50 mL) and the combined organic extracts were washed with deionized water (50 mL), dried over anhydrous Na_2SO_4, filtered, and concentrated in vacuo to get compound **23** (223 mg, 43 % yield) as a red solid. The compound was pure enough to be used as such in the next step.

^{1}H NMR ($CDCl_3$, 400 MHz, 298K): δ (ppm) = 6.85 (d, J = 8.5 Hz, 1H), 6.58 (dd, J_1 = 8.5 Hz, J_2 = 2.6 Hz,1H), 6.53 (d, J = 2.6 Hz, 1H), 4.15-4.12 (m, 4H), 3.93-3.90 (m, 4H), 3.77-3.75 (m, 4H), 3.72-3.70 (m, 4H), 3.68 (s, 4H).

^{13}C NMR ($CDCl_3$, 101 MHz,298K): δ (ppm) = 149.97, 146.25, 133.25, 115.16, 111.07, 105.35, 70.82, 70.80, 70.70, 69.61, 69.49, 69.43, 68.96.

ESI-MS: calculated for $C_{16}H_{23}N_3O_6$ $[M-H]^-$ 352.16, Found: 354.57.

Compound 24

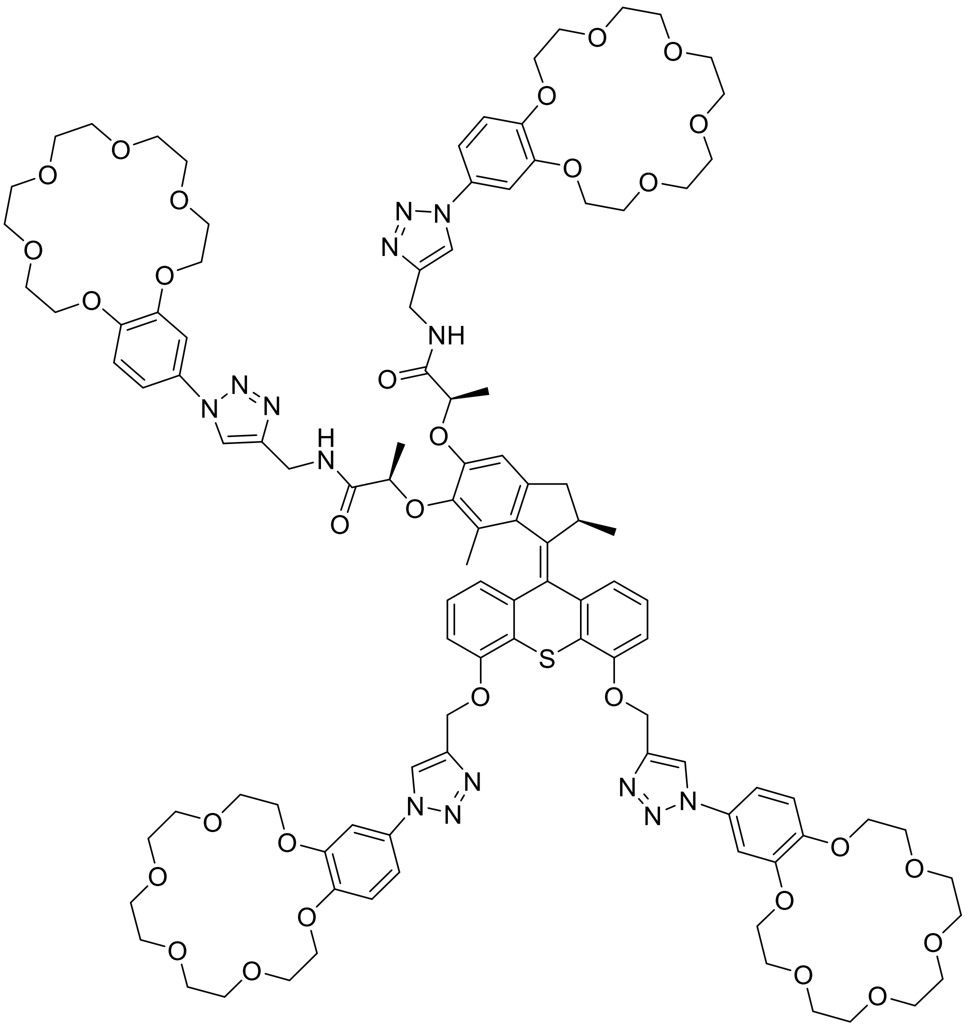

24

To a solution of tetra-alkyne motor **22** (23.0 mg, 0.03 mmol) and azide crown ether **23** (58.2, 0.17 mmol) in DMF (1 mL), was then added $Cu(CH_3CN)_4PF_6$ (2.5 mg, 6.6 μmol). The reaction was heated in a Microwave oven at 50 °C (35 bars) for 2 hours. After evaporation of the solvents, the crude product was washed by EDTA solution (5 mL) and extracted with dichloromethane (20 mL). The organic phase was dried over anhydrous Na_2SO_4 and then evaporated under vacuum. The crude product was first purified through a reverse-phase column (C_{18}, MeOH : H_2O = 60 : 40) and finally by reverse HPLC to give compound **24** (54 mg, 36% yield) as a slightly yellow solid.

^{1}H NMR ($CDCl_3$, 400 MHz, 298 K): δ (ppm) = 8.09 (s, 1H), 8.07 (s, 1H), 7.94 (s , 1H), 7.85 (s, 1H), 7.75 (t, *J* = 5.3 Hz, 1H), 7.64 (t, *J* = 5.8 Hz, 1H), 7.34-7.27 (m, 5H), 7.13-6.97 (m, 7H), 6.93-6.86 (m, 5H), 6.68 (d, *J* = 7.6 Hz, 4H), 5.45-5.30 (m, 4H), 4.75-4.60 (m, 4H), 4.26-4.05 (m, 17H), 4.15-4.07 (m, 4H), 3.95-3.86 (m, 16H), 3.78-3.66 (m,48H), 3.70-3.69 (m, 16H), 3.21 (dd, J_1 = 6.0 Hz, J_2 = 15.2 Hz, 1H), 2.31(dd, J_1 = 6.4 Hz, J_2 = 15.3 Hz, 1H), 1.50(d, J= 6.4 Hz, 3H), 1.30 (d, J = 6.8 Hz, 3H), 1.10 (s, 3H), 0.60 (d, J = 6.7 Hz, 3H);

^{13}C NMR (CDCl$_3$, 126 MHz, 298 K): δ (ppm) = 173.15, 172.47, 155.19, 154.80, 149.66, 149.54, 149.35, 149.22, 145.97, 145.45, 144.79, 144.63, 143.24, 142.70, 141.88, 138.42, 133.57, 127.83, 127.42, 126.91, 125.18, 124.67, 121.31, 121.30, 120.89, 120.76, 120.43, 113.69, 113.63, 112.84, 112.75, 112.69, 112.56, 110.74, 110.22, 108.28, 106.77, 78.32, 75.96, 63.48, 39.48, 38.15, 34.94, 34.58, 29.72, 18.99, 18.80, 18.76, 14.81;

ESI-MS: calculated for $C_{106}H_{130}N_{14}O_{30}S$ $[M+Na^+]^+$ 2133.869, Found: 2133.921.

Compound 25

ethyl 2-{[(2R)-3-[4,5-bis(2-ethoxy-2-oxoethoxy)-9H-thioxanthen-9-ylidene]-6-[(1-ethoxy-1-oxopropan-2-yl)oxy]-2,4-dimethyl-2,3-dihydro-1H-inden-5-yl]ox

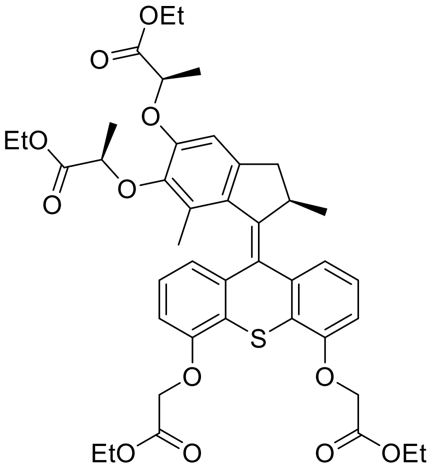

25

To a solution of free-phenol motor **(*R*)-A14** [65] (150 mg, 248 mmol) and ethyl bromoacetate (124.3 mg, 82.5 µL, 0.7442 mmol) in anhydrous DMF (5 mL) was added anhydrous K_2CO_3 (102.8 mg, 0.7442 mmol). The reaction was stirred at room temperature overnight. After evaporating the solvent, the crude product was purified through cholumn chromatography (SiO_2, n-hexane / EtOAc = 50/1-> 10/1) to give compound **25** (180 mg, 93 % yield) as a yellow solid.

^{1}H NMR (CDCl$_3$, 400 MHz, 298K): δ (ppm) = 7.34 (d, J = 7.7 Hz, 1H), 7.19 (dd, J = 8.0, 8.0 Hz, 1H), 6.96 (dd, J = 7.9, 7.9 Hz, 1H), 6.70 (dd, J = 7.7, 1.0 Hz, 1H), 6.65 (dd, J = 8.1, 0.7 Hz, 1H), 6.60 (dd, J = 8.2, 1.0 Hz, 2H), 6.56 (s, 1H), 4.80-4.67 (m, 5H), 4.49 (q, J = 6.8 Hz, 1H), 4.28-4.13 (m, 8H), 3.31 (dd, J = 14.9, 6.2 Hz, 1H), 2.33 (d, J = 15.0 Hz, 2H), 1.60 (d, J = 6.8 Hz, 3H), 1.49 (d, J = 6.8 Hz, 3H), 1.30-1.23 (m, 16H), 1.18 (s, 3H), 0.61 (d, J = 6.8 Hz, 3H);

^{13}C NMR (CDCl$_3$, 100 MHz, 298K): δ (ppm) = δ 172.49, 172.14, 169.00, 168.89, 155.27, 154.89, 150.37, 146.34, 144.93, 142.43, 142.20, 138.70, 133.25, 131.09, 127.45, 127.01, 126.58, 125.39,125.10, 121.77, 121.24, 109.85, 109.50, 108.28, 72.99, 66.68, 61.41, 61.27, 39.64, 38.25, 19.07, 18.87, 18.57, 14.67, 14.32, 14.24;

ESI-MS: calculated for $C_{42}H_{49}N_3O_{12}S$ $[M+H]^+$ 777.29, Found: 777.78.

Compound 26

2-{[(2R)-3-[4,5-bis(carboxymethoxy)-9H-thioxanthen-9-ylidene]-6-(1-carboxyethoxy)-2,4-dimethyl-2,3-dihydro-1H-inden-5-yl]oxy}propanoic acid

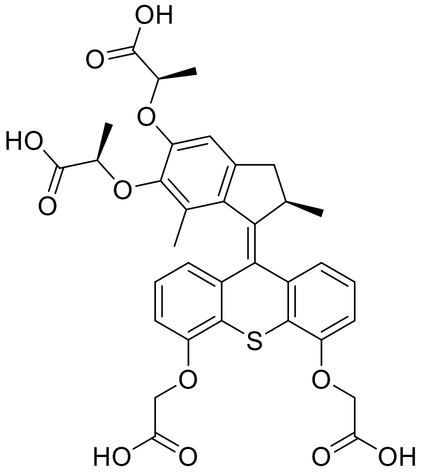

26

To a solution of compound **25** (100 mg) in THF / MeOH (3 mL / 3mL) was added a NaOH (52 mg, 1.287 mmol) solution (in 2 mL H_2O). The mixture was stirred at room temperature for 3h and then quenched by 1 M HCl (1 mL) at 0 °C. The mixture was then washed with dichloromethane (3 × 15 mL). The combined organic phase was dried over Na_2SO_4, concentrated in vacuum and further purified by flash column chromatography (silica gel, CH_2Cl_2 -> CH_2Cl_2:MeOH = 100:1->20:1) affording compound **26** (78 mg, 91% yield) as a green solid.

^{1}H NMR (CD_3OD, 400 MHz, 298 K): δ (ppm) = 7.41 (d, J = 7.6 Hz, 1H), 7.28 (dd, $J_1 = J_2$ 8.0 Hz, 1H), 7.01 (dd, $J_1 = J_2$ = 8.0 Hz, 1H), 6.81 (dd, J_1 = 8.1 Hz, J_2 = 0.7 Hz, 1H), 6.76 (dd, J_1 = 8.2, J_2 = 1.0 Hz, 1H), 6.71 (s, 1H), 6.66 (dd, J_1 = 7.7 Hz, J_2 = 1.0 Hz, 1H), 4.80 (d, J = 4.2 Hz, 2H), 4.78 (s, 2H), 4.50 (q, J = 6.8 Hz, 1H), 4.17 - 4.10 (m, 1H), 3.39 (dd, J_1 = 14.8 Hz, J_2 = 6.2 Hz, 1H), 2.40 (d, J = 15.2 Hz, 1H), 1.62 (d, J = 6.8 Hz, 3H), 1.48 (d, J = 6.8 Hz, 3H), 1.18 (s, 3H), 0.64 (d, J = 6.7 Hz, 3H).

^{13}C NMR (CD_3OD, 100 MHz, 298 K): δ (ppm) = 174.9, 174.3, 171.1, 170.9, 155.4, 154.8, 150.2, 146.0, 144.2, 142.5, 142.1, 138.4, 132.9, 130.6, 127.7, 126.5, 125.1, 124.7, 124.2, 123.7, 121.0, 120.4, 109.3, 109.1, 108.0, 77.1, 72.9, 65.5, 39.0, 37.9, 35.6, 35.3, 34.0, 29.3, 28.5, 17.8, 17.6, 17.4, 13.8.

ESI-MS: calculated for $C_{34}H_{32}O_{12}S$ $[M+H^{+}]^{+}$ 665.1693, Found: 665.63.

Compound 27

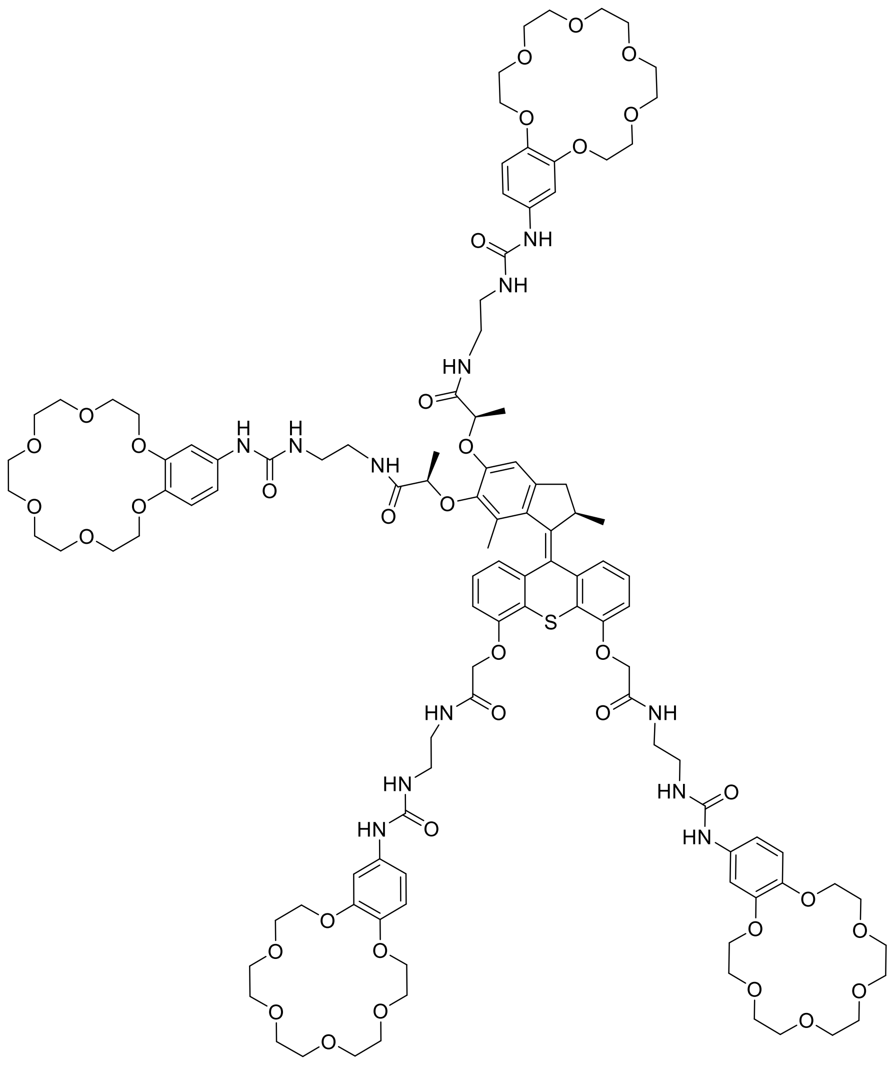

27

To a solution of compound **26** (32.9 mg, 79.5 μmol) and compound **5** (2.0 mg, 36.1 μmol) in DMF (2 mL), was added HOBt (19.5 mg, 144.5 μmol) and EDC (27.7 mg, 144.5 μmol). The reaction mixture was heated in the microwave oven (Power 200W, 50 °C) for 1 hour. After removal of DMF under reduced pressure, the crude residue was dissolved with dichloromethane (20 mL), the organic phase was extracted with H_2O (20 mL) and the aqueous phase was further washed twice with dichloromethane (2 × 20 mL). The combined organic phase was dried over anhydrous Na_2SO_4 and concentrated under reduced pressure. Further purification by reverse-phase HPLC provided compound **27** (14.0 mg, 27 %) as a yellow solid.

^{1}H NMR (CD_3OD, 400 MHz, 298 K): δ (ppm) = 7.36 -7.27 (m, 2H), 7.09 (d, *J* = 6.1 Hz, 2H), 7.04 (m, 2H), 6.87 - 6.77 (m, 12H), 6.76 - 6.66 (m, 12H), 6.54 (d, *J* = 7.6 Hz, 1H), 4.87- 4.57 (m, 6H), 4.11 - 3.95 (m, 18H), 3.85 - 3.72 (m, 18H), 3.71 - 3.57 (m, 50H), 3.50 - 3.32 (m, 10H), 3.21 (d, *J* = 7.2 Hz, 1H), 2.36 (d, *J* = 15.4 Hz, 1H), 1.52 (d, *J* = 6.6 Hz, 3H), 1.35 (d, *J* = 6.8 Hz, 3H), 1.14 (s, 3H), 0.57 (d, *J* = 6.8 Hz, 3H).

ESI-MS: calculated for $C_{110}H_{148}N_{12}O_{36}S$ $[M+Na^+]^+$ 2267.9711, Found: 2267.934.

Compound 28

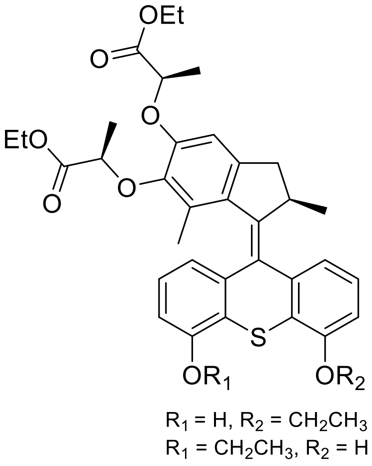

28

To a solution of free phenol motor ***(R)*-A14** [65] (50 mg, 0.08 mmol) and ethyl bromide (3.1 μL, 0.04 mmol) in DMF (10 mL) was added anhydrous K_2CO_3 (34 mg, 0.25 mmol). The reaction mixture was stirred overnight at 80°C. After this time, the reaction mixture was filtered and the collected residue was washed with dichloromethane (20 mL). After concentration under reduced pressure, water (200 mL) was added to the crude product and the mixture was extracted with dichloromethane 3 times (3 × 20 mL). The combined organic phase was washed with brine (50 mL) and subsequently dried over anhydrous Na_2SO_4 and then concentrated under reduced pressure. Further purification of the crude residue by column chromatography (SiO_2, cyclohexane / EtOAc: 40:1→8:1) provided the mono-substituted compound **28** (24 mg, 46%) as a yellow liquid. The mono-substituted compound was a mixture and the properties are similar to each other. Therefore, the mixture was used for the next step directly.

ESI-MS : m/z calculated for $C_{36}H_{40}O_8S$ $[M+H]^+$ 633.25; found: 633.25.

Compound 29

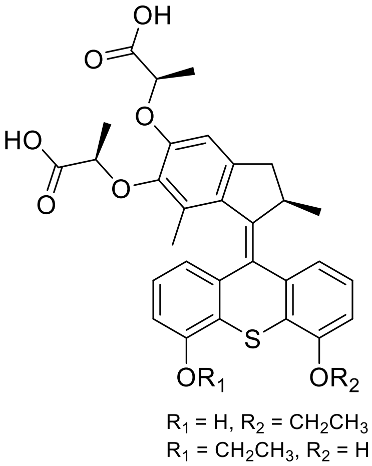

29

To a solution of compound **28** (24 mg, 37.93 µmmol) in a 1:1 mixture of THF and methanol (3 mL / 3 mL) was added a NaOH solution (40 mg in 2 mL of deionized water). The reaction mixture was stirred at room temperature for three hours and then quenched with 1 M HCl (1 mL) at 0°C. The mixture was extracted twice with dichloromethane (2 × 20 mL), the combined organic phase was dried over anhydrous Na_2SO_4 and then concentrated under reduced pressure, providing compound **29** (19 mg, 87%) as a light green solid, which was pure enough to be used as such in the next step. Same as the last step, the mono-substituted compound was a mixture and the properties are similar to each other, the mixture was used for the next step directly.

ESI-MS: m/z calculated for $C_{32}H_{32}O_8S$ $[M+Na]^+$ 577.19; found: 577.21.

Compound 30

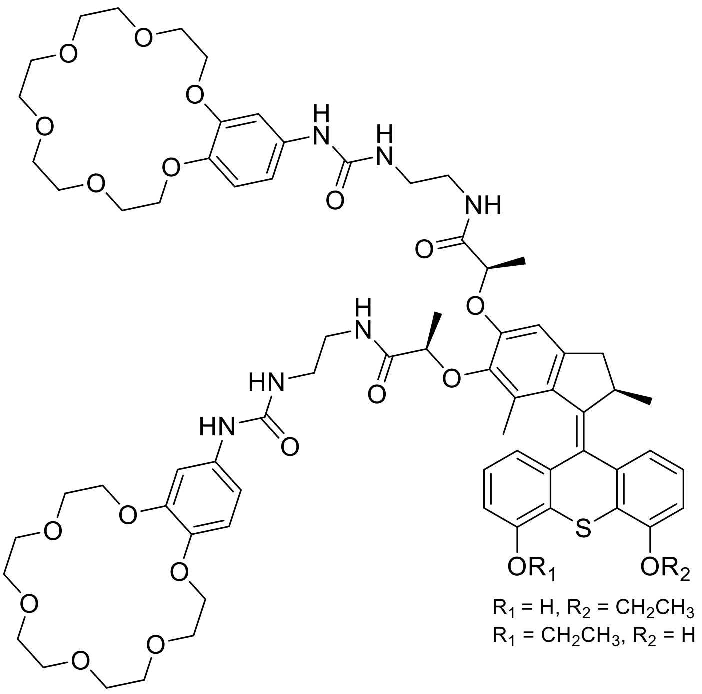

30

To a solution of compound **29** (19 mg, 32.95 µmol) and compound **5** (30.0 mg, 72.5 µmol) in DMF (1 mL) was added successively Hydroxybenzotriazole (HOBt) (17.8 mg, 0.14 mmol) and 1-Ethyl-3-(3-dimethyl aminopropyl) carbodiimide (EDC) (25.3 mg, 0.14 mmol). The reaction mixture was heated in the microwave oven (Power 200W, 50 °C) for 1 hour. After removal of DMF under reduced pressure, the crude residue was dissolved with dichloromethane (20 mL), the organic phase was extracted with H_2O (20 mL) and the aqueous phase was further washed twice with dichloromethane (2 × 20 mL). The combined organic phase was dried over anhydrous Na_2SO_4 and concentrated under reduced pressure. Further purification by reverse-phase column provided the mono-substituted compound **30** (21 mg, 47 %) as a yellow solid.

^{1}H NMR (400 MHz, MeOD, 298 K): δ (ppm) = 7.31 – 7.22 (m, 2H), 7.17 (d, *J* = 1.9 Hz, 2H), 6.87 (ddd, *J* = 13.0, 7.0, 4.0 Hz, 3H), 6.81 (dd, *J* = 8.7, 2.3 Hz, 1H), 6.76 (dd, *J* = 8.3, 2.7 Hz, 2H), 6.73 (d, *J* = 7.7 Hz, 1H), 6.63 (dd, *J* = 8.0, 1.2 Hz, 1H), 6.42 (dd, *J* = 7.6, 1.2 Hz, 1H), 4.76 (q, *J* = 6.6 Hz, 1H), 4.45 (q, *J* = 6.7 Hz, 1H), 4.28 – 4.07 (m, 10H), 4.05 (dd, *J* = 7.8, 3.6 Hz, 2H), 3.85 (dd, *J* = 8.6, 5.7 Hz, 6H), 3.78 – 3.58 (m, 28H), 3.37 (ddd, *J* = 7.3, 5.6, 4.4 Hz, 6H), 3.02 – 3.00 (m, 1H), 2.88 (d, *J* = 0.7 Hz, 1H), 2.37 (d, *J* = 15.2 Hz, 1H), 1.52 (t, *J* = 6.8 Hz, 6H), 1.37 (d, *J* = 6.8 Hz, 3H), 1.22 (s, 3H), 0.60 (d, *J* = 6.7 Hz, 3H);

ESI-MS: m/z calculated for $C_{70}H_{90}N_6O_{20}SNa$ $[M+H]^+$ 1367.60; found: 1367.98.

Compound 31

11-Bromoundecyltrimethoxysilane

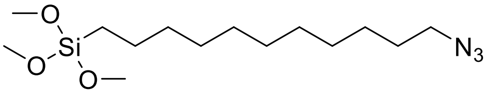

31

(11-bromooctyl) trimethoxysilane (2.5 g, 7.035 mmol) was mixed with sodium azide (549 mg, 8.441 mmol) in dry DMF (20 mL). The mixture was stirred at 50°C overnight. The reaction was then quenched with water (30 mL) and extracted with ether (3×50 mL). The organic layer was then washed again with water (50 mL), dried by sodium sulfate, and concentrated under vacuum to afford compound **31** (2.1g, 6.612 mmol, 94%) as a yellow oil.

^{1}H NMR ($CDCl_3$, 400 MHz, 298 K): δ (ppm) = 3.56 (s, 9H), 3.24 (d, *J* = 7.0 Hz, 2H), 1.58 (tt, *J* = 7.8 Hz, 2H), 1.44 - 1.23 (m, 16H), 0.66 - 0.61 (m, 2H).

Compound 32

PEG bis-alkyne

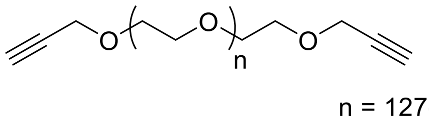

32

α,ω-dihydroxy-poly(ethylene glycol) (4.0 g, 0.71 mmol, Mw: 6086, Mn: 5569, Pol: 1.09) was dissolved in dry tetrahydrofuran (40 mL) at 40 °C during 30 min. After complete dissolution, the system was purged with three freeze-thaw cycles. NaH (68.0 mg, 2.86 mmol) was added carefully until the disappearance of hydrogen bubbles in the reactive media. The system was purged again with three freeze-thaw cycles. After 1 h of stirring, propargyl bromide (0.25 mL, 2.86 mmol) was added dropwise. The mixture was stirred at 40 °C for 12 h under argon. Then the mixture was diluted with dichloromethane (30 mL) and washed with a saturated solution of NaCl (10 mL) and water (10 mL). The organic phases were dried over sodium sulfate, the solvents were removed until the formation of a yellow viscous liquid. The viscous liquid was poured in cold diethyl ether (100 mL). After filtration, the white solid was dried under vacuum affording compound **32** (3.83 g, 0.63 mmol, 86 %).

^{1}H NMR (toluene-d_8, 400 MHz, 298 K): δ(ppm) = 3.93 (d, *J* = 2.7 Hz, 4H), 3.74-3.33 (m, (n+1)*4H).

Compound 33

ethyl (2S)-2-{[(2S)-1-[4,5-bis({2-[2-(2-azidoethoxy)ethoxy]ethoxy})-9H-thioxanthen-9-ylidene]-6-{[(2R)-1-ethoxy-1-oxopropan-2-yl]oxy}-2,7-dimethyl-2,3

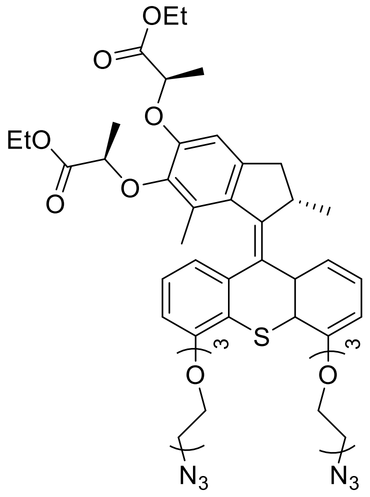

33

Potassium carbonate (10.9 mg, 0.079 mmol) and 2-(2-(2-azidoethoxy)ethoxy)ethyl-4-toluenesulfonate (26.0 mg, 0.079 mmol) were added to a solution of free phenol motor **(*S*)-A14** [65] (15.9 mg, 0.026 mmol) dissolved in DMF (1.6 mL) at room temperature and the reaction mixture was subsequently heated to 45 °C for 16 h. The mixture was cooled to room temperature and diluted with dichloromethane (5 mL) and water (5 mL), and further extracted with dichloromethane (3 × 5 mL). The organic phase was dried over Na_2SO_4 and solvent was removed under vacuum. The crude residue was purified by column chromatography (SiO_2; cyclohexane/EtOAc = 2/1 → 1/1) to yield compound **33** (21 mg, 87%) as a sticky yellow solid.

^{1}H NMR ($CDCl_3$, 400 MHz, 298 K): δ (ppm) = 7.32 (d, *J* = 7.6 Hz, 1H), 7.21 (dd, *J* = 7.9, 7.9 Hz, 1H), 6.94 (dd, *J* = 7.9, 7.9 Hz, 1H), 6.76 (d, *J* = 8.1 Hz, 1H), 6.69 (d, *J* = 8.2 Hz, 1H), 6.64 (d, *J* = 7.6 Hz, 1H), 6.54 (s, 1H), 4.83 - 4.72 (m, 2H), 4.34 - 4.06 (m, 9H), 4.00 - 3.93 (m, 4H), 3.87 - 3.82 (m, 4H), 3.76 - 3.66 (m, 8H), 3.38 (brt, *J* = 4.9 Hz, 4H), 3.37 - 3.32 (m, 1H), 2.33 (d, *J* = 14.9 Hz, 1H), 1.63 (d, *J* = 6.7 Hz, 3H), 1.48 (d, *J* = 6.7 Hz, 3H), 1.29 - 1.18 (m, 9H), 0.64 (d, *J* = 6.6 Hz, 3H);

^{13}C NMR ($CDCl_3$, 101 MHz, 298 K): δ (ppm) = 172.66, 172.12, 155.94, 155.50, 149.78, 146.10, 144.59, 142.08, 141.95, 138.42, 133.48, 131.11, 127.77, 126.93, 126.59, 125.02, 124.72, 121.05, 120.46, 109.62, 109.18, 108.16, 73.06, 71.34 (2C), 70.96, 70.94, 70.21 (2C), 69.90, 69.85, 68.96, 68.92, 61.36, 60.82, 50.88 (2C), 39.63, 38.25, 27.06, 19.10, 18.72, 18.55, 14.64, 14.24, 14.20;

ESI-MS: m/z calculated for $C_{46}H_{58}N_6O_{12}S$ $[M]^+$: 917.375, found 917.375.

Compound 34

(2R)-2-{[(2R)-3-[4,5-bis({2-[2-(2-azidoethoxy)ethoxy]ethoxy})-9H-thioxanthen-9-ylidene]-6-[(1R)-1-carboxyethoxy]-2,4-dimethyl-2,3-dihydro-1H-inden-5-y

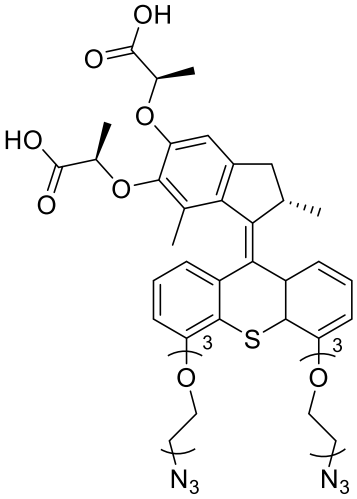

34

Motor compound **33** (20.5 mg, 0.022 mmol) was dissolved in a THF/MeOH/H_2O mixture (1/1/1, 2 mL) along with sodium hydroxide (4.5 mg, 0.11 mmol) and the reaction mixture was stirred at 40 °C for 16 h. The mixture was cooled to room temperature, acidified (1 mL, 2M HCl), and extracted with dichloromethane (5 × 10 mL). The combined organic phase was then dried over Na_2SO_4, and evaporated under vacuum to yield compound **34** (18.6 mg, 97%) as a pale green solid. The crude compound was used without further purification in the next synthetic step.

^{1}H NMR ($CDCl_3$, 400 MHz, 298 K): δ (ppm) = 7.34 (d, *J* = 7.8 Hz, 1H), 7.23 (dd, *J* = 8.0, 8.0 Hz, 1H), 6.96 (dd, *J* = 8.0, 8.0 Hz, 1H), 6.78 (d, *J* = 7.7 Hz, 1H), 6.72 (dd, *J* = 7.5, 1.0 Hz, 1H), 6.69 (s, 1H), 6.65 (dd, *J* = 7.5, 1.0 Hz, 1H), 4.89–4.78 (m, 1H), 4.44–4.34 (m, 1H), 4.34–4.25 (m, 2H), 4.25–4.08 (m, 3H), 4.03–3.90 (m, 4H), 3.89–3.79 (m, 4H), 3.78–3.67 (m, 9H), 3.63 (s, 1H), 3.38 (t, *J* = 5.5 Hz, 3H), 3.35–3.30 (m, 1H), 2.39 (d, *J* = 15.8 Hz, 1H), 1.65 (d, *J* = 7.0 Hz, 3H), 1.43 (d, *J* = 7.0 Hz, 3H), 1.25 (s, 3H), 0.64 (d, *J* = 6.7 Hz, 3H).

^{13}C NMR ($CDCl_3$, 101 MHz, 298 K): δ (ppm) = 175.49, 175.34, 156.20, 155.49, 145.51, 145.38, 143.15, 141.52, 137.89, 131.13, 130.88, 128.65, 126.76, 126.66, 125.23, 124.45, 121.04, 120.27, 110.51, 109.76, 109.37, 71.33 (2C), 70.95, 70.92, 70.23 (2C), 69.88, 69.05, 68.91, 50.87 (2C), 39.71, 38.18, 32.07, 29.84, 19.01, 18.48, 18.21, 15.19, 14.26.

ESI-MS: m/z calculated for $C_{42}H_{50}N_6O_{12}S$ $[M+Na^+]^+$: 885.310, found: 885.312.

Compound 35

(2R)-N-{2-[2-(2-azidoethoxy)ethoxy]ethyl}-2-{[(2R)-6-[(1R)-1-({2-[2-(2-azidoethoxy)ethoxy]ethyl}carbamoyl)ethoxy]-3-[4,5-bis({2-[2-(2-azidoethoxy)etho

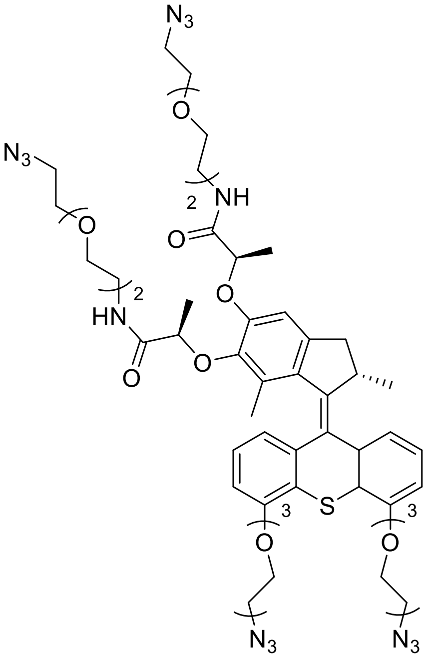

35

To a solution of compound **34** (60 mg, 0.07 mmol) and 2-[2-(2-azido-ethoxy)-ethoxyl]-ethylamine (28 mg, 0.16 mmol) in DMF (5 mL) was added EDC.HCl (80 mg, 0.42 mmol) and HOBt (56.4 mg, 0.42 mmol). The reaction was stirred at room temperature for 12 hours. After removal of DMF under reduced pressure, the crude residue was dissolved with dichloromethane (20 mL), the organic phase was extracted with H_2O (20 mL) and the aqueous phase was further washed twice with dichloromethane (2 × 20 mL). The combined organic phase was dried over anhydrous Na_2SO_4 and concentrated under reduced pressure. Further purification by flash column chromatography (SiO_2, MeOH : CH_2Cl_2 = 100:1 -> 50:1 -> 20:1-> 10:1) provided compound **35** (68.0 mg, 83%) as a yellow solid.

^{1}H NMR ($CDCl_3$, 400 MHz,): δ (ppm) = 7.46 (brt, J = 5.2 Hz, 1H), 7.33 (d, J = 7.8 Hz, 1H), 7.22 (dd, J = 7.9, 7.9 Hz, 1H), 6.98 (d, J = 5.8 Hz, 1H), 6.93 (dd, J_1 = 8.0 Hz, J_2 = 8.0 Hz, 1H), 6.77 (d, J = 8.1 Hz, 1H), 6.71 (d, J = 8.2 Hz, 1H), 6.66 (d, J = 8.0 Hz, 2H), 4.65 (q, J = 6.7 Hz, 1H), 4.45 (q, J = 6.8 Hz, 1H), 4.32 - 4.26 (m, 2H), 4.22 - 4.09 (m, 3H), 4.00-3.91 (m, 4H), 3.71-3.63 (m, 8H), 3.60-3.25 (m, 29H), 2.36 (d, J = 15.2 Hz, 1H), 1.57 (d, J = 6.7 Hz, 3H), 1.28 (d,

J = 6.8 Hz, 3H), 1.13 (s, 3H), 0.61(d, J = 6.7 Hz, 3H);

^{13}C NMR (CDCl$_3$, 101 MHz, 298 K): δ (ppm) = 172.42, 171.96, 155.98, 155.31, 149.73, 145.40, 143.45, 142.89, 141.50, 137.79, 134.17, 130.94, 128.30, 126.71, 126.65, 124.84, 124.22, 120.90, 120.14, 109.52, 109.09, 78.86, 77.30, 76.15, 71.18, 70.80, 70.76, 70.55, 70.46, 70.28, 70.21, 70.09, 70.02, 69.96, 69.84, 69.81, 69.74, 68.85, 68.70, 50.70, 50.55, 39.63, 38.84, 38.79, 38.01, 19.09, 18.93, 18.19, 15.23;

ESI-MS: m/z calculated for $C_{54}H_{75}N_{14}O_{14}S$ [M+H$^+$]$^+$:1175.53, found: 1175.48.

Compound 36

2,3-Dibromo-5-methylthiophene.

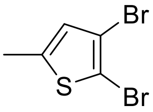

36

A solution of *N*-bromosuccinimide (1.00 g, 5.65 mmol) in DMF (8 mL) was added dropwise to 4-bromo-2-methyl thiophene (0.63 mL, 5.65 mmol) in DMF (10 mL) and stirred overnight at room temperature. Saturated aq. $NaHCO_3$ (20 mL) was added to the mixture slowly and stirred for an additional 1h. The reaction mixture was extracted with hexanes (3 × 30 mL), and the organic phase was washed with H_2O (3 × 30 mL), brine (30 mL), and dried over Na_2SO_4. Removal of the solvent under vacuum yielded compound **36** (1.3 g, 90%) as a colorless oil.

Analyses were in agreement with the literature.[89]

^{1}H NMR (CDCl$_3$, 400 MHz, 298 K): δ (ppm) = 6.62 (s, 1H), 2.44 (s, 3H).

^{13}C NMR (CDCl$_3$, 101 MHz, 298 K): δ (ppm) = 141.31, 127.97, 112.96, 107.47, 15.75.

ESI-MS : m/z calculated for $C_5H_4Br_2S$ [M+H$^+$]$^+$: 256.85, found: 256.88.

Compound 37

(2E,2'E)-diisobutyl-3,3'-(5-methylthiophene-2,3-diyl)diacrylate

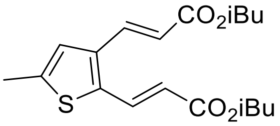

37

Compound **36** (8.0 g, 31.26 mmol), triethylamine (34.69 mL, 249.6 mmol) and isobutyl acrylate (11.27mL, 78.08 mmol) were added to a stirring solution of Pd(OAc)$_2$ (359 mg, 1.6 mmol) and tri(cyclohexyl)phosphine (876 mg, 3.12 mmol) in dry DMF (50 mL) under Argon at room temperature. The reaction mixture was then heated to 110 °C for 4 days until disappearance of the mono-substituted product. The reaction mixture was cooled to room temperature, poured into water (100 mL) and extracted with dichloromethane (3 × 100 mL). The organic layer was washed with water (3 × 100 mL), brine (100 mL), dried over Na$_2$SO$_4$ and the solvent was removed under reduced pressure. The crude product was then purified using column chromatography (SiO$_2$; cyclohexane/ethyl acetate = 200/1→ 50/1) to yield pure diacrylate compound **37** (6.68 g, 61%) as light yellow oil.

Analyses were in agreement with the literature.[89]

R$_f$ = 0.41 (cyclohexane /ethyl acetate = 50/1).

^{1}H NMR ((CD$_3$)$_2$CO, 400 MHz, 298 K): δ (ppm) = 7.98 (d, J = 15.5 Hz, 1H), 7.82 (d, J = 15.7 Hz, 1H), 7.27 (s, 1H), 6.43 (d, J = 15.7 Hz, 1H), 6.19 (d, J = 15.5 Hz, 1H), 3.97 (d, J = 2.4 Hz, 2H), 3.96 (d, J = 2.4 Hz, 2H), 2.50 (d, J = 1.1 Hz, 3H), 1.99 (sept, J = 6.7 Hz, 1H), 1.98 (sept, J = 6.7 Hz, 1H), 0.98 (d, J = 0.8 Hz, 6H), 0.96 (d, J = 0.8 Hz, 6H).

^{13}C NMR ((CD$_3$)$_2$CO, 101 MHz, 298 K): δ = 166.17, 165.73, 143.35, 138.84, 137.84, 134.00, 133.21, 125.14, 120.19, 117.54, 70.19, 70.17, 27.74 (2C), 18.46(4C), 14.73.

ESI-MS: m/z calculated for $C_{19}H_{26}O_4S$ [M+H$^+$]$^+$: 351.16, found 351.37.

Compound 38

Diisobutyl 2-methylbenzo[b]thiophene-5,6-dicarboxylate

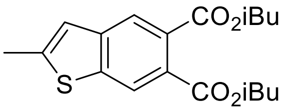

38

In a pressure tube purged with Argon, compound **37** (3.06 g, 8.73 mmol) in diphenyl ether (40 mL) was heated to 270 °C for 24 h. The reaction mixture was cooled to room temperature and 2,3-dichloro-5,6-dicyanobenzoquinone (DDQ) (1.92 g, 8.73 mmol) was added portion-wise to the flask which was subsequently heated to 50 °C for 6 h. The reaction was quenched by the slow addition of sat. aq. NaHCO$_3$ (20 mL) and stirred for an additional 30 min. The resulting mixture was extracted by dichloromethane (3 × 100 mL), the combined organic phase was washed with $NaHCO_3$ (2 × 100 mL), brine (100 mL) and dried over sodium sulfate. The solvent was removed under vacuum and the crude product was purified by column chromatography (SiO_2, cyclohexane /ethyl acetate = 200:1 → 50:1) to yield compound **38** (1.55 g, 51%) as a colorless oil.

Analyses were in agreement with the literature.[89]

R*f* = 0.18 (cyclohexane /ethyl acetate = 5/1)

^{1}H NMR ($CDCl_3$, 400 MHz, 298 K): δ (ppm) = 8.29 (s, 1H), 8.07 (s, 1H), 7.28 (s, 1H), 4.09 (d, *J* = 6.7 Hz, 2H), 4.07 (d, *J* = 6.7 Hz, 2H), 2.65 (d, J = 1.2 Hz, 3H), 2.05 (sept, *J* = 6.8 Hz, 1H), 2.06 (sept, *J* = 6.8 Hz, 1H), 1.01 (d, *J* = 6.7 Hz, 6H), 1.00 (d, *J* = 6.7 Hz, 6H).

^{13}C NMR ($CDCl_3$, 101 MHz, 298 K): δ (ppm) = 168.47, 167.75, 145.93, 142.00, 141.52, 129.13, 126.80, 123.43, 123.27, 121.95, 71.92, 71.90, 27.91, 27.88, 19.36 (2C), 19.35 (2C), 16.55.

ESI-MS: *m*/*z* calculated for $C_{19}H_{24}O_4S$ $[M+Na^+]^+$: 371.1288, found 371.17.

Compound 39

Diisobutyl 2-methyl-3-bromobenzo[b]thiophene-5,6-dicarboxylate

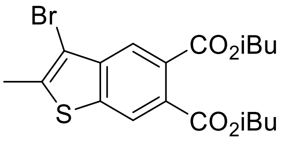

39

A solution of bromine (192 µL, 3.73 mmol) in chloroform (15 mL) was added dropwise to a solution of compound **38** (1.30 g, 3.73 mmol) in chloroform (20 mL) at 0 °C and the reaction was allowed to reach room temperature. After approximately 4 h the reaction mixture went from red to clear and was quenched with the dropwise addition of 10% $NaHCO_3$ (20 mL) at 0 °C. After stirring for 30 mins, the crude mixture was extracted with dichloromethane (3 × 100 mL), the combined organic phase was washed with water (100 mL), brine (100 mL) and dried over sodium sulfate. The solvent was removed under vacuum to yield a crude oil which was purified by column chromatography (SiO_2; cyclohexane/ethyl acetate = 6/4) to yield pure compound **39** (1.20 g, 75%) as a yellow oil.

Analyses were in agreement with the literature.[89]

R*f* = 0.32 (hexanes/ethyl acetate = 9/1)

^{1}H NMR ((CD$_3$)$_2$CO, 400 MHz, 298 K): δ (ppm) = 8.14 (s, 1H), 8.02 (s, 1H), 4.13 (d, *J* = 6.7 Hz, 2H), 4.11 (d, *J* = 6.7 Hz, 2H), 2.59 (s, 3H), 2.04 (sept, *J* = 6.7 Hz, 2H), 1.01 (d, *J* = 6.7 Hz, 6H), 1.00 (d, *J* = 6.7 Hz, 6H).

^{13}C NMR (CDCl$_3$, 101 MHz, 298 K): δ (ppm) = 167.94, 167.22, 140.03, 139.96, 138.92, 129.87, 128.08, 123.53, 123.29, 107.07, 71.98, 71.95, 27.78, 27.76, 19.22 (4C), 15.85.

ESI-MS: *m*/*z* calculated for $C_{19}H_{23}BrO_4S$ $[M+H^+]^+$: 427.08, found 427.19.

Compound 40

2-Methyl-3-bromobenzo[b]thiophene-5,6-dimethanol

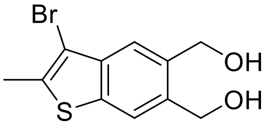

40

A solution of diisobutyl aluminum hydride (13.16 mL, 15.79 mmol, 1M in toluene) was added dropwise to a solution of compound **39** (1.50 g, 2.8 mmol) in dry dichloromethane (40 mL) at 0 °C and stirred for an additional 2 h at the same temperature. The reaction mixture was then quenched at 0 °C with the dropwise addition of sat. aq. rochelle salt (10 mL) which caused the formation of bubbling and salt and this mixture was stirred for 30 mins. The reaction mixture was then filtered and washed with ethyl acetate (3 × 100 mL). The organic layer was then washed with water (3 × 100 mL), brine (100 mL) and dried over anhydrous sodium sulfate. Removal of the solvent provided a crude white powder that was purified by column chromatography (SiO$_2$; cyclohexane/acetone: 8/2 → 7/3) to yield pure compound **40** (635 mg, 63%) as a white powder.

Analyses were in agreement with the literature.[89]

R$_f$ = 0.13 (hexanes/acetone = 8/2)

^{1}H NMR (DMSO, 400 MHz, 298 K): δ (ppm) = 7.88 (s, 1H), 7.69 (s, 1H), 5.40 – 5.27 (m, 2H), 4.63 (dd, J = 8.9, 5.5 Hz, 4H), 2.07 (s, 2H).

^{13}C NMR (DMSO, 400 MHz, 298 K): δ (ppm) = 137.89, 137.65, 136.83, 135.34, 135.23, 120.68, 120.08, 106.19, 60.68, 60.63, 15.58.

HRMS (ESI$^+$): *m*/*z* calculated for $C_{11}H_{11}BrO_2S$ $[M+H^+]^+$: 286.9741, found 286.88.

Compound 41

2-Methyl-3-bromo-5,6-dimethyloxy(tert-butyldimethylsilyl)benzo[b]thiophene

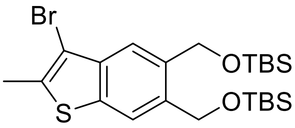

41

Tert-butyldimethylsilyl chloride (525 mg, 3.49 mmol) and imidazole (474 mg, 6.97 mmol) were added to a solution of compound **40** (400 mg, 1.39 mmol) in THF (10 mL) and the resulting mixture was heated to 30 °C for 2 h. The reaction mixture was cooled to room temperature, the precipitate was filtered and washed thoroughly with THF (3× 50 mL). Removal of the solvent and purification of the crude residue by column chromatography (SiO_2; cyclohexane/ethyl acetate = 99/1) provided pure compound **41** (410 mg, 57%) as a white powder.

Analyses were in agreement with the literature.[89]

R_f = 0.21 (hexanes/ethyl acetate = 98/2)

^{1}H NMR ($(CD_3)_2CO$, 400 MHz, 298 K): δ (ppm) = 7.93 (s, 1H), 7.84 (s, 1H), 4.98 (s, 2H), 4.95 (s, 2H), 2.55 (s, 3H), 0.99 (s, 9H), 0.96 (s, 9H), 0.16 (s, 6H), 0.15 (s, 6H).

^{1}H NMR ($CDCl_3$, 400 MHz, 298 K): δ (ppm) =7.79 (s, 1H), 7.75 (s, 1H), 4.86 (s, 2H), 4.84 (s, 2H), 2.55 (s, 3H), 0.96 (d, J = 5.2 Hz, 18H), 0.12 (s, 6H), 0.12 (s, 6H).

^{13}C NMR ($CDCl_3$, 101 MHz, 298 K): δ (ppm) = 137.34, 135.96, 135.87, 135.63, 134.76, 120.67, 119.84, 106.53, 63.10, 62.77, 25.98 (3C), 25.96 (3C), 18.43, 18.38, 15.51, -5.23(2C), -5.25(2C).

ESI-MS: *m*/*z* calculated for $C_{23}H_{39}BrO_2SSi_2$ $[M+H]^+$: 515.1465, found 515.15

Compound 42

2,2'-Dimethyl-3,3'-(perfluorocyclopentene-1,2-diyl)bis(2-methyl-5,6-dimethyloxy(tert-butyldimethylsilyl)benzo[b]thiophene))

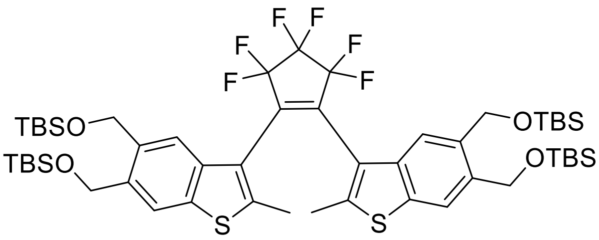

42

sec-BuLi (364 µL, 0.426 mmol, 1.4 M hexanes solution) was added dropwise to a solution of compound **41** (200 mg, 0.387 mmol) in THF (4 mL) at –78°C and the solution was stirred for 30 mins at this temperature. A solution of perfluorocyclopentene (430 µL, 0.194 mmol, 0.45 M in THF) was then added dropwise at -78 °C and the reaction mixture was stirred at this temperature for an additional 2 h. The reaction was quenched with the dropwise addition of dilute acidic ethanol (2 mL, < 1% HCl) at –78°C and was slowly warmed to room temperature. The crude mixture was diluted with water (20 mL), extracted with ethyl acetate (3 × 20 mL), the combined organic phase was washed with brine (30 mL) and dried over sodium sulfate. Removal of the solvent under vacuum left a crude yellow residue including compound **42**, which was carried on to the next step without further purification.

Compound 43

2,2'-Dimethyl-3,3'-(perfluorocyclopentene-1,2,-diyl)bis(2-methylbenzo[b]thiophene-5,6-dimethanol)

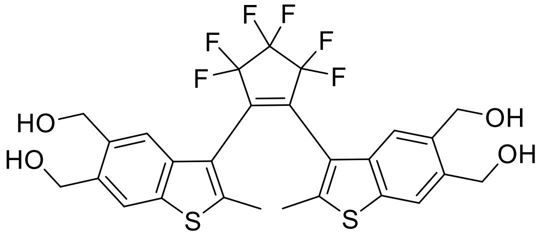

43

The crude residue from **42** was dissolved in 1% HCl–EtOH (10 mL) at room temperature with stirring, and after 2 h the solvent was removed under vacuum to leave a crude yellow residue. This residue was redissolved in ethyl acetate (50 mL) and the organic phase was washed with water (40 mL), brine (40 mL) and the solvent removed under vacuum. Purification of the crude residue by column chromatography (SiO_2; ethyl acetate) yielded pure dithienylethene switch **43** (19 mg, 34% yield over two steps) as a white powder consisting of a mixture of **43** conformers P and AP (Parallel and Antiparallel, respectively).

Analyses were in agreement with the literature.[89]

R_f = 0.26 (ethyl acetate)

^{1}H NMR (($(CD_3)_2CO$, 400 MHz, 298 K): δ (ppm) = 7.82 (s, $1H_P$), 7.81 (s, $2H_{AP}$), 7.75 (s, 3Hp), 4.80 (s, $2H_{AP}$), 4.74 (s, $2H_{AP}$), 4.71 (s, 4Hp), 4.67 (s, 4Hp), 2.59 (s, 6Hp), 2.47 (s, $3H_{AP}$).

ESI-MS: *m*/*z* calculated for $C_{27}H_{22}F_6O_4S_2$ $[M+H]^-$: 589.0936, found 589.17.

Compound 44

2,2′-Dimethyl-3,3′-(perfluorocyclopentene-1,2,-diyl)bis(2-methyl-5,6-dimethyloxy(14-azido-3,6,9,12-tetraoxatetradecan-1-oic ester)benzo[b]thiophene)

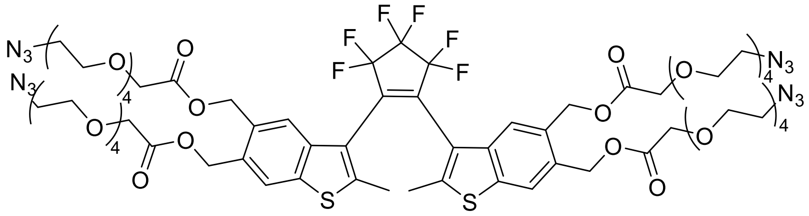

44

N′-Ethylcarbodiimide hydrochloride (EDC) (20.2 mg, 0.21 mmol), dimethyl aminopyridine (19.2 mg, 0.157 mmol) and *N*-hydroxybenzotriazole (HOBt) (7.1 mg, 0.05 mmol) were added to a mixture of compound **43** (14 mg, 2.4×10^{-2} mmol) and 14-azido-3,6,9,12-tetraoxatetradecan-1-oic acid (29 mg, 0.1 mmol) in dry DMF (1 mL) at 0 °C. The reaction mixture was allowed to reach room temperature and stirred for 16 h. The solvent was removed under vacuum and the crude residue purified by reverse phase preparative HPLC to yield pure tetraazide **44** (15 mg, 37%) as a colorless oil.

Analyses were in agreement with the literature.[89]

^{1}H NMR (CD_3CN, 400 MHz, 298 K): δ = 7.88 (s, $2H_{AP}$), 7.83 (s, $2H_{P}$), 7.66 (s, $4H_{P+AP}$), 5.34 (d, J = 10.8 Hz, $6H_{P+AP}$), 5.25 (d, J = 2.8 Hz, $4H_{P+AP}$), 5.14 (d, J = 10.8 Hz, $4H_{P}$), 4.21 – 4.11 (m, $16H_{P}$), 3.67 – 3.53 (m, $108H_{P+AP}$), 3.37 (d, J = 4.6 Hz, $16H_{P+AP}$), 2.52 (s, 6H), 2.40 (s, 6H).

ESI-MS: *m*/*z* calculated for $C_{67}H_{92}F_6N_{12}O_{25}S_2$ $[M+H_2O^+]^+$: 1642.56, found 1642.44.

Annexes

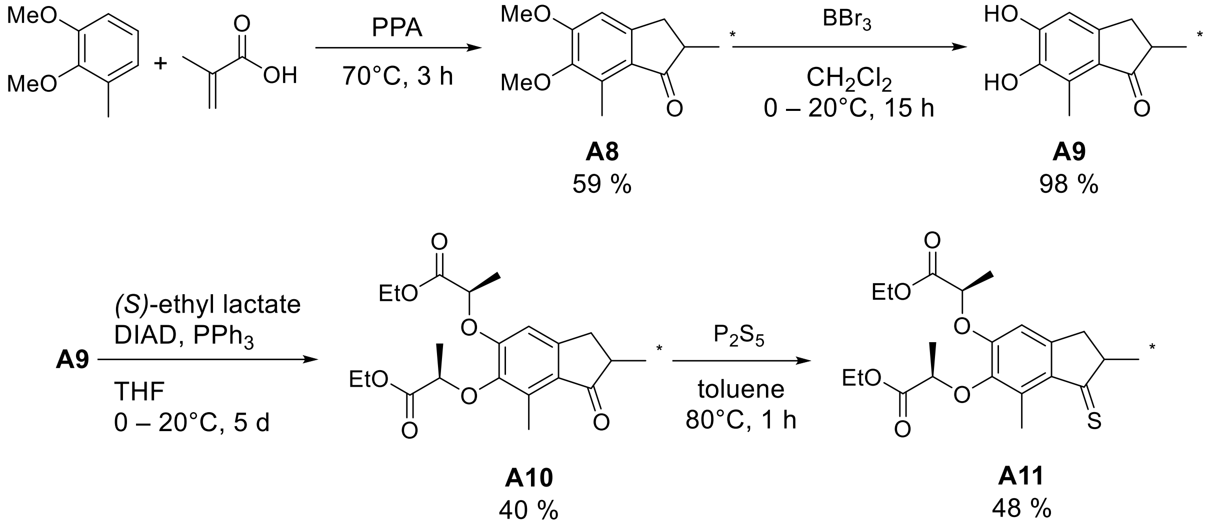

Figure A1. Synthesis of the rotor.[65]

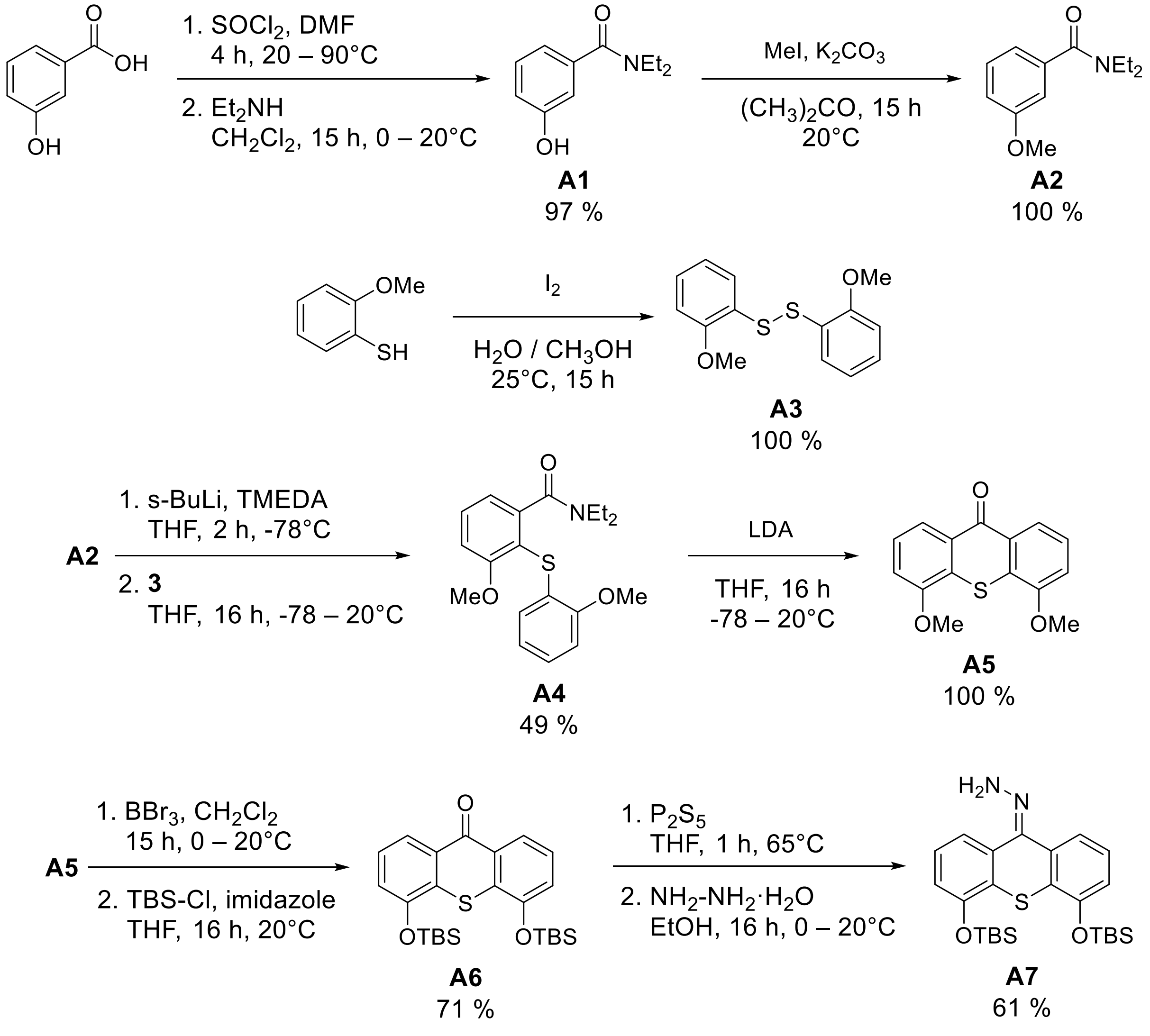

Figure A2. Synthesis of the stator.[65]

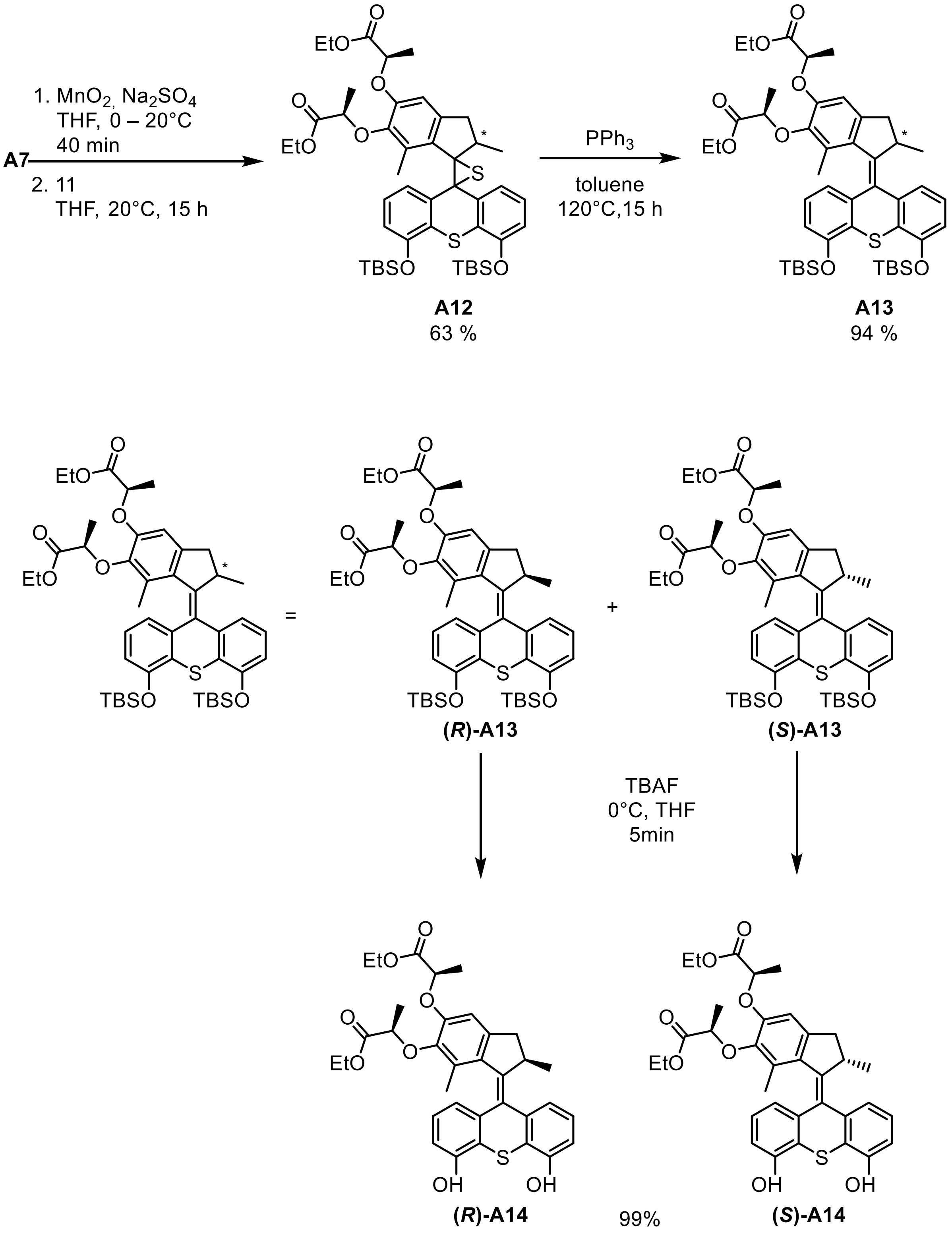

Figure A3. Synthesis of the motor through Barton-Kellogg reaction and deprotection of the stator part to produce the bis-phenol motor.[65]

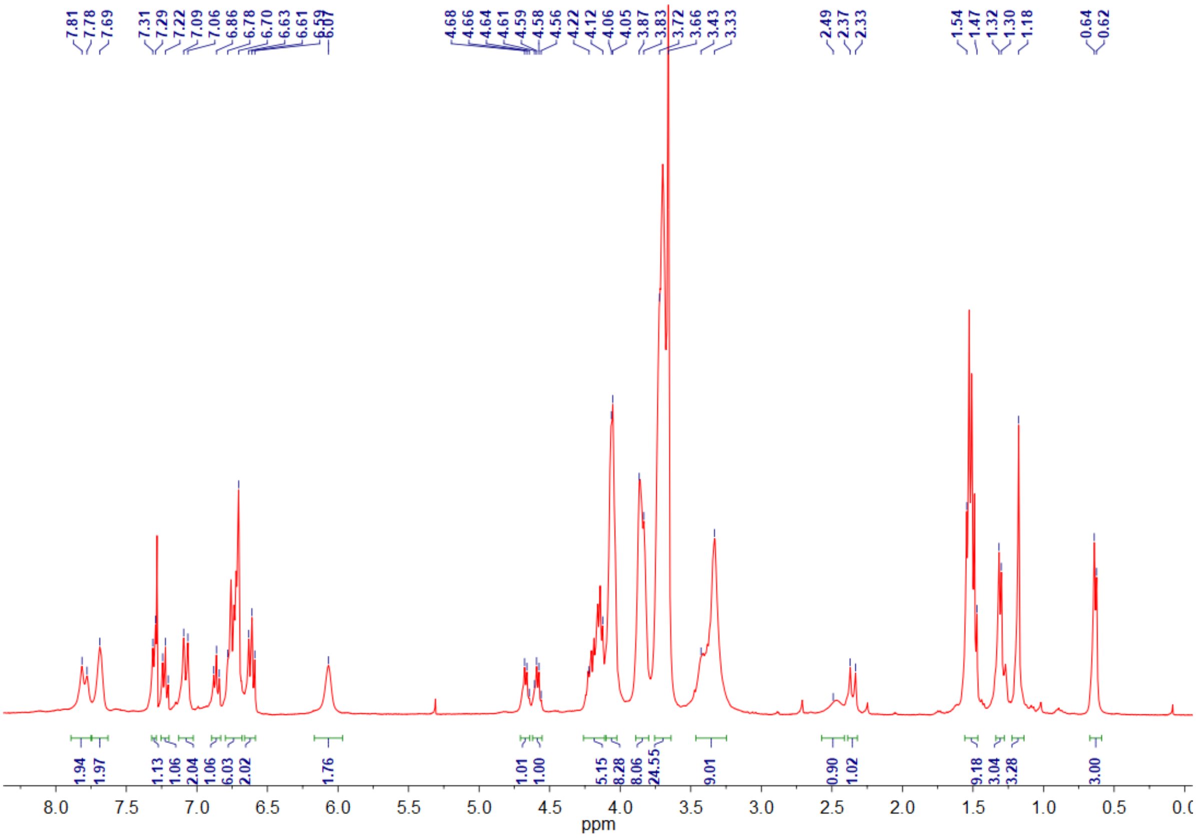

Figure A4. ^{1}H NMR in $CDCl_3$ of Compound **8 (A).**

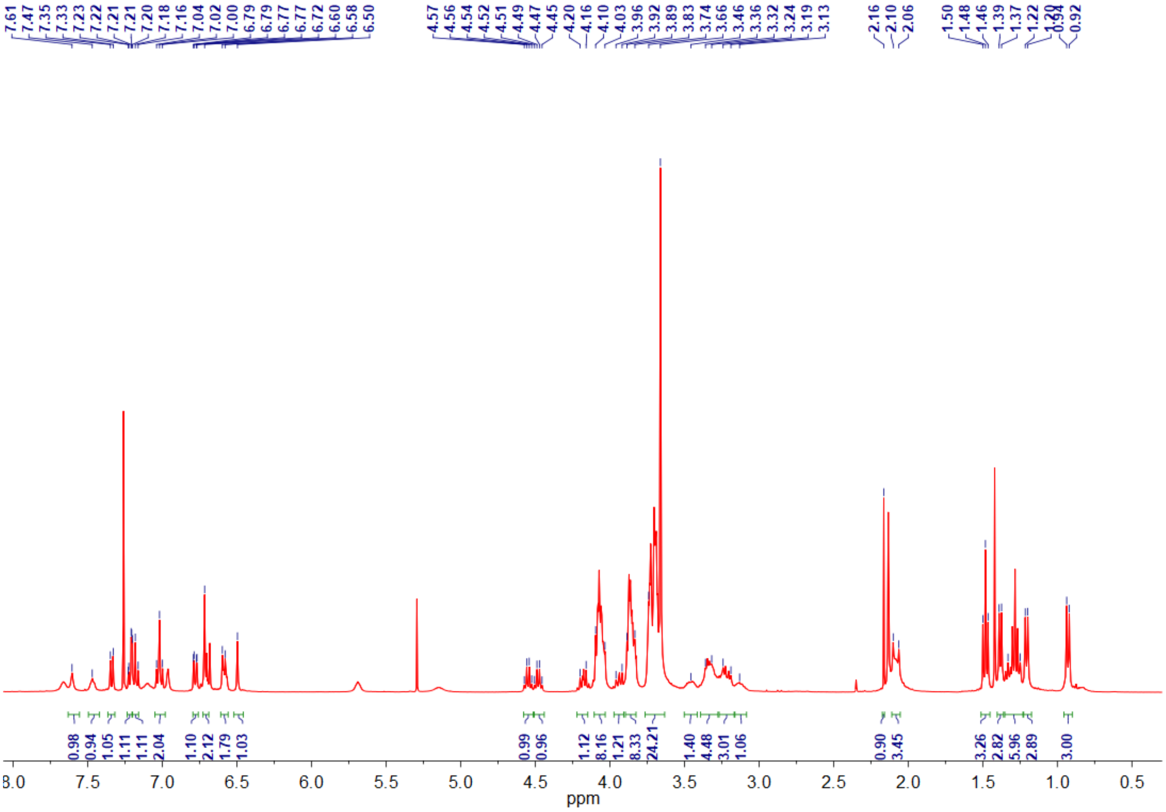

Figure A5. ^{1}H NMR in $CDCl_3$ of Compound **11 (B).**

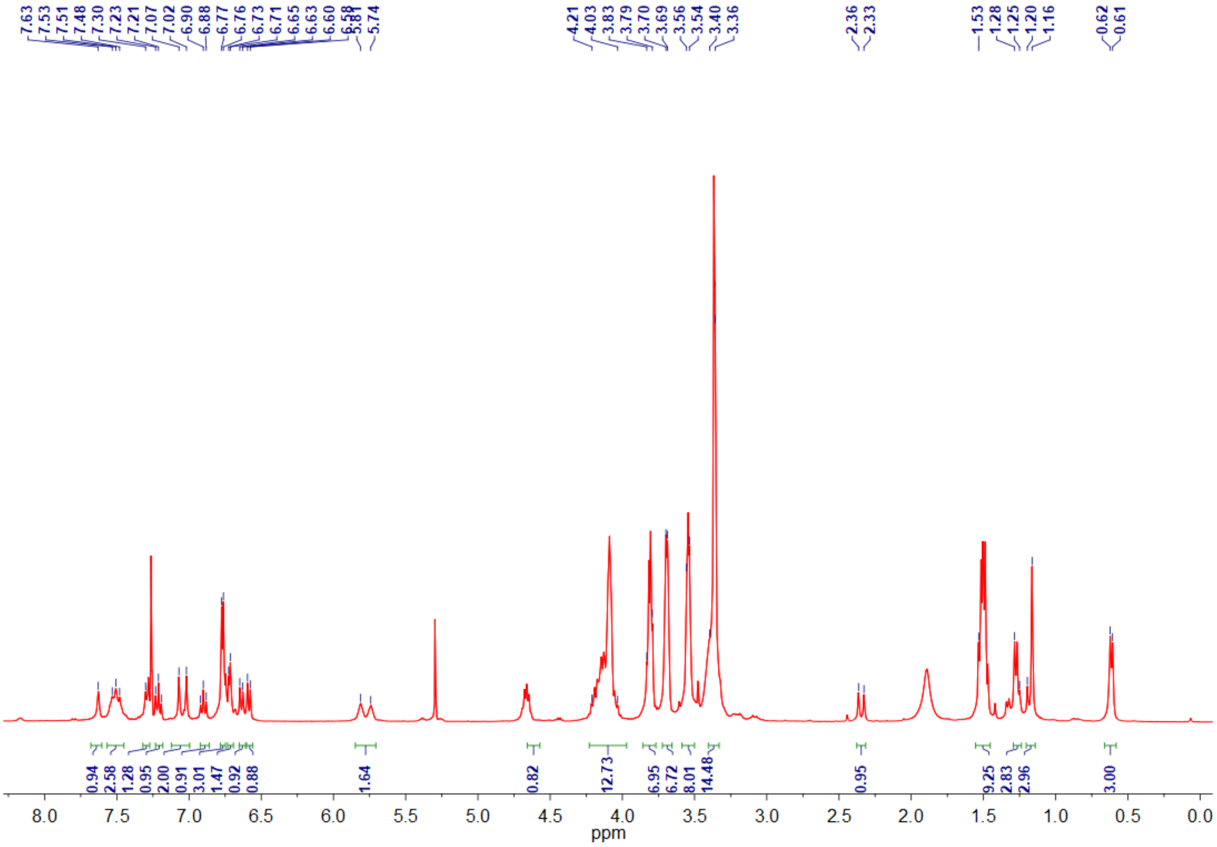

Figure A6. ^{1}H NMR in $CDCl_3$ of Compound **17(C).**

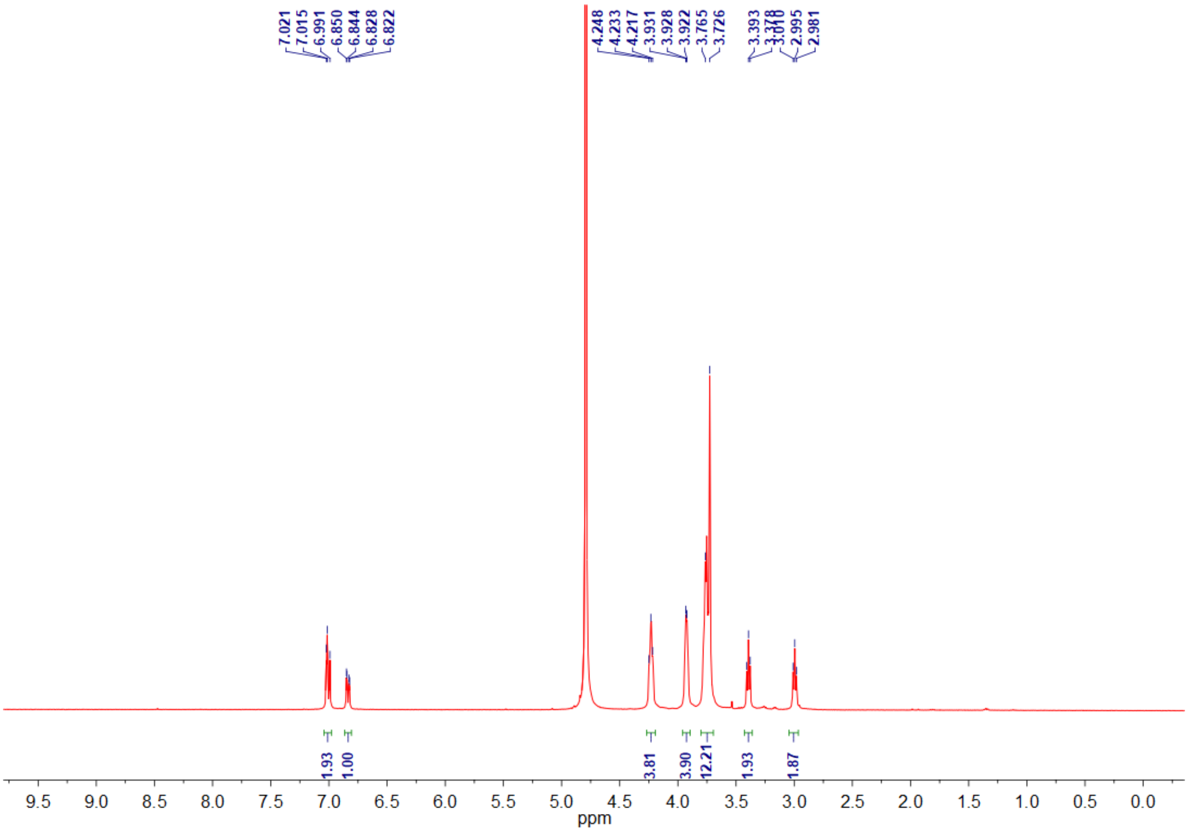

Figure A7. ^{1}H NMR in D_2O of Compound **5**.

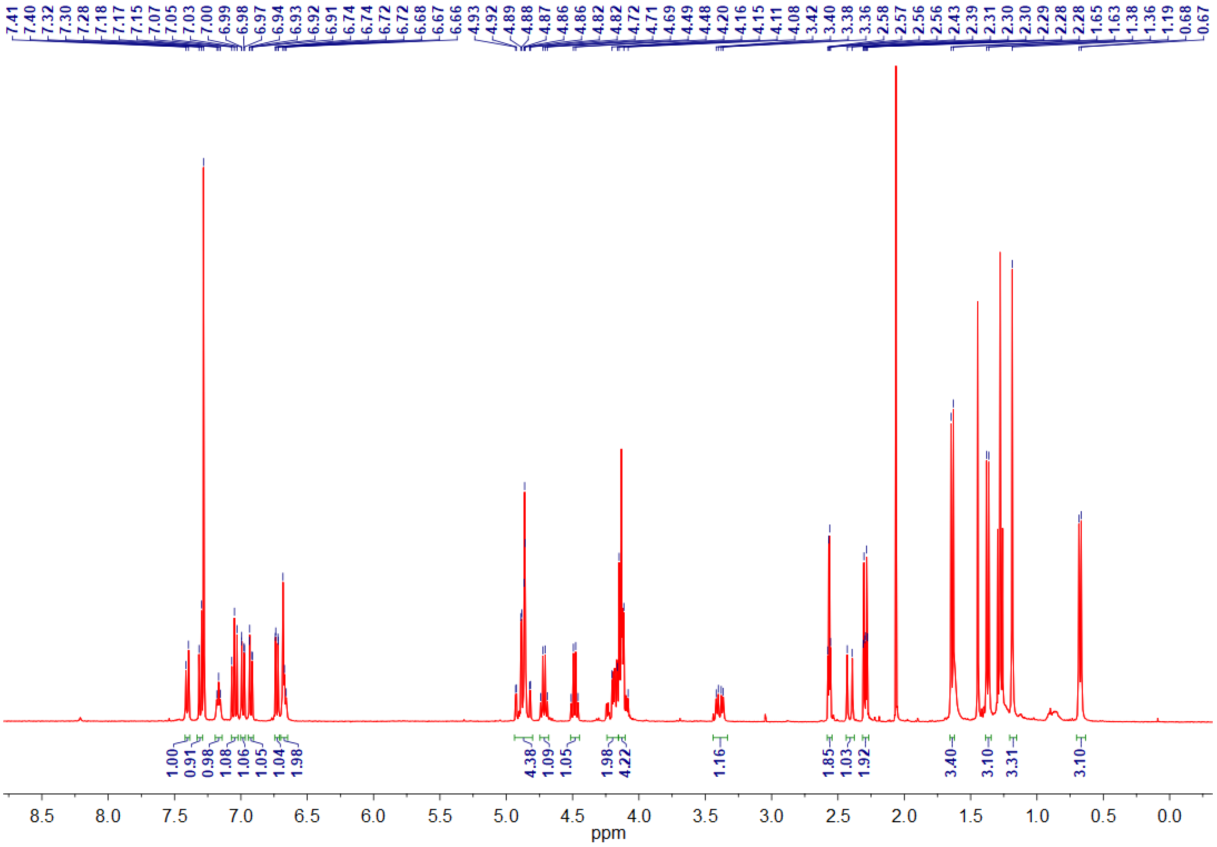

Figure A8. ${}^{1}H$ NMR in $CDCl_3$ of Compound **22**.

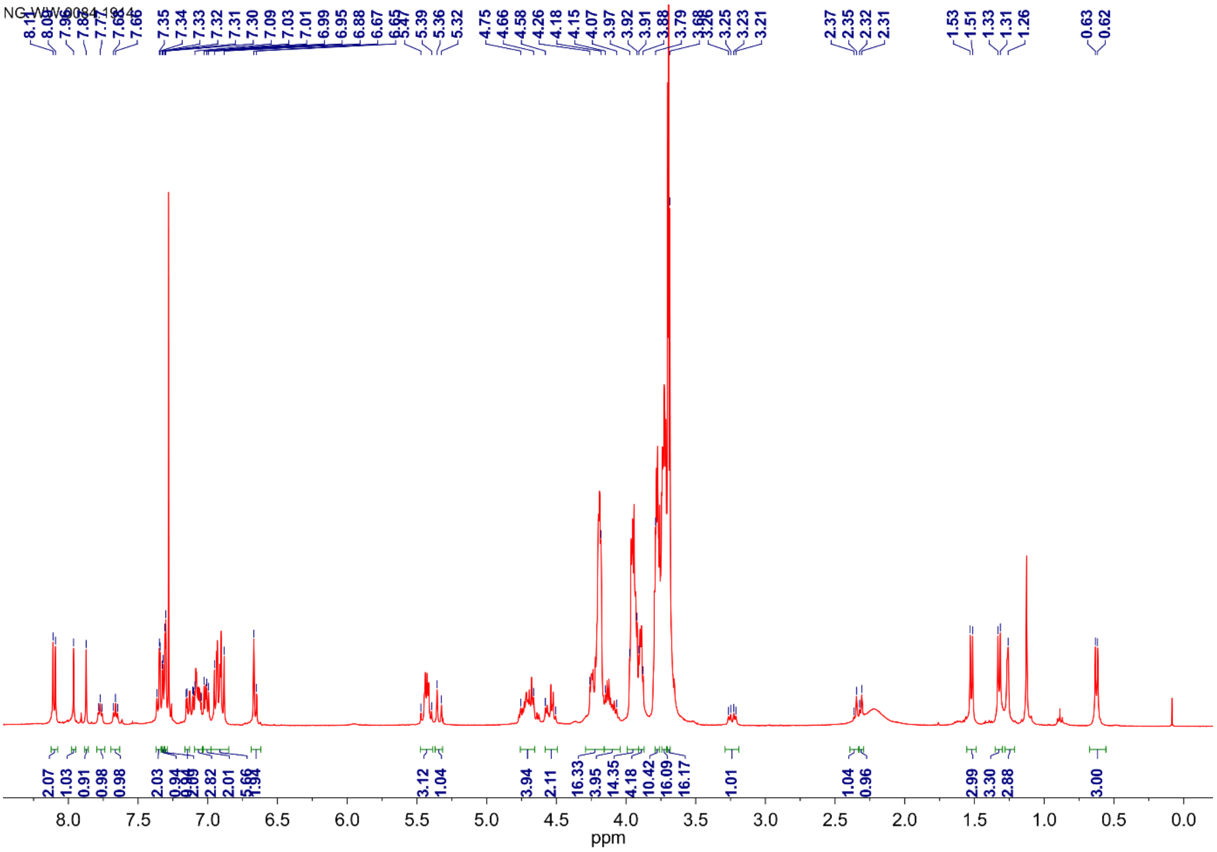

Figure A9. ${}^{1}H$ NMR in $CDCl_3$ of Compound **24 (E)**.

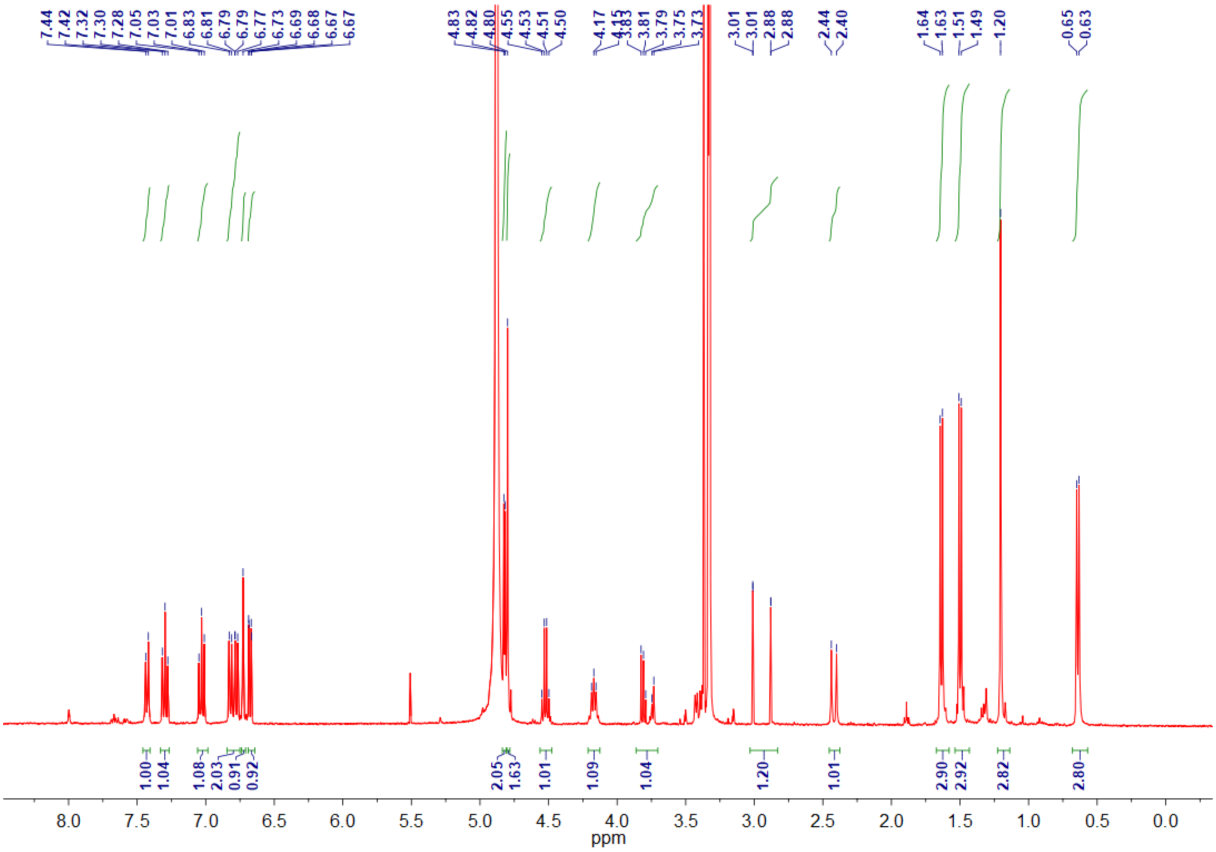

Figure A10. ^{1}H NMR in MeOD of Compound **26**.

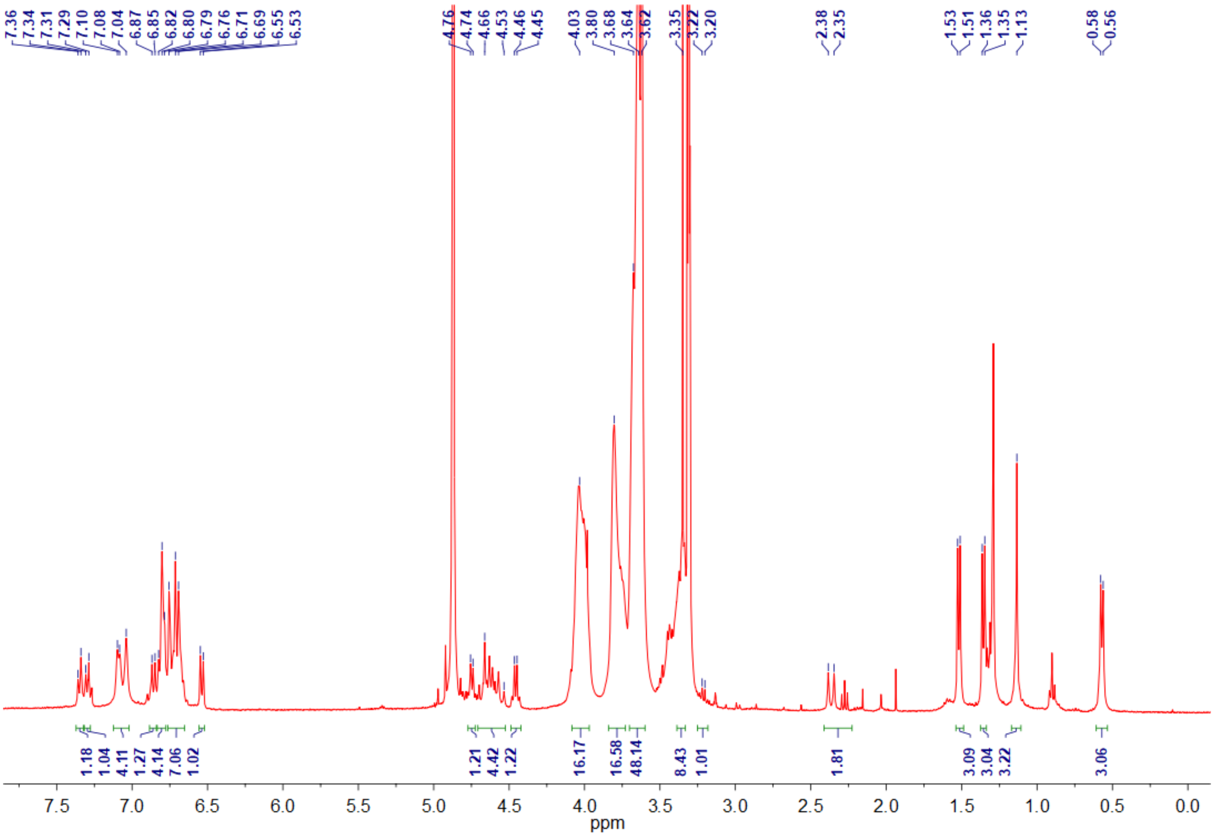

Figure A 11. ^{1}H NMR in MeOD of Compound **27 (F)**.

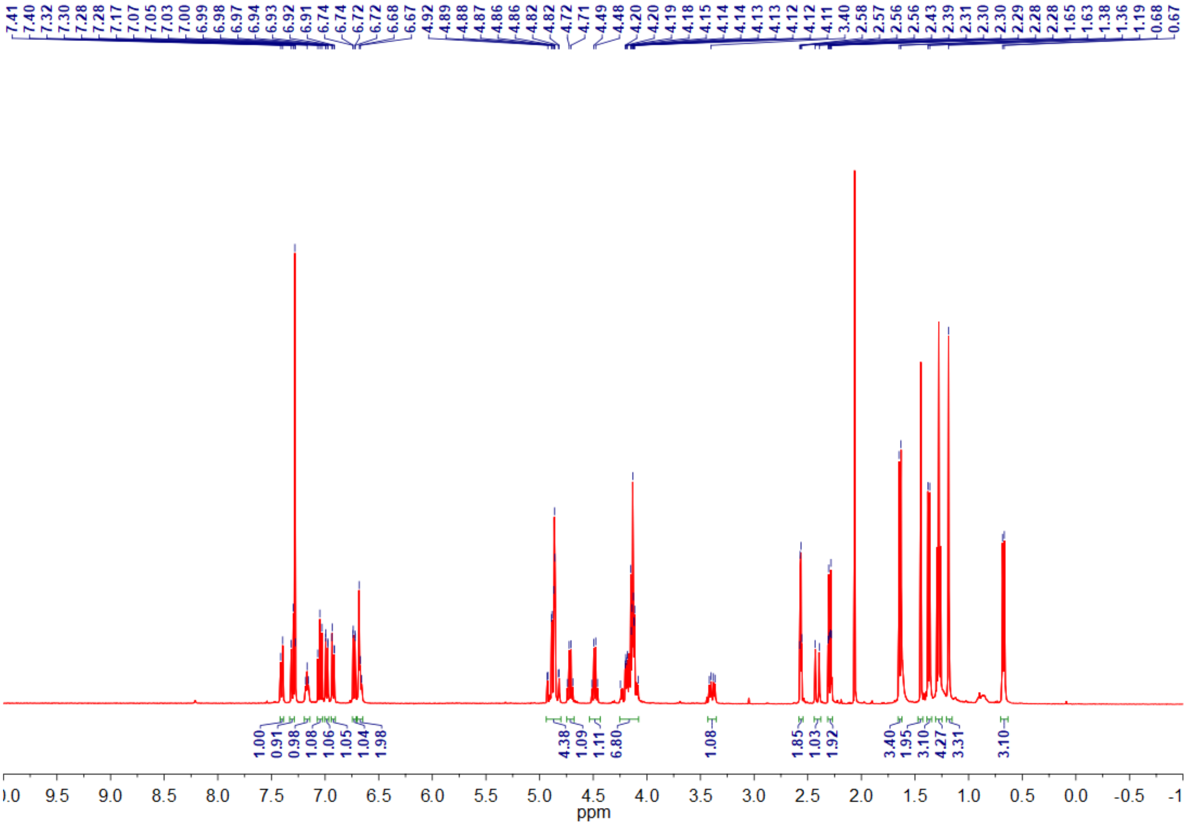

Figure A12. ^{1}H NMR in $CDCl_3$ of Compound **30**.

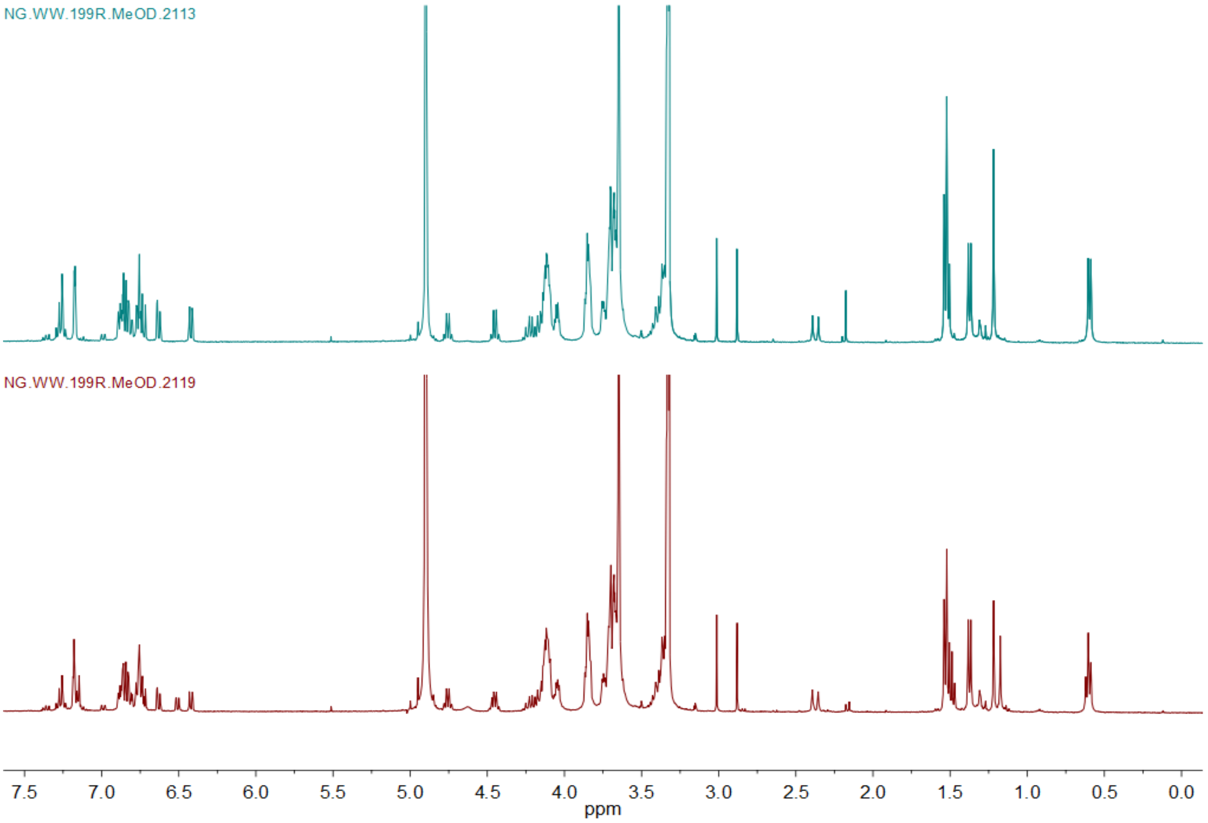

Figure A13. Comparison of the ^{1}H NMR in $CDCl_3$ of Compound **30** Initial (Up) and After UV irradiation 5min (Down).

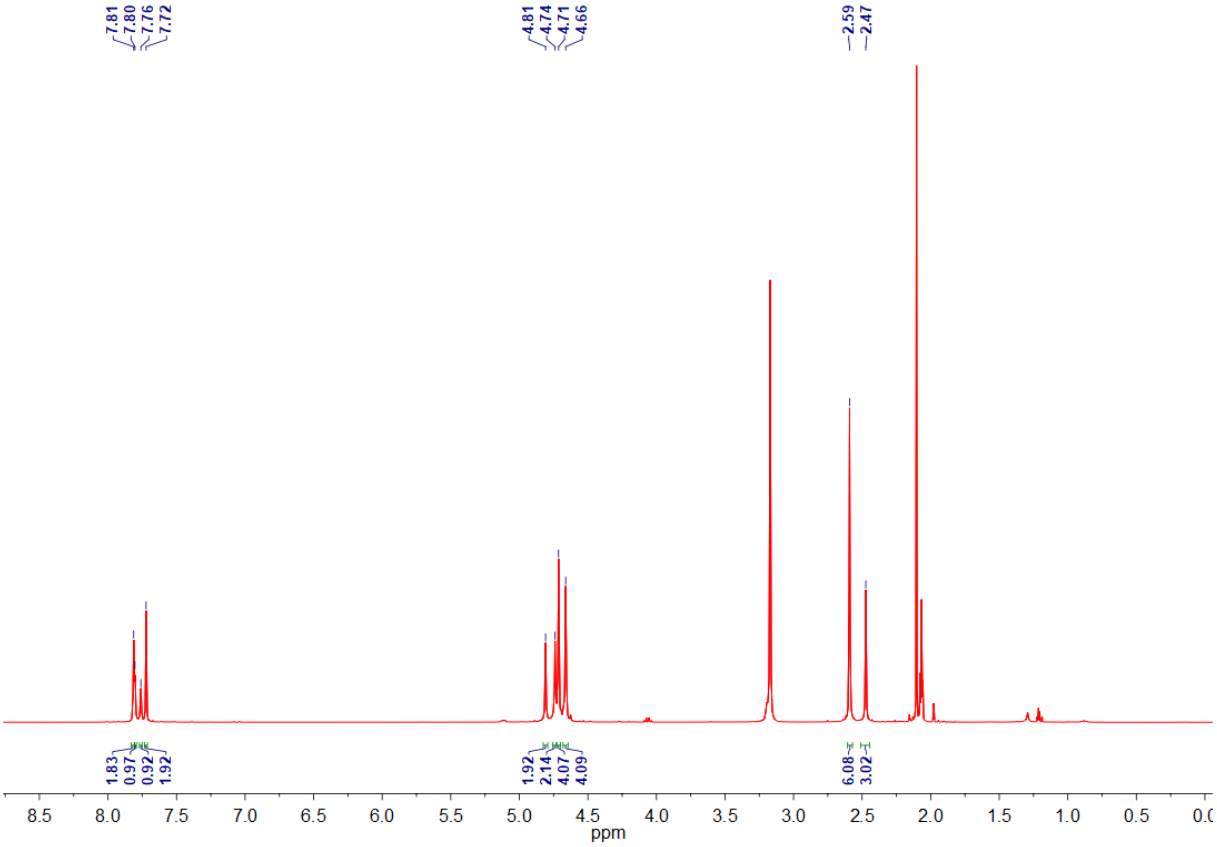

Figure A14. ^{1}H NMR in $(CD_3)_2CO$ + 1 drop D_2O of Compound **43**.

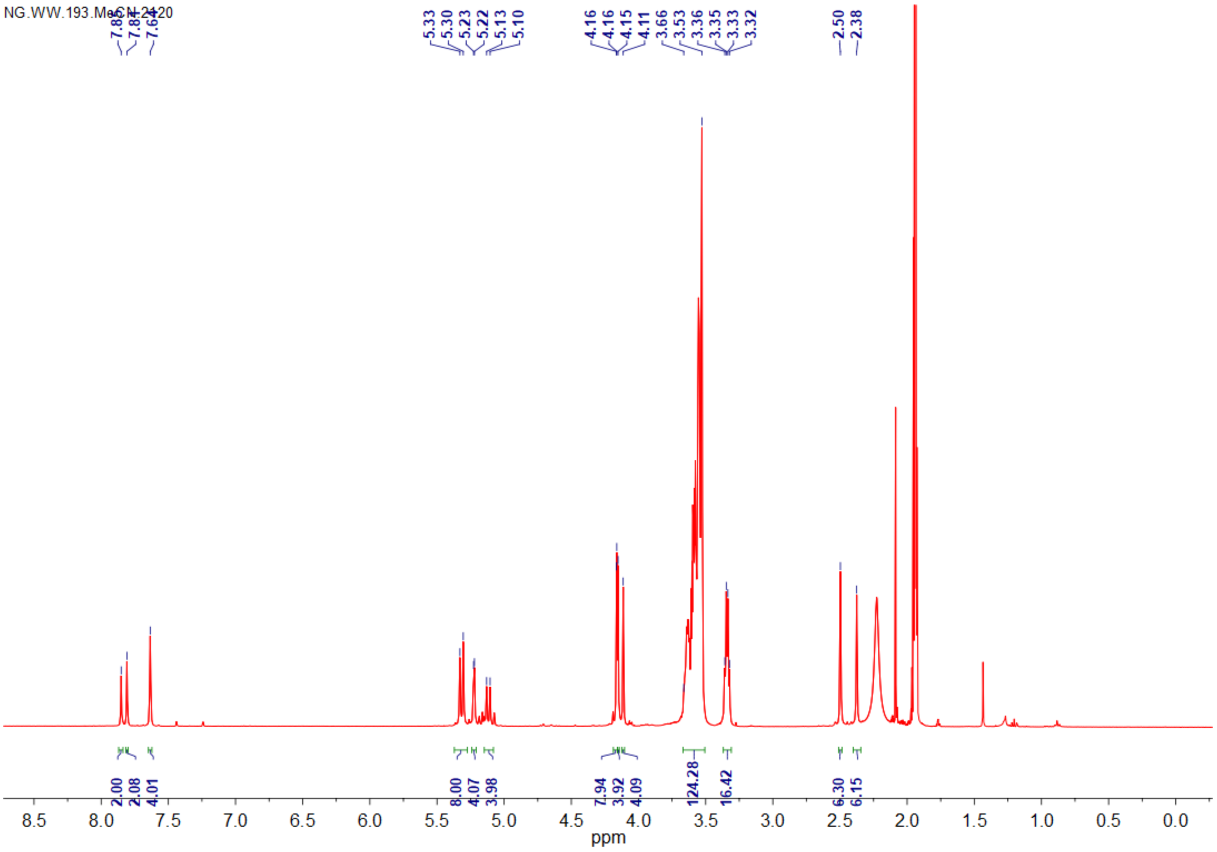

Figure A15. ^{1}H NMR in CD_3CN of Compound **44**.

References

[1] Mann, S. Life as a Nanoscale Phenomenon. *Angew. Chem., Int. Ed.* **2008**, 47, 5306–5320.

[2] von Ballmoos, C.; Cook, G. M.; Dimroth, P. Unique Rotary ATP Synthase and its Biological Diversity. *Annu. Rev. Biophys.* **2008**, 37, 43–64.

[3] Foth, B. J.; Goedecke, M. C.; Soldati, D. New Insights into Myosin Evolution and Classification. *Proc. Natl. Acad. Sci. U. S. A.* **2006**, 103, 3681–3686.

[4] Hirokawa, N.; Noda, Y.; Tanaka, Y.; Niwa, S. Kinesin Superfamily Motor Proteins and Intracellular Transport. *Nat. Rev. Mol. Cell Biol.* **2009**, 10, 682–696.

[5] Feynman, R. P. There's Plenty of Room at the Bottom. *Eng. Sci.***1960**, 23, 22–36.

[6] Bonnet, S.; Collin, J.-P. Ruthenium-Based Light-Driven Molecular Machine Prototypes: Synthesis and Properties. *Chem. Soc. Rev.* **2008**, 37, 1207–1217.

[7] Peplow, M. March of the Machines. *Nature* **2015**, 525, 18–21.

[8] Sauvage, J.-P. From Chemical Topology to Molecular Machines (Nobel Lecture). *Angew. Chem., Int. Ed.* **2017**, 56, 11080–11093.

[9] Stoddart, J. F. Mechanically Interlocked Molecules (MIMs) -Molecular Shuttles, Switches, and Machines (Nobel Lecture). *Angew. Chem., Int. Ed.* **2017**, 56, 11094–11125.

[10] Feringa, B. L. The Art of Building Small: From Molecular Switches to Motors (Nobel Lecture). *Angew. Chem., Int. Ed.* **2017**, 56, 11060–11078.

[11] García-López, V.; Liu, D.; Tour, J. M. Light-Activated Organic Molecular Motors and Their Applications. *Chem. Rev.* **2020**, *120* (1), 79–124.

[12] Balzani, V.; Credi, A.; Raymo, F. M.; Stoddart, J. F. Artificial Molecular Machines. *Angew. Chem., Int. Ed.* **2000**, 39, 3348–3391.

[13] Astumian, R. D. Design Principles for Brownian Molecular Machines: How to Swim in Molasses and Walk in a Hurricane. *Phys. Chem. Chem. Phys.* **2007**, 9, 5067–5083.

[14] Ashton, P. R.; Ballardini, R.; Balzani, V.; Gómez-López, M.; Lawrence, S. E.; Martínez-Díaz, M. V.; Montalti, M.; Piersanti, A.; Prodi, L.; Stoddart, J. F.; Williams, D. J. Hydrogen-Bonded Complexes of Aromatic Crown Ethers with (9-Anthracenyl)- methylammonium Derivatives. Supramolecular Photochemistry and Photophysics. pH-Controllable Supramolecular Switching. *J. Am. Chem. Soc.* **1997**, 119, 10641–10651.

[15] Balzani, V.; Credi, A.; Venturi, M. Light Powered Molecular Machines. *Chem. Soc. Rev.* **2009**, 38, 1542–1550.

[16] Bissell, R. A.; Córdova, E.; Kaifer, A. E.; Stoddart, J. F. A Chemically and Electrochemically

Switchable Molecular Shuttle. *Nature* **1994,** 369, 133–137.

[17] Dasgupta, S.; Wu, J. Template-Directed Synthesis of Catenanes. *In Comprehensive Supramolecular Chemistry II; Elsevier,* **2017**; pp 251–268.

[18] Pearson, R. G.; Schmidtke, H. H.; Basolo, F. The mechanism of base hydrolysis and base catalyzed reactions of some cobalt(III) ammine complexes. *J. Am. Chem. Soc.* **1960**, 82 (16), 4434–4435.

[19] Dietrich-Buchecker, C. O.; Sauvage, J. P.; Kintzinger, J. P. Une Nouvelle famille de molecules: les metallo-catenanes. *Tetrahedron Lett.* **1983,** 24, 5095–5098.

[20] Buchecker, D.; Sauvage, J. P. Une Nouvelle Famille De Molecules: Les Metallo-Catenanes. *Tetrahedron Letters.* **1983**, 24 (46), 5095 - 5098.

[21] Leigh, D. A.; Wong, J. K. Y.; Dehez, F.; Zerbetto, F. Unidirectional Rotation in a Mechanically Interlocked Molecular Rotor. *Nature.* **2003,** 424 (6945), 174–179.

[22] Anelli, P. L.; Spencer, N.; Stoddart, J. F. A Molecular Shuttle. *J. Am. Chem. Soc.* **1991**, 113 (13), 5131–5133.

[23] Bissell, R. A.; Cordova, E.; Kaifer, A. E. A Chemically and Electrochemically Switchable Molecular Shuttle. *Nature* **1994**, 369, 133-137.

[24] Cheng, C., McGonigal, P., Schneebeli, S. Li, H. Vermeulen, N. Ke, C. Stoddart, J.F. An artificial molecular pump. *Nature Nanotech.* **2015**,10, 547–553.

[25] Koumura, N.; Zijlstra, R. W. J.; van Delden, R. A.; Harada, N.; Feringa, B. L. Light-Driven Monodirectional Molecular Rotor. *Nature.* **1999**, *401* (6749), 152–155.

[26] Koumura, N.; Geertsema, E. M.; Meetsma, A.; Feringa, B. L. Light-Driven Molecular Rotor: Unidirectional Rotation Controlled by a Single Stereogenic Center. *J. Am. Chem. Soc.* **2000**, *122* (48), 12005–12006.

[27] Pérez-Hernández, G.; González, L. Mechanistic Insight into Light-Driven Molecular Rotors: A Conformational Search in Chiral Overcrowded Alkenes by a Pseudo-Random Approach. *Phys. Chem. Chem. Phys.* **2010**, *12* (38), 12279-12289.

[28] Koumura, N.; Geertsema, E. M.; van Gelder, M. B.; Meetsma, A.; Feringa, B. L. Second Generation Light-Driven Molecular Motors. Unidirectional Rotation Controlled by a Single Stereogenic Center with Near-Perfect Photoequilibria and Acceleration of the Speed of Rotation by Structural Modification. *J. Am. Chem. Soc.* **2002**. 124(18), 5037-5051.

[29] Mallik, R.; Gross, S. P. Molecular Motors: Strategies to Get Along. *Curr. Biol.* **2004**, 14, R971–R982.

[30] Ruangsupapichat, N.; Pollard, M. M.; Harutyunyan, S. R.; Feringa, B. L. Reversing the Direction in a Light-Driven Rotary Molecular Motor. *Nature Chem.* **2011**, *3* (1), 53–60.

[31] Kinbara, K.; Aida, T. Toward Intelligent Molecular Machines: Directed Motions of Biological and Artificial Molecules and Assemblies. *Chem. Rev.* **2005**, 105, 1377–1400.

[32] Hernandez, J. V. A Reversible Synthetic Rotary Molecular Motor. *Science.* **2004**, *306* (5701), 1532–1537.

[33] Leigh, D. A.; Wong, J. K. Y.; Dehez, F.; Zerbetto, F. Unidirectional Rotation in a Mechanically Interlocked Molecular Rotor. *Nature.* **2003**, 424 (6945), 174–179.

[34] Kistemaker, J. C. M.; Štacko, P.; Visser, J.; Feringa, B. L. Unidirectional Rotary Motion in Achiral Molecular Motors. *Nat. Chem.* **2015**, 7, 890.

[35] Guentner, M.; Schildhauer, M.; Thumser, S.; Mayer, P.; Stephenson, D.; Mayer, P. J.; Dube, H. Sunlight-Powered KHz Rotation of a Hemithioindigo-Based Molecular Motor. *Nat Commun.* **2015**, 6 (1), 8406.

[36] Greb, L.; Lehn, J.-M. Light-Driven Molecular Motors: Imines as Four-Step or Two-Step Unidirectional Rotors. *J. Am. Chem. Soc.* **2014**, 136 (38), 13114–13117.

[37] Danowski, W.; van Leeuwen, T.; Abdolahzadeh, S.; Roke, D.; Browne, W. R.; Wezenberg, S. J.; Feringa, B. L. Unidirectional Rotary Motion in a Metal–Organic Framework. *Nat. Nanotechnol.* **2019**, 14 (5), 488–494.

[38] Castiglioni, F.; Danowski, W.; Perego, J.; Leung, F. K.-C.; Sozzani, P.; Bracco, S.; Wezenberg, S. J.; Comotti, A.; Feringa, B. L. Modulation of Porosity in a Solid Material Enabled by Bulk Photoisomerization of an Overcrowded Alkene. *Nat. Chem.* **2020**, 12 (7), 595–602.

[39] Rayment, I. Kinesin and Myosin: Molecular Motors with Similar Engines. *Structure.* **1996**, 4, 501−504.

[40] Schliwa, M.; Woehlke, G. Molecular Motors. *Nature.* **2003**, 422,759−765.

[41] Shirai, Y.; Osgood, A. J.; Zhao, Y.; Kelly, K. F.; Tour, J. M. Directional Control in Thermally Driven Single-Molecule Nanocars. *Nano Lett.* **2005**, 5, 2330−2334.

[42] Morin, J.-F.; Shirai, Y.; Tour, J. M. En route to a Motorized Nanocar. *Org. Lett.* **2006**, 8, 1713−1716.

[43] García-López, V.; Chu, P.-L. E.; Chiang, P.-T.; Sun, J.; Martí, A. A.; Tour, J. M. Synthesis of a Light-Driven Motorized Nanocar. *Asian J. Org. Chem.* **2015**, 4, 1308−1314.

[44] García-López, V.; Alemany, L. B.; Chiang, P.-T.; Sun, J.; Chu, P.-L.; Martí, A. A.; Tour, J.M.Synthesis of Light-Driven Motorized Nanocars for Linear Trajectories and their Detailed NMR Structural Determination. *Tetrahedron.* **2017**, 73, 4864−4873.

[45] Kudernac, T.; Ruangsupapichat, N.; Parschau, M.; Maciá, B.; Katsonis, N.; Harutyunyan, S. R.; Ernst, K.-H.; Feringa, B. L. Electrically Driven Directional Motion of a Four-Wheeled Molecule on a Metal Surface. *Nature.* **2011**, 479 (7372), 208–211.

[46] van Delden, R. A.; ter Wiel, M. K. J.; Pollard, M. M.; Vicario, J.; Koumura, N.; Feringa, B. L. Unidirectional Molecular Motor on a Gold Surface. *Nature.* **2005**, 437 (7063), 1337–1340.

[47] Pollard, M. M.; Lubomska, M.; Rudolf, P.; Feringa, B. L. Controlled Rotary Motion in a Monolayer of Molecular Motors. *Angew. Chem., Int. Ed.* **2007**, 46, 1278–1280.

[48] London, G.; Chen, K.-Y.; Carroll, G. T.; Feringa, B. L. Towards Dynamic Control of Wettability by Using Functionalized Altitudinal Molecular Motors on Solid Surfaces. *Chem. - Eur. J.* **2013**, 19, 10690–10697.

[49] Chen, K.-Y.; Ivashenko, O.; Carroll, G. T.; Robertus, J.; Kistemaker, J. C. M.; London, G.; Browne, W. R.; Rudolf, P.; Feringa, B. L. Control of Surface Wettability Using Tripodal Light-Activated Molecular Motors. *J. Am. Chem. Soc.* **2014**, 136 (8), 3219–3224.

[50] Pijper, D.; Feringa, B. L. Molecular Transmission: Controlling the Twist Sense of a Helical Polymer with a Single Light-Driven Molecular Motor. *Angew. Chem. Int. Ed.* **2007,** 46 (20), 3693–3696.

[51] Van Leeuwen, T.; Heideman, H.; Zhao, D.; Wezenberg, S. J.; Feringa, B. L. In Situ Control of Polymer Helicity with a NonCovalently Bound Photoresponsive Molecular Motor Dopant. *Chem. Commun.* **2017**, 53, 6393–6396

[52] Zhao, D.; van Leeuwen, T.; Cheng, J.; Feringa, B. L. Dynamic Control of Chirality and Self-Assembly of Double-Stranded Helicates with Light. *Nat. Chem.* **2017**, 9, 250.

[53] Liu, Y.; Zhang, Q.; Crespi, S.; Chen, S.; Zhang, X.; Xu, T.; Ma, C.; Zhou, S.; Shi, Z.; Tian, H.; Feringa, B. L.; Qu, D. Motorized Macrocycle: A Photo-responsive Host with Switchable and Stereoselective Guest Recognition. *Angew. Chem.* **2021**, 133 (29), 16265–16274.

[54] Wang, J.; Feringa, B. L. Dynamic Control of Chiral Space in a Catalytic Asymmetric Reaction Using a Molecular Motor. *Science*. **2011**, 331 (6023), 1429–1432.

[55] van Leeuwen, T.; Lubbe, A. S.; Štacko, P.; Wezenberg, S. J.; Feringa, B. L. Dynamic Control of Function by Light-Driven Molecular Motors. *Nat Rev Chem.* **2017**, 1 (12), 0096.

[56] Vlatković, M.; Bernardi, L.; Otten, E.; Feringa, B. L. Dual Stereocontrol over the Henry Reaction Using a Light- and Heat- Triggered Organocatalyst. *Chem. Commun.***2014**,50,7773–7775.

[57] García-López, V.; Chen, F.; Nilewski, L. G.; Duret, G.; Aliyan, A.; Kolomeisky, A. B.; Robinson, J. T.; Wang, G.; Pal, R.; Tour, J. M. Molecular Machines Open Cell Membranes. *Nature.* **2017**, *548* (7669), 567–572.

[58] García-López, V.; Chiang, P.-T.; Chen, F.; Ruan, G.; Martí, A. A.; Kolomeisky, A. B.; Wang, G.; Tour, J. M. Unimolecular Submersible Nanomachines. Synthesis, Actuation, and Monitoring. *Nano Lett.* **2015**, *15* (12), 8229–8239.

[59] Zheng, Y.; Han, M. K. L.; Zhao, R.; Blass, J.; Zhang, J.; Zhou, D. W.; Colard-Itté, J.-R.; Dattler, D.; Çolak, A.; Hoth, M.; García, A. J.; Qu, B.; Bennewitz, R.; Giuseppone, N.; del Campo, A. Optoregulated Force Application to Cellular Receptors Using Molecular Motors. *Nat Commun.* **2021**, 12 (1), 3580.

[60] Zhou, Q.; Chen, J.; Luan, Y.; Vainikka, P. A.; Thallmair, S.; Marrink, S. J.; Feringa, B. L.; van Rijn, P. Unidirectional Rotating Molecular Motors Dynamically Interact with Adsorbed Proteins to Direct the Fate of Mesenchymal Stem Cells. *Sci. Adv.* **2020**, 6 (5), eaay2756.

61 Doyle, D. A. The Structure of the Potassium Channel: Molecular Basis of K^+ Conduction and Selectivity. *Science.* **1998**, 280 (5360), 69–77.

[62] Chen, S.; Wang, Y.; Nie, T.; Bao, C.; Wang, C.; Xu, T.; Lin, Q.; Qu, D.-H.; Gong, X.; Yang, Y.; Zhu, L.; Tian, H. An Artificial Molecular Shuttle Operates in Lipid Bilayers for Ion Transport. *J. Am. Chem. Soc.* **2018**, *140* (51), 17992–17998.

[63] Credi, A. A Molecular Cable Car for Transmembrane Ion Transport. *Angew. Chem. Int. Ed.* **2019**, *58* (13), 4108–4110.

[64] Qu, D.-H.; Wang, C.; Wang, S.; Yang, H.; Xiang, Y.; Wang, X.; Bao, C.; Zhu, L.; Tian, H. A Light-Operated Molecular Cable Car for Gated Ion Transport. *Angew. Chem. Int. Ed.* **2021**, ange.202102838.

[65] Li, Q.; Foy, J. T.; Colard-Itté, J.-R.; Goujon, A.; Dattler, D.; Fuks, G.; Moulin, E.; Giuseppone, N. Gram Scale Synthesis of Functionalized and Optically Pure Feringa's Motors. *Tetrahedron,* **2017**, 73 (33), 4874–4882.

[66] Alexandratos, S. D.; Stine, C. L. Synthesis of Ion-Selective Polymer-Supported Crown Ethers: *A Review. React. Funct. Polym*. **2004**, 60, 3–16.

[67] Kado, S.; Takeshima, Y.; Nakahara, Y.; Kimura, K. Potassium-Ion-Selective Sensing Based on Selective Reflection of Cholesteric Liquid Crystal Membranes. J. Incl. Phenom. *Macrocycl. Chem.* **2012**, 72 (1–2), 227–232.

[68] Yu, H.-R.; Hu, J.-Q.; Lu, X.-H.; Ju, X.-J.; Liu, Z.; Xie, R.; Wang, W.; Chu, L.-Y. Insights into the Effects of 2:1 "Sandwich-Type" Crown-Ether/Metal-Ion Complexes in Responsive Host–Guest Systems. *J. Phys. Chem. B,* **2015**, 119 (4), 1696–1705.

[69] Otis, F.; Racine-Berthiaume, C.; Voyer, N. How Far Can a Sodium Ion Travel within a Lipid Bilayer? *J. Am. Chem. Soc.* **2011**, 133 (17), 6481–6483.

[70] Gilles, A.; Barboiu, M. Highly Selective Artificial K + Channels: An Example of Selectivity-Induced Transmembrane Potential. *J. Am. Chem. Soc.* **2016**, 138 (1), 426–432.

[71] Benke, B. P.; Madhavan, N. Active Ion Transporters from Readily Accessible Acyclic Octapeptides Containing 3-Aminobenzoic Acid and Alanine. *Chem. Commun.* ***2013***, 49 (66), 7340–7342.

[72] Chui, J. K. W.; Fyles, T. M. Ionic Conductance of Synthetic Channels: Analysis, Lessons, and Recommendations. *Chem. Soc. Rev.* ***2012***, 41 (1), 148–175.

[73] Cazacu, A.; Tong, C.; van der Lee, A.; Fyles, T. M.; Barboiu, M. Columnar Self-Assembled Ureido Crown Ethers: An Example of Ion-Channel Organization in Lipid Bilayers. *J. Am. Chem. Soc.* ***2006***, 128 (29), 9541–9548.

[74] Moorhouse, A.J.; Keramidas, A.; Zaykin, A.; Peter R. Schofield, P.R.; Barry, P.H. Single Channel Analysis of Conductance and Rectification in Cation-selective, Mu-tant Glycine Receptor Channels; *J. Gen. Physiol,* **2002**, 119, 411-425.

[75] Chen, J.; Kistemaker, J. C. M.; Robertus, J.; Feringa, B. L. Molecular Stirrers in Action. *J. Am. Chem. Soc.* **2014**, 136 (42), 14924–14932.

[76] Out-of-Equilibrium (Supra)Molecular Systems and Materials; Giuseppone, N., Walther, A., Eds.; *John Wiley and Sons*, **2021**.

[77] Barry, J.; Gu, C. Coupling Mechanical Forces to Electrical Signaling. *Neurosci*. **2013**, 19 (2), 145–159.

[78] Guidry, E. N.; Li, J.; Stoddart, J. F.; Grubbs, R. H. Bifunctional [C2]Daisy-Chains and Their Incorporation into Mechanically Interlocked Polymers. *J. Am. Chem. Soc.* **2007**, *129* (29), 8944–8945.

[79] Clark, P. G.; Day, M. W.; Grubbs, R. H. Switching and Extension of a [C2]Daisy-Chain Dimer Polymer. *J. Am. Chem. Soc.* **2009**, *131* (38), 13631–13633.

[80] Antoine, A.; Moulin, E.; Fuks, G.; Giuseppone, N. [C2]Daisy Chain Rotaxanes as Molecular Muscles. *CCS Chem* **2019**, 83–96.

81 Goujon, A.; Du, G.; Moulin, E.; Fuks, G.; Maaloum, M.; Buhler, E.; Giuseppone, N. Hierarchical Self-Assembly of Supramolecular Muscle-Like Fibers. *Angew. Chem. Int. Ed.* **2016**, *55* (2), 703–707.

[82] Goujon, A.; Mariani, G.; Lang, T.; Moulin, E.; Rawiso, M.; Buhler, E.; Giuseppone, N. Controlled Sol–Gel Transitions by Actuating Molecular Machine Based Supramolecular Polymers. *J. Am. Chem. Soc.* **2017**, *139* (13), 4923–4928.

[83] Goujon, A.; Lang, T.; Mariani, G.; Moulin, E.; Fuks, G.; Raya, J.; Buhler, E.; Giuseppone, N. Bistable [c 2] Daisy Chain Rotaxanes as Reversible Muscle-like Actuators in Mechanically Active Gels. *J. Am. Chem. Soc.* **2017**, 139, 14825−14828.

[84] Iwaso, K.; Takashima, Y.; Harada, A. Fast Response Dry-Type Artificial Molecular Muscles with [C2]Daisy Chains. *Nature Chem.* **2016**, *8* (6), 625–632.

[85] Ikejiri, S.; Takashima, Y.; Osaki, M.; Yamaguchi, H.; Harada, A. Solvent-Free Photoresponsive Artificial Muscles Rapidly Driven by Molecular Machines. *J. Am. Chem. Soc.* **2018**, *140* (49), 17308–17315.

[86] Kobatake, S.; Takami, S.; Muto, H.; Ishikawa, T.; Irie, M. Rapid and Reversible Shape Changes of Molecular Crystals on Photoirradiation. *Nature.* **2007**, *446* (7137), 778–781.

[87] Chen, J.; Leung, F. K.-C.; Stuart, M. C. A.; Kajitani, T.; Fukushima, T.; van der Giessen, E.; Feringa, B. L. Artificial Muscle-like Function from Hierarchical Supramolecular Assembly of Photoresponsive Molecular Motors. *Nature Chem.* **2018**, *10* (2), 132–138.

[88] Li, Q.; Fuks, G.; Moulin, E.; Maaloum, M.; Rawiso, M.; Kulic, I.; Foy, J. T.; Giuseppone, N. Macroscopic Contraction of a Gel Induced by the Integrated Motion of Light-Driven Molecular Motors. Nature Nanotech 2015, 10 (2), 161–165.

[89] Foy, J. T.; Li, Q.; Goujon, A.; Colard-Itté, J.-R.; Fuks, G.; Moulin, E.; Schiffmann, O.; Dattler, D.; Funeriu, D. P.; Giuseppone, N. Dual-Light Control of Nanomachines That Integrate Motor and Modulator Subunits. Nature Nanotech 2017, 12 (6), 540–545.

[90] Tengho Toguem, S.-M.; Malik, I.; Hussain, M.; Iqbal, J.; Villinger, A.; Langer, P. Synthesis of Functionalized Benzothiophenes and Dibenzothiophenes by Twofold Heck and Subsequent 6π-Electrocyclization Reactions of 2,3-Dibromothiophenes and 2,3-Dibromobenzothiophenes. *Tetrahedron.* **2013**, 69 (1), 160–173.

[91] Hanazawa, M.; Sumiya, R.; Horikawa, Y.; Irie, M. Thermally Irreversible Photochromic Systems. Reversible Photocyclization of 1,2-Bis (2-Methylbenzo[*b*]Thiophen-3-yl)Perfluorocyclocoalkene Derivatives. *J. Chem. Soc., Chem. Commun.* **1992**, 3, 206-207.

[92] Matile, S.; Sakai, N. The Characterization of Synthetic Ion Channels and Pores. In Analytical Methods in Supramolecular Chemistry; Schalley, C., Ed.; *Wiley-VCH Verlag GmbH & Co. KGaA: Weinheim, Germany,* **2006;** pp 391–418.

Résumé en français

Introduction

De nombreux moteurs moléculaires existent dans le monde biologique, exploitant différents types d'énergie pour générer un mouvement mécanique unidirectionnel.[1] Ils sont généralement composés de protéines ou d'acides nucléiques. Les moteurs biologiques les plus connus incluent l'ATP synthase, les myosines, les kinésines et les dynéines.[2] Ils agissent pour maintenir des activités cellulaires essentielles telles que la contraction musculaire et le transport des vésicules intracellulaires en consommant respectivement de l'énergie chimique telle que l'ATP ou en générant un gradient de protons à travers la membrane cellulaire.[3]

Inspirés par le prinicipe de ces moteurs biologiques, les chimistes ont développé des moteurs moléculaires artificiels capables d'effectuer diverses tâches dans différents environnements.[4] Diverses sources d'énergie (ou stimuli) peuvent être utilisées pour activer ces moteurs moléculaires, comme notamment le pH, la lumière, les réactions chimiques ou électrochimiques. Parmi ces stimuli, l'utilisation de la lumière présente de nombreux avantages tels que la non-toxicité, la commande à distance et l'absence de « déchets ». En particulier, des moteurs moléculaires rotatifs, unidirectionnels et activables par la lumière ont été développés par l'équipe du Prof. Feringa.[5] Récemment, notre équipe a développé un système collectif stimulable intégrant ces moteurs au sein d'un gel de polymères.[6] Durant mon doctorat, je me suis intéressé à d'autres aspects de travail collectif pouvant être effectués par ces moteurs: i) leur intégration dans des bicouches phospholipidiques pour le transport des ions; ii) leur intégration en surface d'un matériau polymère pour le rendre stimulable.

1. Synthèse et auto-assemblage de moteurs moléculaires au sein de membranes phospholipidiques

Dans les organismes vivants, les machines biomoléculaires remplissent des fonctions biologiques clés telles que, par exemple, le contrôle du transport d'un substrat à travers les membranes phospholipidiques. Imiter ces processus en utilisant des machines moléculaires artificielles synthétiques permettrait non seulement une meilleure compréhension des canaux ioniques biologiques, mais ouvrirait également des portes à des applications potentielles en sciences de la vie et en sciences des matériaux.[7] De ce fait, concevoir des canaux ioniques artificiels intelligents basés sur des machines moléculaires sensibles aux stimuli nous est apparu particulièrement intéressant, notamment du fait de la possiblité de précisément contrôler leur mouvement.[8] Les stratégies actuelles impliquant la lumière comme stimulus reposent prinicipalement sur des canaux ioniques protéiques modifiés par des ligands synthétiques photosensibles.[9] Dans le cadre de cette thèse, en collaboration avec l'équipe du Dr. Barboiu (Université de Montpellier), nous avons envisagé l'utilisation de moteurs moléculaires artificiels activables par la lumière pour effectuer ce transport d'ions.[10] Ainsi, nous avons conçu un moteur moléculaire incorporant des groupements éthers couronnes (18-crown-6) qui sont connus pour transporter sélectivement les cations notamment les ions potassium et les ions rubidium via une complexation de style sandwich (Figure 1, composé **A**). Afin de favoriser un meilleur assemblage des éthers couronnes, nous avons également prévu l'insertion de groupements urées liés directement aux éthers couronnes.

Le moteur moléculaire **A** a été préparé en six étapes à partir du 4-nitrocatechol (Figure 1). Cette synthèse nécessite l'obtention du moteur moléculaire **3** et du dérivé éther 18-couronne-6 **4**. Le moteur moléculaire **3** a été préparé en deux étapes selon une méthode déjà décrite dans notre équipe, qui nécessite une protection des groupements phénols puis une déprotection sélective des esters éthyliques.[5] Le composé **4** est obtenu en cinq étapes à partir du 4-nitrocathécol selon la séquence suivante : a) formation de l'éther couronne, b) réduction du groupement nitro, c) formation d'une liaison urée en utilisant l'isocyanate de 2-chloroéthyle, d) substitution nucléophile du chlore avec l'azidure de sodium, et e) réduction de l'azide en amine via une réaction de Staudinger conduisant au composé **4**. Le composé cible **A** est ensuite formé en une étape via un double couplage peptidique entre les composés **3** et **4**. Une purification par HPLC préparative en phase inverse permet l'obtention du composé **A** avec une bonne pureté.

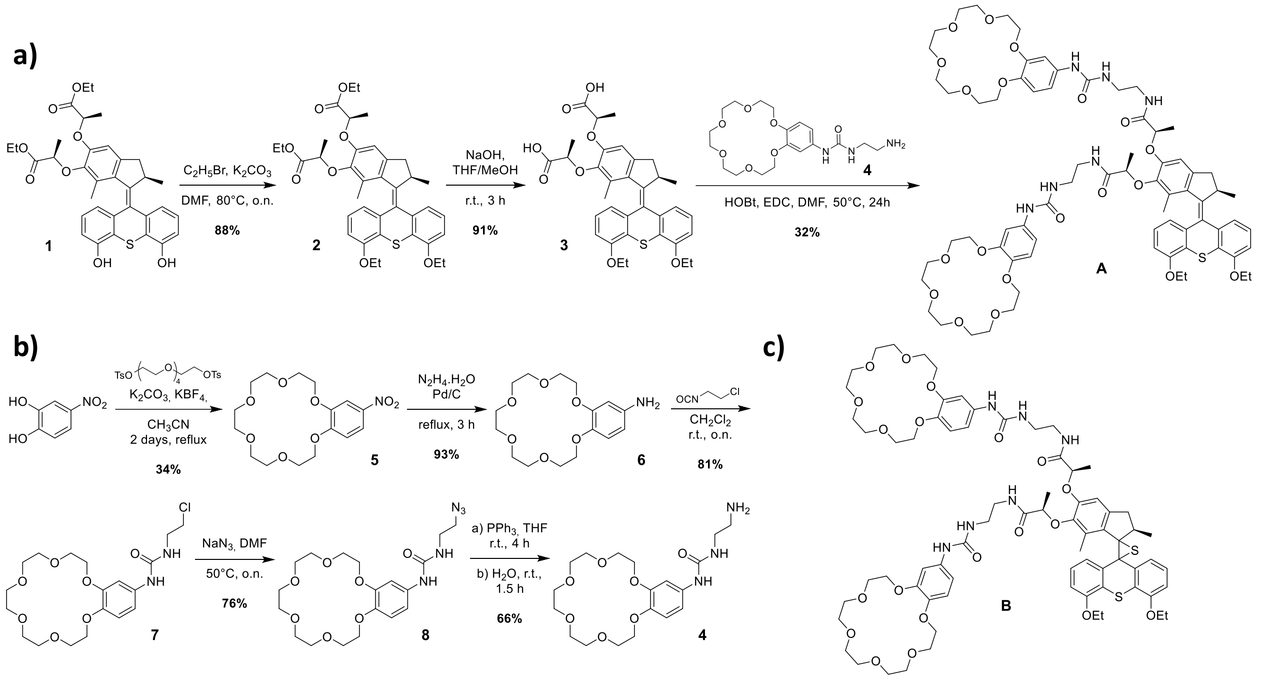

Figure 1. Voies de synthèse pour a) le moteur moléculaire A et b) le dérivé d'éther couronne 4, c) structure chimique de l'épisulfure B.

Ce composé a ensuite été inséré au sein de vésicules géantes unilamellaires afin d'étudier ses propriétés de transport. Des mesures de fluorescence HPTS permettant de mettre en évidence de possibles sélectivités ioniques de la membrane incorporant le moteur **A** ainsi que les constantes de vitesse de transport des ions ont été réalisées. Nous avons également étudié l'influence de l'irradiation par lumière UV sur le transport des ions. La figure 2 montre l'évolution en fonction du temps des rapports d'intensité de fluorescence normalisés pour le transport sélectif des cations K^+, Na^+ ou Rb^+ par le composé **A** à une concentration de 10^{-4} M (concentration finale de **A** dans la quantité totale de suspension de vésicules). Tous les cations se sont révélés être transportés très activement. De manière intéressante, une amélioration de l'activité de transport des ions a été observée sous irradiation UV. Les constantes de vitesse d'ordre pseudo-premier mesurées pour différentes concentrations d'ions K^+ démontrent également que l'irradiation UV améliore l'activité de transport des ions.

Le transport d'ions alcalins à travers les bicouches lipidiques en présence du moteur moléculaire **A** a été étudié par des mesures de fluorescence HPTS sur des vésicules géantes unilamellaires (LUV). Les expériences réalisées démontrent le transport négligeable des ions alcalins en l'absence de **A**. En présence du composé **A** sans irradiation UV, une forte augmentation de l'activité de transport a été mesurée dont l'activité varie en fonction de la nature du cation alcalin (Figure 2a-c). De plus, l'évaluation de l'activité de transport sans irradiation avec une concentration croissante de **A** permet de mettre en évidence la formation de canaux ioniques agrégés *via* les cations (Figure 2d-f, barres bleues). L'utilisation de l'éther couronne benzo-18-crown-6 présent sur le composé **A** au sein de la membrane assure la reconnaissance de cations avec une sélectivité pour les ions potassium à des concentrations faibles et moyennes (0-40 µM), puis pour les cations rubidium à plus fortes concentrations (60-100 µM). Les mécanismes mis en jeu pour ces processus de reconnaissance ne sont pas définis avec précision. Cependant, des données de la littérature indiquent qu'une reconnaissance macrocyclique de type sandwich permette le transport des plus gros cations et que les cations dont la taille est la plus adaptée à la structure macrocyclique s'insèrent *via* une liaison équatoriale. Ce comportement rappelle le positionnement spatial des fragments carbonyle au sein du canal potassique naturel KcsA, qui coorespond parfaitement à la sphère d'hydratation des ions K^+. Dans le cadre de nos travaux, il est fort probable que les cations se transloquent *via* des macrocycles proches au sein des structures auto-assemblées formées dans l'environnement membranaire, créant ainsi des pores dynamiques.

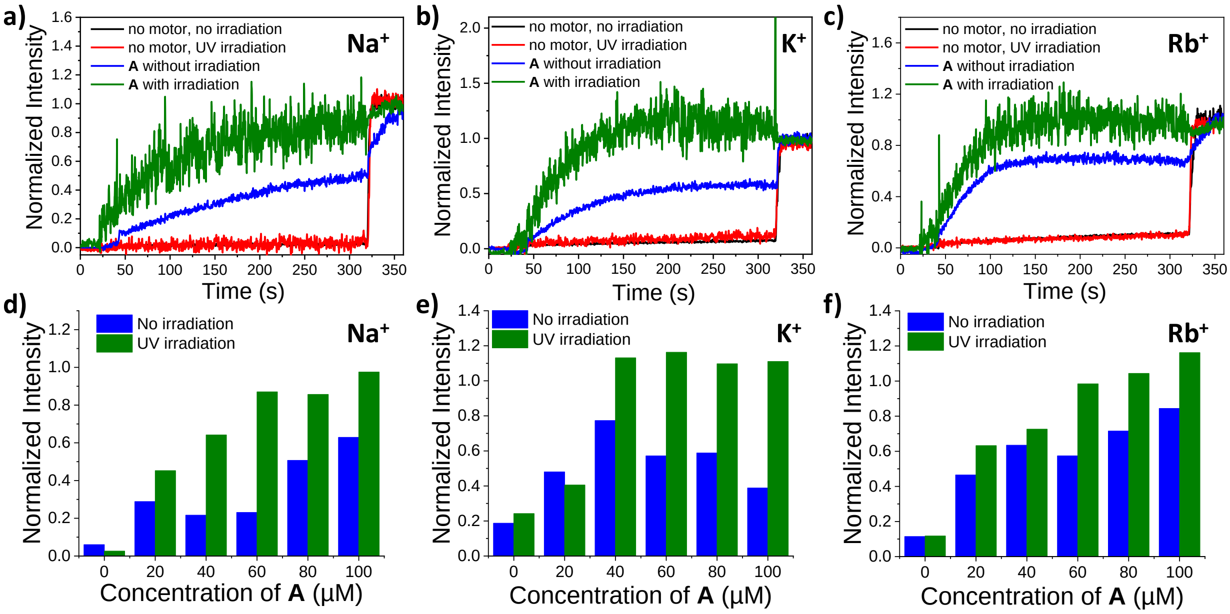

Figure 2. a-c) Evolution de l'activité de transport des cations en fonction du temps pour les cations a) Na^+, b) K^+ et c) Rb^+ en l'absence de moteur moléculaire A et sans (noir) ou avec (rouge) irradiation UV (365 nm, 7,5 $mW.cm^{-2}$, durant 330 s); et en présence de moteur moléculaire A (80 µM) et sans (bleu) ou avec (vert) irradiation UV (365 nm pendant 330 s); d-f) Evolution de l'activité de transport de cations en fonction de la concentration en moteur moléculaire A dans la membrane bicouche à 300 s pour d) Na^+, e) K^+ et f) Rb^+ sans (bleu) et avec (vert) irradiation UV. La composition interne des LUVs est : NaCl 100 mM, tampon phosphate à pH 6.4 (10 mM) et HPTS 10 M. Les compositions externes sont 100 mM de a,d) NaCl, b,e) KCl ou c,f) RbCl dans 10 mM de tampon phosphate à pH 6.4.

Nous avons ensuite étudié l'effet de l'irradiation UV, et donc indirectement l'effet de la rotation du moteur moléculaire, sur l'activité de transport de Na^+, K^+ et Rb^+ *via* les même mesures de fluorescence (Figure 2a-c, courbes vertes). Les résultats obtenus s'avèrent différents de ceux observés sans irradiation, avec une forte augmentation de l'activité de transport pouvant atteindre 400 % pour les cations sodium en présence du composé **A** à une concentration de 60 µM. Pour les trois cations étudiés, l'activité de transport est toujours supérieure d'au moins un ordre de grandeur par rapport aux résultats obtenus sous irradiation UV mais en l'absence de **A**. Ces résultats suggèrent que cette augmentation est le résultat d'un mécanisme de transport activé mécaniquement. La sélectivité de transport déjà observée pour le composé A en l'absence d'irradiation a été confirmée sous irradiation lumineuse, avec une sélectivité S_{K^+/Na^+}= 1,8 pour une concentration en composé **A** de 40 µM et une sélectivité S_{Rb^+/K^+}= 2 pour des concentrations plus élevées. Cette étude démontre la possibilité de fortement accélérer le processus de transport sous irradiation lumineuse, tout en préservant les aspects de sélectivité observés entre les différents ions en fonction de la concentration en composé **A**.

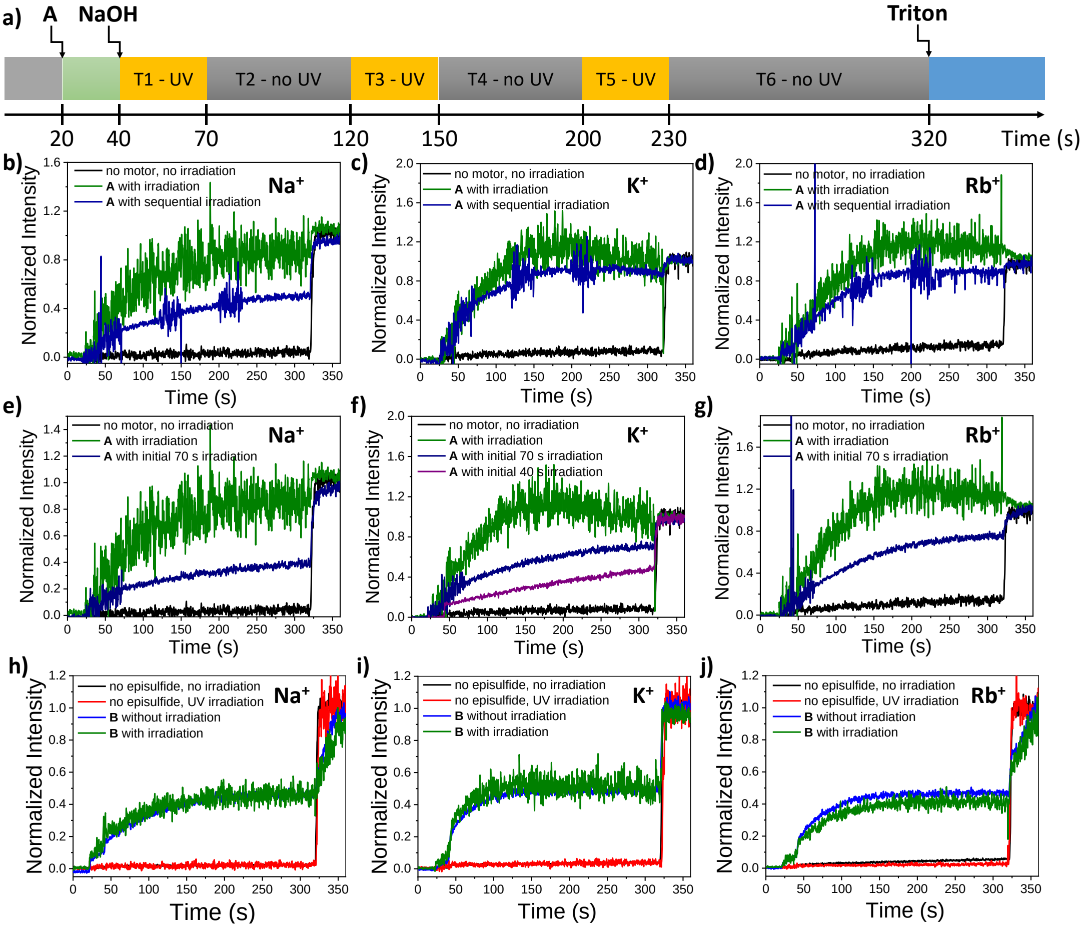

Figure 3. a) Protocole d'irradiation UV séquentielle sur 360 s pour les expériences de transport d'ions : à 20 s, ajout du composé A ; pas d'irradiation UV de 20 à 40 s ; Irradiation UV à 365 nm de 40 à 70 s (T1), 120 à 150 s (T3) et 200 à 230 s (T5) ; pas d'irradiation UV de 70 à 120 s (T2), 150 à 200 s (T4) et 230 à 320 s (T6) ; b-d) Evolution de l'activité de transport d'ions ([A] = 40 µM) en fonction du temps pour les cations b) Na^+, c) K^+ et d) Rb^+ sans irradiation UV (noir), lors d'une irradiation UV continue (rouge) et selon le procédé d'irradiation UV séquentiel (bleu) ; e-g) Evolution de l'activité de transport ([A] = 40 µM) en fonction du temps pour les cations e) Na^+, f) K^+ et g) Rb^+ sans irradiation UV (noir), lors d'une irradiation UV continue (rouge) , selon un processus d'irradiation UV initial de 70 secondes (bleu) et selon le processus d'irradiation UV initial de 40 secondes (violet) ; h-j) Evolution de l'activité de transport en fonction du temps pour les cations h) Na^+, i) K^+ et j) Rb^+ sans irradiation UV et sans épisulfure B (noir), sous irradiation UV mais sans épisulfure B (rouge), en présence d'épisulfure B mais sans irradiation UV (bleu), et en présence d'épisulfure B avec irradiation UV (vert), avec [B] = 100 µM.

Afin d'étudier si le transport nécessite une irradiation continue pour fonctionner, nous avons réalisé des expériences d'irradiation séquentielle. Pour les 3 ions métalliques, l'alternance de périodes sous irradiation UV et sans irradiation conduit à une intensité globale du transport plus faible comparée à une irradiation continue (Figure 3b-d). Ainsi, pour des irradiations de seulement 70 s (Figures 3e-g) ou 40 s (Figure 3f) en début d'expérience, l'activité de transport chute immédiatement après extinction de la lumière, et le régime de transport devient alors comparable à l'expérience de référence « sans lumière » (Figure 2a-c). De plus, les expériences réalisées sous irradiation UV continue ou séquentielle conduisent à un comportement de transport de saturation, du fait de la diminution du gradient de concentration M^+ entre les milieux intra- et extra-vésiculaires, et de l'augmentation de la concentration M^+ dans le milieu intra-vésiculaire. Ces expériences démontrent que la principale force motrice conduisant à l'afflux de cations est le potentiel de concentration transmembranaire, complété par une activation UV spécifique des moteurs moléculaires. Enfin, le transport accéléré des ions métalliques sous irradiation UV s'avère être un processus réversible qui s'interrompt lorsque l'irradiation s'arrête. Des expériences complémentaires de patch-clamp suggèrent la présence d'échanges dynamiques entre les constituants du canal assurant le transport des ions et permettent par ailleurs de démontrer que le transport ne résulte probablement pas du perçage de la membrane.

Ces travaux suggérent que la rotation continue hors équilibre du moteur est à l'origine de l'amélioration des propriétés de transport d'ions, ce qui correspond à un processus de fonctionnement très différent des commutateurs moléculaires déjà décrits pour ces applications.

2. Production d'un travail mécanique par un gel de moteurs moléculaires

L'incorporation de machines moléculaires au sein de réseaux de polymères a permis de démontrer la possible amplification du mouvement moléculaire aux échelles supérieures. En particulier, notre équipe a démontré qu'en incorporant des moteurs moléculaires comme nœuds de réticulation au sein de réseaux de polymères, nous obtenions un gel chimique capable de se contracter sous irradiation UV du fait de la rotation du moteur qui enroule les chaines de polymères.[6, 11] D'autres études ont depuis ouvert la voie à d'autres applications telles que la diffusion contrôlée des gazs ou les dispositifs optiques.[12] A partir de nos connaissances sur les matériaux incorporant des moteurs moléculaires rotatifs activables par la lumière, nous avons envisagé de revêtir la surface d'un polymère inactif par un gel actif afin de permettre une inflexion de la surface polymère inactive sous l'influence d'une irradiation UV.

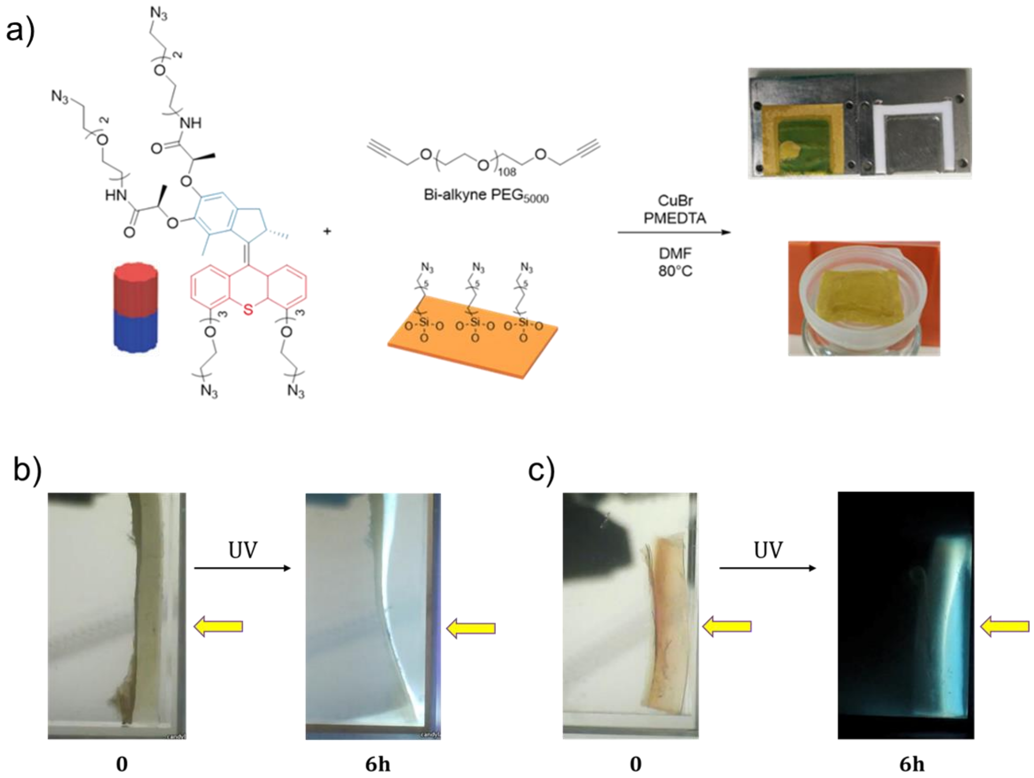

Figure 5. a) Revêtement du gel moteur actif sur une surface polymère inactive. La photographie de droite correspond au gel avant (en haut) et après (en bas) lavage par une solution d'EDTA. Photographies du gel de surface du moteur moléculaire irradié sous lumière UV dans du toluène (b) et de l'eau déminéralisée (c).

Nous avons tout d'abord entrepris la synthèse d'un gel de moteurs moléculaires à la surface d'un film de silicone. Pour cela, nous avons modifié la surface du polymère silicone par des fonctions alcynes (Figure 5a). Cette surface a ensuite été mise en présence d'un moteur moléculaire tétra-alcyne, d'un polymère PEG bis-alcyne dans des conditions de chimie click conduisant à la fonctionnalisation de la surface de silicone par un gel de moteurs moléculaires. Ces surfaces ont ensuite été irradiées sous lumière UV dans le toluène ou dans l'eau déminéralisée. Lorsque l'expérience a été réalisée dans le toluène (Figure 5b), après 6 heures d'irradiation UV, le gel constitué de moteurs est complétement dissous. Dans l'eau déminéralisée, sous irradiation UV pendant 6 heures, le gel présente un léger comportement de flexion (Figure 5c). Cependant, la bande de gel apparait déconnectée de la surface de polymère inactif. Ces résultats suggèrent des problèmes lors de la fonctionnalisation de la surface de silicone.

Néanmois, la possibilité d'actuer le gel dans l'eau déminéralisée sous irradiation UV nous a conduit à étudier le comportement d'un gel autoportant sous irradiation (Figure 6). Ce gel a été synthétisé selon un protocole similaire à celui précédemment décrit dans des moules métalliques de taille 15 × 5 × 2 mm^3 (Figure 6a). L'étude des comportements des gels sous irradiation a été réalisée dans l'eau déminéralisée dégazée. Sous irradiation UV, le gel de moteur moléculaire se courbe vers la source lumineuse. La Figure 6c montre l'évolution de l'angle de flexion du gel en fonction du temps d'irradiation. Initialement, le gel moteur est inactif malgré l'irradiation et ne commence à se plier qu'aux alentours de 60 minutes d'irradiation. Cette observation peut s'expliquer par le temps nécessaire aux moteurs moléculaires pour activer l'enroulement des chaines polymères constituant le réseau (ce qui signifie que les premières torsions ne sont pas efficaces pour les contractions macroscopiques). Lorsque l'état tendu est atteint, le volume du gel commence réduire. Cela signifie que la rotation du moteur moléculaire à l'échelle nanométrique est amplifiée à l'échelle macroscopique. L'angle de flexion θ est maximal après ~5h d'irradiation UV et se maintient sans irradiation UV pendant plus d'une semaine. La vitesse de rotation a été calculée à 0.3°/min. Lorsque l'angle maximum est atteint, la face opposée du gel (i.e. celle n'ayant pas encore été irradiée) a été soumise à la lumière UV. Comme pour la première contraction, le gel se plie en direction de la lumière UV et peut être ramené à sa forme droite initiale. Du fait de la forte tension présente dans le gel contracté, la vitesse du processus de courbure dans le sens opposé est légèrement plus lente (0.24 °/min). Ce processus ne peut cependant pas conduire à une courbure dans le sens opposé après avoir atteint sa forme droite initiale, du fait du caractère unidirectionnel du moteur utilisé.

L'actionnement du gel pouvant être influencé par différents facteurs, nous avons souhaité étudier l'influence de l'intensité lumineuse, ou d'un poids de chargement sur le processus de courbure. En effet, des expériences précédemment réalisées dans notre équipe à la fois en solution et à l'état de gel démontrent que l'intensité lumineuse affecte fortement la vitesse de rotation du moteur moléculaire bien qu'il soit communément admis que l'inversion thermale de l'hélice correspond à l'étape cinétiquement limitante du processus de rotation. Par conséquent, nous avons l'influence de l'intensité lumineuse sur le processus d'actionnement anisotrope du gel.

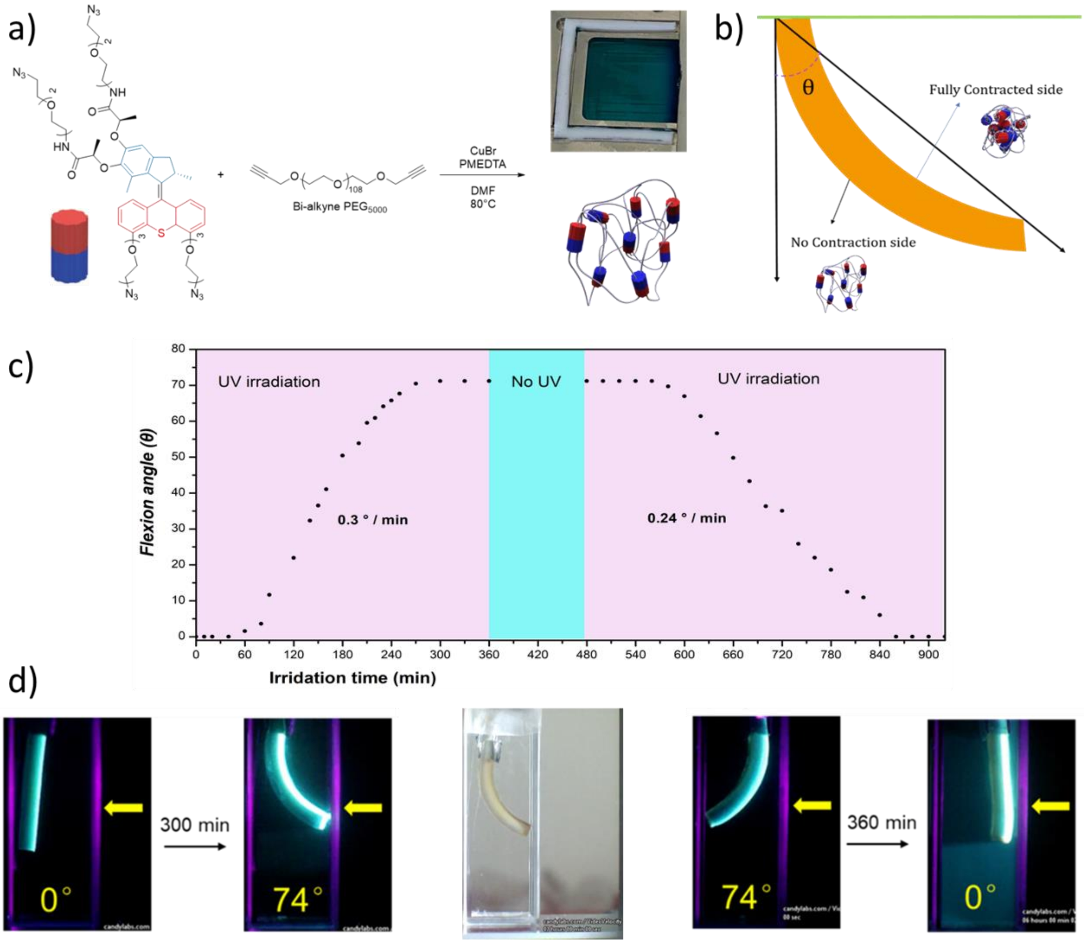

Figure 6. a) Processus de construction de gels constitués de moteurs moléculaires comme points de réticulation. b) Présentation schématique de la flexion de l'hydrogel lors de la photoirradiation sur le côté droit. La lumière ultraviolette induit une diminution de la surface exposée de l'hydrogel, mais la surface du côté non irradié reste dans l'état relaxé d'origine. La contrainte entre les zones exposées et non exposées entraîne une flexion. c) Evolution de l'angle de flexion en fonction du temps d'irradiation de l'hydrogel (puissance du laser : 6.5

mW/cm^2). Les zones violettes et bleues correspondent respectivement à l'irradiation UV et à l’absence d’irradition. d) Photographies de l'hydrogel avant irradiation et irradié durant 300 min sous lumière UV, la chaîne d'hydrogel du moteur moléculaire se penche vers la droite. L’irradiation durant 360 min sur la face non irradiée initialement permet de revenir à l’état initial.

Le comportement en flexion du gel décrit en Figure 6a sous différentes intensités lumineuses a été réalisé dans l'eau. Les gels utilisés dans les expériences provenaient du même lot de gel. Comme le montre la Figure 7a, plus l'intensité lumineuse augmente, plus la vitesse de flexion du gel augmente. Lorsque le gel est exposé à une intensité lumineuse de 1.6 mW/cm^2, l'angle de flexion atteint 9.2° après 230 min (0.04°/min). Lorsque l'intensité lumineuse augmente à 6.5 mW/cm^2, l'angle de flexion peut atteindre à 51.9° après 270 min (0.19 °/min). Pour une intensité lumineuse de 13 mW/cm^2, le gel peut être actionné beaucoup plus rapidement: 43.2° après 100 min (0.43°/min). Lorsque l'intensité lumineuse atteint 19.8 mW/cm^2, le gel peut atteindre un angle de flexion de 45.9° (0.46°/min). Ces résultats montrent que l'intensité lumineuse influence le comportement de flexion du gel, notamment la vitesse de flexion et l'angle de flexion maximal.

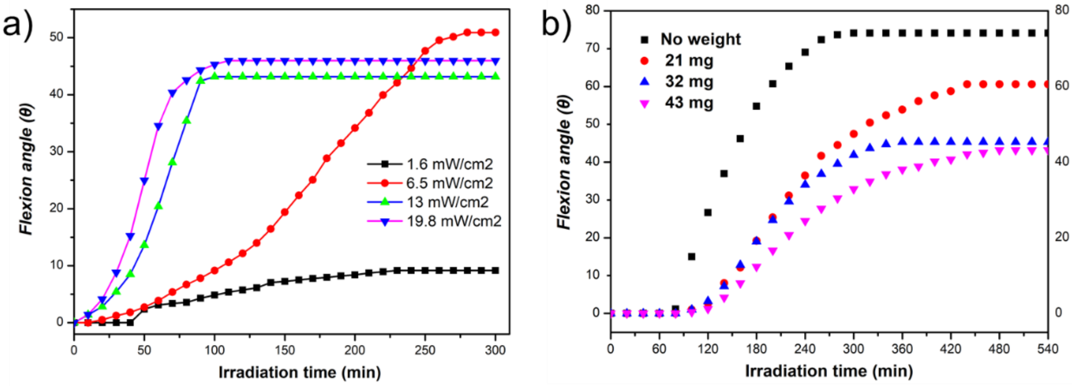

Figure 7. Relation entre l'angle de flexion et le temps d'irradiation a) sous différentes intensités lumineuses ; b) avec des poids différents pour les gels formés selon le processus décrit en Figure 6a.

Comme démontré dans des publications précédentes,[6] les moteurs moléculaires présents dans un gel chimiques peuvent induire une importante contraction du gel sous irradiation par lumière UV. Cependant, l'extraction du travail réalisé par ces hydrogels n'a jamais été déterminé. Pour cela, nous avons fixé un poids en bas du gel et étudié l’évolution de l’angle de flexion en fonction du temps d’irradiation (Figure 7b). Malgré la présence de poids à l'extrémité du gel, le processus d'actionnement sous irradiation UV s’avère toujours efficace. Cependant, plus la masse du poids augmente, plus la vitesse d’actionnement du gel et l’angle de flexion diminuent. Ces résultats démontrent l’influence du poids sur la mobilité du gel sous irraidation.

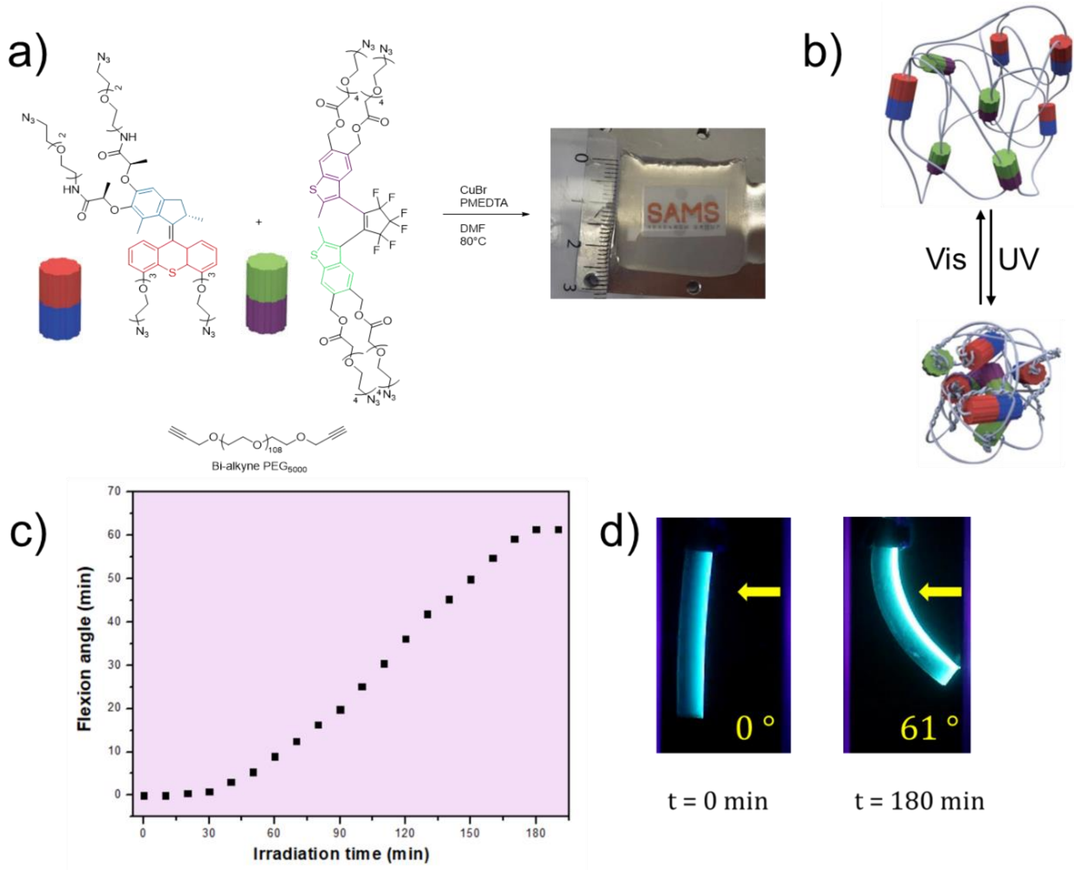

Figure 8. a) Structures chimiques des moteurs et modulateurs mis en jeu pour former un gel contractile réversible. b) Représentation schématique du comportement d'un gel contractile contenant moteurs et modulateurs comme uintés de réticulation sous irradiation UV et sous lumière visible. c) Evolution de l'angle de flexion en fonction du temps d'irradiation du gel contenant moteurs et modulateurs. d) Photographies du comportement du gel réversible dans l'eau. L'irradiation UV par la droite conduit à une flexion vers la source lumineuse de 0° à 61° en 180 min.

Un gel comportant des unités orthogonales de type moteurs moléculaires et modulateurs a ensuite été synthétisé.[11] Sous irradiation UV (365 nm), le gel peut atteindre un angle de flexion maximal de 61°. Il est à noter que, dans cette expérience, le modulateur était sous forme ouverte car aucune irradiation UV (312 nm) n'avait été appliquée. La raison pour laquelle le gel peut fléchir malgré la présence d'un modulateur sous forme ouverte s'explique par le fait que la quantité d'unité motrice est bien plus importante que l'unité modulatrice (moteur : modulateur = 9:1). La vitesse d'enroulement causée par le moteur est supérieure à la vitesse de libération causée par le modulateur, par conséquent, le système est poussé loin de l'équilibre, ce qui entraîne la flexion de l'hydrogel.

Ce résultat est très intéressant car il confirme la possibilité d'actionner des matériaux autoportés grâce à notre approche moteur-modulateur. Pour tirer pleinement parti de ce système, des expériences sont en cours pour observer une flexion entièrement réversible dans les deux sens par des irradiations UV séquentielles.

3. Conclusion générale

Le domaine émergent des machines moléculaires artificielles est particulièrement attractif en raison de son potentiel unique pour contrôler l'actionnement mécanique et le travail à l'échelle nanométrique. Les moteurs moléculaires rotatifs initialement développés par l’équipe du Prof. Feringa sont devenus l'un des objets dynamiques les plus importants de cette grande famille car ils sont sensibles à la lumière, avec des avantages évidents tels que leur caractère non invasif et la possibilité de contrôle à distance, mais également parce qu'ils peuvent, en principe, produire un travail continu sur leur environnement (même si très peu d'exemples pratiques ont été effectivement développés jusqu'à présent). Dans ce manuscrit de thèse, après avoir résumé l’état de l’art dans le domaine des machines moléculaires, j'ai décrit les avancées que j'ai réalisées sur deux sujets principaux liés aux applications de ces machines moléculaires en exploitant ces deux principaux atouts.

Dans le deuxième chapitre, j'ai décrit le transport d'ions stimulé par des moteurs moléculaires insérés au sein d’une membrane bicouche lipidique. Bien qu'une série de machines moléculaires artificielles telles que la navette moléculaire et les molécules à base d'azobenzène aient déjà été étudiées pour ces applications, le transport d'ions basé sur des moteurs moléculaires hors équilibre n'avait jamais été décrit dans la littérature. La conception et la synthèse de moteurs moléculaires combinés à des macrocycles benzo-18-crown-6 ont permis de contribuer à ce développement. Cette molécule relativement hydrophobe peut être insérée dans les bicouches phospholipidiques au sein desquelles les éthers-couronnes peuvent s'auto-assembler en canaux ioniques, conduisant à un transport sélectif des ions alcalins. Lorsque la lumière UV est appliquée au système, le taux de transport peut être fortement augmenté (jusqu'à 400 %) tout en conservant sa sélectivité. Sur la base de tests de fluorescence HPTS, de mesures Patch-clamp et d'un certain nombre d'expériences de contrôle, cet effet stimulant a été attribué à la rotation continue des moteurs moléculaires, un mécanisme totalement différent de ceux impliquant des commutateurs moléculaires basés sur des changements de configuration/conformation à l'équilibre thermodynamique. Ce travail décrit le premier transporteur d'ions artificiel basé sur un moteur moléculaire, et devrait avoir un impact fondamental important dans le domaine des machines moléculaires, avec des applications potentielles dans le domaine du transport moléculaire.

Outre leur utilisation à l'échelle nanométrique, les moteurs moléculaires artificiels ont également été récemment appliqués dans le monde macroscopique. La construction de matériaux conjuguant des moteurs moléculaires à des chaines de polymères a permis d’ouvrir la voie au développement de matériaux hors d'équilibre stimulables. Ainsi, dans le troisième chapitre, j’ai décrit la synthèse et l’étude du comportement de gels contractiles autoportés contenant des moteurs rotatifs comme unités de réticulation actives. Sous lumière UV, ces gels peuvent être courbés de manière anisotrope vers la source lumineuse à un angle important et générer un travail. En plaçant un poids à l’extrémité basse du gel, le poids peut être soulevé avec succès pendant l'irradiation et le travail produit - provenant à nouveau de l'actionnement hors d'équilibre du moteur - peut atteindre des valeurs beaucoup plus élevées que pour l'autre système existant à ce jour dans la littérature.[13] De plus, un « modulateur » moléculaire a pu être combiné avec succès dans ce gel moteur, permettant la régulation du processus d'actionnement du gel afin de le rendre entièrement réversible. Les premières expériences montrent qu'un tel système moteur-modulateur peut revenir à son état initial, et des expériences sur l'actionnement en va-et-vient sont actuellement en cours. Une détermination complète du travail et de la puissance produite par les deux types de matériaux (avec et sans modulateur) sera alors effectuée pour compléter cette étude.

References :

[1] Mehta, A. D. Single-Molecule Biomechanics with Optical Methods. *Science* **1999**, *283* (5408), 1689–1695.

[2] García-López, V.; Liu, D.; Tour, J. M. Light-Activated Organic Molecular Motors and Their Applications. *Chem. Rev.* **2020**, *120* (1), 79–124.

[3] Lancia, F.; Ryabchun, A.; Katsonis, N. Life-like Motion Driven by Artificial Molecular Machines. *Nat. Rev. Chem.* **2019**, *3*, 536–551.

[4] Dattler, D.; Fuks, G.; Heiser, J.; Moulin, E.; Perrot, A.; Yao, X.; Giuseppone, N. Design of Collective Motions from Synthetic Molecular Switches, Rotors, and Motors. *Chem. Rev.* **2020**, *120* (1), 310–433.

[5] Li, Q.; Foy, J. T.; Colard-Itté, J.-R.; Goujon, A.; Dattler, D.; Fuks, G.; Moulin, E.; Giuseppone, N. Gram Scale Synthesis of Functionalized and Optically Pure Feringa's Motors. *Tetrahedron* **2017**, *73* (33), 4874–4882.

[6] Li, Q.; Fuks, G.; Moulin, E.; Maaloum, M.; Rawiso, M.; Kulic, I.; Foy, J. T.; Giuseppone, N. Macroscopic Contraction of a Gel Induced by the Integrated Motion of Light-Driven Molecular Motors. *Nature Nanotech* **2015**, *10* (2), 161–165.

[7] Schneider, S.; Licsandru, E.-D.; Kocsis, I.; Gilles, A.; Dumitru, F.; Moulin, E.; Tan, J.; Lehn, J.-M.; Giuseppone, N.; Barboiu, M. Columnar Self-Assemblies of Triarylamines as Scaffolds for Artificial Biomimetic Channels for Ion and for Water Transport. *J. Am. Chem. Soc.* **2017**, *139* (10), 3721–3727.

[8] Qu, D.-H.; Wang, C.; Wang, S.; Yang, H.; Xiang, Y.; Wang, X.; Bao, C.; Zhu, L.; Tian, H. A Light-Operated Molecular Cable Car for Gated Ion Transport. *Angew. Chem. Int. Ed.* **2021**, DOI: 10.1002/anie.202102838.

[9] García-López, V.; Chen, F.; Nilewski, L. G.; Duret, G.; Aliyan, A.; Kolomeisky, A. B.; Robinson, J. T.; Wang, G.; Pal, R.; Tour, J. M. Molecular Machines Open Cell Membranes. *Nature* **2017**, *548* (7669), 567–572.

[10] Wang, W.-Z.; Huang, L.-B.; Zheng, S.-P.; Moulin, E.; Gavat, O.; Barboiu, M.; Giuseppone, N. Light-Driven Molecular Motors Boost the Selective Transport of Alkali Metal Ions through Phospholipid Bilayers. *J. Am. Chem. Soc.* **2021**, 143 (38), 15653–15660.

[11] Foy, J. T.; Li, Q.; Goujon, A.; Colard-Itté, J.-R.; Fuks, G.; Moulin, E.; Schiffmann, O.; Dattler, D.; Funeriu, D. P.; Giuseppone, N. Dual-Light Control of Nanomachines That Integrate Motor and Modulator Subunits. *Nature Nanotech* **2017**, *12* (6), 540–545.

[12] Danowski, W.; van Leeuwen, T.; Abdolahzadeh, S.; Roke, D.; Browne, W. R.; Wezenberg, S. J.; Feringa, B. L. Unidirectional Rotary Motion in a Metal–Organic Framework. *Nature Nanotech* **2019**, *14* (5), 488–494.

[13] Chen, J.; Leung, F. K.-C.; Stuart, M. C. A.; Kajitani, T.; Fukushima, T.; van der Giessen, E.; Feringa, B. L. Artificial Muscle-like Function from Hierarchical Supramolecular Assembly of Photoresponsive Molecular Motors. *Nature Chem* **2018**, 10 (2), 132–138.

Wenzhi WANG

Synthèse et auto-assemblage de moteurs moléculaires aux interfaces

Résumé

Dans cette thèse, nous avons décrit deux exemples basés sur le moteur moléculaire entraîné par la lumière de Feringa, qui effectue un travail continu avec des avantages non invasifs et de contrôle à distance. Dans le premier chapitre, une série de machines moléculaires artificielles représentatives ont été décrites, en particulier le moteur moléculaire de Feringa entraîné par la lumière. Les principales applications de ces moteurs rotatifs sont également présentées. Le deuxième chapitre décrit comment les moteurs moléculaires synthétiques peuvent stimuler sélectivement le transport des ions. Le composé à base de moteur révèle une bonne activité de transport pour les ions alcalins en raison de la propriété d'auto-assemblage de la molécule et de la cavité des macrocycles d'éther couronne. Sous irradiation UV, l'activité de transport est fortement améliorée, en raison de la rotation du moteur moléculaire. Une série d'expériences telles que le test de fluorescence HPTS et le patch-clamp ont été réalisées et prouvent cette observation sans précédent. En particulier, un certain nombre d'expériences de contrôle montre comment la rotation hors équilibre du moteur moléculaire joue un rôle important dans le transport des ions. Le troisième chapitre se concentre sur le mouvement collectif de moteurs moléculaires rotatifs individuels réticulés dans des gels chimiques. Les gels contractiles rapportés précédemment ont été optimisés et utilisés pour des actionnements macroscopiques et anisotropes afin d'effectuer des tâches de levée de poids. Les résultats montrent que de tels gels peuvent subir un actionnement directionnel parfait avec une force élevée. La dernière partie de ce manuscrit est consacrée aux protocoles expérimentaux et aux descriptions de nouveaux produits chimiques.

Mots-clés: Moteur moléculaire entraîné par la lumière, transport d'ions, rotation hors équilibre, mouvement collectif, gel contractile, actionnement anisotrope, contraction macroscopique.

Résumé en anglais

In this thesis, we described two examples based on Feringa's light-driven molecular motor, which performs continuous work with non-invasive and remote control advantages. In the first chapter, a series of representative artificial molecular machines have been described, especially Feringa's light-driven molecular motor. The prominent applications of these rotary motors are also introduced. The second chapter describes how synthetic molecular motors can selectively boost ion transportation. The motor-based compound reveals good transportation activity for alkali ions because of the self-assembly property of the molecule and the cavity of the crown ether macrocycles. Under UV irradiation, the transportation activity is highly enhanced, owing to the rotation of the molecular motor. A series of experiments such as the HPTS fluorescence test and patch-clamp has been performed and prove this unprecedented observation. In particular, a number of control experiments supports how the out-of-equilibrium rotation of the molecular motor plays an important role in ion transportation. The third chapter is focused on the collective motion of individual rotary molecular motors crosslinked in chemical gels. Contractile gels reported previously have been optimized and used for macroscopic and anisotropic actuations in order to perform weight lift-up tasks. The results show that such gels can undergo perfect directional actuation with high force. The last part of this manuscript is dedicated to experimental protocols and descriptions of new chemical products.

Keywords: Light-driven molecular motor, ion transportation, out-of-equilibrium rotation, collective motion, contractile gel, anisotropic actuation, macroscopic contraction.